OPTICAL PROPERTIES AND PHOTOLUMINESCENCE QUANTUM YIELDS OF CARBON NANOTUBE DISPERSIONS

DAVID RICKARD

A thesis submitted for the degree of
Doctor of Philosophy

School of Physics

Trinity College

University of Dublin

2011

DECLARATION

I declare that this work has not previously been submitted as an exercise for a degree at this or any other university.

Furthermore, I declare that the work here submitted is entirely my own, save for where I have received assistance and acknowledged as much in the text and where I have collaborated on the listed publications.

I hereby agree that the Library of Trinity College Dublin may lend or copy this thesis upon request.

Dedicated to my parents,

Joseph and Evelyn,

and to my godparents,

Derek and Hillary.

Try to learn something about everything and everything about something.

Thomas Henry Huxley

Le mieux est l'ennemi du bien—The perfect is the enemy of the good.

Voltaire

I hate quotation. Tell me what you know.

Ralph Waldo Emerson

SUMMARY

The absorbance and photoluminescence (PL) spectra of single-walled carbon nanotubes (SWNTs) dispersed in deuterium oxide (D_2O) using various surfactants were examined in order to estimate the photoluminescence quantum yield (PLQY) of individual species of SWNT present in the dispersion.

The susceptibility of our experimental set-up to effects caused by the concentration-dependent inner-filter effect was examined. A fluorescent polymer with a well-documented aggregation state, PFO, was used as a model system. A theoretical model describing the behaviour of PL intensity as a function of sample absorbance of both the excitation beam and emitted fluorescence was developed. This model was applied to PL data for PFO in numerous solvents, with the change in concentration and solvent providing control over both absorbance and aggregation. It was found that our experimental set-up could provide accurate PL data free from inner-filter effects up to a 1 cm sample absorbance of approximately 1, and that our predicted PL intensities matched those recorded from samples with an absorbance of at least 10.

Analysis of our model polymer system dispersed in solvents of varying suitability—identified by Hildebrand solubility parameters—permits the isolation of inner-filter effects from those of aggregation, which are similarly detrimental to measured PL intensity. It is shown that the deviation from theory in the behaviour of PL as a function of concentration can be correlated with aggregation, whereas our approach is sufficient to model

PL from samples with absorbance values up to the limits mentioned above when aggregation is not a factor.

Absorbance and photoluminescence data for dispersions of SWNTs in D_2O were recorded, in the regime for which the inner-filter effects explored above were negligible. In order to correlate PL data with absorbance, a method of deconvoluting the absorbance and PL spectra of ensemble dispersions of SWNTs was developed. A method previously developed elsewhere describing the analysis of absorbance spectra and their reduction to contributions from different species of SWNT was adapted and expanded on. A similar method was applied to the deconvolution of the PL excitation-emission data. Atomic force microscopy was employed to estimate the proportion of individualised tubes in the dispersion.

A piece of MATLAB code was developed to combine and correlate this data and produce an estimate for the relationship between absorbance and PL for individualised tubes of numerous different SWNT species. Measurements under identical experimental conditions of absorbance and PL data for fluorescent dyes of known quantum yield value allow the estimation of absolute PLQY values of the SWNT species. This analytical approach was successfully applied to a range of SWNT dispersions in surfactants and other dispersant media, yielding data for E_{11}^S and E_{22}^S transition energies, amplitudes and widths.

The effect of centrifugation time on measured PLQY values from a series of dispersions using the surfactant SDS was investigated, as was the effect of a change in dispersion environment through a change in surfactant and solvent. Trends in PLQY were examined in terms of nanotube diameter and wrapping angle, and compared to those predicted in the current literature. The highest PLQY values estimated approached 1.5 %, which is in line with values published elsewhere.

ACKNOWLEDGEMENTS

Foremost among those whom I wish to mention are my supervisors, Profs. Werner Blau and Jonathan Coleman. I would like to thank them both for allowing me the opportunity to work with them and their groups, and for overseeing groups with such a pleasant and welcoming environment. In particular Prof Coleman has been outstanding over the last couple of years, steering my work as it encountered numerous ups and downs and seemingly interminable issues, small and large. I am sure I am not the only one who is glad to see this thesis finally complete. I hope their faith will be in some way rewarded, despite the tenuous link between the project I set out to work on and the work I submit here.

In science as in life, there is more to be gained from sharing than proceeding in isolation. Over these last few years I have had the pleasure of working alongside some very fine people, both as colleagues and as friends, and I would like to thank them all for what they have contributed to my work and my time here. For making everything from lunches and ice-creams in the sun to early mornings and late nights in the lab more enjoyable, I am most grateful.

Working in such a large group has given me many names to highlight for their particular contributions, as office-mates, advisers, footballers and serious scientists: Darren Lee, Niall McEvoy, Mustafa Lotya, Brian Tuffy, Paul King, Peter May, Sophie Sorel, Arlene O'Neill, Paula Russel-Hill, Ronan Smith, Evelyn Doherty, Karen Young, Marguerite Hughes, Fiona Blighe, Helen Cathcart, Shane Bergin, Edward Moore, Trevor Woods, Anna

Drury, Umar Khan, Sukanta De, Zhenyu Sun, Robert Murphy, James Doyle, Denis McCarthy, Silvia Giordani and Valeria Nicolosi have all played their part. Thanks also to Connie Crowley-Cribben and Alex Young in the Schools of Microbiology and Genetics, respectively, for allowing me access to their ultracentrifuge apparatus.

I have made many close friends in College away from the group, some of whom I am sure have both helped and hindered my academic progress. I would like to acknowledge the friendship and support of Ryan Hanley, Emma Siddall, Eoin Naughton, Louise McGuigan, Darren Caulfield, Elaine Breen, Cian Ó Móráin, Sophie Davies and David Misstear for making these years what they were. Sophie deserves special mention for her unwavering support, love and patience, which was more than I could have asked for.

I wish to thank sincerely my family: my brother Brian and sister Laura, and in particular my parents Joe and Evelyn. They have always allowed me and encouraged me to pursue something I enjoy simply because I enjoy it, trusting me to make the most of my opportunities regardless of how far-fetched my ideas may seem. Their steady and unquestioning support has always been a source of great strength. They have always been proud of anything I have done, but in truth I am more proud of them.

Thank you.

PUBLICATIONS

Some ideas and figures submitted here have appeared previously in the following publications:

- "Observation of Extremely Low Percolation Threshold in $MoS_4 \cdot 5I_4 \cdot 5$ nanowire/polymer composites" Coleman, J.N., Murphy, R., Nicolosi, V., Hernandez, Y., McCarthy, D., Rickard, D., Vrbanic, D., Mrzel, A., Mihailovic, D., Blau, W.J. *Scripta Materialia 54 (3), 416–420* (2006)
- "Large Populations of Individual Nanotubes in Surfactant-Based Dispersions Without the Need for Ultracentrifugation," Bergin, S.D., Nicolosi, V., Cathcart, H., Lotya, M., Rickard, D., Sun, Z., Blau, W.J., Coleman, J.N. *Journal of Physical Chemistry C 112 (4), 972–977* (2008)
- "Quantifying the contributions of inner-filter, re-absorption and aggregation effects in the photoluminescence of high-concentration polymer solutions," Rickard, D., Giordani, S., Blau, W.J., Coleman, J.N. *Journal of Luminescence 128 (1), 31–40* (2008)
- "Quantitative evaluation of surfactant-stabilized single-walled carbon nanotubes: Dispersion quality and its correlation with zeta potential," Sun, Z., Nicolosi, V., Rickard, D., Bergin, S.D., Aherne, D., Coleman, J.N. *Journal of Physical Chemistry C 112 (29), 10692–10699* (2008)
- "Multicomponent solubility parameters for single-walled carbon nanotube–solvent mixtures," Bergin, S.D., Sun, Z., Rickard, D., Streich, P.V., Hamilton, J.P., Coleman, J.N. *ACS Nano 3 (8), 2340–2350* (2009)
- "Measurement of Multicomponent Solubility Parameters for Graphene Facilitates Solvent Discovery," Hernandez, Y., Lotya, M., Rickard, D., Bergin, S.D., Coleman, J.N. *Langmuir 26 (5) 3208-3213* (2010)

CONTENTS

LIST OF FIGURES

LIST OF TABLES

1 INTRODUCTION

A brief introduction to the subject of carbon nanotubes is given in Section 1.1, highlighting their physical properties and indicating how the work presented here relates to current research in nanotube physics. Section 1.2 provides an outline of the topics explored in the remainder of this thesis.

1.1 BACKGROUND AND MOTIVATION

Since their discovery by Iijima in 1991 [94], carbon nanotubes have been the subject of intense research.* Interest has been fuelled by their unique properties and their illustration of the promise and possibilities of the developing field of nanotechnology. While the dimensions alone of carbon nanotubes are noteworthy—with diameters and lengths on the order of nanometres and microns, respectively, they have widths tens of thousands of times narrower than the average human hair and can be many thousands of times as long as they are wide—it is comparison of their physical and electronic properties with those of more well-known materials that highlights their appeal to scientists and engineers. Carbon nanotubes exhibit extraordinary strength and stiffness: at a strength of $\sim 50\,\mathrm{GPa}$ and with a Young's modulus of the order of 1.0 TPa they are approximately fifty times stronger than steel and five times stiffer [221, 203, 222]; with

* While Iijima's paper was influential in increasing awareness of carbon nanotubes, they had been observed in several papers over the preceding decades. See References [31] and [150] for a more detailed discussion.

a density† of only 1800 $kg \cdot m^{-1}$, they are one-quarter the density of steel and two-thirds as dense as aluminium. Nanotubes have high thermal conductivities, measured at 6600 $W \cdot m^{-1} \cdot K^{-1}$ [19], an order of magnitude greater than most metals and several times higher than carbon in the form of diamond or single graphite layers [18]. Carbon nanotubes occur in both semiconducting and metallic varieties [178]: semiconducting tubes exhibit first-order band-gaps in the near-infrared and optical region [217]; the metallic variety have been shown to exhibit ballistic conduction of electrons [215, 168], and with measured current densities of 10^9 $A \cdot cm^{-2}$ they have carried the highest current densities yet measured, thousands of times that which would damage common metals [218, 136].

These unusual properties of carbon nanotubes have led to intense research interest regarding both the fundamental physics involved and potential applications. The use of nanotubes in nanoscale electronic devices [1] and as the building blocks of transistors [211, 201], as filler material in polymer composites to enhance electrical conductivity [112, 3], thermal properties [28] and mechanical strength [53, 49], and as chemical and biological sensors [114, 209, 210] along with many other applications have all been explored [18, 79]. One aspect of nanotubes' behaviour that has limited their use is the tendency to aggregate into bundles or ropes of tubes. Many of the remarkable properties of nanotubes hold true for specific types of tubes or for individual tubes only. Aggregation of tubes can partially negate many of their most promising features: relative movement of tubes in a bundle results in a composite strength and toughness far below that of individual tubes [36]; close contact of metallic and semiconducting tubes means the bundles act as metallic ropes, but with a lower conductivity

† See the supporting information accompanying reference 23 for details regarding the volumetric mass of HiPCO nanotubes.

than an individual metallic tube [202]. The ability to separate nanotube types from each other and to actively select tube types based on structural and electronic properties remains one of the greatest challenges to their widespread adoption in more everyday applications [8, 133, 63, 193, 32].

For many applications dispersion of nanotubes in a host material matrix is desirable, either as a processing step or as an overall goal. Solutions of dispersed nanotubes were considered until relatively recently difficult to produce due to the general insolubility of nanotubes and their high aggregation rate. Progress has been made on a number of fronts in this regard. Nanotubes have been functionalised, i.e. chemically altered or bonded to smaller molecules which will increase their solubility [185, 30]. The use of chemical and biological molecules to act as surfactants, i.e. coating the nanotubes with a material which will allow it to be dispersed in water or other solvents, has become common [21, 70, 227]. Recent work suggests the correct choice of solvent alone enables nanotubes to become soluble [69, 23, 25]. Once in solution, efforts have been made to separate nanotubes into different types [60, 51, 75, 8].

The dispersion state of nanotubes in a solution is monitored easily and non-destructively using optical spectroscopy [159, 98, 62]. Carbon nanotubes are strong absorbers of electromagnetic radiation, with different tube types displaying signature peaks in absorbance at particular energies corresponding to the van Hove peaks in their electronic density of states. A dispersion of many types of tube exhibits an absorption spectrum which is the superposition of many such peaks, while the peak intensity and resolution can be used to estimate the relative populations of different tube types [181, 152, 140] and the extent to which they are individually dispersed [91, 21]. Further complications arise from the presence of 'background' absorbance not due to the strong signature peaks of specific tube

types [107], and so estimating the precise contribution to the ensemble dispersion of one tube type is not straightforward [171, 152, 160].

In 2003 O'Connell *et al.* measured the photoluminescence from nanotubes dispersed in a surfactant-aided deuterium oxide (D_2O, deuterated water or 'heavy water') solution, and spectral features were later assigned to various semiconducting tube types [159, 15]. Photoluminescence spectroscopy allows us to probe the quality of dispersion achieved and the quality of the nanotube sample used [98, 97]. Bundles containing both metallic and semiconducting tubes are unlikely to fluoresce as the contacting metallic tubes will provide additional potential non-radiative relaxation pathways for semiconducting tubes, quenching the emission. Similarly, tubes with many defects will have many non-radiative relaxation pathways for excited electron-hole pairs and will thus exhibit a lower emission intensity [129].

In order to make comparisons between photoluminescence spectroscopy measurements taken in various local solution environments and taken using different instruments, several issues must be addressed. Corrections for various instrumental artefacts are relatively common [120, 145, 122], but the lack of a well-defined standard scale for photoluminescence intensity makes comparing several measurements from different instruments difficult. For comparisons of intensity of emission from different tube types, it is essential to have some knowledge of their photoluminescence quantum yield (their 'conversion efficiency' from light absorbed to light emitted). Current literature resources regarding the photoluminescence quantum yield of carbon nanotubes are very much incomplete. Reported values range over several orders of magnitude [159, 104], with a lack of consistency regarding procedures and methods of analysis [194], as outlined in more detail in 2.2.5.

This thesis deals with several of the issues mentioned above: in outlining a procedure for measuring the photoluminescence quantum yield of semiconducting single-walled carbon nanotubes, it is necessary to deal with the problems of concentration, aggregation and instrumental effects, of dealing with several tube types in an ensemble solution, and of interpreting the absorbance and photoluminescence spectra in terms of contributions from specific tube types.

Much of the analysis has been automated through the use of a custom-written MATLAB program, and this approach could aid in comparative analysis of large numbers of samples, containing many distinct types of carbon nanotube, by other groups.

The approach to measuring photoluminescence quantum yield values developed here is then applied to dispersions of carbon nanotubes in different surfactant environments. Estimates of quantum yield values for a range of carbon nanotube species in various dispersions are produced, discussed, and compared to theoretical predictions relating to both the variation of quantum yield with nanotube species and the effect of environment on the exhibited quantum yield.

1.2 THESIS OUTLINE

CHAPTER TWO The essential background theory of carbon nanotubes and their properties is explained. An overview of the current literature is presented.

CHAPTER THREE Details on the materials used throughout the work and on the various methods of analysis are provided.

CHAPTER FOUR The effects of solution concentration on the measured photoluminescence of a solution are examined, and methods to predict and account for non-linear effects in the high-concentration regime such as inner-filter and re-absorption effects are detailed.

CHAPTER FIVE Work carried out on the measurement of photoluminescence quantum yield of ensembles of SWNTs through the deconvolution of both absorbance and photoluminescence spectra is introduced, and the MATLAB program written to aid this analysis is explained.

CHAPTER SIX The quantum yield measurement developed above is applied to solutions of carbon nanotubes dispersed using SDS under a variety of preparation conditions; variations in the estimated PLQY values of a range of nanotube species are explored.

CHAPTER SEVEN This method of analysis is extended to dispersions of SWNTs in a variety of dispersant media, and the effect of dispersant media on the optical properties and PLQY values of numerous tubes in an ensemble dispersion is examined.

CHAPTER EIGHT A review of the main results is presented, along with a discussion of future work.

INTRODUCTORY THEORY AND LITERATURE REVIEW

2

Section 2.1 contains background information and theoretical foundations for the properties of nanotubes, emphasising topics of relevance to the experimental work presented later. The current literature on dispersions, photoluminescence and photoluminescence quantum yields of carbon nanotubes is reviewed in Section 2.2.

2.1 INTRODUCTORY THEORY OF CARBON NANOTUBES

2.1.1 *Discovery and Synthesis*

Carbon nanotubes gained widespread exposure through the work of Sumio Iijima, whose 1991 paper [94] showed transmission electron microscope images of carbon nanotubes found in the soot deposited at graphitic electrodes during the arc-evaporation production of fullerenes [117]. Carbon nanotubes are essentially long, cylindrical macromolecules of carbon, closed at each end. Like fullerenes, they are an elemental form of carbon, and thus an allotrope of more well known forms such as graphite and diamond.

The atomic structure of carbon nanotubes is similar to a rolled-up single layer of graphite—termed a *graphene* sheet—capped at both ends. Single-walled carbon nanotubes (SWNTs) have diameters ranging from ~ 0.5–$2\,\text{nm}$, while their lengths can be up to the millimetre range [92], giving them an aspect ratio (the ratio of length to diameter) that can exceed 1×10^6. Multi-

walled carbon nanotubes (MWNTs) consist of several concentric tubes, resembling 'nested' SWNTs, with outer diameters of tens of nanometres. Iijima's initial 1991 paper showed MWNTs, while SWNTs were observed by the same author in 1993 [95].

Several methods of production of SWNTs have been demonstrated. The most common methods currently in use are: the arc-discharge method [27, 103], in which carbon nanotubes are formed from sublimation of carbon in graphite electrodes caused by high temperatures found at the electrode during discharge; laser ablation [202], i.e. using a pulsed laser striking a graphite target to vapourise carbon atoms, which form nanotubes as they condense; and the chemical vapour deposition (CVD) method [52, 46, 132].

In the CVD process, gaseous hydrocarbons are mixed with an inert carrier gas and passed over a catalyst in a furnace heated to between 600° C and 1100° C for several hours. When hydrocarbons are exposed to sufficiently high temperatures they can decompose, a reaction known as pyrolysis. The HiPCO (**hi**gh **p**ressure **c**arbon mon**o**xide) variant of CVD involves the decomposition of $Fe(CO)_5$ to produce Fe clusters which act as nucleation sites for the growth of nanotubes via the disproportionation of carbon monoxide [156]:

$$CO + CO \longrightarrow CO_2 + C \ (\dashrightarrow \text{nanotubes})$$

Amorphous carbon and graphite are also commonly formed during CVD; as well as temperature and pressure the size and nature of the catalytic particles have a profound effect on the resulting yield of nanotubes, their dimensions and the number of defects they contain [134, 41].

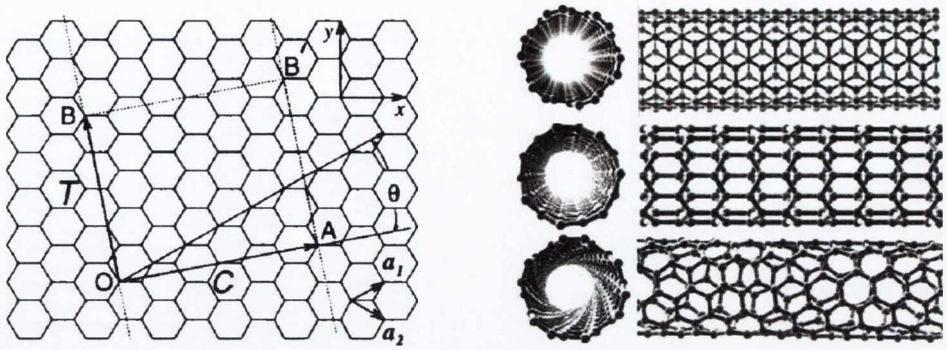

(a) (b)

Figure 1: The relationship between the 2D atomic structure of graphene and the different (*n*,*m*) indices of SWNTs. (a) The hexagonal atomic structure of graphene, with the unit cell of a (4, 2) SWNT depicted by the rectangle $OAB'B$. (b) Representative classes of SWNT. From top: armchair, zig-zag and chiral nanotubes, showing cross section and side view (without caps). (Adapted from references 18, 178).

2.1.2 *Physical Structure*

Carbon nanotubes have an atomic structure identical to that of a seamlessly rolled up sheet of graphene. Starting with a flat graphene sheet, there are many ways of 'rolling up' this sheet to form the structure of a carbon nanotube, and thus there are many different 'species' of nanotube. These species are defined by their *(n, m) index*. In describing the physical and geometric characteristics of nanotubes, the work of Mildred Dresselhaus and co-workers is particularly instructive [178, 57].

Figure 1a represents the hexagonal lattice arrangement of the carbon atoms in a flat sheet of graphene. In order for the resulting carbon nanotube to be seamless along its length, the vector representing the circumference of the tube must map a carbon atom in this lattice to an equivalent atom in the lattice (in Figure 1a, O to A and B to B'), and must do this for all atoms along the line representing the nanotube's length (the line OB). This

vector is known as the wrapping vector, **C**, and can be resolved into two unit vectors $\hat{\mathbf{a}}_1$and $\hat{\mathbf{a}}_2$ at an angle of 60° as shown. The wrapping angle θ is defined as the angle between **C** and $\hat{\mathbf{a}}_1$; the symmetry of the hexagonal graphene sheet limits the value of θ to between 0° and 30°.* A particular nanotube species is identified by the direction and length of the wrapping vector. This leads to two common and equivalent methods of identifying carbon nanotubes: specifying the nanotube diameter d and wrapping angle θ, or specifying the (n, m) index, where $\mathbf{C} = n\hat{\mathbf{a}}_1 + m\hat{\mathbf{a}}_2$, with $0 \leq m \leq n$.† Given the (n, m) index of a tube, it is possible to calculate d and θ through geometry: $\theta = tan^{-1}[\sqrt{3}m/(2n + m)]$ and $d = \sqrt{3}a(m^2 + n^2 + nm)^{\frac{1}{2}}/\pi$, where a is the distance between nearest-neighbour carbon atoms in the hexagonal lattice (1.42 Å in graphene).

An analysis of the geometric structures of the carbon nanotubes formed above highlights three cases (see Figure 1b): $\theta = 0°$ or $(n, 0)$ tubes are known as zigzag tubes (a perpendicular cross-section would reveal carbon atoms in a symmetric zigzag formation); $\theta = 30°$ or (n, n), i.e. $n = m$, tubes are known as armchair tubes (again due to the pattern formed by their cross-section); all cases in between are called simply chiral tubes.‡

While our treatment of the electronic structure of carbon nanotubes in Section 2.1.3 will consider the tubes to be infinite in length, in reality they are capped by roughly hemispherical structures composed of hexagonal

---

* Intuitively, the six-fold symmetry of the graphene sheet might suggest confining θ to between 0° and 60°, or −30° and 30°, inclusive. Nanotubes with wrapping angles $0° \leq |\theta| \leq 30°$, however, are equivalent for θ and $-\theta$ in all but the *handedness* or the *chirality* of the tube, i.e. the tube is not symmetric under a reflection through a cross section. This can be safely ignored for most purposes.

† (n, m) represents $(n, |m|)$, where $0 \leq |m| \leq n$, again neglecting handedness of the tubes. The mirror-image tube of opposite handedness is described by (m, n) (for $0° \leq \theta \leq 60°$, or equivalently by $(n + m, -m)$ for $0° \leq |\theta| \leq 30°$).

‡ In some texts, the wrapping vector and wrapping angle as they are defined for all tubes are described as the 'chiral vector' and 'chiral angle'. Given that usage in these cases does not invoke the symmetry-related meaning of chirality, while our use of 'chiral tubes' does, these terms are avoided here to minimise confusion.

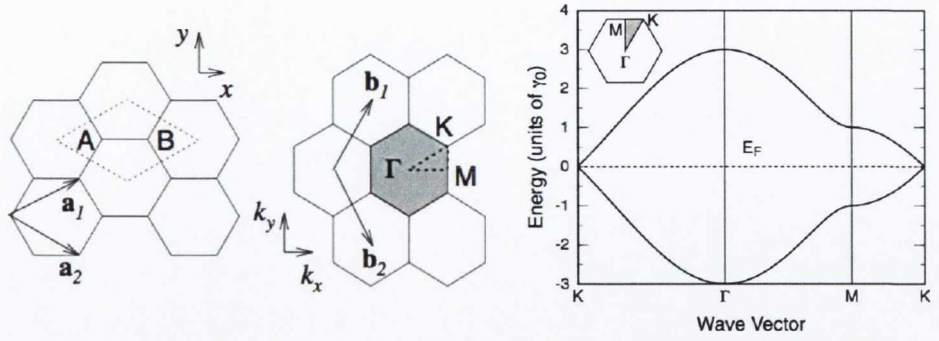

(a) (b)

Figure 2: The unit cell, Brillouin zone, and π-band energy dispersion structure of graphene. (a) The unit cell in real space (left, dotted rhombus) and first Brillouin zone in reciprocal space (right, shaded hexagon). (b) The π-band energy dispersion structure of graphene. (Adapted from references 58, 2.)

and pentagonal arrangements of carbon atoms [96], much like one half of the famous C_{60} macromolecule, Buckminsterfullerene [118].

In MWNTs, the individual nanotubes which make up the structure are typically of different species, such that the tubes 'fit' over each other more favourably. The inter-tube spacing of MWNTs is typically ~ 3.4 Å, close to the inter-plane spacing of graphite [224].

2.1.3 *Electronic Properties*

In Section 2.1.2 the various species and indices of nanotubes were explained in terms of how the nanotube could be formed from a 'rolled up' graphene sheet. The resulting nanotubes vary not only in geometric structure but in electronic behaviour also. This is due to the relationship between nanotube index, the relevant underlying unit cell, and the electronic properties of graphene. (Again, we follow much of the work and nomenclature of Dresselhaus and co-workers.)

Electronic Properties of Graphene

Figure 2a shows the unit cell in real space and Brillouin zone in reciprocal space of graphene. In the hexagonal Brillouin zone, the centre, corner and edge-centre of the zone are points of high symmetry and are marked Γ, K, and M respectively. Also shown are reciprocal lattice vectors $\mathbf{b_1}$ and $\mathbf{b_2}$, where $\hat{\mathbf{a}}_\mathbf{i} \cdot \mathbf{b_j} = 2\pi\delta_{ij}$, with $\delta_{ij} = 1$ if $i = j$ and $\delta_{ij} = 0$ otherwise [11].

The bonding of the carbon atoms in the hexagonal lattice of graphene is known as sp^2-hybridised [12], which results in each carbon atom forming three strong co-planar σ-bonds to its closest neighbouring atoms and having one p-orbital remaining unhybridised and not involved in interatomic bonding. The overlapping of these p-orbitals results in the formation of a bonding π-band and an anti-bonding π^*-band.

An analysis of the reciprocal-space energy dispersion relations for graphene in two dimensions (see Figure 3) reveals that the π and π^* bands are equal in energy at the K points of the Brillouin zone [205]. Graphene is thus considered a zero-band gap semiconductor. In graphite, the influence of other graphene sheets causes these bands to overlap slightly (~ 40 meV) at room temperature, giving graphite a metallic character.

Electronic Properties of Carbon Nanotubes

By analogy with graphene, we can examine the reciprocal-space energy dispersion relations for carbon nantotubes. SWNTs, however, do not share the same continuous reciprocal space as an infinite planar sheet of graphene due to their restricted dimensions.

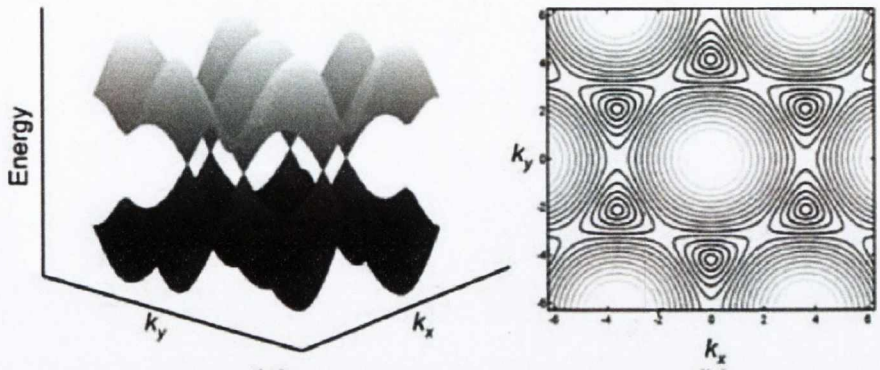

(a) (b)

Figure 3: Surface and contour plots of the graphene energy dispersion in reciprocal space. (a) 3D surface and (b) 2D contour plot of the graphene energy dispersion. Note that the band gap is zero at the six K points, making ideal graphene a zero-band gap semiconductor. (Adapted from reference 99.)

In the circumferential direction, the wave vector is restricted by periodic conditions known as the Born-von Karman conditions [54, 56]:

$$\mathbf{k} \cdot \mathbf{C} = 2\pi j \tag{2.1}$$

where j is an integer such that $(1 - \frac{N}{2}) \leq j \leq \frac{N}{2}$, where N is the number of carbon atoms in the unit cell of the nanotube. N is calculated for each SWNT from the relationship between the area of the nanotube unit cell in Figure 1a and the area of one hexagon of the graphene lattice: $N = |\mathbf{C} \times \mathbf{T}| \,/\, |\hat{\mathbf{a}}_1 \times \hat{\mathbf{a}}_2|$ which can be reduced to $N = 2(n^2 + nm + m^2)/\gcd(2n + m, 2m + n)$, where $\gcd(a, b)$ is the greatest common denominator of integers a and b.

The comparatively vast length of the nanotube means there are effectively no such restrictions on the allowed states along the axial direction of the tube. The allowed k-space of the nanotube is thus a set of N straight lines in reciprocal space, each separated by $2/d$ where d is the tube diameter.

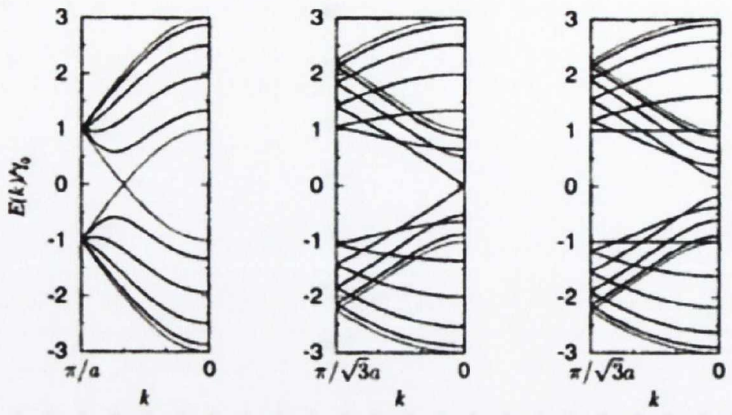

(a) (b) (c)

Figure 4: Representative nanotube energy band dispersions. Sample energy band dispersions for three (n,m)-species, obtained with cutting line 'cross-sections' of the graphene dispersion relation. (a) Armchair $(5,5)$ nanotube (metallic), (b) zigzag $(9,0)$ nanotube (semiconducting) and (c) zigzag $(10,10)$ nanotube (semiconducting).

Combining the energy dispersion properties of graphene with the allowed k-space of the relevant SWNT, we can calculate the band structure of the tube by cutting cross-sections of the graphene energy dispersion along those lines of allowed k-space, known as 'cutting lines' [182], superimposed on the graphene energy dispersion shown in Figure 3. If the cutting lines pass through the K points of the Brillouin zone (where the graphene π and π^* bands are equal), there will be no gap between the conduction and valence bands and the nanotube will be metallic. Where the cutting lines do not include the K points, the tube will be a semiconductor with a band gap depending on the precise (n,m) species.

To calculate those (n,m) tubes which have cutting lines including the K point, we compare the criteria for the set of allowed circumferential wave vectors with the vector $\mathbf{K}$ from the centre of the Brillouin zone to the K point:

$$\mathbf{K}\cdot\mathbf{C} = 2\pi j \quad \text{where} \quad \mathbf{K} = (\mathbf{b}_1 - \mathbf{b}_2)/3 \quad \text{and} \quad \mathbf{C} = (n\hat{\mathbf{a}}_1 + m\hat{\mathbf{a}}_2)$$

$$\begin{aligned}
\mathbf{K}\cdot\mathbf{C} &= \frac{(\mathbf{b}_1-\mathbf{b}_2)}{3}\cdot(n\hat{\mathbf{a}}_1+m\hat{\mathbf{a}}_2)\\
&= \frac{(n\mathbf{b}_1\cdot\hat{\mathbf{a}}_1-m\mathbf{b}_2\cdot\hat{\mathbf{a}}_2)}{3}\\
2\pi j &= \frac{2\pi(n-m)}{3}\\
3j &= n-m
\end{aligned} \tag{2.2}$$

where j is an integer. Thus if $\mathrm{mod}(n-m,3)=0$ the nanotube is metallic or semi-metallic in character, while the other tubes—approximately two-thirds of carbon nanotubes—are semiconductors [178]. These semiconducting tubes are further classed as 'mod 1' or 'mod 2' tubes according to the value of $\mathrm{mod}(n-m,3)$.

The size of the band gap in a semiconducting nanotube is generally inversely proportional to the nanotube's diameter. As the diameter increases, so too do the number of cutting lines, and the dispersion energy gap formed by two cutting lines on either side of a K point decreases.

For large-diameter nanotubes the energy gap is approximated by

$$E_{gap} = 2\gamma_0 a_{cc}/d$$

where γ_0 is the tight-binding overlap of the carbon–carbon bond and a_{cc} is the nearest-neighbour separation [217]. For small-diameter tubes, several other effects cause a deviation from this value. The increased curvature of the nanotube causes a change in the bond length, introducing more sp^3 bonding character, while the threefold anisotropy of the energy dispersion surface near the K points means that when the number of cutting lines is reduced the resulting energy gap is heavily dependent on the wrapping angle—a phenomenon known as *trigonal warping* [179].

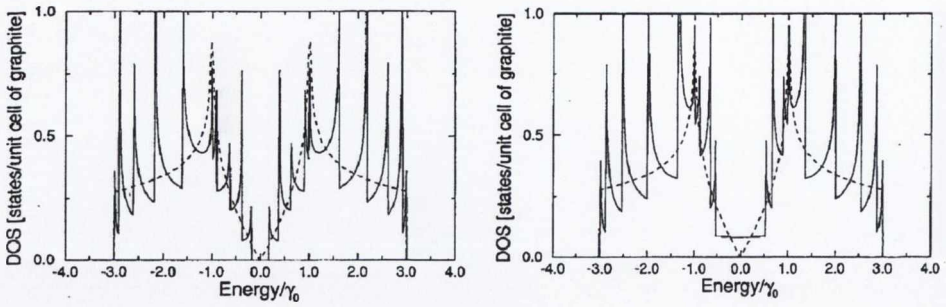

(a) (b)

Figure 5: Electronic density of states for semiconducting and metallic nanotubes. Sample electronic density of states, showing (a) a semiconducting (10,0) nanotube and (b) a metallic (9,0) tube. (Adapted from reference 180.)

The electronic density of states (DoS) per unit energy range, $g(E)$, of a material can be calculated as

$$g(E) = \frac{2g(k)}{\mathrm{d}E/\mathrm{d}\mathbf{k}}$$

where $g(\mathbf{k})$ is the density of states in reciprocal space and E and $\mathbf{k}$ come from the electronic dispersion relations [66]. The nature of these dispersion relations for carbon nanotubes, with $\mathrm{d}E/\mathrm{d}\mathbf{k} = 0$ at $\mathbf{k} = 0$, results in strong peaks known as *van Hove singularities* [179] in the DoS at the minima of each band. Figure 5 represents the DoS as a function of energy for a semiconducting $(10,0)$ and a metallic $(9,0)$ tube. Van Hove singularities are present in both the semiconducting and metallic tube; the key difference in their respective DoS profiles is that the metallic nanotube displays a non-zero DoS at the Fermi level.

2.1.4 *Optical Properties*

Light absorption by carbon nanotubes

Light absorption in a material is the result of interaction between the electric field of the electromagnetic light wave and the electrons of the absorbing material, causing electronic transitions between different energy states [66]. The magnitude of absorption by a given material at a given photon energy is determined by Fermi's *golden rule* [64, 66]:

$$W_{i\to f} = \frac{2\pi}{\hbar} |\mathbf{M}|^2 g(E)$$

where $W_{i\to f}$ is the transition rate for the transition of electrons from an initial state to a final state, $\mathbf{M}$ is a matrix describing the transition dipole moment, and $g(E)$ is the electronic joint density of states in the material at the photon energy. The transition dipole moment represents the movement of charge density as an electron is promoted to a state with higher energy. The larger the moment, the greater the absorption. Clearly, absorption will only take place if $\mathbf{M}$ is non-zero. Transitions are subject to selection rules governing 'allowed' transitions: these selection rules can be established by determining the conditions for which $\mathbf{M} \neq 0$ [17].

For an electron to absorb a photon, to observe conservation of momentum we must have:

$$\hbar\mathbf{k_f} = \hbar\mathbf{k_i} \pm \hbar\mathbf{k_p}$$

where $\mathbf{k_i}$ and $\mathbf{k_f}$ are the wave vectors of the initial and final electron states, and $\mathbf{k_p}$ the wave vector of the photon. For a photon the wave-vector is defined as $2\pi/\lambda$, where λ is the wavelength of the light. The value of $\mathbf{k_p}$

is negligible compared to the value of the electron wave vector, giving the first selection rule:

$$\Delta \mathbf{k} \approx 0$$

Thus, the wave vector of the electron is essentially unchanged by the absorption of a photon, and transitions are direct (vertical) on the band-structure diagram in Figure 6. (Indirect transitions are possible, but require the involvement of phonons—quantised vibrations—to conserve momentum. Direct transitions are the dominant type.) The minima of the bands in the dispersion relation have approximately parallel conduction and valence bands ($\mathrm{d}E/\mathrm{d}\mathbf{k} = 0$), and thus coincide with the van Hove singularities in the DoS: electrons with a large range of $\mathbf{k}$ values can thus be excited across the band gap by photons with the appropriate energy, and a van Hove singularity in the DoS results in a peak in the absorbance spectrum.

Due to symmetry considerations, non-zero transition dipole moments only exist in two directions—parallel and perpendicular to the nanotube axis—and so the polarisation direction of the light is important. The transition dipole moment is far larger in the parallel direction, owing to what is known as the 'antenna effect' [158], a result of the very large aspect ratio and small diameter of carbon nanotubes. The van Hove singularities in the DoS of a nanotube are labelled E_{ij} according to the quasi-angular momentum quantum number (J) from their corresponding electronic bands. Figure 6 illustrates the relationship between the valence and conduction bands of the DoS and the E_{ii} transitions. Transitions between bands of the same symmetry, i.e. where $\Delta J = 0$, are only allowed for incident light polarised parallel to the nanotube axis, while transitions between

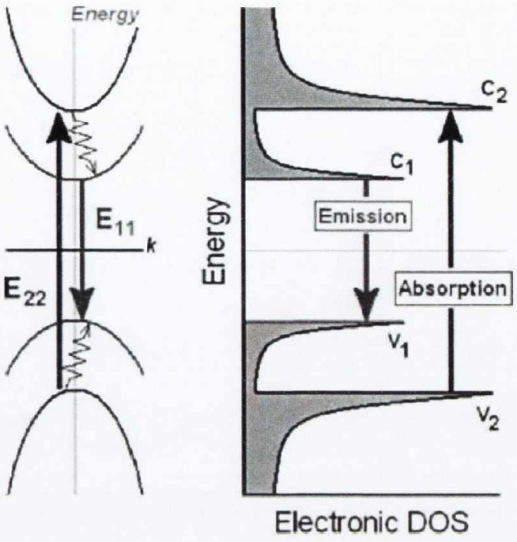

(a) (b)

Figure 6: Optical processes in a carbon nanotube, illustrated using (a) a simplified band structure and (b) an electronic density of states representation. The upward arrow represents E_{22}^S absorption, while the downward arrow represents emission from the E_{11}^S band gap. The thin jagged arrows illustrate relaxation from E_{22}^S to E_{11}^S. (Adapted from reference 129.)

bands of different energy, where $\Delta J = \pm 1$, are allowed for light polarised perpendicular to the nanotube axis.

The observed absorption spectrum for SWNTs is thus dominated by transitions between bands of the same symmetry (E_{11}, E_{22}, etc.), appearing as sharp peaks due to the van Hove singularities in the DoS at those energies corresponding to the inter-band transitions. As illustrated in Figure 7, semiconducting SWNTs with diameters around 1 nm typically have $E_{11}^S \approx 0.75$–1.55 eV ($\lambda \approx 1600$–800 nm) and $E_{22}^S \approx 1.35$–2.5 eV ($\lambda \approx 900$–500 nm), while metallic SWNTs have their first transition energies $E_{11}^M \approx 2.0$–3.1 eV ($\lambda \approx 600$–400 nm) [15].

Observed absorption spectra are typically broadened due to bundling of tubes into aggregates and 'ropes' of tubes, which is highly dependent on sample preparation [76]. For ensemble samples of many types of nanotube,

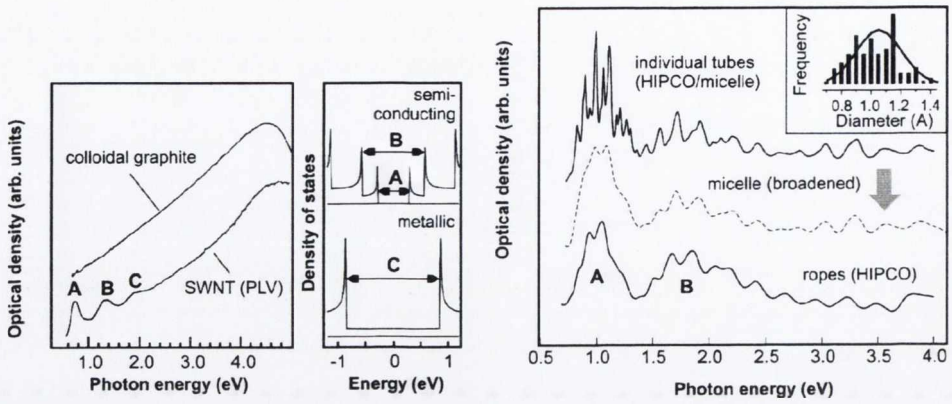

(a) (b) (c)

Figure 7: UV-Vis-NIR absorbance spectra for nanotube and graphite dispersions. (a) Absorbance spectrum of 'rope' material formed by pulsed laser vapourisation compared with that of colloidal graphite, with (b) the peaks observed in the absorption spectrum assigned to E_{ii} transitions, and (c) comparison of background-corrected spectra showing broadening and red-shifting of the sharp peaks as the well-dispersed SWNTs aggregate. (Adapted from reference 76.)

absorbance peaks are ill-defined due to the superposition of component peaks representing different E_{ii} transitions for each tube type present (see Figure 7). There is also a large contribution from the plasmon resonance of the nanotubes [107], which increases at higher energies before peaking at approximately 4.0–4.5 eV [171, 160]. This can be seen clearly in Figure 7a, where the plasmon resonance dominates the absorption spectrum of colloidal graphite.

Photoluminescence from carbon nanotubes

The excited state created by the absorption of a photon described above is short-lived [141], resulting either in the dissipation of energy thermally (carbon nanotubes are excellent thermal conductors and quantized vibrations known as phonons propagate easily along the tube [19]) or via the recombination of the electron-hole pair and emission of a photon of light. The

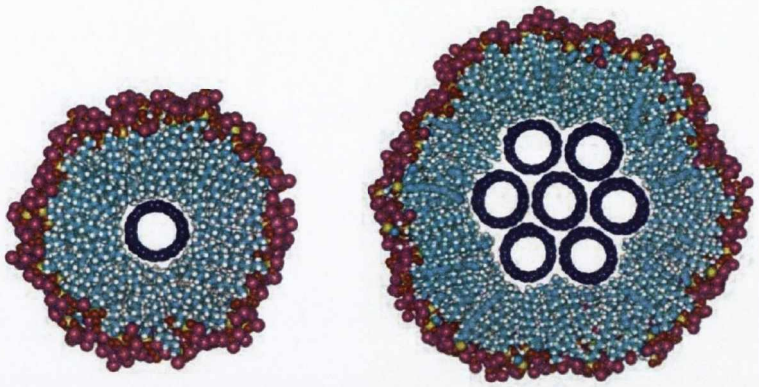

(a) (b)

Figure 8: Surfactant micelle formation around nanotubes. (a) Individual SWNT and (b) 7-tube SWNT bundle encapsulated in surfactant micelle. (Adapted from reference 159.)

process of light absorption followed by re-emission at a different energy is known as photoluminescence. More specifically, we may term the process *fluorescence* given that the timescales involved are short (a few nanoseconds or less [207, 100]) and the transitions are between 'allowed' states. Light emission from transitions which are not 'allowed' in terms of selection rules takes place over longer timescales and is termed *phosphorescence* [122]. As fluorescence is the dominant radiative emission process in nanotube photophysics, the term is used synonymously with photoluminescence in much of the literature.

Given that approximately one-third of nanotubes are metallic in character with no or zero band gap, bundles of tubes are expected not to exhibit photoluminescence as they will likely contain metallic tubes in contact with any semiconducting tubes and thus non-radiative relaxations via these metallic tubes are expected to dominate. Photoluminescence across the band gap in SWNTs was not observed until O'Connell and co-workers [159] were able to isolate individual nanotubes by dispersing them in a surfactant

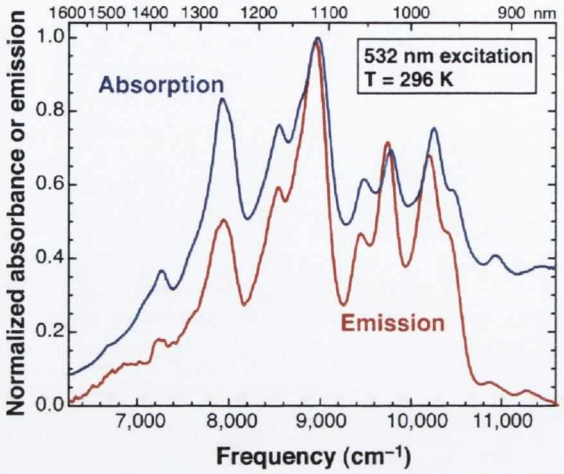

Figure 9: Absorption and emission spectra for SDS-encapsulated SWNTs in D_2O. The correspondence of absorption and emission peaks allowed the classification of the observed emission as band gap photoluminescence from individualised SWNTs. (Adapted from reference 159.)

solution, with individual nanotubes enclosed in surfactant micelles as illustrated in Figure 8. Emission from SWNTs shows very little Stokes shift in the E_{11}^S region, as can be seen in Figure 9, being detected in the near infra-red region.

Surfactant-assisted dispersions remain the most common approach for studying SWNT photoluminescence, and an overview of research on solutions and dispersions of SWNTs is included in 2.2.1.

A common method of analysis in PL spectroscopy is the use of PL excitation-emission maps (PL maps): 2D orthogonal plots of PL intensity as a function of excitation and emission energy, as illustrated in Figure 10. Data presented in this manner shows spots of high intensity corresponding to the dominant resonant absorbance at a band gap E_{ii}^S and emission from E_{11}^S. Typically, $E_{22}^S \rightarrow E_{11}^S$ resonant transitions are explored although higher-band absorption resonances could also be used. The unique position on the PL map of the peaks of high intensity allows the assignment of PL signals

to particular (n, m)-species of nanotube, and thus the $E_{22}^S \rightarrow E_{11}^S$ region (as highlighted in Figure 10b) is often termed the 'fingerprint region' [15, 213].

A simple treatment of the relationship between transition energies, for a linear dispersion displaying no chiral angle dependence, yields the value $E_{22}/E_{11} = 2$ [180, 57], and so the PL map might be expected to show a series of peaks along a line of slope 2. Clearly this is not the case, and analysis of PL maps and Kataura plots (plots of transition energies E_{ii} as a function of diameter, used as a guide for researchers probing optical properties of nanotubes, particularly using Raman spectroscopy [107]), such as that shown in Figure 11, show a much more complex picture.

The observed median value for the E_{22}/E_{11} ratio tends to be closer to 1.7–1.8, which was highlighted in early reports of nanotube PL and became known as the 'ratio problem' [106]. This was later explained as concerning the the self-energy correction in the more complete exciton picture of nanotube photophysics, discussed briefly below. The locations of the emission peaks are also observed to peel away above and below the median line. This can be related to the trigonal warping of the graphene energy dispersions around the K points. The wrapping angle of the SWNT greatly affects the positioning of the cutting lines with respect to these K points: tubes with a small wrapping angle (those close to armchair tubes) sit close to the median line while tubes with a large wrapping angle (those close to zigzag tubes) are found further away. Those tubes above and below the median line in the PL map are found to be of the same class in terms of the value of $\mathrm{mod}(n - m, 3)$, with mod 2 tubes below the line (displaying a 'low' value of E_{22} relative to E_{11}) and the mod 1 tubes above ('high' relative E_{22} value). This occurs because the mod 1 and mod 2 tubes have their closest cutting line on opposite sides of the K point. Also, E_{11} and E_{22} cutting lines for semiconducting tubes relate to opposite sides of the energy

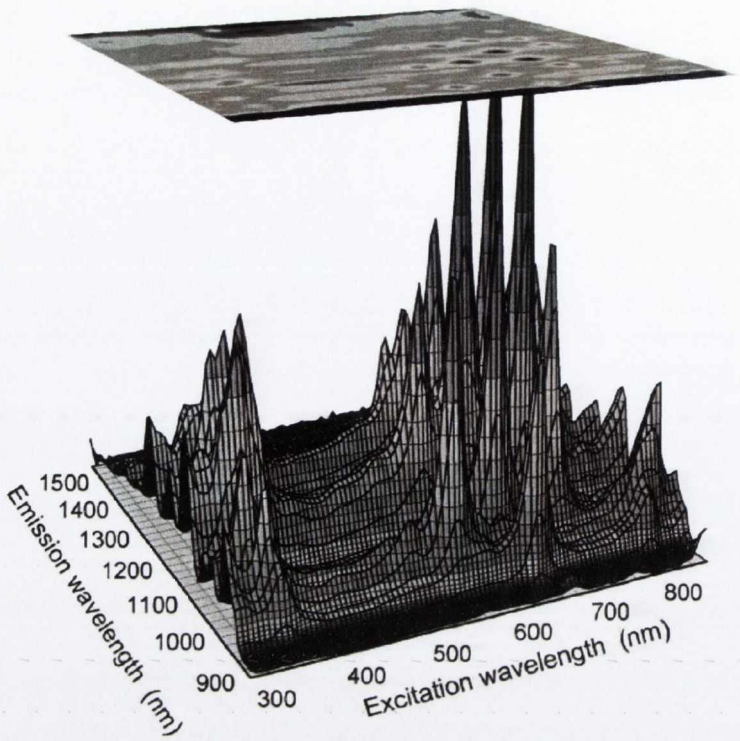

(a)

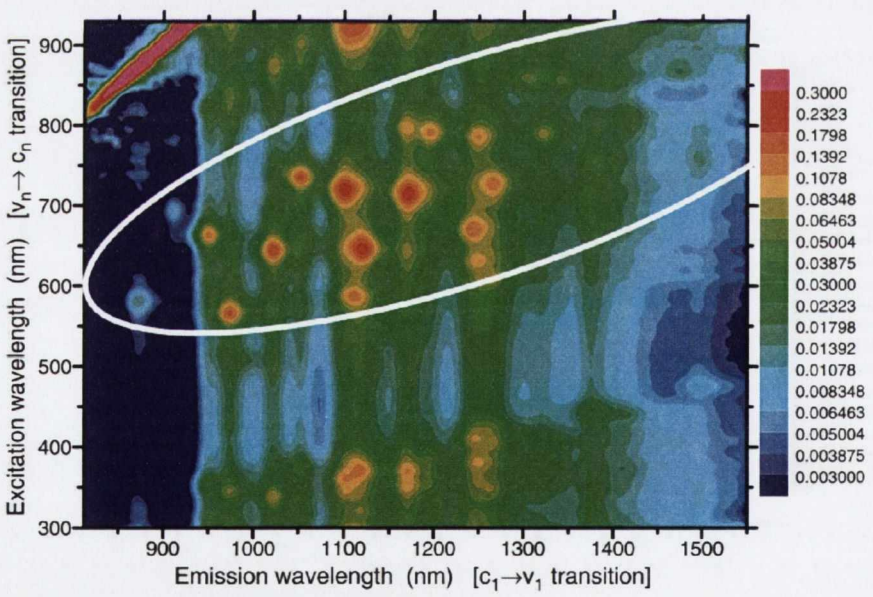

(b)

Figure 10: Photoluminescence excitation-emission maps for SWNT dispersions. (a) Combined contour and surface plot of the PL excitation-emission map and (b) contour plot of the PL map in plan view. The 'fingerprint region' is highlighted by the white ellipse. (Adapted from references 15, 213.)

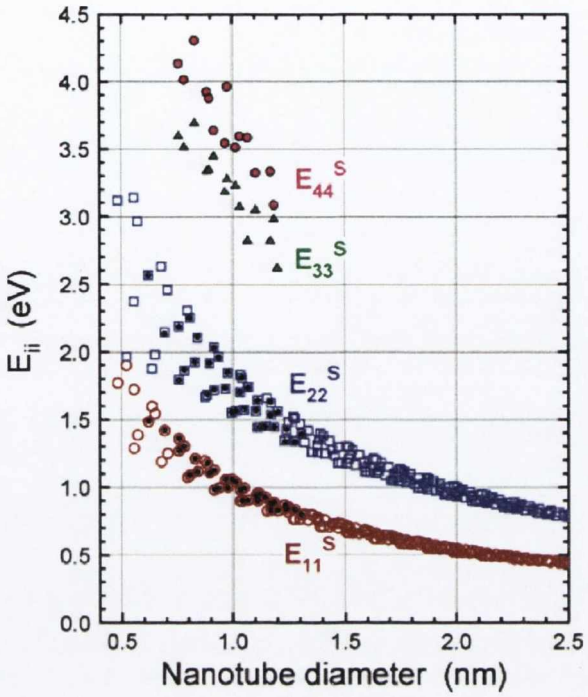

Figure 11: 'Kataura Plot', showing E_{ii}^{S} versus diameter. The behaviour of branches corresponding to constant values of $2n + m$ is especially apparent at low diameters. The superscript 'S' refers to semiconducting, as opposed to metallic, tubes. (Adapted from reference 212.)

dispersion. In the Kataura plot, this means mod 1 tubes are found below the median line for E_{11} and above it for E_{22} (the reverse is true for mod 2 tubes) and this has the effect of increasing the perceived deviation from the median in the PL map, which effectively plots E_{22} against E_{11}.

In peeling away from the median line in both Kataura plots and PL maps, the position of nanotube peaks is seen to follow certain 'branches', corresponding to constant values of $2n + m$. The meaning of these branches is essentially geometric: these tubes all have similar diameters but a range of wrapping angles, meaning they are found close to each other on the Kataura plot, with increasing deviations from the median as the wrapping angle increases.

Excitons in carbon nanotubes

The complete picture of photophysics of carbon nanotubes requires the development of an excitonic picture of the excited state [2, 189, 206], as opposed to the simple single particle excitation scheme used thus far.

Excitons are bound quasi-particles, whereby the electron-hole pair created on absorption of a photon is bound via the Coulomb interaction. In the excitonic representation of the excited states of SWNTs there are contributions from the electron-hole interaction as well as the 'many-body effects' such as electron-electron repulsion. SWNTs are exceptionally useful for the study of exciton photophysics as their effectively one-dimensional nature and unique structure allow both simple modelling and relatively straightforward observation of the influence of excitons.

The initial relevance of the exciton model for SWNT excitation became apparent with the 'ratio problem' of observed transition energies mentioned above in 2.1.4. The ratio of E_{22}^S to E_{11}^S should, to a first approximation, approach a value of 2, which is not what is observed in PL maps [180, 57]. When the contributions from the excitonic model (namely, a blue-shift from the electron-electron repulsion and a red-shift from the excitonic electron-hole attraction) are included a net blue shift in both the E_{22}^S and E_{11}^S energies is found. This produces a ratio of $E_{22}^S / E_{11}^S \simeq 1.8$ for large diameter tubes, matching experimental observations.

More evidence for the excitonic nature of the excited state of SWNTs comes from two-photon absorption experiments [206, 144]. For a system described by the single-particle approach, it is possible to observe absorption transitions at E_{ii} when the material is illuminated by light of energy $E = 0.5E_{ii}$. However, two-photon absorption experiments with SWNTs have shown that the absorbance peak occurs not at $0.5E_{11}$, but at a slightly

higher energy. In the one-dimensional excitonic description, the excitonic states appear in a series of bands below the single particle band gap (analogous to the hydrogen Rydberg series of s, p, d... levels). The transitions from the ground state to these levels have definite parity and selection rules, with single-photon absorptions exciting the s-level exciton and two-photon absorption exciting the higher p-level exciton. Experimental evidence for two photon absorbance exciting this higher 1-p exciton level, above the E_{11}^S ground state from which single-photon emission is observed, thus provided strong evidence for excitons in carbon nanotubes. Further evidence comes from the observation of resonances from bound exciton-phonon states observed as side bands in the PL map [167]

SWNTs have generated intense interest as a material in which to study excitonic effects which would typically require very low temperatures to observe. In most bulk materials the binding energy of excitons is approximately 10 meV, but in SWNTs it has been shown to be far higher, in the range 0.1–1.0 eV [206, 144], thus being a considerable fraction of the band gap. The exciton binding energy has been shown to have a dependence on diameter p/d, where $p = 1$, 2, 3, 4 and 5 for E_{11}^S, E_{22}^S, E_{11}^M, E_{33}^S and E_{44}^S respectively [178, 179] and d is the tube diameter. This dependence is not linear due to many-body effects, in much the same way that the 'ratio problem' discussed above was due to these effects. The excitation energy (and the binding energy and self-energy terms which contribute to it) also has a chiral dependence which is a maximum for armchair tubes (where $\theta = 30°$) and a minimum for zigzag tubes ($\theta = 0°$), and takes the approximate form $B_p \cos 3\theta / d^2$, where B_p is a constant depending on the value of p. The Kataura plot shown in Figure 11 is thus modelled by a relationship of the form $E_{ii} = 1241/(A_1 + A_2 d) + B_p \cos 3\theta / d^2$ [15].

The lifetime of the excited state in SWNTs is extremely short, with most of the excitons formed decaying non-radiatively on a timescale of hundreds of femtoseconds [90]. The excitons may decay through a number of channels, including via the emission of (one or more) phonons, recombination at defect or dopant sites or at nanotubes ends, or through an Auger process involving the transfer of energy and momentum to a resultant charge carrier or pair of carriers [113, 87]. The radiative lifetime is considerably longer, measured in the tens of picoseconds range [164] (and in some cases estimated as being as long as 100 ns or more [207]). In bundles of tubes tunnelling of excitons to tubes of lower band gap and to metallic tubes can occur at a sufficiently high rate to prevent any appreciable photoluminescence [172].

2.1.5 *Photoluminescence Quantum Yield*

A property of fundamental importance to the study of photoluminescence is the photoluminescence quantum yield (PLQY), ϕ. This is the ratio of emitted photons to photons absorbed by the material [122]:

$$\phi = \frac{\Sigma(\textit{emitted photons})}{\Sigma(\textit{absorbed photons})}$$

and is thus expressed as $0 \leq \phi \leq 1$.

For a substance in an excited state after the absorption of a photon, there are typically both radiative and non-radiative decay pathways available for that material to relax to the ground state. Each of these is a random

process, giving rise to a statistical decay rate. With a rate of non-radiative decay κ and a rate of radiative decay K, the lifetime of an excited state is

$$\tau = \frac{1}{\kappa + K}$$

and the quantum yield is equal to the fraction of decays which take place via the radiative channel:

$$\phi = \frac{K}{\kappa + K}$$

Even without non-radiative decays, the excited state is unstable and so there is an intrinsic or natural radiative lifetime, τ_{rad}:

$$\tau_{rad} = \frac{1}{K}$$

These equations can be combined to give

$$\phi = K \cdot \frac{1}{\kappa + K} = K\tau = \frac{\tau}{\tau_{rad}}$$

The PLQY can thus be calculated from the characteristics of the absorption and fluorescence spectra of a sample, or more directly by estimating the fraction of absorbed photons which are emitted. In relation to the discussion of excited state lifetimes in 2.1.4 above, we can see that where the radiative lifetime τ_{rad} is an order of magnitude or more greater than the non-radiative lifetime τ_{non} ($= \kappa^{-1}$), then $\tau \approx \tau_{non}$ and the PLQY value ϕ is approximately given by $\phi \approx \tau_{non}/\tau_{rad}$.

Precise figures of numbers of photons absorbed/emitted are difficult to calculate, though with particular experimental set-ups such as integrating spheres good estimates can be made. A more common approach is to

compare the ratio, m, of integrated fluorescence to absorbance for a sample material to that measured for a substance of known PLQY under identical experimental conditions. The PLQY of the sample under investigation, ϕ_x, is then calculated relative to that of the standard, ϕ_{st}, as follows [122]:

$$\phi_x = \phi_{st} \cdot \left(\frac{m_x}{m_{st}}\right) \cdot \left(\frac{n_x}{n_{st}}\right)^2 \tag{2.3}$$

where m is the slope of the line representing integrated PL as a function of absorbance, n is the refractive index of the solution, and the subscripts x and st signify the material under investigation and the standard material of known PLQY, respectively. The inclusion of the refractive index in this equation is necessary to account for the effective dispersion of light emitted from the sample. Samples are typically in solution, with the sample cell surrounded by air, and the extent of the ensuing refraction as the emitted light exits different sample cuvettes varies depending on the samples' refractive index.

Photoluminescence Quantum Yields of Carbon Nanotubes

Given the unique properties of carbon nanotubes, PLQY is a parameter of fundamental interest both in terms of understanding the science of SWNTs and in order to use PL data quantitatively for applications. Measurement of ϕ, however, is not trivial. Measured PLQY values are dependent on the absorbance and PL intensity values recorded in any given set-up. The complexity of SWNT absorbance spectra was illustrated in Section 2.1.4, and this makes (n,m)-specific measurements of absorbance extremely difficult. PLQY values will also necessarily be adversely affected by phenomena which act to quench the PL signal, thus it is expected that individual SWNTs will exhibit higher PLQY values than ensembles, where defects,

bundling and energy transfer between tubes become an issue. SWNTs are generally known for having low PLQY values, with the first reported value being ~ 0.001 [159]. Higher quantum yield values have since been reported, up to two orders of magnitude greater [104, 204], though this is still low compared to some other fluorescent materials.

The low PLQY values of SWNTs can be attributed to a number of processes. The presence of dark excitons below the lowest bright exciton state will affect the emission rate [59], though at room temperature the splitting between the lowest energy dark and bright excitons is expected to be ~ 10 meV and thus easily overcome through thermal excitation. Non-radiative recombination of bright excitons is the primary decay process [207, 172]. Given the large exciton mobilities in SWNTs [187], diffusion to recombination centres is easily achieved [87] and so the PL is expected to be sensitive both to doping and to interactions with the local environment, for example the ability of surfactant micelles or polymer wrapping to exclude molecules of oxygen or water from the surface of the nanotube [104]. In addition, PL emission will be reduced through energy transfer to other tubes, particularly in the presence of small bundles [200, 169], and through Auger decay processes.

In terms of (n,m)-specific PLQY values, a number of features are expected. Firstly, the phonon-mediated non-radiative decay channel becomes less efficient and less statistically likely as the number of phonons required for a successful recombination to occur increases, which implies a greater proportion of radiative decays and thus a higher quantum yield for SWNTs with a higher E_{11}^S band gap (i.e. narrower diameter) [204].

Secondly, it has been proposed that fluorescence is quenched in nanotubes for which the E_{22}^S energy level is more than twice the E_{11}^S energy level [173]: the excited state can thus decay into two E_{11} excitons, open-

ing up a further Auger decay channel by analogy with electron-electron scattering in graphite, the dominant relaxation process in that material for high energy carriers. From the Kataura plot and the family behaviour of the mod 1 and mod 2 tubes peeling away from the main trend-line in opposite directions along the y-axis, it is clear that the condition $E_{22}^S \geq E_{11}^S$ is fulfilled by mod 1 tubes, where E_{22}^S is increased while E_{11}^S is decreased. It is therefore predicted that mod 1 tubes will show a lower fluorescence efficiency than mod 2 SWNTs, while the chirality of the tubes will play a role in so far as this effect is more pronounced for smaller diameter tubes of smaller chiral angle (close to armchair structure).

2.2 LITERATURE REVIEW

2.2.1 *Dispersant Media for SWNTs*

The first demonstration of photoluminescence from SWNTs came in 2002 when O'Connell *et al.* published their paper, 'Band gap fluorescence from individual single-walled carbon nanotubes' [159]. Their general approach of dispersing nanotubes in surfactant solutions was not new. SWNTs had by this time been dispersed in a range of surfactants [138, 60] and solvents [13, 16], including via end-cap and sidewall functionalisation [45, 33, 109] and via polymer wrapping [158]. The key advance their paper illustrated was the benefit of high-powered sonication to disperse the tubes followed by ultracentrifugation to remove larger remaining bundles and impurities. In this way, individual tubes and small bundles, enclosed in surfactant micelles, were sufficiently isolated from each other and from any metallic tubes to produce bright photoluminescence. A similar method of preparation was published independently shortly afterwards by Kappes and co-workers [124].

Since then, the routine of sonication and (typically ultra-)centrifugation has been employed by a number of groups, with the successful observation of PL from SWNTs dispersed in a range of solvents [143, 142, 24, 25], using an array of surfactants [151, 15] or polymers [131, 93, 157] and biomolecules [81, 214, 146, 62]. Here in this group, there has been considerable focus on the mechanism behind successful dispersal of SWNTs. It has been observed that the quality of the dispersion (measured by statistical AFM analysis [23], see 3.2.3) correlates strongly with the ζ-potential at the nanotube surface [198]. The relationship between concentration achieved

through ultracentrifugation or dilution and debundling has been explored in surfactant-aided dispersions, with debundling shown to be concentration dependent, with spontaneous debundling occurring in dilute solutions (though the degree of exfoliation and number of individual tubes was improved via ultracentrifugation as opposed to dilution alone) [21]. Concentrations of tubes and small bundles are generally observed to be higher in surfactant-aided dispersions than in solvent-only dispersions [16, 37, 55], though again not always with the same degree of exfoliation of individual tubes [21, 198]. Novel solvents such as cyclohexylpyrrolidone (CHP), γ-butyrolactone and 1-benzyl-2-pyrrolidinone (NBenP) have been identified on the basis of their surface energy [22] and two-phase SWNT dispersions with comparable concentrations of individual tubes and small bundles to that achieved in three-phase surfactant assisted dispersions have been observed [25]. However, very little PL has been recorded from these two-phase dispersions, for reasons that are still being investigated. Given their good ability to disperse nanotubes together with their relative lack of toxicity and low cost, surfactants remain the most common method for creating nanotube dispersions.

While SDS- and SDBS-dispersed nanotubes remain the *de facto* standards for liquid-phase photoluminescence studies [159, 124] several other dispersing agents are worthy of note. Sodium deoxycholate (DOC) has been shown to allow more intense photoluminescence peaks [61], while a derivative of the biomolecule flavin mononucleotide (FMN) synthesised by the group of Papadimitrakopoulos was shown to deliver very high-efficiency photoluminescence [104], and increased selectivity of tube species remaining in the suspension has been shown using aromatic polymers such as polyfluorene derivatives [157]. A selection of these surfactant systems is studied here.

2.2.2 *Sample Preparation: Sonication and Centrifugation*

With the adoption of the sonicate-and-centrifuge routine discussed above, several groups have explored the effects these preparation methods have on the physical properties of the dispersed nanotubes [85, 10, 153, 192].

The potential of sonication to cut the length of the nanotubes in a dispersion has been examined and modelled [7, 85, 139]. Scission occurs due to hydrodynamic shear when bubbles induced by the sonication collapse, a process known as cavitation. It has been observed that the scission of dispersed nanotubes is primarily a length-dependent phenomenon, scaling with the square of the nanotube length [85]. The continual shortening of the tubes down to a terminal length of approximately 200 nm has been proposed, though it has also been suggested that with a sufficiently long sonication time the scission continues further [139], and ultra-short nanotubes have also been observed after long sonication periods [197].

The length of nanotubes has been shown to be of critical importance for PL efficiency [84], with nanotube ends acting as defect sites to induce the non-radiative recombination of excitons and hence lowering the efficiency [170]. The exciton transport length in nanotubes has been estimated to be as high as 200–300 nm [220, 187], suggesting that longer tubes or those with fewer defects will have a higher PLQY [87]. Scission has a diameter dependence also, affecting narrow tubes more strongly than those of larger diameter as the force necessary to break a tube scales linearly with diameter [139]. This preferential scission is likely to cause a shift in observed PL intensities according to diameter and energy, with small diameter (higher band gap) tubes appearing to have relatively lower emission intensities after sonication [40].

Centrifugation does not impose the same stresses on the nanotube as sonication. It has also been observed that over time the supernatant in a centrifuged solution contains a higher proportion of shorter tubes [40], and in the case of rate-zonal separation it is expected that longer tubes are to be found towards the bottom of the centrifuge tube [197, 63]. The dynamics of a nanotube in a centrifugal field have been modelled and fitted according to the theory proposed by Lamm in the 1920s [8, 153, 10]. A simpler sedimentation theory was used by researchers in this group to measure static sedimentation of nanotube dispersions [155].

A very useful advance in separation of nanotubes by species was published by Arnold *et al.* in 2005 [9]. Building on a technique widely used in biology, they used density gradient ultracentrifugation to separate nanotubes into distinct layers based on buoyant density in the supernatant which could then be fractionated, yielding diameter-sorted dispersions [8]. Similar methods have been employed in the rate-zonal regime to sort dispersions by length [63].

2.2.3 *Absorbance of SWNTs*

Early reports of absorbance spectra of SWNTs revealed broad peaks which were assigned to the E_{11}^S, E_{22}^S and E_{11}^M transitions [107]. These peaks were later shown to be the superposition of numerous individual peaks and also the result of broadening due to aggregation. In well dispersed samples, sharp peaks in the absorbance spectrum are found, corresponding to van Hove peaks in the electronic density of states [191, 135]. These peaks are affected by the covalent functionalisation of nanotubes, which disrupts their electronic structure [43]. In order to measure concentrations via the

Beer-Lambert Law, the energy region above the resonant E_{11}^S transitions is typically probed. In this region absorbance values at particular wavelengths are less susceptible to shifts in the absorbance spectra than those for those near the sharper peaks in the E_{11}^S region. In calculating concentrations in this work, an average absorbance for the 550–700 nm range is compared, where possible, to a similar absorbance value for a solution of known concentration. The extinction coefficient for dispersions of SWNTs has been measured to be greater than 30 $\mathrm{mL \cdot mg^{-1} \cdot cm^{-1}}$ for wavelengths around 660 nm [123, 69].

Absorbance spectroscopy is used to measure the relative populations of (n, m) species of nanotube [140], as well as the more general ratio of metallic to semiconducting tubes in a dispersion [91, 89]. Absorbance measurements have been found to be a reliable indicator of nanotube sample purity [97], however the non-resonant background poses a problem which has not been adequately dealt with analytically [98, 225]. Where background subtraction has been employed to reveal the absorbance of SWNTs in sharper relief, several methods have been proposed including a linear background [86], a power law [177], combinations of Lorentzian curves and exponential decays [121] and a more detailed background spectrum obtained from the difference between consecutive absorbance spectra of the same sample after increasing centrifugation times [160].

2.2.4 *PL from SWNTs*

After the initial publications of O'Connell *et al.* [159] and Lebedkin *et al.* [124], PL spectroscopy quickly became a common tool for researchers investigating the fundamental physics of carbon nanotubes. Many groups

have worked to increase the number of known surfactants which can be used in a similar manner. Dispersion of individual debundled nanotubes has also been demonstrated using polymer [93, 157] and DNA wrapping [62, 227], surface functionalisation [137, 116], and choice of solvent [69, 23, 193].

Assignment of peaks in the PL excitation-emission to transitions from particular (n, m)-species were not made immediately, but followed analysis of Raman spectroscopy results [15]. The $E_{22}^S \rightarrow E_{11}^S$ transition energies of dozens of distinct semiconducting nanotubes have been identified from combinations of PL and Raman spectroscopy. From this data, empirical models for Kataura plots have been established [212], and together with Raman spectra of metallic tubes this has enabled the transition energies of SWNTS contained in typical HiPCO samples to be well documented.

PL peaks have been used in an attempt to identify the (n, m)-species content of samples of SWNTs [140, 154, 102, 204], but this approach is hindered by the lack of PL signal from metallic and bundled tubes. PL emission tends to be stronger from near-armchair nanotubes and from mod 2 tubes [15, 126]. This structure-dependent PL intensity has been interpreted as an indication of (n, m)-population heterogeneities [165], owing to preferential growth of such tubes, and alternatively as an indication of PL quenching by exciton resonances in mod 1 tubes (particularly zigzag tubes), without any chirality dependence of population [173]. Luo and colleagues [140] analysed both of these theories and their ability to reconstruct absorbance spectra (i.e. abundances) from PL data, and the results favoured the former theory.

As a result of the quenching of PL signal from bundled nanotubes, PL has been identified as a method for quantifying the quality of dispersion in

a sample [78]. PL has also been observed from small bundles as a result of energy transfer between nanotubes [169, 108].

Comparison of PL transition energies from air-suspended nanotubes and surfactant-suspended nanotubes has allowed observation of the shift in transition energy as a result of local dielectric environment [128], a shift known as the solvatochromic effect [47]. Several investigations of the effect of local dielectric constant have been made [148, 161, 162]. Analysis of the transition widths has revealed larger widths for higher energy transitions, with E_{11}^S widths on the order of 25 meV, E_{22}^S widths closer to 60 meV, and E_{11}^M widths around 90 meV [152, 105].

Inner-filter effects in SWNT spectroscopy

Given the highly absorbing nature of carbon nanotube dispersions, distortions of the relationship between absorbance and photoluminescence due to the inner-filter effect [166] are to be expected. However, there has been very little explicit reference to this effect in the literature, with the likelihood that these effects go unaccounted for.

The inner-filter effect has produced several studies illustrating corrective strategies [120, 175, 219, 195, 223], however these appear to be primarily aimed at the biological sciences, for example dealing with highly absorbant non-emissive material like cell cultures [175, 223].

2.2.5 *PLQY of carbon nanotubes*

Quantitative comparisons of PL data require knowledge of the (n, m)-species dependence of the nanotube PLQY. Little by way of standard procedure exists in this area. Reported values for PLQY of SWNTs range from

$\sim 10^{-4}$–10^{-1} [104, 159], though the methods by which these measurements are taken vary considerably.

Isolated individual nanotubes have been examined, either suspended in air or dispersed using a surfactant before being deposited on a substrate or microscope slide [38, 204, 130]. These micro-PL measurements involve recording PL emission from along the length of an individual tube. Generally, tubes must be of a sufficient length to overcome quenching issues connected with tube ends [48]. The determination of absorbance values for such experiments typically relies on calculations involving some or all of the nanotube cross-section, the absorbance of carbon on a per-atom basis, the size and power of the excitation beam, and any necessary corrections for reflectance of the apparatus, coherence of reflections, etc. Values for the reported PLQY of individual nanotubes range up to ~ 0.08 [204].

In some cases, PLQY values are estimated from the decay lifetime of PL emission from the individual tubes, with no absorbance data required [100].

In general, lower values of PLQY are recorded for ensemble dispersions of SWNTs [38, 159, 77, 207, 90]. Values ranging as low as 10^{-4} have been reported, though this is for the absolute PLQY of the solution and not a value for any specific nanotube. Measurements of the absorbance background of samples containing many (n, m)-species of tubes is difficult, and numerous approaches have been taken. Linear baselines have been used [82], as have linear offsets of individually-scaled absorbance peaks [100]; Ju and colleagues use both original and background-subtracted absorbance values [104]. In order to reduce the complexity of the task, SWNT dispersions have been fractioned into density-dependent sections containing fewer (n, m)-species [51]. Values of PLQY reported for ensemble dispersions have been quoted for the solution in total and for some of the distinct (n, m)-species contained therein.

A structure-resolved relationship between PLQY and E_{11} was proposed based on measurements for individual nanotubes by Tsyboulski and co-workers [204], where the product of absorbance and quantum yield was reported (but not the individual values). An increase in PLQY with increasing band gap was suggested, explained by the reduced availability of sufficient phonons of the desired energy to allow non-radiative decay at higher band gap energies. Reich *et al.* [173] have proposed a method by which PL emission from mod 1 tubes is quenched relative to mod 2 types, due to exciton resonances when $E_{22}^S > 2E_{11}^S$. They propose that excitons of a sufficiently high E_{22}^S energy can decay into two E_{11}^S excitons, which are then likely to decay non-radiatively, thus reducing the emission intensity from those species. This effect is more pronounced for mod 1 tubes. Hertel *et al.* [87] have proposed an exciton-diffusion limited model of PLQY, where the high exciton mobility allows for diffusion to nanotube endpoints or recombination centres within the excited state lifetime, thus leading to non-radiative decay and overall PLQY values of a few percent at best. No consistent set of values for (n, m)-species dependent quantum yields of carbon nanotubes has been published for either individual or ensemble dispersions.

2.2.6 *Standards used for PLQY*

There is little consensus on the use of a reference standard for the measurement of PLQY for nanotubes. While some of the methods outlined above allow direct calculation of PLQY values from individual nanotube parameters or from lifetime measurements, solution-based ensemble measurements and some isolated-nanotube spectroscopy employ reference

standards. Quantum dots of CdTe [38] and numerous infra-red dyes (IR-26 [90, 38], Styryl-13 [104, 51], lumogen F Red 300 [100]) have been used, as has singlet oxygen emission [194]. Styryl-13, in particular, has been the focus of some recent interest when it was used as a standard in a paper by Ju *et al.* reporting PLQY values of 0.20 for solution-dispersed nanotubes [104]; a later paper by Stürzl and co-workers questioned the efficiency of the standard, and suggested it was overstated by a factor of ~ 5.5 [194].

2.2.7 *Discussion*

From the above survey of the published literature, it is clear that there are several unresolved questions in carbon nanotube spectroscopy.

The value of the intrinsic PLQY of carbon nanotubes and the relationship between PLQY and nanotube environment, length and defect population is still an open question, and has not been helped by the lack of a consistent approach to the estimation of PLQY. This lack of an accepted approach extends to the analysis of ensemble absorption spectra and the identification of contributing absorption spectra from different species of nanotube in a dispersion. This thesis contains a proposed framework for the analysis of absorption and PL emission from SWNTs, allowing a repeatable and objective method to estimate PLQY values. This may allow in future the analysis of optical properties and PLQY values of SWNTs under a wide range of conditions and thus help to elucidate the relationship between environment and nanotube photophysics.

Part of our proposed procedure involves issues which are infrequently, if ever, dealt with in the above literature: inner-filter effects and the proportion

of individual tubes in a dispersion absorbing light from the excitation beam. It is hoped these issues will become more widely acknowledged.

From the published literature, we expect to find transition widths in the range from approximately 10 meV to above 100 meV, and expect an apparent PLQY for dispersed s-SWNTs to be lower than 0.1. The intrinsic PLQY may well be considerably higher than this, but likely only for isolated tubes and not SWNTs in a surfactant-aided dispersion.

Some areas of concern remain: a suitable infra-red emitting standard has not been identified, although in practice the substitution of absorbance and emission data from one standard for another at a later date to update PLQY estimates is not a difficulty. The chief difficulty in the implementation of our method of analysis is expected to be the application of the deconvolution routine published by Nair *et al.* [152] to numerous samples with widely different transition energies and underlying populations of SWNTs.

MATERIALS AND METHODS

3

An overview is given of those materials, instruments and methods of analysis used throughout this work, including some of the key principles involved.

3.1 MATERIALS

The primary materials dealt with in this work are solutions and liquid-phase dispersions, in particular surfactant- and polymer-stabilised dispersions of carbon nanotubes and dye-solvent solutions.

Carbon nanotubes

The carbon nanotubes used in this work were raw HiPCO nanotubes, produced by Unidym (currently distributed by NanoIntegris), lot #R0554. Some residual iron catalyst is expected to be present, at $< 35\,\text{wt\%}$ in the original product. The tubes are typically 0.8–1.2 nm in diameter and 100–1000 nm in length. No direct population analysis was performed, but information on transition energies from a number of published sources [212, 105, 152] was combined to create a dataset of E_{11}^S, E_{22}^S, and E_{11}^M values for all SWNTs with a diameter in the range 0.6–1.4 nm. This dataset was used in assigning PL peaks to individual (n, m) species and in fitting absorbance curves.

Stabilising Agents

Nanotube dispersions were produced using the following surfactant and polymer materials, details of which are summarised in Table 1 :

SODIUM DODECYL SULFATE (SDS), an anionic surfactant commonly found in cleaning and hygiene products.

SODIUM DODECYLBENZENESULFONIC ACID (SDBS), another anionic surfactant also used as a detergent.

SODIUM CHOLATE (SC), an ionic bile salt also commonly used in laboratory preparations of liposomes and lipids.

SODIUM TAURODEOXYCHOLATE (TDOC), a bile salt with uses as a detergent.

POLYSORBATE-80 (T80), a non-ionic surfactant and emulsifier often used in food products (sold as 'Tween-80').

FLAVIN MONONUCLEOTIDE (FMN), a biomolecule related to riboflavin (vitamin B_{12}), used as a coenzyme in oxidation reactions and as a water-soluble form of riboflavin in food (additive E101a).

POLY(9,9-DIOCTYLFLUORENYL-2,7-DIYL) (PFO), a blue-light-emitting fluorescent conductive polymer with uses in organic optoelectronics.

Some of these surfactants are very commonly used in SWNT dispersions (particularly SDS, SDBS and SC), and as such represent standard practice in the production of nanotube dispersions. The original paper from O'Connell *et al.* showing PL from s-SWNTs was based on SDS-dispersed nanotubes [159], while Lebedkin *et al.* employed both SDS and SDBS [126]. FMN has gained considerable attention recently as reports of nanotubes

Table 1: Properties of dispersants used
Chemical Abstracts Service (CAS) numbers included for identification purposes

DISPERSING AGENT	DESCRIPTION	WATER-SOLUBLE?	MOLAR MASS [g·mol^{-1}]	CAS #
SDS	Surfactant	Yes	288.4	151-21-3
SDBS	Surfactant	Yes	348.5	25155-30-0
TDOC	Bile Salt	Yes	521.7	207737-97-1
SC	Bile Salt	Yes	430.6	206986-87-0
T80	Surfactant	Yes	1,310	9005-65-6
FMN	Biomolecule	Yes	456.3	146-17-8
PFO	Polymer	No	58,000	19456-48-5

suspended with FMN and its derivatives have shown high PLQY values [105, 104]. PFO has also been noted for its selectivity in suspending nanotubes [157].

Dyes

Comparative and absolute photoluminescence quantum yields were produced with reference to standard dyes. While dyes emitting across a range of energies were employed, those emitting in the NIR range are less photostable and there is no agreement in the literature on a research standard for PL efficiency for emission in the infra-red.

RHODAMINE B has an absorption peak at 545 nm and emission peak at 610 nm, and a PLQY value of $\phi = 0.65$ in ethanol [119].

RHODAMINE 6G has an absorption peak at 530 nm and emission peak at 565 nm, and a PLQY value of $\phi = 0.95$ in ethanol [119].

RHODAMINE 101 has an absorption peak at 568 nm and emission peak at 627 nm, and a PLQY value of $\phi = 0.96$ in ethanol [119].

Rhodamine dyes are strong emitters with high PLQY values, hence their frequent use as standards. They show good reproducibility but do photodegrade after some time, especially in solution.

STYRYL-13 has an absorption peak at 580 nm and emission peak at 925 nm. The emission and excitation spectra are very closely aligned with that of the (6,5) tube, making it a suitable candidate for a standard. The exact value of its quantum yield has been called into question, however: several groups have used it assuming a PLQY $\phi = 0.11$ in methanol [51, 50, 104], though this has been questioned and a lower value of $\phi = 0.02$ proposed after comparison with rhodamine 6G [194].

IR-26 has a broad absorption peak around 980 nm and emission peak near 1125 nm. It has a reported quantum yield of between $\phi =$ 0.0005–0.005 in 1,2-dichloroethane [115, 184]. Similarly to Styryl-13, the overlap of its absorption and emission ranges with those of $E_{22} \rightarrow E_{11}$ s-SWNT transitions have led to its use as a reference standard [29, 188, 38, 101], though its PLQY value does not appear to be consistent.

SINGLET OXYGEN has a narrow emission peak at 1270 nm. It is usually excited by energy transfer from a donor molecule, in our case C_{70} molecules act as photosynthesisers suspended in carbon tetrachloride (CCl_4). In their critique of the use of Styryl-13 as a standard, Kappes

and co-workers suggest the adoption of singlet oxygen as a near-infrared emission standard, and report a value of $\phi = 0.014$ for its PLQY value [194]. However, they note that values for ϕ have been reported ranging from 1.38×10^{-3} to 4.9×10^{-2} [186, 183], which they suggest is due to the differing rate of generation of singlet oxygen by the different photosynthesisers used, and suggest more work must be done to establish it as a reliable and versatile standard.

Solvents

While surfactants are commonly used to aid dispersion/solubility of hydrophobic materials in aqueous solution, in this work where possible we have used deuterium oxide (D_2O) rather than water (H_2O). D_2O shows greater transparency in the near infra-red absorption range, as well as being considerably more dense ($1105\,kg{\cdot}m^{-3}$ vs $1000\,kg{\cdot}m^{-3}$; refractive index = 1.32), meaning it is more suitable for both determining absorption spectra and for use in ultracentrifugation. Apart from these two aspects, D_2O behaves comparably to water. PFO is not soluble in D_2O, and so most of the PFO work was done using toluene as a solvent.

Dye solutions employed a number of solvents (ethanol, methanol, carbon tetrachloride, toluene), which were ordered from Sigma Aldrich and used without further purification.

Concentrations in Solution

Surfactant-assisted dispersions were prepared using an ice-cooled sonication routine of 5 min high-powered sonication with a sonic tip, 1 hr sonic bath, and 5 min sonic tip again. The concentrations of solutions were calculated via absorbance measurements, where we have taken the absorbance at 650 nm of the initial dispersion—of known concentration—and compared it

to absorbances of the other solutions to calculate absorbance. All dilutions are performed with a stock solution of the surfactant in D_2O, in order to maintain the surfactant concentration above the critical micelle concentration. Above this concentration, the formation of stable micelles around a dispersed nanotube or nanotube bundle could becomes energetically favourable and leads to stable dispersions. This critical concentration was previously found to be on the order of $1\,mg{\cdot}mL^{-1}$ for the surfactants used here [198], while for the polymer PFO and biomolecule FMN, for which we expect stabilisation to occur as a result of molecular wrapping of the nanotubes, initial solution concentrations corresponding to those found in the literature were utilised (that is, $0.6\,mg{\cdot}mL^{-1}$ for PFO [157] and $1\,mg{\cdot}mL^{-1}$ for FMN [105]).

3.2 INSTRUMENTS

In measuring the optical properties of liquid-phase dispersions and solutions, the primary instruments used were the absorbance spectrometer and the photoluminescence spectrometer, while material preparation involved use of sonication equipment and centrifuges.

3.2.1 *Absorption Spectroscopy*

While an analysis of the absorption spectrum of a given material can give insights into the size and nature of suspended or dispersed particles, the primary uses are in determination of concentrations and in observing electronic transitions in the material.

Concentration and Absorbance

On passing through a material, the intensity of transmitted light is found to decay exponentially:

$$I_x = I_0 e^{-A'} = I_0 10^{-A} \tag{3.1}$$

where I_0 is the incident light intensity and I_x is the light intensity at a depth x in the sample. The quantity $A = A' / \ln 10$ is known as the *absorbance*, and its relationship to the (molar) concentration of a solution, c, optical pathlength l, and molar absorptivity ϵ is described by the Beer-Lambert law:

$$A = \epsilon c l \tag{3.2}$$

Absorbance is thus measured using the base-10 logarithm approach. The *transmission*, T of a material is defined as

$$T = \frac{I_x}{I_0} = 10^{-A}$$

meaning that a piece of material with an absorbance of 1 has a transmission of 0.1, i.e. the intensity of light exiting the material is just 10 % of the intensity of light incident upon the material. This is illustrated in Figure 12.

Given the linear relationship between absorbance and concentration in the Beer-Lambert law, unknown concentrations can be determined by measuring A in a spectrometer, using a known pathlength, and comparing to this to another value of A measured for a sample of the same material with known concentration (and pathlength).

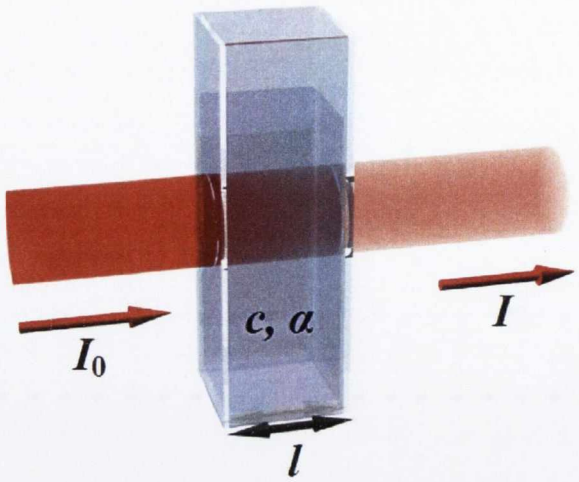

Figure 12: Illustration of absorption and transmission. Light of intensity I_0 passes through a material of concentration c and absorptivity α, emerging after travelling a pathlength l with transmission intensity I, where $I = I_0 e^{-\alpha c l}$. From (3.1) and (3.2), we see that $\alpha = \epsilon \ln 10$.

In the case of very high concentration of absorbing material, some of the underlying assumptions regarding the Beer-Lambert Law (such as the idea of independent absorbing centres, homogeneously distributed, without scattering) may fail to hold, but for most purposes the linear relationship is a very good model.

Absorbance Spectrometer

Figure 13 shows the schematic set-up of the absorbance spectrometer. The absorbance is determined by comparison of the light intensity measured at the detector with a reference measurement, treated as I_x and I_0 respectively. In 'single beam mode', only one of the two sample chambers are used. A reference cell (typically containing e.g. solvent only, or a surfactant dispersion of comparable concentration) is put in place and its absorbance spectrum measured. This spectrum is recorded and used as the reference when the same, or an optically matched, sample cell is used containing

the material to be examined. 'Dual beam mode' involves the splitting of the lamp beam, to be passed along two equivalent paths and through two matched sample cells. One cell is the reference cell as described above, the other contains the material to be examined. The light detected after passing through these cells is treated as I_0 and I_x respectively.

The light source is broad, and so must be passed through a monochromator to select the energy/wavelength of interest. Where possible it is advisable to match the bandpass of this monochromator setting to any other monochromators used in measurements on the same material. In particular, if we are to correlate relative absorbances measured at different nominal wavelengths with different quantities of light absorbed from an excitation beam in the PL spectrometer at corresponding nominal wavelengths, it is important to ensure similar spectral distributions for both the illuminating beams.

Clearly an absorbance value of, say, 2 (and thus a transmission of 0.01) means that 1 % of the reference beam intensity is recorded by the sample beam detector. As such, absorbance measurements are generally seen as less reliable above approximately 2–3, and experiments are ideally arranged to give an absorbance value close to 1.

Since absorbance A is a linear function of pathlength l, it is generally advised to use as long a pathlength as possible to reduce errors in the absorbance value. Measurements using different pathlengths can then be scaled appropriately. 10 mm pathlengths are most common. In our work pathlengths used were 1 mm, 5 mm and 10 mm, depending on the concentration and maximum resulting absorbance recorded.

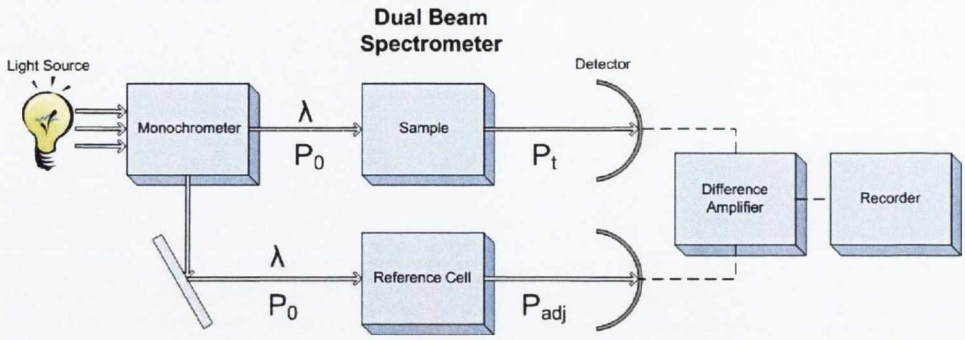

Figure 13: Schematic illustration of absorption spectrometer. The sample and reference cells are illuminated by light of the same intensity and spectral characteristics, with the difference between the subsequent transmitted light intensities allowing calculation of the absorbance of the sample relative to the reference material.

3.2.2 *Photoluminescence Spectroscopy*

As a technique that probes the relationship between absorption and emission, PL spectroscopy is used to investigate the electronic states of materials with a high degree of selectivity and sensitivity.

Principles of PL Spectroscopy

The fundamental difference between absorption and PL spectroscopy is that PL spectroscopy is concerned with the detection of light emitted by the sample, not light generated by the excitation lamp. The detection apparatus is thus decoupled from the excitation beam, and both can be controlled independently. In this way, both emission spectra (emission intensity as a function of energy) for a range of excitation energies and excitation spectra (emission intensity at a given detection energy as a function of excitation energy) are obtainable. Several emission or excitation scans can be combined into a PL excitation-emission map, as illustrated in Figure 14.

In contrast to the absorbance spectrometer, there is generally no need for a comparable 'dual beam' mode. Rather than compute an absorbance value

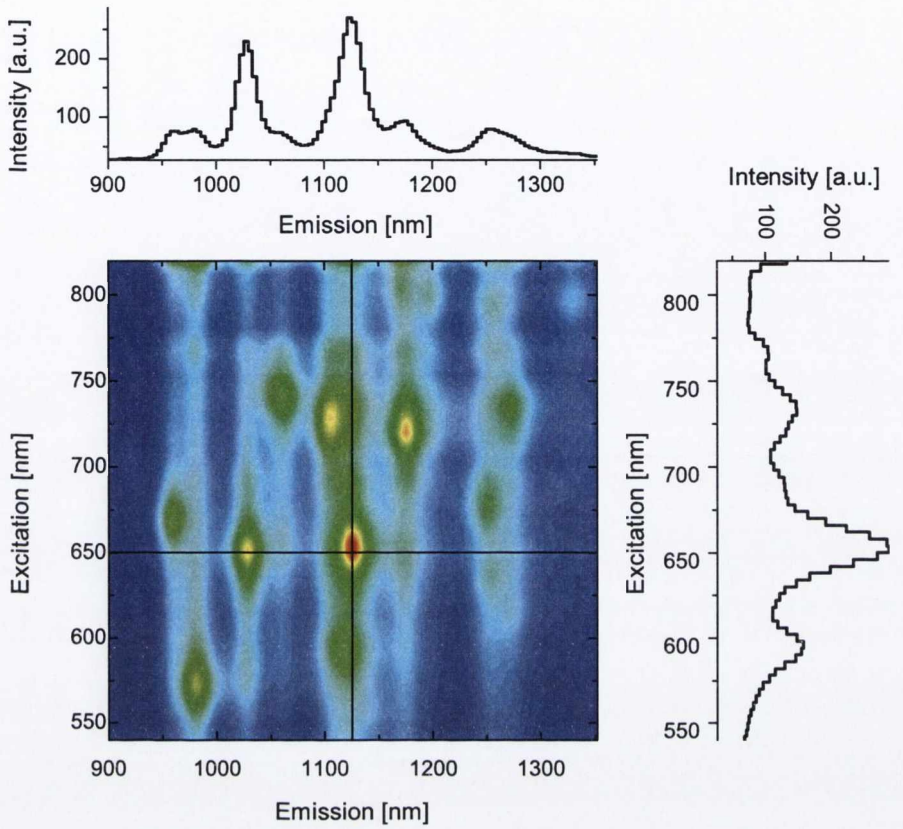

Figure 14: Sample photoluminescence excitation-emission map with cross-sections. The PL map is composed of several individual emission line scans compiled in sequence. The horizontal and vertical lines through the resulting PL map correspond to a PL emission line scan (shown above the map) and a PL excitation line scan (shown on the right) respectively.

with reference to the uninterrupted excitation beam, the reference value for the detector is simply the detector's own dark count. (Of course where the solvent exhibits some photoluminescence at the energies in question then a reference emission spectrum can be recorded, analogous to the operation of the absorbance spectrometer in 'single beam' mode.) However, the output is typically modified to correct for the variation in excitation light intensity with changing excitation energy, measured using a reference detector into which a portion of the excitation beam is deflected. PL spectrometers are generally more sensitive than absorbance spectrometers

at low concentrations: a small amount of emission above a low dark count is more easily recorded than a small difference in two high intensity light sources.

There are several ways in which information regarding the sample's internal electronic structure may be obtained from PL spectroscopy. Stokes shifts (differences in the peak absorbance and emission from the same electronic transition) can be observed and related to the internal band structure. Linewidths and broadening of emission peaks may indicate aggregation and other interactions between species. Absorption by one species may lead to emission from another, either through charge transfer or resonant energy transfer. Where emission at a particular energy is being monitored, differences between the excitation spectrum and the absorbance spectrum may indicate changes in the concentration or may also indicate energy transfer.

Kinetics of reactions and photophysics of materials can also be probed using PL spectroscopy. Repeating a PL emission or excitation scan over time can help to identify changes in the sample owing to intermolecular reactions or dynamic interactions. Time decay PL can be used instead of steady-state excitation beam illumination to probe the decay of emission over time and thus gain insight to the excited states of the sample. In this work steady-state illumination has been used exclusively, though repeat measurements over a period of several weeks showed a high level of stability for the SWNT dispersions and their aggregation state.

PL Spectrometer

The PL spectrometer used in this work is an Edinburgh Instruments FLS 920 unit, incorporating a 450 W Xe broad excitation source and a liquid-nitrogen cooled photomultiplier tube for detection in the range 500–1500 nm as well

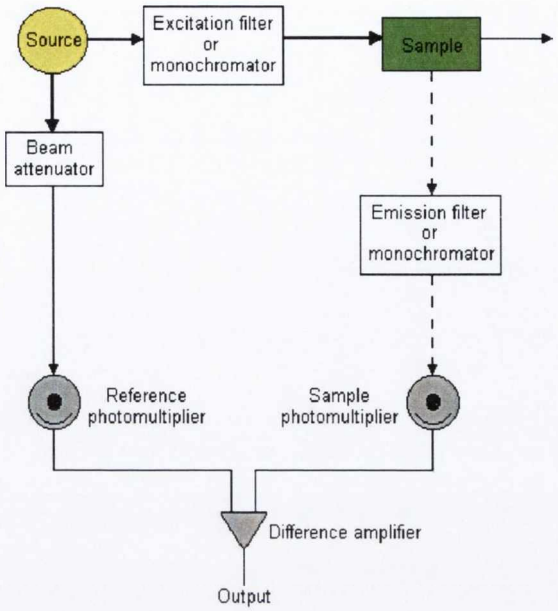

Figure 15: Schematic illustration of PL spectrometer. Light is collected from the sample in our set-up at right angles to the incident excitation beam. The detected light intensity is corrected to take account of the changes in intensity of the excitation beam as a function of excitation energy.

as a InGaS detector for the range 300–900 nm. The apparatus is configured in the 'L-shaped' set-up to reduce the detection of light from the excitation source, either directly or through reflection. A schematic of the instrument set-up is shown in Figure 15.

The liquid-phase cuvette holder is designed to hold 10×10 mm cuvettes, though in the case of 2 and 1 mm cuvettes an adaptor piece is available.

The spectrometer set-up includes an iris for modifying the intensity of the illumination by the excitation beam and a Si-diode reference detector into which a small portion of the excitation beam is deflected. This allows a profile of the excitation beam intensity as a function of wavelength to be recorded. The spectral performance of the detector is included in a data file provided by the manufacturer. Recorded intensities are thus corrected for both excitation and detection efficiencies.

Both the excitation beam and the detector unit are fitted with monochromators to select light of the appropriate wavelength, and are adjustable independently. Bandpasses from 1–15 nm are available.

3.2.3 *Atomic Force Microscopy*

For sub-micron resolution spectroscopy, the use of optical microscopes is prohibited not just by practical implications regarding the size of the lens or the technical specifications required, but by the nature of light itself: visible light, with a wavelength of about half a micron, cannot be used to satisfactorily resolve details on a comparable or smaller scale. However, nm-scale resolution of morphology, charge distribution, conductivity, and many other characteristics are available using the various techniques of scanning probe microscopy. In our work we examined the size distribution of dispersed nanotubes on a silicon substrate using an atomic force microscope.

Atomic Force Microscope (AFM)

The AFM was one of the earliest types of scanning probe microscope developed, and reveals details about the physical structure of materials. In a simple schematic representation of the AFM as in Figure 16, we see the sharp AFM tip is located at the end of a narrow cantilever. This cantilever can be driven to vibrate at a known frequency, however if it (or, more precisely, the tip) comes close to contact with another material then the resulting repulsive force alters the vibrations of the cantilever. As the sample stage is scanned by piezo-electric elements beneath the cantilever, the AFM adjusts the height of the cantilever above the sample surface to

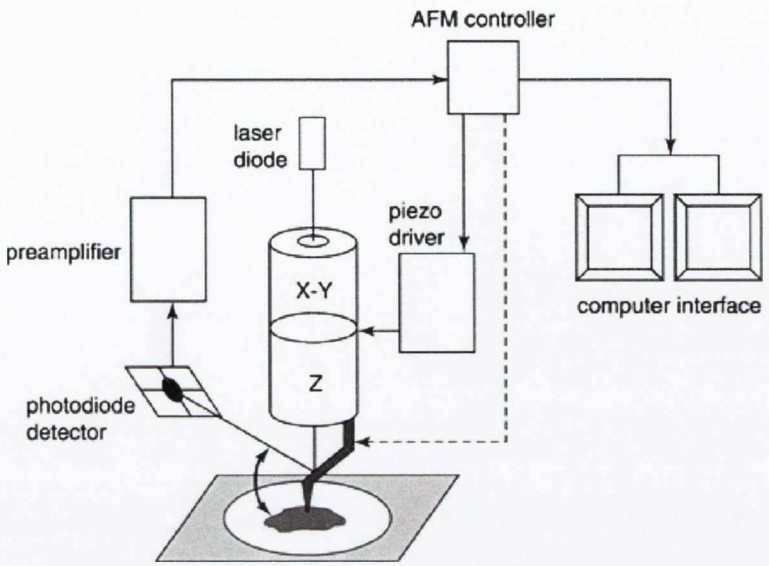

Figure 16: Schematic illustration of atomic force microscope (AFM). Subtle changes in the position of the cantilever tip scanning across the sample are detected via changes in the position of a laser signal reflected from the back of the tip. Adjustments to the relative tip position made via the piezo-electric stage to keep the laser signal constant are interpreted by the software to produce a 3D map of the sample surface.

maintain a constant level of vibration in the cantilever and thus a constant height above the sample. A laser trained on the upper surface of the cantilever and reflecting on to some light-sensitive diodes monitors the movement of the cantilever. This information is then processed to give high-resolution images of the height profile of the material.

Diameter, Length and Mass Fraction Analysis

Extensive work has been carried out in this group on the relationship between concentration, nanotube bundle dynamics and bundle diameter as measured using the AFM [198, 21, 69, 42]. From a measurement of bundle length and diameter for a large number ($\geq$ 150) of tubes and bundles on a substrate, we can calculate the mass fraction of individual tubes in the dispersion, M_{Ind}/M_{Tot}, as follows.

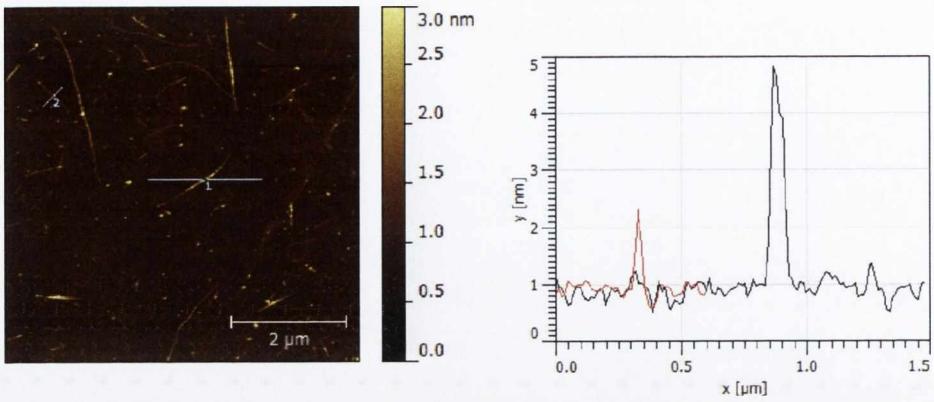

(a) (b)

Figure 17: AFM of SWNTs on a silicon substrate, with profile analysis. As detailed in the text, from an analysis of over 150 SWNTs (or small bundles of SWNTs) identified in images such as (a) above, measurements of the diameter and length of the SWNTs lead to an estimate of the mass fraction of individual tubes in the dispersion. The profiles illustrated in (b) are marked in grey on the AFM image: the black profile across a bundle is marked '1' and the red profile across a smaller tube '2'.

Given the diameter range of HiPCO nanotubes (0.8–1.4 nm), we treat any 'bundle' of diameter ≤ 1.4 nm as an individual tube, and any with larger diameter as a small bundle of two or more tubes. This gives us the number fraction of individual tubes as a proportion of all the objects in the sample, N_{Ind}/N_{Tot}. We then define the mass fraction as

$$\frac{M_{Ind}}{M_{Tot}} = \frac{M_{NT}N_{Ind}}{V}\frac{V}{M_{Tot}} = \frac{M_{NT}}{C_{NT}}\frac{N_{Ind}}{V}$$

where M_{Ind} and M_{Tot} represent the mass of all individualized nanotubes and the total mass of all dispersed nanotubes and bundles, respectively, while M_{NT} is the average mass of an individual SWNT and M_{Tot}/V is the total nanotube mass per volume (i.e., the concentration, C_{NT}). Writing M_{NT}

in terms of the individual nanotube diameter and length and the mass per unit area of a graphene sheet (M/A), we get:

$$\frac{M_{Ind}}{M_{Tot}} = \left(\frac{M}{A}\right) \frac{\pi \langle D_{NT} \rangle \langle L_{NT} \rangle}{C_{NT}} \left(\frac{N_{Ind}}{V}\right)$$

where $\langle D_{NT} \rangle$ is the mean individual nanotube diameter and $\langle L_{NT} \rangle$ is the mean length. The term N_{Ind}/V, the number of individual tubes per volume, can be calculated using N_{Ind}/N_{Tot}, according to [69]:

$$\frac{N_{Ind}}{V} = \frac{N_{Ind}}{N_{Tot}} \frac{N_{Tot}}{V} \approx \frac{N_{Ind}}{N_{Tot}} \frac{4C_{NT}}{\rho_{NT} \pi \langle D^2 \rangle \langle L \rangle}$$

where $\langle D \rangle$ and $\langle L \rangle$ are the mean object (individual tubes *and* bundles) diameter and length, respectively. Measurement of the mass fraction of individual tubes thus involves measurement of the length and diameter of a representative sample (usually over 150) of SWNT-like objects found through AFM scans.

A typical AFM scan is shown in Figure 17, along with sample images from the analysis software used to measure the length and diameter.

3.2.4 *Centrifugation: centrifuge and ultra-centrifuge*

Centrifugation is commonly used to remove unsuspended SWNTs or carbonaceous material, impurities and large bundles of tubes, which over time under normal conditions may fall out of suspension or act as seeds for further aggregation. In order to remove all but the smallest bundles, ultracentrifugation is usually required. The use of ultracentrifugation was one of the key components in O'Connell's work [159] on dispersing individualised nanotubes leading to the observation of PL.

Centrifugation and ultracentrifugation

While the principle underpinning centrifugation is relatively simple, a number of different approaches and apparatus have been developed. The differences between these generally fall into a number of categories:

ROTOR SPEED AND RELATIVE CENTRIFUGAL FORCE The rotor speed and relative centrifugal force are related by the equation $v = \omega^2 r$ which gives RCF $= 1.12 \times 10^{-3} \cdot r \cdot \text{RPM}^2$ where RCF is the relative centrifugal force, r the distance from the axis of the centrifuge rotor in metres, and RPM the revolutions per minute. Desktop centrifuges generally provide up to 15000 rpm (RCF $\sim$ 25000 g) while larger ultracentrifuges can provide up to $\sim 100,000$ rpm (RCF $\sim 400,000$ g).

ROTOR ANGLE Rotors generally come either with sample chambers set at a fixed angle (including vertical orientation) in the rotor, or with swinging bucket sample containers. As the force field of the RCF is always directed away from the axis of rotation, the field gradient is then either angled across the sample tube or in the case of swinging bucket rotors (where the buckets will swing out to a horizontal orientation at high speeds) aligned along the length of the tube.

RATE OF SEDIMENTATION Depending on the relative density of the suspended material, the medium in which it is suspended, and the relative centrifugal force applied, centrifugation can be either isopycnic or rate-zonal. In the first case, the density of the medium is greater than that of at least some of the suspended material. Under centrifugation, material will move to its equilibrium buoyant density level. A medium with a progressive density gradient may be used, allowing the separation of numerous components within the

suspended material according to density, to be separated later. This is known as isopycnic centrifugation. Rate-zonal centrifugation occurs when the medium is less dense than the suspended material, with the rate at which the suspended particles sediment then governed by their size. After centrifugation, the larger particles are closer to the bottom of the tube (that is, the side furthest from the rotation axis).

Centrifuge Details

The ultracentrifugation work presented here was performed using a Beckman-Coulter LP Optima-100 ultracentrifuge, using either rotor SW-41i (swing bucket rotor, 13 mL tube volume) or SW-55 (swing bucket rotor, 5 mL tube volume).

3.2.5 *Sonication: Sonic Bath and Sonic Tip*

The most practical way to overcome the strong attractive force between nanotubes in a bundle is the application of ultrasonic energy.

Sonication Bath

Ultrasonic baths provide low-level sonic energy to a small volume ($\sim$ 1 L) of water, in which the sample is suspended. Because of the standing waves set up in the bath there are typically nodes and antinodes within the bath, and the amount of energy absorbed by the sample is affected by its position in the bath, the sample's container shape (e.g. equal volumes of sample solution in round bottom flasks and conical flasks may absorb different amounts of energy). Reproducibility is therefore an issue when the sonic bath is the primary source of energy to separate nanotube bundles. The

sonic bath used here was a Branson 1510, frequency 42 kHz, power output 80 W.

Sonic Tip

Where more power is needed, sonic tips are used instead of baths. The high-frequency vibration of the tip submerged in the sample provides more power, and in a more concentrated volume. While the criteria for standing waves may exist in the sample container, the solution is generally in such a state of chaotic motion that the entire sample absorbs a uniform amount of sonic energy. The sonic tip used here was a Sonics VibraCell VCX 750, 750 W unit with a tapered tip.

Effects of Sonication

Use of the sonic tip to disperse SWNTs has been shown to cause scission of the nanotubes, with longer sonication times leading to shorter average lengths [85, 139, 83]. The intense localised heat caused by the sonic tip may also contributes to the introduction of defects and other sonochemistry effects [83, 68], and so in our routines for sonication we have used ice-water mixes to cool our samples during sonication.

4 CONCENTRATION-DEPENDENT EFFECTS ON THE INTENSITY OF MEASURED PHOTOLUMINESCENCE

The influence of inner-filter and reabsorption effects on the photoluminescence data obtained from highly-absorbing sample solutions is introduced in Section 4.1, along with our model polymer/solvent system. A predictive model showing how these effects are manifested in our experimental set-up is developed in Section 4.3, and used to account for the observed PL intensity at 1 cm sample absorbances up to 10*. The same model is then applied with a change in solvent to differentiate between absorbance-related effects and those of aggregation. The implications for photoluminescence spectroscopy of carbon nanotube solutions are discussed.

4.1 INTRODUCTION

Photoluminescence spectroscopy (see 2.1.4) has become a key investigative tool in carbon nanotube research over the past number of years, as outlined in 2.2.4. Numerous difficulties arise when comparing results obtained from different apparatus or different samples. In any effort to produce quantitative measurements or analysis—particularly when contrasting data from different experimental set-ups—there are several precautions and procedures which should be taken into account. The instrument-related

* Corresponding to a concentration of $\sim 0.1\,\mathrm{mg \cdot mL^{-1}}$. We employ the common dimensionless unit of absorbance here, measured here using a 1 cm pathlength cuvette.

issues such as corrections for beam intensity, monochromator efficiency and the spectral sensitivity of the detector system were summarised in 3.2.2 and are not discussed further. All results presented here have incorporated the standard corrections as per manufacturer's instructions and best practice [145]. However, instrument corrections alone do not necessarily result in PL data which is truly representative of the emission from the sample, and it is important to address some issues which may be caused by the absorbance of the sample if reliable quantitative work is to be undertaken.

Two sets of absorption- and concentration-dependent issues in particular are likely to affect PL results from SWNT dispersions, which are known to be highly absorbant and prone to aggregation. These effects relate independently to absorbance (inner-filter and reabsorption effects) and to the aggregation and bundling dynamics of nanotubes in solution (reduced PL signal, broadened peaks), both of which are in turn related to concentration.

Concentration, inner-filter and reabsorbance effects

While the Beer-Lambert Law indicates that concentration is linearly related to absorbance, the relationship between concentration and photoluminescence is more complex. Given the high extinction coefficients (greater than $30\,\mathrm{mL{\cdot}mg^{-1}{\cdot}cm^{-1}}$ in the visible to near-infrared range [123, 69]) and generally low reported quantum yields (of the order of 0.001 for ensemble dispersions [51]) of SWNTs, it is worth exploring the complications likely to arise in measuring PL emission from solutions with relatively high absorbances.

At low concentrations, PL intensity is observed to scale linearly with concentration and with absorbance, and this relationship is used implicitly in our definition of photoluminescence quantum yield in (2.3), where the quantity m is defined as the slope of integrated PL emission versus

absorbance. Photoluminescence in the simplest case depends linearly on the quantity of light absorbed by the material, which for a material of thickness x can be calculated from Equation 3.1 as $I_0 - I_x = I_0(1 - 10^{-A})$. Thus PL emission is linearly related to $(1 - 10^{-A})$, not A. The approximation, using the first two terms of the Taylor series expansion $e^x = 1 + \frac{x^1}{1!} + \frac{x^2}{2!} + \ldots$, giving $1 - 10^{-A} = 1 - e^{-A \ln 10} = A \ln 10$, remains close to linear for values of A less than 0.1. The difference between a and $1 - e^{-a}$ is less than 10 % of a when $a \lesssim 0.1$. Obviously at high absorbance values, when a significant amount of the available light is absorbed, a large increase in the the concentration will no longer result in an equally large increase in PL emission, as the fraction of available light absorbed begins to saturate and will tend towards unity. An accurate examination of PL emissions as a function of absorbance or concentration must therefore avoid this approximation when operating outside the low absorbance regime.

Instead of simply saturating, the measured PL is typically observed to decrease as the concentration of absorbing material is increased. The measured PL is not directly related to absorbance alone, but to the quantity of light that is absorbed and emitted such that this emission is then measured by the detector. The influence that the absorbance characteristics of a material and the geometry of the set-up have on this measured PL emission is described by the inner-filter effect.

There are two distinct contributions to the inner-filter effect: attenuation of the excitation beam, and absorption of emitted light by the sample itself before it emerges. While many terms are used to describe one or both of these effects (pre-absorption, post-absorption, self-absorption, reabsorption, screening and inner-filter effects ...) in this work the phrase 'inner-filter effect' shall be used as an over-arching term to describe the complete

effect, while 'reabsorption' shall be used to refer specifically to that second contribution mentioned above.

In the first instance, absorption and attenuation of the excitation beam by the sample may result in the emission of light from close to the front face of the sample cuvette, which may be outside the field of view of the detector, and a simultaneous decrease in the amount of light reaching and being absorbed by that part of the sample upon which the detector is focused. This issue can be exaggerated by large sample cuvettes, when the lens set-up collecting emitted light is trained on a small volume. Thus the recorded PL emission signal will increase, reach a maximum, and then decrease with increasing absorbance.

In the case of re-absorption, an overlap of the absorption and emission spectra of the sample may result in a significant fraction of the emitted PL being re-absorbed by other molecules in the sample material. In this case it is possible that very little of the PL emitted other than from the edge of the cuvette nearest the detector will actually be recorded. Both of these effects are subject to the detailed absorbance spectrum of the material: for energies at which the absorbance is low, 'normal' contributions to the PL emission will continue, even while inner-filter effects reduce other contributions from certain absorbance and emission energies to near zero.

The consequences of inner-filter effects can be dramatic in terms of PL measured as a function of concentration or absorbance: (i) at increasing concentration of fluorophore, we may see a levelling or decrease in measured PL; this can also be seen at constant fluorophore concentration when increasing concentrations of non-fluorescent absorbing material are added, (ii) measured PL intensity becomes sensitive to the region in the sample cuvette from which emission is measured, as emission intensity becomes higher nearer the illuminated face; (iii) PL excitation spectra may deviate

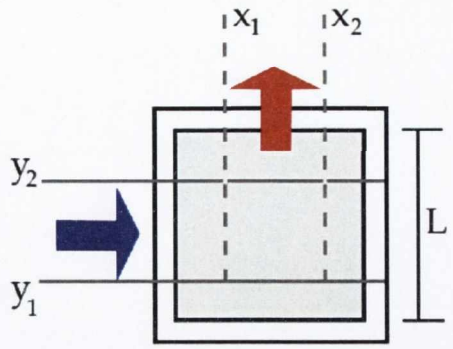

Figure 18: Cross section of photoluminescence sample cuvette. The internal dimensions are $L \times L$. The excitation beam travels parallel to the x-axis as shown by the filled blue arrow and illuminates the sample, striking the cuvette face between y_1 and y_2. Light is absorbed and re-emitted in all directions but only that light emitted parallel to the y-axis from points in the sample in the range between x_1 and x_2 is collected by the detector (red arrow). The active area of the cuvette, contributing to the observed PL, is thus bounded by the lines shown.

from their typical form matching the absorbance curve: emission arising from excitation at energies corresponding to high absorbance levels will be suppressed relative to other excitation energies, (iv) where there is an overlap between emission and absorbance curves, PL emission may be reduced according to the strength of the absorbance.

The inner-filter effect must clearly be mitigated as far as possible when dealing with PL spectroscopy and particularly when trying to make quantitative measurements or deductions. Where the effect can not be eliminated (primarily through the use of sufficiently low concentrations, or collecting emission from the front face of the sample cuvette) it should be corrected for as far as possible. There are a number of broadly similar methods for correcting for the inner-filter effect and in this work one such model is adapted and used to describe the effects as manifested in our particular experimental set-up.

Effects of aggregation

Aggregation is known to reduce the emission intensity of SWNT solutions, and the major advance in the original paper showing band gap PL emission was one of separation and individualisation of the nanotubes. Given that aggregation can both reduce the intensity (through quenching of PL emission by metallic tubes) and the shape (aggregates show broadened peaks) it can be difficult to resolve the influence of aggregation from that of inner-filter effects mentioned above. The picture, simplified though it is, becomes increasingly complicated if one considers the many species of SWNT present in a sample as behaving independently of each other. To simplify the system and attempt to separate these distinct effects on the PL emission of a sample, we have employed a single fluorescent polymer/solvent solution with some useful properties regarding aggregation.

Poly(9,9-dioctylfluorene) (PFO) has been used extensively in the study of luminescent conjugated polymers, particularly as a component of organic blue-light-emitting diodes [147, 73, 26, 74, 216], as part of wider research into conjugated polymers and applications in organic electronics and optoelectronics [67, 34]. It has a typically high extinction coefficient ($\sim 100\,\mathrm{mL{\cdot}mg^{-1}{\cdot}cm^{-1}}$), thus inviting complications from the inner-filter effect, but also has a distinctive and well-documented behaviour regarding aggregation.

It has been observed that PFO exhibits distinct phases, with much interest in the contrasting behaviour and properties of the so-called 'bulk' or glassy phase and the crystalline aggregate β-phase [72]. It is possible to control the morphological state of thin films of PFO by careful choice of solvent, specifically through altering solubility parameters and boiling point [71, 110], and through physical post-deposition procedures such as thermal

treatments and exposure to gaseous solvents [71, 35, 72, 5]. There has been much interest in studying this material in its multiple phases as it offers the chance to investigate the influence of morphological and chain conformational differences on the emission properties and charge and exciton-transport behaviour of the material, without any issues associated with changes in chemical structure [39, 80, 35, 5, 6]. While the majority of these studies have been conducted on solid-state samples, similar distinct phases have been observed in solutions of PFO [71]. As a result of this previous research, the behaviour of PFO is reasonably well known, allowing us to use it as a model compound for the study of non-linear changes in PL intensity with concentration.

The highly non-linear relationship between PFO concentration, absorbance and PL is modelled using a method similar to others outlined in the literature to account for concentration and inner-filter effects mentioned above. The behaviour of PFO—and the ability of this model to account for it—in numerous solvents as a function of concentration is also explored.

The aim of this exploration of concentration and inner-filter effects on PL measurements is to verify that we can correct, where necessary, for these effects in relatively high concentrations and also to investigate whether we can separate their influence on PL from the effects of aggregation. The model itself is not material-dependent and can then be applied to any other system where inner-filter effects and re-absorption are considered to be an issue, such as solutions of SWNTs.

4.2 EXPERIMENTAL METHOD

PFO (purchased from American Dye Sources, ADS 129 BE and used as received) was dispersed in toluene (spectrophotometric grade, from Sigma Aldrich) using an ultrasonic tip processor (Sonics Vibra-Cell VCX 750; 750 W, 20 %, 60 kHz, 5 min). Concentrations ranged from $2\,\mathrm{mg{\cdot}mL^{-1}}$ to $0.00025\,\mathrm{mg{\cdot}mL^{-1}}$.

PL measurements were taken using a Perkin-Elmer LS-55 spectrometer employing a 2×2 mm microcuvette and a suitable holder in the standard perpendicular geometry unless otherwise stated. Excitation–emission contour maps were constructed using emission wavelength ranges from 400–600 nm (3.10–2.07 eV) at 0.5 nm intervals, and employing excitation wavelengths from 375–445 nm (3.31–2.79 eV) in 2 nm intervals. Absorbance spectra were taken using a Shimadzu UV- 2401PC spectrophotometer using a 1 cm path length cuvette and with a solvent-only cuvette used as a baseline reference sample.

4.3 RESULTS AND DISCUSSION

Solutions of PFO, in common with those of many other organic polymers, have a high extinction coefficients of $\sim 100\,\mathrm{mL{\cdot}mg^{-1}{\cdot}cm^{-1}}$ at their peak absorption wavelength, here around 385 nm (3.220 eV). Figure 19 shows normalised absorption and emission spectra for PFO at low concentration in toluene. We note a strong, broad absorption band, rising below 425 nm (= 2.917 eV) and peaking at approximately 385 nm (= 3.220 eV), with no strong vibronic structure in the region studied. The PL emission spectrum

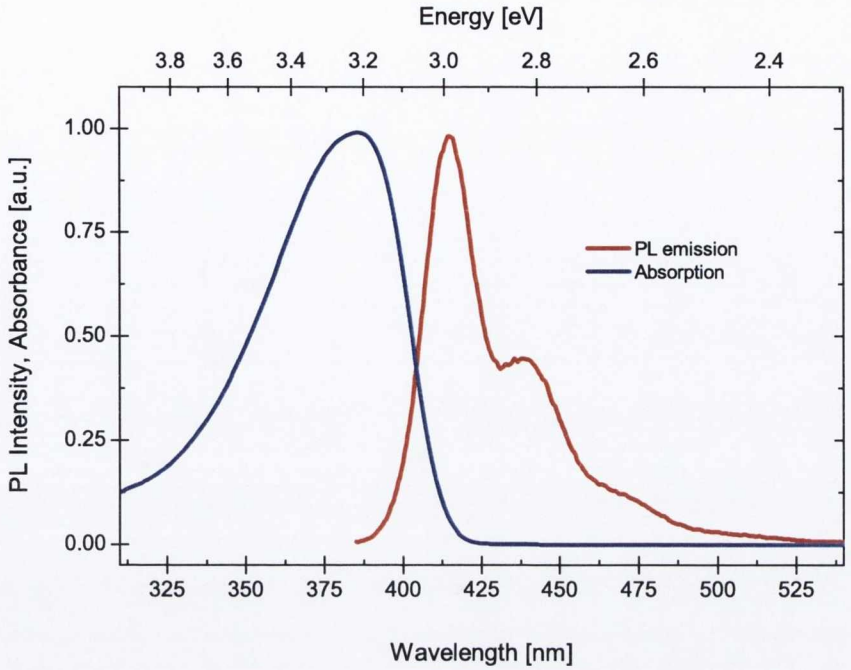

Figure 19: Photoluminescence and absorbance spectra for PFO in toluene. Curves are normalised to their maximum value. Note the region of the emission above 2.9 eV ($\lambda < 425$ nm), which is subject to re-absorption as shown by the overlap of the two spectra.

shows a primary peak at 416 nm (= 2.980 eV), with weaker structured peaks appearing at 439, 465, and 500 nm (= 2.824, 2.666, 2.480 eV, respectively).

Figure 20 shows, in 20a, the absorption spectrum of PFO in toluene, between 375 and 445 nm, and in Figure 20b and 20c excitation-emission maps for low (0.00025 mg·mL^{-1}) and high (1.0 mg·mL^{-1}) concentrations respectively of PFO in toluene, in a 2 × 2 mm microcuvette (Figure 20d will be discussed below). A linear increase in PL with concentration would result in these PL maps retaining their spectral profiles at all concentrations, with only an increase in intensity observed. However, as described above, some deviation from this behaviour was expected, particularly at higher concentrations, due to effects related to the high absorbance value of PFO. This deviation was indeed observed, the features of the contour maps

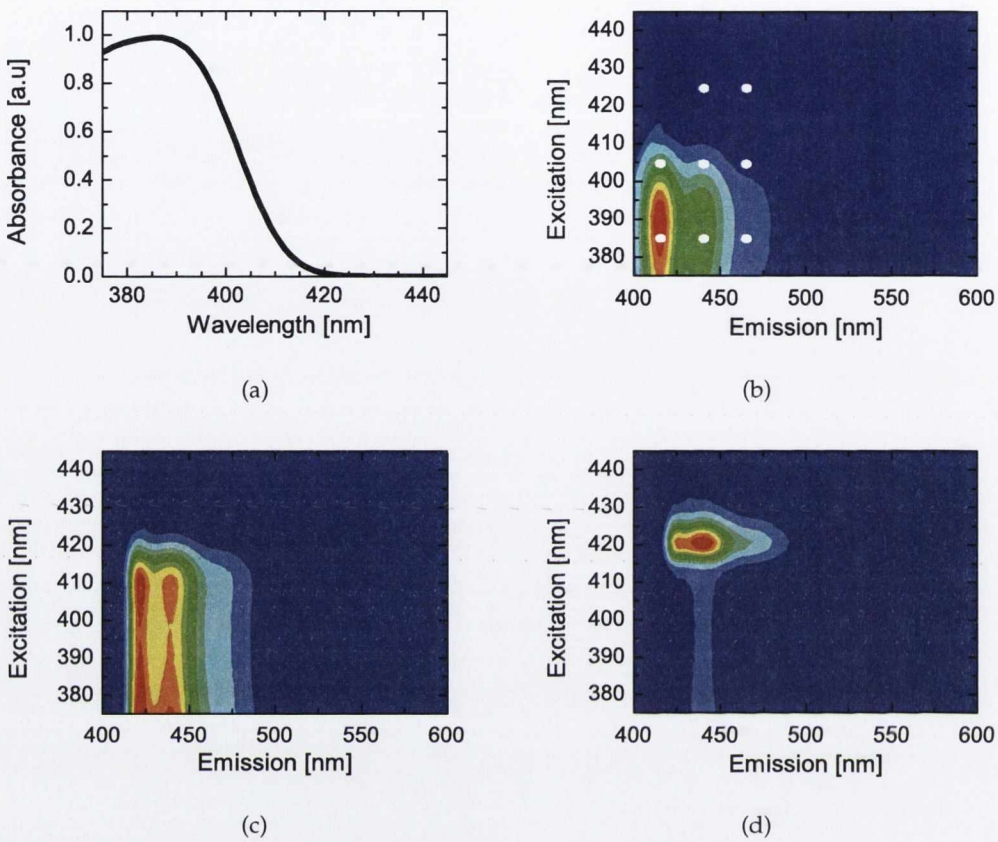

Figure 20: Effect of concentration on the PL contour map of PFO in toluene. (a) An absorption spectrum for PFO at low concentration. (b) PFO at 0.00025 $mg \cdot mL^{-1}$ in a 2×2 mm microcuvette set-up. The open circles represent those excitation–emission wavelength combinations for which PL intensities are tracked across a range of concentrations in Figure 21. Note the correlation between the PLE curve (horizontal cross-section) and the absorption curve in (a). (c) PFO at 1.0 $mg \cdot mL^{-1}$ in the same set-up. Note the reduction and red-shifting of the emission (vertical cross-section) peak at 416 nm, and the broadening and flattening of the PLE curve, which is beginning to show a dip for excitations just below 400 nm. (d) PFO at 1.0 $mg \cdot mL^{-1}$ in a 10×10 mm cuvette set-up. Here the sample is identical to that in (c) except for the cuvette size. We note a dramatic decrease in PL intensity for all excitation wavelengths below approx. 416 nm, and also further reduction/red-shifting of the 416 nm emission peak.

beginning to change appreciably at concentrations above $0.05\,mg{\cdot}mL^{-1}$ with quenching of the primary emission peak at 416 nm.

It is clear from a comparison of the PL maps in Figure 20b and 20c that the relationship between PL intensity and concentration is highly non-linear for certain points on the excitation-emission map. The emission peak centred at 416 nm has been greatly reduced and red-shifted by 6 nm on going from low to high concentration. Also apparent is a broadening of the PLE peak (a vertical cross-section in these excitation-emission maps) at high concentrations. Figure 20d shows the contour map for the same high concentration of PFO but using a 10×10 mm cuvette instead of the 2×2 mm microcuvette. Here the change is even more dramatic with an apparent shift in the PLE peak from its absorption maximum at 385 nm to a sharp peak near the absorption edge at 423 nm, with a generally constant value for excitation wavelengths from 375 to 420 nm. The differences between Figure 20c and 20d illustrate the importance of accounting for factors inherent in the set-up of the sample measurement, as the sample solution in each is the same but the measured PL maps are markedly different.

In order to illustrate the observed changes in features of the PL maps, the intensity of several points (referenced by their co-ordinates on the contour map in terms of excitation and emission detection wavelengths in nanometres: [*Ex*, *Em*]; the points we used are marked with white dots in Figure 20c) was tracked as a function of concentration. Figure 21 shows our results for PFO in toluene in a 2×2 mm microcuvette. While the behaviour is linear at low concentrations there are marked deviations from linearity at concentrations above $0.05\,mg{\cdot}mL^{-1}$, with some points showing a significant drop in intensity at high concentrations. In order to understand the contributions to this non-linearity from the inner-filter

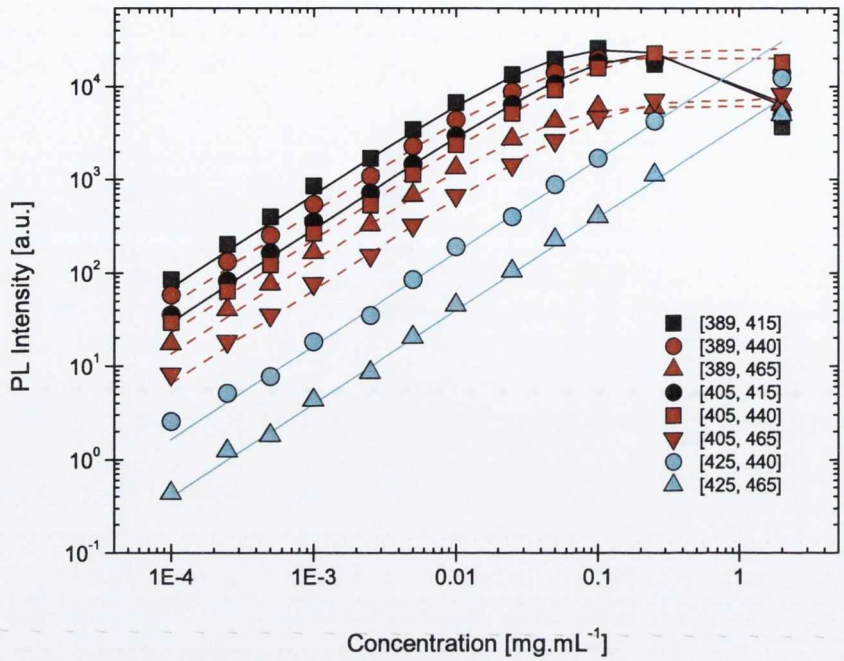

Figure 21: Observed PL intensity as a function of concentration for solutions of PFO in toluene. Shown here are PL intensities of particular excitation and emission wavelength combinations across a range of concentrations: the [385,415] series represents PL intensity detected at 415 nm using an excitation wavelength of 385 nm, etc. The solid and dashed curves indicate the predicted behaviour of these PL intensities obtained from the theoretical model, from Equation 4.1

effect and re-absorption we develop a model to describe the observed PL intensity as a function of concentration. This method is similar to the procedure outlined by Miller [145] and to that used by Riesz *et al.* [175].

Shown in Figure 18 is the cross-section of a cuvette, illuminated by an excitation beam entering the cuvette parallel to the x-axis. The emitted light is collected at right angles to this beam, and fluorescence emitted parallel to the y-axis from the area between x_1 and x_2 will be seen by the detector. The width of the excitation beam is delimited by y_1 and y_2. The excitation beam strikes the cuvette such that N photons per second per unit area with wavelength, λ_1, fall upon the cuvette surface. In the sample, both

the excitation beam and the emitted fluorescence follow the Beer–Lambert law,

$$I_{\lambda_1}(x) = I_{\lambda_1}(0)e^{-\alpha(\lambda_1)cx} = (I_0)_{\lambda_1}e^{-\alpha(\lambda_1)cx}$$

for the intensity, I, of light of wavelength λ_1 travelling a distance, x, through a solution of concentration c of a solute of absorption coefficient α. The change in photon flux (photons·m^{-2}·s^{-1}), F_λ due to absorption in distance $\mathrm{d}x$ is then

$$\mathrm{d}F_{\lambda_1}(x) = -\alpha c(F_0)_{\lambda_1}e^{-\alpha(\lambda_1)cx}\mathrm{d}x$$

The number of photons absorbed in an infinitesimal volume of the cuvette, $\mathrm{d}x\mathrm{d}y\mathrm{d}z$, per second is then

$$\mathrm{d}N_{\lambda_1} = -\mathrm{d}F_{\lambda_1}\mathrm{d}y\mathrm{d}z$$

These photons are absorbed to create excitons which then decay to emit photons of wavelength, λ_2, with probability ϕ (the quantum efficiency). If the number of emitted photons per second is L_{λ_2} , we can write:

$$\mathrm{d}L_{\lambda_2}(x) = \phi\alpha c(F_0)_{\lambda_1}e^{-\alpha(\lambda_1)cx}\mathrm{d}x\mathrm{d}y\mathrm{d}z$$

Some of this emitted light will be re-absorbed before leaving the cuvette. To account for re-absorption, which also follows the Beer–Lambert law, we introduce a factor $e^{-\alpha(\lambda_2)c(L-y)}$ where $\alpha(\lambda_2)$ is the absorption coefficient of the sample at the emission wavelength, λ_2, and L is the length of the cuvette in the y-direction. Introducing a constant K to account for the detection efficiency and geometry of our set-up, integration gives us an

expression for the number of observed photons, L_{obs}, due to fluorescence from the volume $(x_2 - x_1) \times (y_2 - y_1) \times z$:

$$\begin{aligned}(L_{obs})_{\lambda_1,\lambda_2} &= Kz(F_0)_{\lambda_1}\phi(e^{-\alpha(\lambda_1)cx_1} - e^{-\alpha(\lambda_1)cx_2}) \\ &\times \left(\frac{e^{-\alpha(\lambda_2)c(L-y_2)} - e^{-\alpha(\lambda_2)c(L-y_1)}}{\alpha(\lambda_2)c}\right)\end{aligned}$$

The observed fluorescence intensity, I_{obs}, is then $L_{obs}h\nu/A_{eff}$, where $h\nu$ is the energy of the photon and A_{eff} is the effective area of the cuvette, as seen by the detector. Noting that $A_{eff} = z(x_2 - x_1)$ we get

$$\begin{aligned}(I_{obs})_{\lambda_1,\lambda_2} &= \left(\frac{h\nu Kz(F_0)_{\lambda_1}\phi}{(x_2 - x_1)}\right)(e^{-\alpha(\lambda_1)cx_1} - e^{-\alpha(\lambda_1)cx_2}) \\ &\times \left(\frac{e^{-\alpha(\lambda_2)c(L-y_2)} - e^{-\alpha(\lambda_2)c(L-y_1)}}{\alpha(\lambda_2)c}\right) \qquad (4.1)\end{aligned}$$

At low concentrations, we can simplify Equation 4.1 by using the first two terms in an expansion of the exponential terms, giving

$$(I_{obs})_{\lambda_1} = [h\nu K(F_0)_{\lambda_1}\phi\alpha(\lambda_1)(y_2 - y_1)]c \qquad (4.2)$$

This shows clearly that the observed PL intensity is linear with concentration at low concentration.

In our experiments we do not measure F_0 and nor do we estimate a value for K or ϕ. By fitting the linear behaviour of the fluorescence intensity at low concentrations, we are able to measure a value for the product of all the components in the square brackets on the right-hand side of Equation 4.2 As long as x_1, x_2, y_1 and y_2 are all known, the value obtained from the fit can then be used to generate model values for I_{obs} as a function of concentration for the entire concentration range using Equation 4.1.

The form of Equation 4.1 is instructive. The second bracketed term is dependent on the strength of absorption of the excitation beam, the

chromophore concentration and the amount of sample outside the active area of the cuvette through which the excitation beam must travel: it represents the inner-filter effect. The third term in parentheses accounts for the re-absorption effect. The inner-filter and re-absorption effects are independent of each other. Looking again at the difference between Figure 20b, 20c and 20d, we can ascribe the reduction and red-shifting of the 416 nm emission peak to the re-absorption effect, which corresponds to that region of overlap between the absorption and emission spectra in Figure 19. We also suggest the changes in the PLE spectra are due to the inner-filter effect. In this case, only light that is weakly absorbed penetrates far enough into the cuvette to be absorbed and re-emitted by chromophores which are in the field of view of the detector. Thus, in a 10×10 mm cuvette only a small amount of light corresponding to excitations at strongly absorbing wavelengths generates detected emission from the PFO, whereas the excitations at the weakly absorbing tail of the absorption spectrum (above 420 nm) contribute significantly more to the detected PL intensity. The same solution, when placed in a 2×2 mm microcuvette (which thus has most of the sample held within the field of view of the detector) produces a much less affected PL map, though some broadening of the PLE peak is still seen.

In principle, the model could be used to correct the experimental data to remove the effects of inner-filter and re-absorption. However, it was found that where an intensity has been reduced to near-zero such a procedure becomes difficult to carry out without small fluctuations in observed data giving large variations in corrected results. It is also worth noting that, with high concentration, a saturation of PL is expected and "linearity" is not something that we would expect to measure, even without inner-filter and re-absorption effects. Detected fluorescence is intrinsically linked to

the intensity of the excitation beam, and when the optical density of the sample solution is such that a high proportion of the excitation beam is absorbed we see a resultant saturation of the detected fluorescence. Thus, instead of aiming to correct the data in order to regain linearity, the model was used to predict the observed PL intensities of those points on the PL map which we studied.

Our model curves were generated using Equation 4.1 above, using absorbance values obtained from our UV–Vis absorption measurements, and empirical data for the dimensions x_i and y_i of the "active volume" of the cuvette (that portion of the cuvette which is both illuminated by the excitation beam and in the field of view of the detector; estimated from comparisons of PL results from cuvettes of varying cross-section and/or position to be $(x_1, x_2) = (0.1\,\text{mm}, 1.9\,\text{mm})$ and $(y_1, y_2) = (0\,\text{mm}, 2\,\text{mm})$; that is, the front face is illuminated across its full width but the detector is not focused on the entirety of the emission face). The first term in square brackets in Equation 4.2, representing the ideal linear relationship between PL intensity and chromophore concentration, was obtained from the experimental data at low concentration where this linearity holds, that is, for concentrations below $0.002\,\text{mg}\cdot\text{mL}^{-1}$ in Figure 21.

Examining Figure 21 again, three distinct behavioural cases are observed: points which show a linear relationship between PL intensity and concentration; points which show a linear relationship at low concentrations but a relatively constant value of PL intensity with high concentration; and points which show a linear increase at low concentrations, a maximum value, and a decrease at high concentrations. On examination again of the absorption and emission spectra for PFO given in Figure 19, and taking into account the results of inner-filter and re-absorption effects from Equation 4.1, a number of points become apparent. (i) Points defined by excitation at a

weakly absorbing wavelength and emission at another weakly absorbing wavelength (or "[weak, weak]") are not expected to show any significant effects from either inner-filter or re-absorption effects and a linear relationship across all concentrations is expected. (This data is coloured light blue in Figures 21 and 22) (ii) For those points that could be described as [strong, weak] high concentrations of chromophore are expected to lead to a maximum "saturation" level of PL intensity, due to almost complete absorption of the excitation beam, but re-absorption effects are expected to be negligible. A significant drop in PL intensity is only expected at very high concentrations, when much of the absorption and emission will take place at the front edge of the cuvette, outside the active area seen by the detector. (This data is coloured red.) (iii) For points that are [strong, strong], along with a saturation value in the PL intensity, a reduction in the detected PL intensity is expected at high concentrations due to the re-absorption effect. (This data is coloured black.)

We employed our model to predict the behaviour of the observed intensities of those points tracked on the PL map, taking the slope in the linear low-concentration regime as a guide. The relevant predicted behavioural curves are shown in Figure 21 as solid lines, and a good fit to the data is observed. Those points marked [425, 440] and [425, 465] typify case (i) above, those labelled [385, 440], [385, 465], [405, 440] and [405, 465] illustrate case (ii) and the behaviour of case (iii) can be examined through those points labelled [385, 415] and [405, 415]. Note that for excitation at 385 nm, where the absorbance is greater than at 405 nm, saturation of PL intensity is reached at lower concentrations. The re-absorption process continues to reduce the observed PL intensity as concentrations are increased above the level which gives a saturation of PL emission.

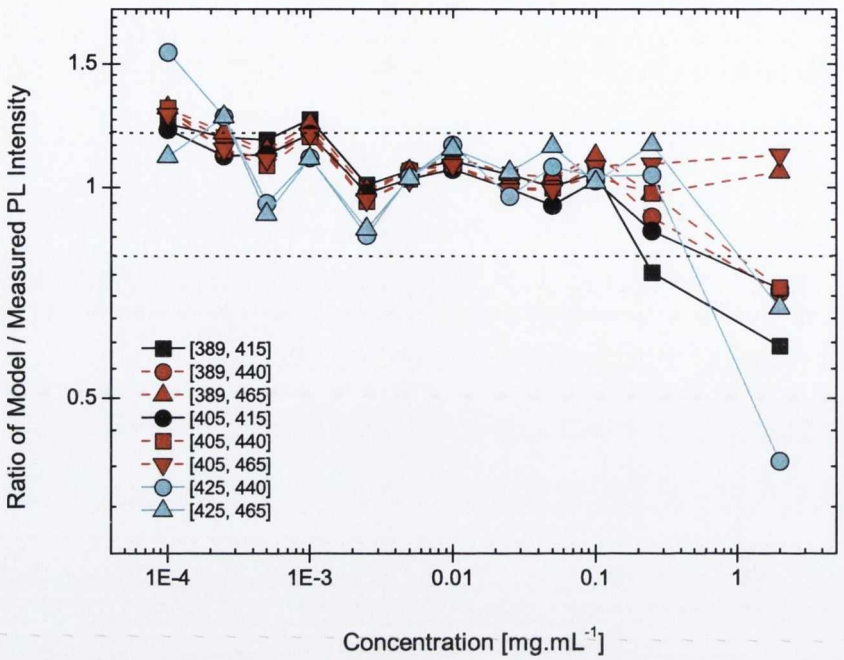

Figure 22: Predicted and observed PL intensities as a function of concentration for PFO in toluene. The horizontal lines are a guide for the eye and represent an accuracy of $\pm 20\,\%$.

Figure 22 shows the accuracy of our approach. We calculated the relative difference between the theoretically predicted PL intensity (using Equation 4.1) and that which was observed, and plotted this ratio (observed PL/predicted PL) as a function of concentration. The two added horizontal lines are a guide for the eye and indicate an accuracy of $\pm 20\,\%$. Reasonable accuracy is observed across concentrations ranging as high as $0.25\,\mathrm{mg{\cdot}mL^{-1}}$. At such high concentrations, solutions of PFO are approaching the overlap concentration, whereby the volume of solvent associated with an average-length polymer chain (as calculated from the concentration of the solution and molecular weight) is equal to the pervaded volume of such a chain [176]. Aggregation is expected to occur at concentrations above the overlap concentration. The overlap concentration c^* is given by $c^* = M_w / R_0^3$, where M_w is the average molecular weight of the poly-

mer chain and R_0 its average size; $R_0 = bN^{0.5}$ and $bN = nl$, where b is the Kuhn length, N the number of corresponding Kuhn segments in a chain, n the average number of monomer units in a chain and l the length of one monomer unit. Values for the monomer and Kuhn length were taken from the literature [71], and the molecular weight calculated from gel permeation chromatography (GPC) measurements. This gives a value of $c^* \approx 1\,\mathrm{mg{\cdot}mL^{-1}}$. This value is reasonably close to the concentration where the experimental PL intensity deviates from the predicted value strongly suggesting that the deviation is due to aggregation effects. In fact, one would expect the polymer chains to uncoil more in a good solvent, increasing their pervaded volume. Thus we might expect aggregation to occur slightly below the overlap concentration as is suggested by the data.

Solution aggregation studies of PFO have indicated that it has a Hildebrand solubility parameter, δ, of approximately 18.5–19.0 $\mathrm{MPa}^{1/2}$ [71]. The Hildebrand parameter of a given material is equal to the square root of its cohesive energy density [88, 196]. This allows the calculation of the enthalpy of mixing of a solution, $(\Delta H/V)_{Mix}$ as [88]

$$\left(\frac{\Delta H}{V}\right)_{Mix} = (\delta_{solute} - \delta_{solvent})^2 \phi_{solvent} \phi_{solute}$$

where ϕ represents volume fraction. Dissolution is favourable when the enthalpy of mixing is minimised, i.e. the enthalpy of mixing represents the energy expended in order to create a mixture, with lower values meaning mixtures are more energetically favourable. Therefore, solvents and solutes with similar or equal Hildebrand parameters form solutions easily as the energy input required to do so is low; substances with differing parameters do not. Thus good solvents are expected to include chloroform, tetrahydro-

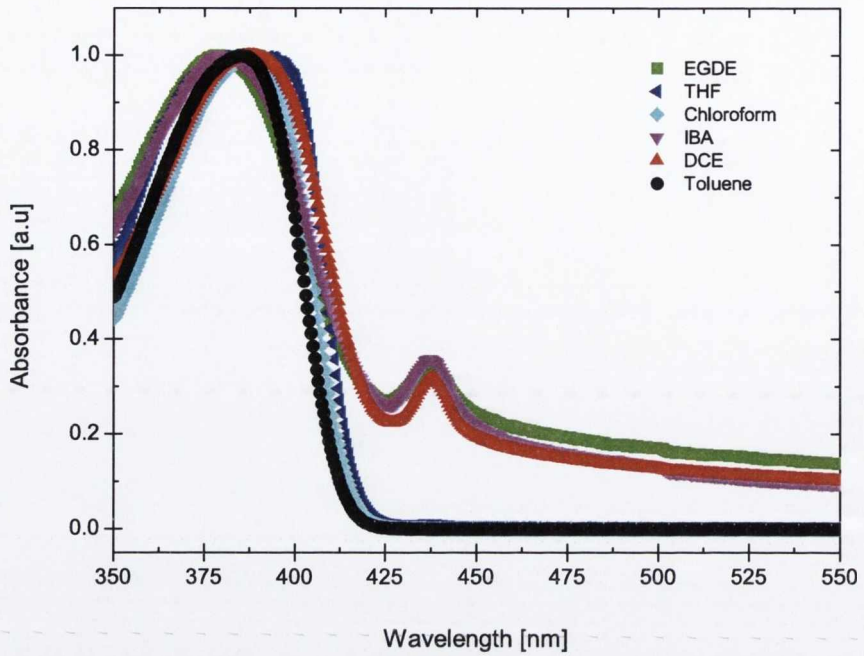

Figure 23: Normalised absorbance spectra for PFO in solution at $0.2\,\mathrm{mg{\cdot}mL^{-1}}$ in various solvents. While the concentration of PFO is identical in each sample, an absorbance peak identified with β-phase PFO is visible in some solvents at approximately 435 nm.

furan (THF) and, to a lesser extent, toluene, having solubility parameters of $\delta = 19.0$, 18.6 and $18.2\,\mathrm{MPa}^{1/2}$, respectively.

PFO, in low-concentration solution using a good solvent, shows a strong and broad absorption peak with an onset at approximately 415 nm and peak at 385 nm as illustrated earlier in Figure 19. Such an absorption curve remains, under normal conditions, characteristic of PFO in the solid state for what has been termed the "bulk" or glassy phase. At high concentrations and in the solid state, PFO has been shown to have a more crystalline aggregate state termed the β-phase. The presence of this phase of PFO has been shown to be clearly indicated by the appearance of a well-defined absorption peak at 437 nm (= 2.837 eV), a feature present in both solution and solid-state absorption spectra [71, 35, 72]. It has been shown that

thermal treatments and post-deposition procedures can lead to a transition between phases in thin films of PFO.

To approach the PL behaviour of PFO in a poor solvent in a similar manner to the way we examined it in toluene, we first recorded absorption spectra for PFO solutions at various concentrations and across a range of solvents. Figure 23 shows the results for six of these solvents at concentrations of $0.2\,\mathrm{mg{\cdot}mL^{-1}}$, normalised to their absorption maximum. A marked difference can be seen between good solvents (toluene, chloroform, THF) and poor solvents (DCE, EGDE, isobutyl acetate; Hildebrand solubility parameters $\delta = 20.1$, 17.6 and 17.1 $\mathrm{MPa}^{1/2}$, respectively). The spectra from good solvents conform to our expectations of spectra for solutions containing bulk phase PFO only, while the poor solvents display spectra indicative of the presence of β-phase PFO as well as bulk phase PFO.

Clearly, a simple change of solvent can drive the formation of this aggregate through thermodynamic processes. It is energetically favourable for the PFO to align into a crystalline domain to promote the exclusion of solvent molecules, providing more polymer–polymer interactions at the expense of polymer-solvent ones. We note that this characteristic β-phase absorption peak is weakly present, if detectable at all, in solutions employing good solvents, at high concentrations. Figure 24 shows absorbance spectra for solutions of PFO in toluene and DCE, at low and high concentrations. Whereas the presence of β-phase PFO is clearly indicated by the appearance of the absorption peak at 437 nm in low-concentration DCE solution, this peak is barely detectable in the higher concentration toluene solution.

The relationship between Hildebrand solubility parameter and β-phase formation was explored further. UV–Vis absorption spectra for different solvents were recorded, and the relative amount of β-phase PFO present in

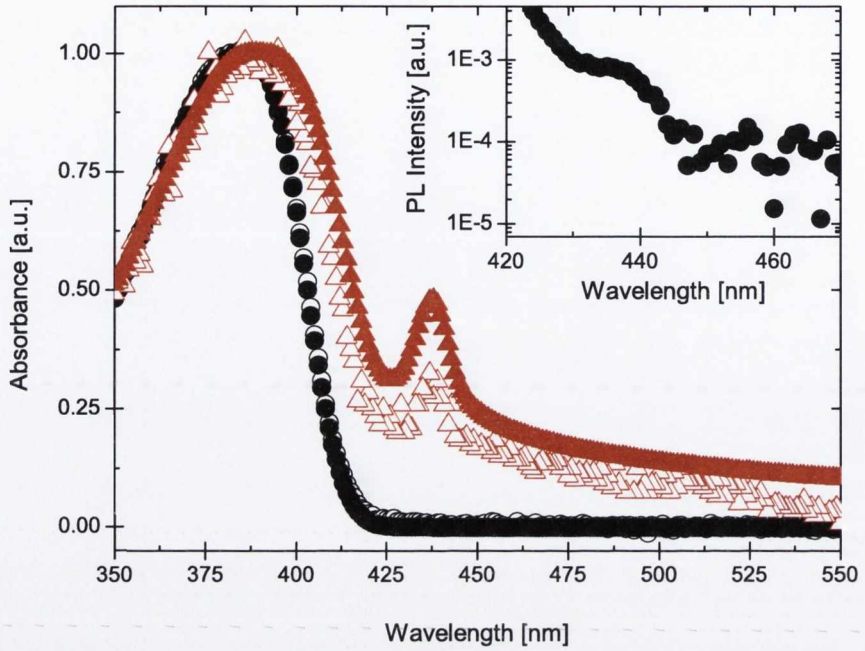

Figure 24: Absorbance spectra for solutions of PFO in toluene (circles) and DCE (triangles), both with concentrations of $0.002\,\mathrm{mg{\cdot}mL^{-1}}$ (open symbols) and $0.2\,\mathrm{mg{\cdot}mL^{-1}}$ (filled symbols). Inset shows PFO in toluene at $0.2\,\mathrm{mg{\cdot}mL^{-1}}$ on a semi-log scale, illustrating the onset of the β-phase absorbance peak at 437 nm in high concentration toluene solutions.

solution was estimated by comparing the ratio of absorbance values for the solution at 437 nm and at its absorbance maximum around 385 nm. Figure 25 shows a plot of this ratio of absorbance values against the Hildebrand solubility parameter of the solvent. We observe that for poor solvents, i.e. those with δ-values on either side of the proposed range for the δ-value of PFO, ratios of β-phase PFO greater than 0.33 are detected, as opposed to ratios of less than 0.003 for good solvents having a comparable δ-value to that of PFO. While the Hildebrand model does not include every factor in the complex process of polymer behaviour in solution, these results agree with the suggestion that the formation of β-phase PFO aggregates is favoured thermodynamically in poor solvents [71].

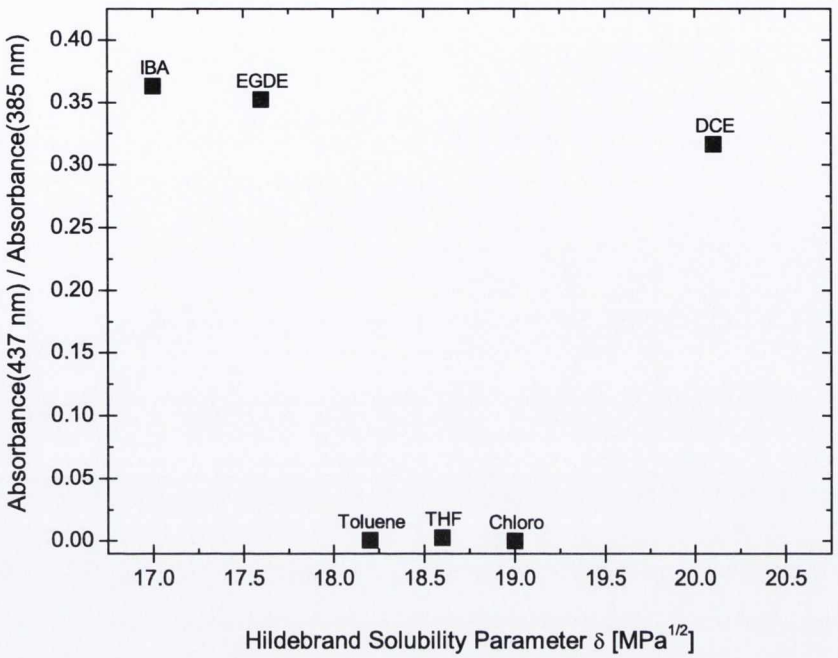

Figure 25: Prevalence of β-phase PFO as measured by the ratio of absorbance peaks at 437 nm and 385 nm for solutions of PFO at 0.2 mg·mL^{-1} in solvents of varying Hildebrand solubility parameter δ.

The ratio of β-phase to bulk phase in all PFO solutions was observed to increase with concentration, as would be expected for an aggregate state (see Figure 29 for the relationship between amount of β-phase present and PFO concentration in DCE.) It has been shown that β-phase PFO has a more rigid structure, with greater chain stiffness and increased coherence length along the chain than the glassy phase [35, 72]. We suggest that such an ordered structure permits the expulsion of solvent from between polymer chains, and such "bundling" would be the preferred mechanism of aggregation for PFO in poor solvents [69]. This is in contrast to many other polymers that favour a tightening of the "random walk" or "worm-like" chain conformation of individual polymer chains and the agglomeration of polymer chains into multi-chain aggregates as a method of solvent exclusion, to ensure an increase in the energetically

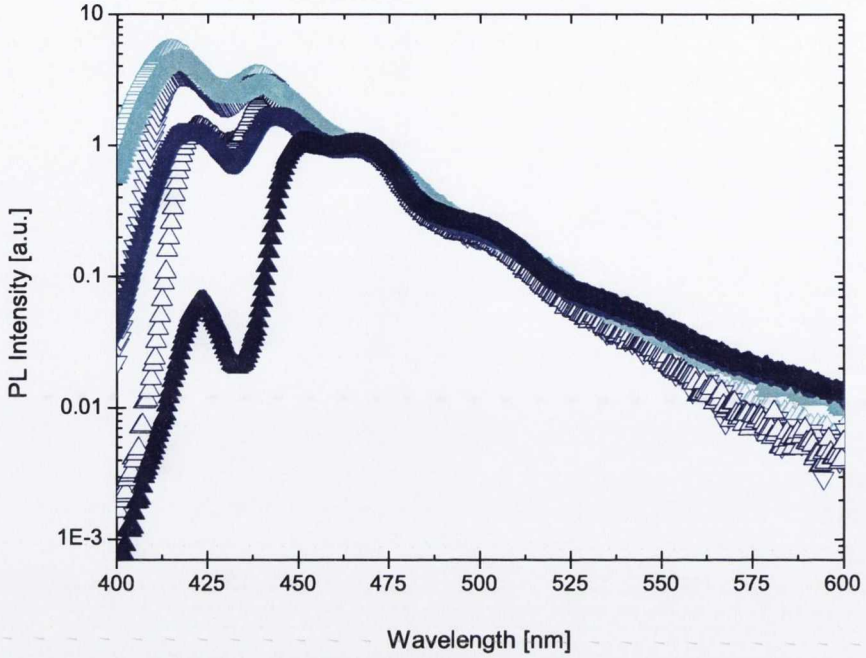

Figure 26: Emission spectra for PFO in toluene (open symbols) and in DCE (filled symbols) at concentrations of 0.0025 mg·mL^{-1} (cyan), 0.25 mg·mL^{-1} (blue) and 2.0 mg·mL^{-1} (navy). Spectra are normalised to their emission value at 465 nm.

favourable polymer–polymer interaction at the expense of slightly less favourable polymer–solvent interaction. This bundling of β-phase chains is reminiscent of aggregation effects in systems of long rigid molecules such as carbon nanotubes [69].

Figure 26 illustrates the change in the observed emission spectra for PFO in toluene and in DCE, with increasing concentration. We note the similarities in behaviour of both types of solution: the decrease and red-shifting of the $\pi - \pi^*$ peak at 416 nm and red-shifting of the first lower energy peak at 439 nm as concentration increases. The emission of PFO in DCE shows an increase in the vibronic structure [44] of the lower energy peaks, with more defined peaks compared with PFO in toluene, owing to the more rigid chain conformation.

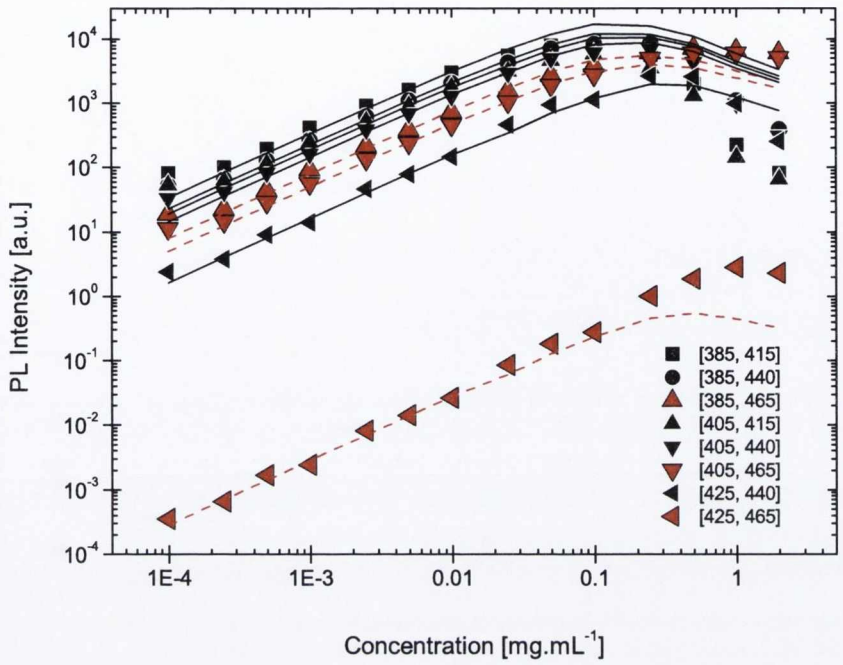

Figure 27: Observed PL intensity as a function of concentration for PFO in DCE. PL intensities are for a number of particular excitation and emission wavelength combinations as indicated, corresponding to those examined in Figure 21, for a range of concentrations. All predicted curves (again from Equation 4.1) show a saturation maximum, with some followed by a reduction in intensity. In contrast to Figure 21 (where they are coloured light blue), there are no "weak-weak" linear trends observed.

In order to examine further these changes in the spectra with increasing concentration in DCE, we applied again our model equation to account for the effects of concentration and the inner-filter and re-absorption effects, using values of the absorption co-efficient for PFO in DCE. Contour maps for all concentrations were generated as before but are not shown here. Both observed and predicted PL intensity curves for individual excitation–emission values (same as previous analysis) are shown in Figure 27 (by analogy with Figure 21). The accuracy of our procedure is shown through an analysis of observed and predicted values, in an identical method to that used to generate Figure 22, illustrated here in Figure 28.

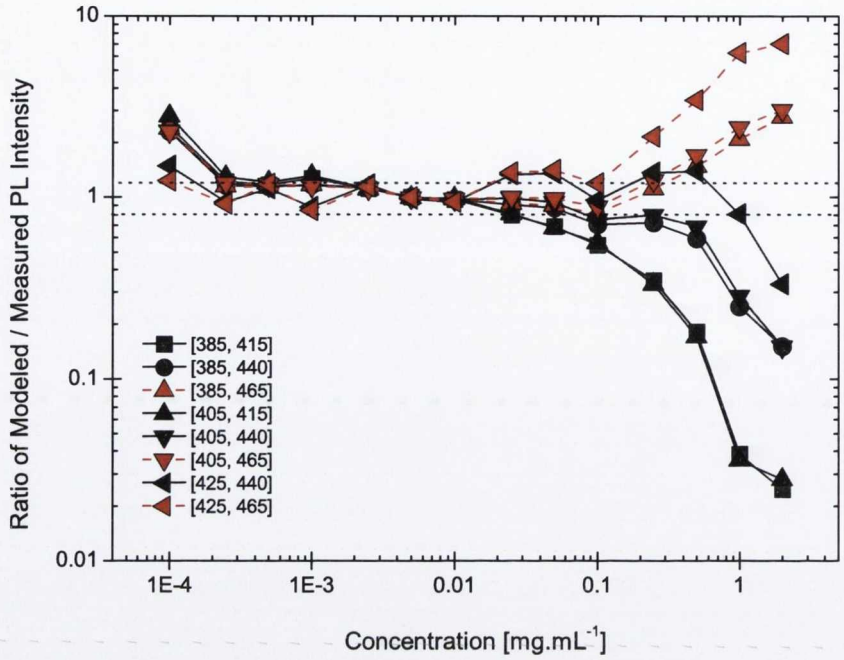

Figure 28: Comparison of predictive model of PL intensities with observed results, as in Figure 22, shown here for PFO in DCE. Again, horizontal guidelines representing deviations of 20 % have been added. Note change in vertical scale relative to Figure 22.

Although at low concentrations we again see a linear relationship between PL intensity and PFO concentration, here we see that at high concentrations every set of points reaches a maximum value and some of the data points show a reduction in intensity at high concentration. This is in contrast to the data in Figure 23 where we had some data points ($\lambda_{Em}, \lambda_{Ex}$) exhibiting linearity across all concentrations.

Some differences are expected between Figure 23 and Figure 27 because while we have chosen to analyse the same points on the contour plots in each case, the absorbance values which correspond to these points have been altered due to the β-phase absorption peak at 437 nm and its extended low-energy tail. To account for the non-linearity of PL intensity with concentration we again introduced our model and the predicted PL

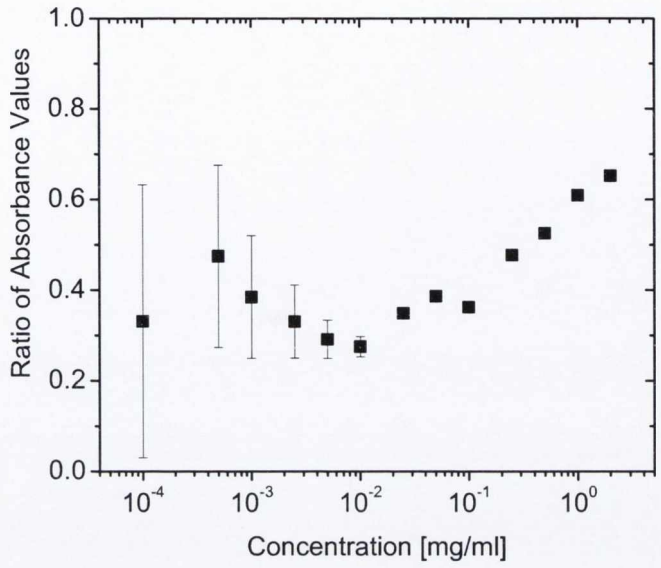

Figure 29: Ratio of absorbance values at 437 nm and 385 nm, illustrating quantity of β-phase PFO present, for PFO in DCE. Low concentration solutions provided weaker absorption signals with increased noise, leading to the large error values shown.

intensity curves. Compared with the data used in Figure 23, none of the excitation-absorption values are really classed as "weak" and thus, all curves show the [strong, strong] and [strong,weak] behaviour of saturation and reduction in PL intensity. (The [425, 465] curve is close to, but not quite, "weak-weak".) While the predicted curves for Figure 27 are significantly different from those in Figure 23, we see that they do not match the observed data to the same extent at high concentrations.

Figure 28, by analogy with Figure 22, shows the accuracy of our model. Whereas for PFO in a quite good solvent like toluene the PL intensities were predicted to within 20 % up to a concentration of 0.1 mg·mL^{-1}, the same treatment adapted for PFO in DCE fails to keep this level of accuracy at any concentration above approximately 0.01 mg·mL^{-1}. At 2.0 mg·mL^{-1}, some observed measurements are a factor of 40 lower than those predicted, while

others are almost a full order of magnitude greater than those predicted. Clearly, some process other than radiative energy transfer (absorption and emission by one chromophore, and re-absorption by another) and inner-filter effects is occurring here.

Examining Figures 28 and 29, we can explore the relationship between quantity of β-phase PFO present (measured by the relative values of the 437 nm peak and the 385 nm peak in PFO absorbance) and concentration. While relatively constant at around 0.33 for concentrations below $0.25\,\mathrm{mg{\cdot}mL^{-1}}$, we see an increase above this concentration, reaching 0.65 at $2.0\,\mathrm{mg{\cdot}mL^{-1}}$. This rise in the amount of β-phase PFO correlates strongly with the increased deviations from our predicted model curves for PL intensity. This strongly suggests that the deviations from the predicted PL intensity as a function of concentration are due to the formation of β-phase aggregates. In thin films it has been observed that for β-phase concentrations of only a few percent the PL emission of glassy phase PFO is almost entirely quenched due to highly efficient exciton transfer from the glassy to the β-phase, showing a large radius for Förster resonance energy transfer (FRET) [111]. FRET is a non-radiative process by which energy is transferred between two chromophores (typically in very close proximity, with an effective separation of $< 10\,\mathrm{nm}$), through a resonant dipole-dipole coupling. The energy transfer does not involve emission or absorption of a photon, but is intrinsically related to these processes in that it is most effective when the emission spectrum of the donor molecule overlaps with the absorption spectrum of the acceptor molecule, allowing coupling of dipoles where the molecules have a high oscillator strength. We note from Figure 26 that solutions containing significant amounts of β-phase PFO are stronger emitters at low energies than bulk PFO samples. Looking again at the data in Figure 28, we see that all those observed PL intensities that

were measured to be higher than predicted were for low-energy emission at 465 nm; those higher energy emission spectra, emitting at 440 and 415 nm, are measured substantially below what was predicted.

Effective FRET is dependant on the existence of an overlap between the emission spectrum of the exciton donor material and the absorption spectrum of the acceptor [65]. In the case of PFO, the characteristic absorption peak of β-phase PFO at 437 nm lies at a region of strong emission for bulk phase PFO. We note that the measured PL intensity for our PFO samples appears to be lower than that predicted for any emitting wavelength near this level or below it and higher than that expected for lower wavelengths. The magnitude of the deviation from predicted PL intensities correlates well with the quantity of β-phase present, and so we suggest that what we are observing is FRET in solutions of PFO whenever a substantial amount of β-phase PFO forms to act as an acceptor material.

4.4 CONCLUSIONS

We have developed a model to account for the non-linearity of PL intensity with concentration for solutions of a highly absorbing chromophore. The model accounts for the effects of high concentration and total absorption of the excitation beam, and the phenomena of the inner-filter and re-absorption effects, and can be used to predict PL intensities observed at given combinations of excitation and emission wavelengths for a given concentration. This model was successfully applied to our results to explain measured non-linear values for PL intensity of PFO in toluene.

The inability of the same model, modified to account for changes in absorption spectra, to explain the observed PL behaviour of PFO in DCE,

a poor solvent for PFO in which β-phase PFO is present in significant amounts, signifies that another process is at work in this solution. Due to the absorption and emission spectral characteristics of the bulk and aggregate β-phase PFO, showing a high overlap between emission spectrum of bulk phase PFO and absorption spectrum of β-phase PFO, we suspect that Förster resonance energy transfer to the β-phase PFO is most likely occurring.

In order to generate the model curves for PL emission as a function of concentration, it was necessary to establish the correct linear relationship between these parameters at a concentration and absorbance low enough that the inner-filter effect was absent from the data. In cases where the exact photoluminescence quantum yield of the material is known (allowing for factors such as the apparatus collection efficiency), this step becomes unnecessary. Without the effects of aggregation, the model is accurate up to an absorbance of approximately 10, and the effects of aggregation are apparent as deviations from the predicted behaviour.

5 MEASUREMENT OF THE PHOTOLUMINESCENCE QUANTUM YIELD FOR ENSEMBLE DISPERSIONS OF SINGLE-WALLED CARBON NANOTUBES

Having examined in previous chapters some of the issues likely to be encountered in absorbance and fluorescence spectroscopy of SWNTs, in this chapter we analyse the absorbance spectrum and PL map and estimate photoluminescence quantum yield (PLQY) values for numerous tube types. Much of our work is automated through the use of MATLAB computational software, where we have custom written an extensive program to analyse the spectroscopic data, and a detailed explanation of the program is given.

5.1 INTRODUCTION

Photoluminescence (PL) from semiconducting (s-) single-walled carbon nanotubes (SWNTs) has been widely used in nanotube research since first being observed in 2002 [159]. PL spectroscopy allows researchers to examine the fundamental physics of excitons in quasi-1-dimensional structures [2, 226], to explore applications in optoelectronics and biology [14, 190, 208], to probe and compare the state of dispersions achieved using various surfactants and other methods [21, 62, 97], and to enable (n,m)-resolved population studies of nanotube samples [102, 163].

The absorption and emission of light by carbon nanotubes is excitonic in nature [206]. Excitons may decay and recombine radiatively or non-

radiatively: the photoluminescence quantum yield (PLQY) is determined by the probability of each of these decays, and may be defined as the number of photons emitted by the s-SWNT as a fraction of the number of photons absorbed. The PLQY of s-SWNTs is thus a property of significant interest to researchers employing PL measurements for any sort of quantitative analysis.

For s-SWNT PLQY, measurement techniques and values reported in the literature vary considerably: values have been reported for individual tubes [77, 130, 38, 20, 204], ensembles [159, 207, 90, 100, 51, 4], and specific (n,m)-species [204, 100, 51], with reported values ranging from $\sim 10^{-4}$ to ~ 0.1. PLQY measurements commonly involve calculating the number of photons emitted and absorbed (for individual tubes [77, 130, 207]) or comparison with a reference standard of known quantum yield (for ensemble dispersions [38, 90, 100, 51, 4, 104]). In general the integrated PL is related to the absorbance at the excitation wavelength and the PLQY, ϕ, at low solution optical densities via the following expression:

$$I_{PL}/\eta_{det} = (I_{exc}\eta_{exc})A\phi K \tag{5.1}$$

where I_{PL}/η_{det} is the integrated PL intensity, corrected for the spectral performance of the emission monochromator and detector, $I_{exc}\eta_{exc}$ is the intensity of the excitation beam at the absorbing wavelength, accounting for spectral performance of the excitation monochromator and light source, A is the absorbance of the emitting material at the excitation wavelength, and K is a constant incorporating factors relating to the geometry of the instrument set-up such as the fraction of emitted light detected.

Each of these methods for measuring the PLQY can introduce further complications. For measurements on individual tubes, the absolute ratio

of photons emitted/absorbed is a difficult quantity to measure accurately. For measurements on ensembles, four main difficulties exist. It is critical to know the absolute resonant absorbance at the excitation wavelength for each emissive tube type. However, the measured absorbance spectrum may be the sum of the absorbances of ~ 60 different tube types (and, typically, a large non-resonant background). At any given excitation wavelength, 10 or more different tube types may simultaneously absorb light. Thus any successful measurement must take into account the relative contributions of each tube type. In addition, the suitability of some of the 'standard' fluorescent materials has been questioned, with the suggestion that some reported PLQY values may have been over-estimated by a factor of five [194]. Further uncertainties regarding the measurement of PLQY values for ensemble solutions arise from concentration-dependent practical issues. With their low PLQY values, working solutions can easily exhibit absorbance values (in both the E_{22}^S and E_{11}^S transition range) for which inner-filter and re-absorbance effects in the PL data, explored in detail in Chapter 4 become important [166, 174]. Concentration also affects the bundling dynamics of SWNTs [22], which can lead to quenching of emission and energy transfer within (and potential light emission from) bundles [199, 200].

Thus any accurate measurement of PLQY in nanotube ensembles will have to:

1) Ascertain the relative absorbances of all excited tube species,

2) Take care to accurately account for the quantum yield of the standard,

3) Make sure the samples are in the low-concentration regime where PL intensity is linear with sample concentration, and

4) Account for the fact that only a fraction of the nanotubes are individualized and so are free to emit photons.

As far as I am aware, all four issues have never been satisfactorily dealt with in one study, but shall be addressed here.

A key element will be our use of specially written software to reduce a sample absorbance spectrum to its component transitions. We have adapted and expanded the published MATLAB code of Nair *et al.* [152] to produce a program that analyses absorbance and PL data, fits the spectra with contributions from distinct (n,m)-species of nanotube and thus correlates absorption and emission data for specific s-SWNT tube types in an ensemble dispersion. We employ two emissive dyes of known quantum yield and operate in a suitable concentration range to avoid inner-filter and re-absorption effects. Finally, we have employed AFM analysis to account for the bundling of nanotubes and the consequent reduction in the emissive fraction of dispersed tubes [22].

We thus present a method to estimate the PLQY values for several distinct (n,m)-species in an ensemble dispersion of SWNTs, which can in principle be applied to any liquid phase nanotube dispersion.

5.2 EXPERIMENTAL PROCEDURE

A dispersion of 1 mg·mL^{-1} of raw HiPCO SWNTs (purchased from Unidym, Inc.—lot #R0554) in a stock solution of 5 mg·mL^{-1} sodium decasulfate (SDS) in deuterium oxide (D_2O) (both purchased from Sigma-Aldrich and used without further purification) was prepared as previously described using an ice-cooled sonication routine [42]. The dispersion was centrifuged for 4 hrs at approx 120,000 g using a Beckman-Coulter Optima L-100 XP ultra-centrifuge (rotor SW-41; 35,000 rpm; 20° C) to remove larger bundles and aggregates. The supernatant was decanted and further diluted using the

stock SDS-D_2O solution to give a series of samples, here labelled A–E. UV-Vis-NIR absorbance spectra were recorded for the original, uncentrifuged dispersion and for the supernatant and diluted solutions, using a Varian Cary 6000i spectrometer (dual beam mode against stock SDS solution, 1 nm interval, 2 nm bandpass).

Crystalline silicon samples were submerged in the supernatant solution for 1 hour, removed, rinsed in methanol and dried with compressed air for tapping-mode atomic force microscope (AFM) analysis using a DI Multimode Nanoscope IIIA.

PL measurements were recorded using an Edinburgh Instruments FLS920 photoluminescence spectrometer with a CW 450 W Xe excitation source and Hamamatsu R5509-72 nitrogen-cooled photomultiplier tube detector. Settings used: excitation in 2 nm steps from 540 nm (2.296 eV) to 820 nm (1.512 eV), 15 nm monochromator slit width; detection in 2 nm steps from 850 nm (1.459 eV) to 1350 nm (0.918 eV), 10 nm monochromator slit width. The cuvette pathlength dimensions were 2×2 mm. PL maps were corrected for the spectral performance of the excitation and emission monochromator and lamp/detector set-up. UV-Vis-NIR absorbance and PL measurements were recorded for a number of dilute solutions of the fluorescent dyes rhodamine B and rhodamine 6G under identical conditions. Dyes were purchased from Radiant Dyes.

Much of the analysis is automated through the use of a MATLAB routine, examined in detail in the next section. A brief overview is as follows. Given the PL map and absorbance data, the program is designed to do the following:

1) Read in SWNT transition data, absorbance and PL data, and any other parameters, from a file.

2) Identify peaks in the PL map, and compare these to known transition en-

ergies for s-SWNTs to identify species present in the dispersion. Estimates of full width at half maximum (FWHM) for each identified E_{ii} transition for these species are also made from the PL map.

3) Fit the absorbance spectrum in a manner similar to that used by Nair, using estimated peak positions and FWHM data from PL map to inform some of the input parameter starting values.

4) Adjust the values of the component absorbance peak parameters (centre, width, and amplitude) within set bounds using a non-linear least-squares optimization routine.

5) Optimise the component E_{11}^S emission peak parameters (centre and width) for those s-SWNT species identified in the PL map using a similar routine, except now fitting emission spectra from the PL map, before fitting the E_{11} emission amplitudes to each emission spectrum in turn using a quadratic programming routine.

6) Integrate the PL emission from each nanotube species in each fitted emission spectrum.

7) Calculate the ratio of integrated PL emission to absorbance for a number of excitation energies near the E_{22}^S resonance for each s-SWNT species identified in the PL map, corrected for the emissive fraction of tubes in solution (from AFM data).

8) Estimate the PLQY value for each of these (n,m)-species, relative to our standard dyes.

9) Write output data to file.

5.3 ANALYSIS

Absorbance and photoluminescence data were analysed using a custom written MATLAB program. Presented here is a detailed outline of the analytical routine. Our code for the MATLAB program 'APLQY.m' is reproduced in the Appendix in Section A.1. In it, we incorporate and build upon the code published by Nair *et al.* [152]. Nair's code was designed to reduce the absorption spectrum of a dispersion of several species of SWNTs into its component spectra. This reduction involved (i) generating individual model absorption curves for each $E_{ii}^{(n,m)}$ transition, from information on a range of (n,m)-tubes given by the user, where $ii = 11$ for metallic tubes and $ii = 11$, 22 for s-SWNTs; (ii) grouping model curves into 'parent peaks' to match each peak identified in the absorption spectrum and applying a weighting system for the ratio of amplitudes of component curves within each parent peak; and (iii) adjusting the amplitudes of these parent peaks to fit the spectrum.

We have expanded the method for fitting the absorption spectrum, fitting more parameters for each model transition peak and allowing these parameters some limited freedom. We then use a similar method to fit the emission lines in the photoluminescence excitation-emission map ('PL map'—concerned here with $E_{22}^{(n,m)}$ excitation and $E_{11}^{(n,m)}$ emission), giving the PL contributions from numerous s-SWNT species.

We compare the integrated $E_{11}^{(n,m)}$ PL emission for various semiconducting tube types with the corresponding fitted $E_{22}^{(n,m)}$ absorbance value, examining PL excitation values around the $E_{22}^{(n,m)}$ absorbance peak. Absorbance values are corrected for the mass fraction of individual tubes, found using atomic force microscopy (AFM) analysis and set as an input parameter by the user.

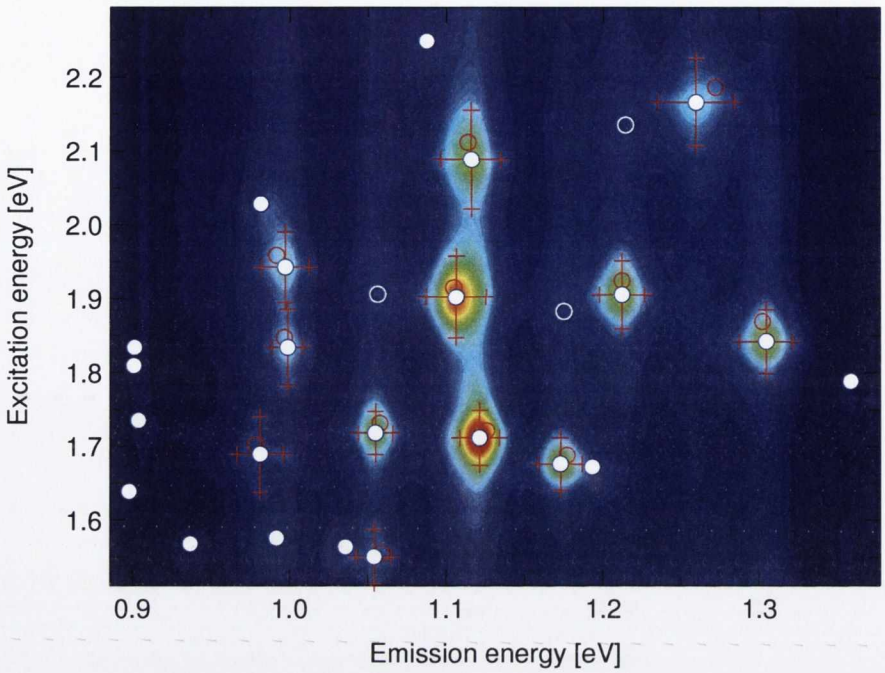

Figure 30: PL map illustrating peak identification and analysis, for HiPCO SWNTs in SDS-D_2O dispersion. Initial values for $E_{22}^{(n,m)} \rightarrow E_{11}^{(n,m)}$ transitions (open red circles) are adjusted to match relevant peaks in the PL map (open white circles). Final values are marked with white dots, with FWHM estimates as red lines and crosses.

A plot of integrated PL emission versus corrected absorbance is then used to estimate the environment- and (n,m)-specific PLQY of several tube types, relative to a standard substance of known quantum yield.

The 'APLQY.m' program is designed to do the following:

1. Read in PL map and absorption spectrum data for a SWNT dispersion, along with data for other parameters (including expected SWNT $E_{ii}^{(n,m)}$ transition energies, and various instrument parameters).

2. Identify peaks in the PL map, and match these to known s-SWNT transition energies to identify (n,m) species. Estimates of full width at half maximum (FWHM) values for each identified $E_{ii}^{(n,m)}$ transition are also made from the PL map.

Values for transition energies and widths are derived, where possible, from the PL map. Peaks in the PL map are identified, with the data interpolated to overcome limitations imposed by the excitation and detection step-size used in recording the map. These peaks are compared to the expected energy values for semiconducting $E_{ii}^{(n,m)}$ transitions. PL map peaks are matched to $E_{22}^{S} \rightarrow E_{11}^{S}$ transitions for specific (n,m) tube types if they occur sufficiently close to the expected E_{22}^{S} and E_{11}^{S} resonance peaks. Our initial data for the SWNTs expected to be present in the dispersion and values for the transition energies and widths, was based on the information provided by Nair *et al.* and by Ju *et al.* [152, 105].

These matched s-SWNT peaks in the PL map are then analysed to obtain estimates for the FWHM of each $E_{ii}^{(n,m)}$ transition. Those s-SWNTs not identified with a peak in the PL map have their inputted E_{ii} transition widths modified by the average percentage change in E_{ii} width found for the matched s-SWNTs peaks. Figure 30 shows the peak analysis as performed by the program, comparing identified peaks to expected values and analysing transition widths.

From Figure 30, we can see three empty white circles, highlighting peaks in the PL data that have not been assigned to any s-SWNT transition. Such peaks have been assigned to exciton energy transfer (EET) from a 'donor' SWNT absorbing light from the excitation beam to an 'acceptor' tube with a smaller band gap, before contributing to emission from this acceptor tube [200, 169]. EET could occur via exciton tunnelling, Förster resonance energy transfer (FRET) or through the emission and absorption of a photon. Tan *et al.* [200], in examining these peaks in the PL map, have assigned the process to FRET between nanotubes in a bundle.

Resonant emission peaks having both E_{22}^{S} and E_{11}^{S} within approximately 0.05 eV of these unassigned peaks in the PL map are easily identified,

suggesting possible donor species. (The donor species have higher energies than those observed for the acceptor species, while the unassigned PL emission occurs at the same emission energy as the resonance peak for the acceptor species; the donor and acceptor species have resonant peaks to the right and directly below the unassigned peak in Figure 30.) Given the typically low emission efficiency from s-SWNTs and the significant intensity of these EET peaks in the PL map, it is clear that a significant proportion of the excitons formed in the donor species must transfer to the acceptor. PLQY as measured via absorbance and emission near the $E_{22}^S \rightarrow E_{11}^S$ resonance peak would then produce an underestimate for the donor species. The acceptor species' PLQY estimate will be unaffected while the EET peak is sufficiently well separated from the resonance peak.

This identification of the unassigned PL map peaks in Figure 30 with EET has been called into question. Instead, Lebedkin *et al.* argue [125] that these features are the result of emission sidebands caused by coupling with phonons, together with the observation of PL from weaker perpendicular excitation of the SWNTs, as observed elsewhere [149]. This explanation also removes the need to explain why the unassigned peaks do not show a true correlation to the E_{22}^S energy of the identified donor species, with each peak being misaligned with the 'donor' by a different amount.

For fitting the absorbance spectrum, 4 meV is added to the E_{11}^S emission peak values obtained from the PL map to reflect the small Stokes shift expected for the s-SWNTs [212].

At this point, users are given the opportunity to correct any values for peak parameters which may have been poorly estimated by the program.

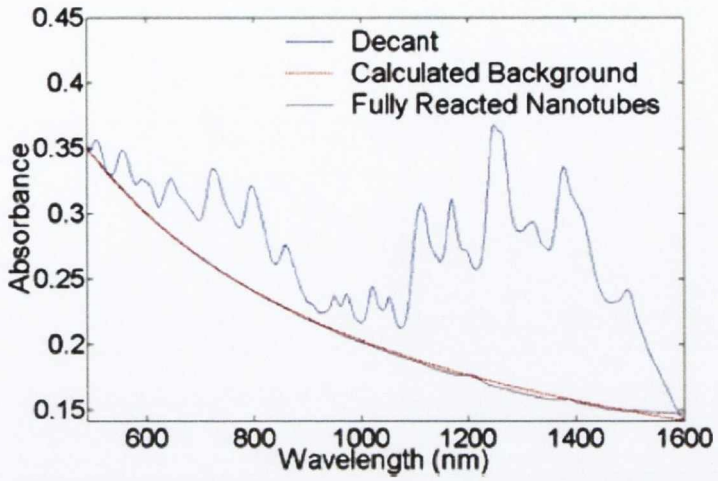

Figure 31: Background of fully reacted HiPCO nanotubes, as published by Nair *et al.* [152]. The fully reacted background is fitted with a background of the form $A_{bkg} = a\lambda^b$, with $b = -0.7733$.

3. Fit the absorbance spectrum using this updated energy and FWHM data in a similar manner to that given in the program by Nair *et al.*, with transitions grouped to match absorbance peaks.

While much of our code was modelled on that provided by Nair *et al.*, we have expanded on their method for fitting the absorbance spectrum, and we made two significant changes.

Firstly, we adopt a different method of fitting a non-resonant background. Nair's work employed a background of the form $A_{bkg} = a\lambda^b$ and optimised a and b in order to minimise the difference between the background and measured absorbance. Nair's paper shows excellent agreement between this calculated background and the absorbance spectrum of completely fictionalised SWNTs, reproduced here in Figure 31. Analysis of the figure gives a value of -0.7733 for the parameter b. We fix this value, and then optimise the parameter a such that the measured spectrum and background converge at low energies.

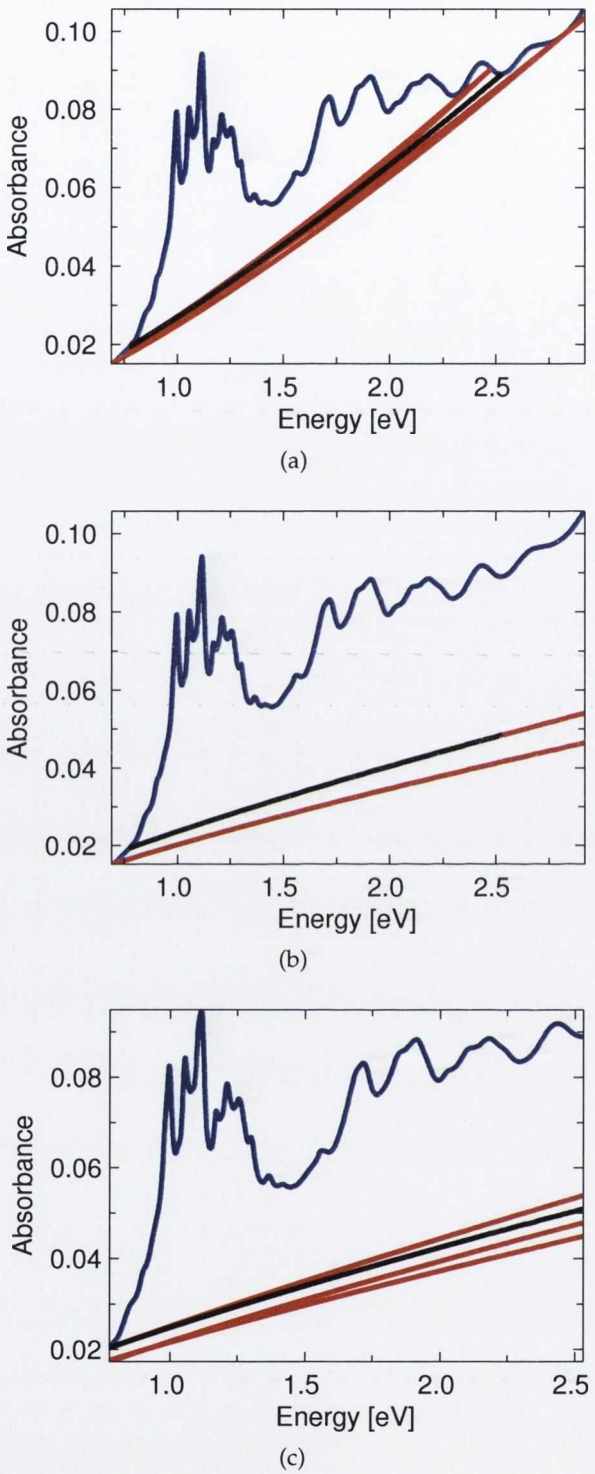

Figure 32: A typical SWNT dispersion absorbance curve (blue), showing various calculated non-resonant backgrounds (red) calculated according to (a) Nair's approach and (b) our modified approach. The black line represents a choice of energy range identical to that used in Nair's program, i.e. corresponding to 490–1600 nm. (c) The four backgrounds used in our analysis, derived from perturbations to the baseline calculated in (b), shown in black in both plots.

An important issue is the choice of energy range in the analysis, as both Nair's method and our own are sensitive to changes in the end-points. Figure 32 shows the multiple background fits produced by Nair's original program for a single absorbance spectrum, when these end-points are changed. While our method is dependent only on the choice of low-energy endpoint, the effect of small variations here can be significant also. We perform our complete analysis for four different backgrounds as shown. We also repeat the fit using the background corresponding to Nair's work (shown in black), with preference given to the s-SWNTs identified in the PL map (discussed in more detail below). We then present the average of the five results together with upper and lower bounds corresponding to the range of PLQY values calculated for each s-SWNT over the five analyses. The identification of the true background absorbance from non-emissive material and any intrinsic population-related effects remain matters for further investigation.

Secondly, we have taken a different approach to the shape of the modelled transition profiles. Nair employed Voigt profiles, and their use in spectroscopy is common as the inherent combination of Lorentzian and Gaussian curve features results in a curve which mimics observed lineshapes, affected by natural and Doppler broadening, quite well. We have opted for pseudo-Voigt profiles, which are almost identical but easier to calculate, and are defined as:

$$V_{ii}^{*(n,m)}(E) = \beta_{ii}^{(n,m)} L_{ii}^{(n,m)} + (1 - \beta_{ii}^{(n,m)}) G_{ii}^{(n,m)}$$

where L is a Lorentzian curve and G is a Gaussian curve:

$$L_{ii}^{(n,m)}(E) = \alpha_{ii}^{(n,m)} \frac{(\Gamma_{L,ii}^{(n,m)}/2)^2}{(E - E_{0,ii}^{(n,m)})^2 + (\Gamma_{ii}^{(n,m)}/2)^2}$$

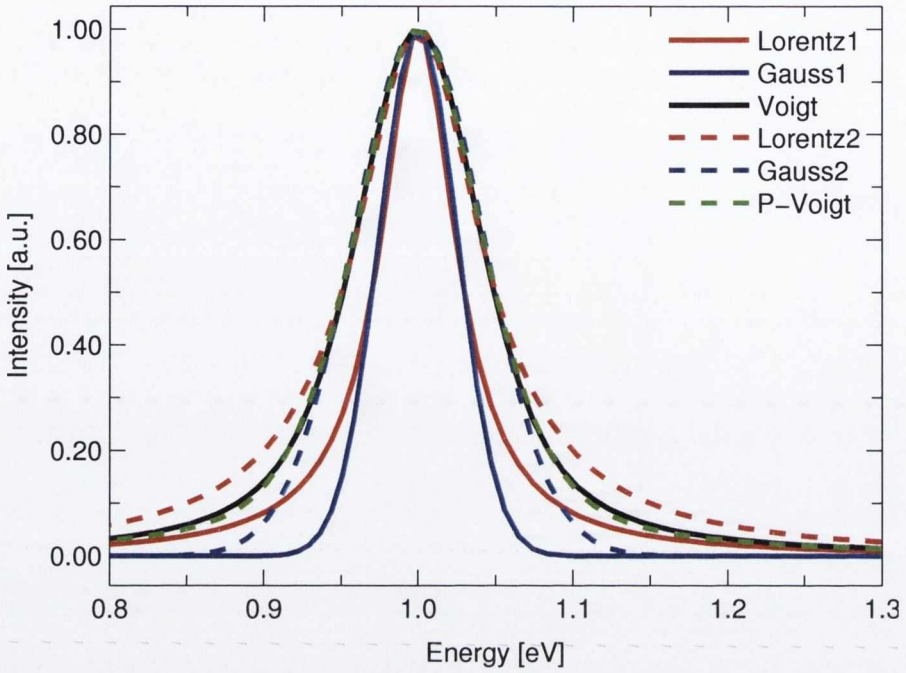

Figure 33: Illustration of pseudo-Voigt profile. Nair's work uses Voigt profiles of width Γ derived from the convolution of Lorentzian and Gaussian line-shapes of equal width $\Gamma' = \Gamma/1.637$ (shown by *Voigt*, *Lorentz1*, and *Gauss1*, respectively). Our work uses a pseudo-Voigt profile of width Γ derived from the partial addition of Lorentzian and Gaussian line-shapes, both having width Γ (shown by *p-Voigt*, *Lorentz2*, and *Gauss2*). The resulting Voigt and pseudo-Voigt profiles are nearly identical.

$$G_{ii}^{(n,m)}(E) = \alpha_{ii}^{(n,m)} \exp\left[-\frac{4\ln 2}{\left(\Gamma_{G,ii}^{(n,m)}\right)^2}(E - E_{0,ii}^{(n,m)})^2\right]$$

both having the same peak centre $E_{0,ii}^{(n,m)}$, full width at half maximum $\Gamma_{ii}^{(n,m)}$ and amplitude $\alpha_{ii}^{(n,m)}$, and where the parameter $\beta_{ii}^{(n,m)}$ $(0 \leq \beta_{ii}^{(n,m)} \leq 1)$ thus dictates the overall line-shape of the pseudo-Voigt curve $V_{ii}^{*(n,m)}$. The Voigt profile used in Nair's work,

$$V_{ii}^{(n,m)}(E) = \int_{-\infty}^{\infty} G_{ii}^{(n,m)}(E')L_{ii}^{(n,m)}(E_{ii}^{(n,m)} - E')dE'$$

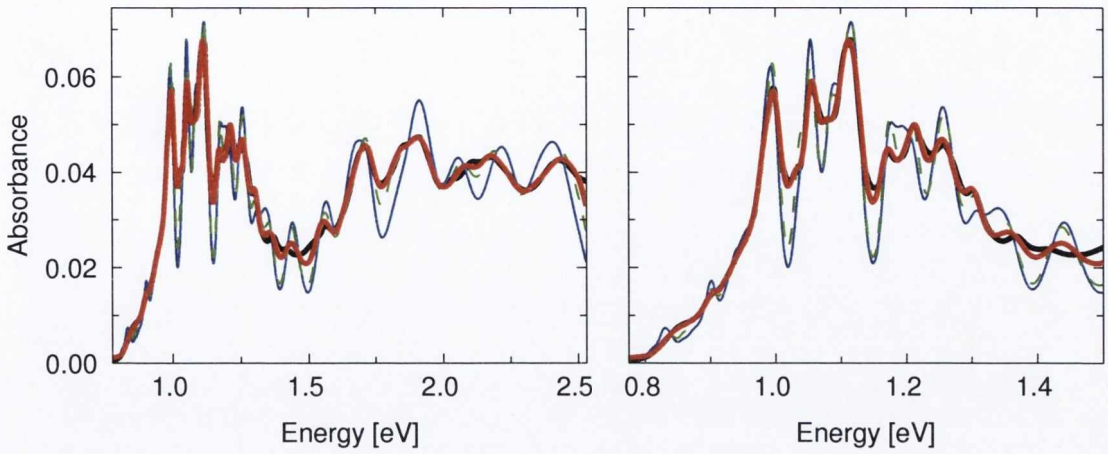

(a) (b)

Figure 34: Initial and final fits to absorbance curve for SWNTs in SDS-D_2O (a) The absorbance spectrum (black line) of our dispersion of SWNTs showing the fit obtained using an approach akin to Nair's program (thin blue line), and our initial fit (green dashed line), which allows further variation of amplitudes. This fit was then refined (red line), by optimizing all component peak parameters simultaneously. (b) Detail of the E_{11}^S region of the plot, with its narrow spectral features.

must be evaluated numerically, and it is thus rather more computationally intensive to fit several parameters of a true Voigt profile. Figure 33 shows a comparison of Voigt and pseudo-Voigt ($\beta = 0.5$) profiles derived from their respective underlying Gaussian and Lorentzian functions. Using the pseudo-Voigt profile allows us an easier way to access and fit the energy, width and amplitude parameters of our peaks while essentially retaining the Voigt line profile.

As a starting point, we fix the energies, widths and profile shapes as they were at the end of step 2 above (we will adjust them in the next step) and fit only the amplitudes, according to Nair's method. We then relax Nair's condition on the internal ratio of amplitudes of component peaks within a parent peak, allowing individual peak amplitudes to vary $\pm 50\,\%$. These fits are performed using MATLAB's quadratic programming routine,

'quadprog'. A comparison of this initial fit with the starting fit achieved using Nair's program can be seen in Figure 34 .

4. Adjust the values of the model peak parameters (centre $E_{0,ii}^{(n,m)}$, width $\Gamma_{ii}^{(n,m)}$, and amplitude $\alpha_{ii}^{(n,m)}$) within set bounds.

We now adjust our individual fit parameters, fixing bounds as follows:

- The absorbance energy at E_{11} or E_{22}, as modified where appropriate in step 2, is allowed to vary by ± 5 meV, or ± 2.5 meV for those energies measured directly from the PL map.
- The FWHM, supplied by the user as $\Gamma_{ii}^{(n,m)}$ and measured in step 2 to be $\Gamma_{ii}^{\prime(n,m)}$, may vary between $0.7 \times \min(\Gamma_{ii}^{(n,m)}, \Gamma_{ii}^{\prime(n,m)})$ and $1.3 \times \max(\Gamma_{ii}^{(n,m)}, \Gamma_{ii}^{\prime(n,m)})$. For those s-SWNTs identified in the PL map, we set the upper bound on the FWHM to be $1.1 \times \Gamma_{ii}^{\prime(n,m)}$, as our absorbance data was recorded using a smaller bandpass than the excitation monochromator slit width.
- The amplitude $\alpha_{ii}^{(n,m)}$ may continue to vary between 0.5 and 1.5 times the starting value found by fitting the absorbance spectrum according to Nair's method.
- $\beta_{ii}^{(n,m)}$ is fixed at 0.5 throughout.

We use the non-linear least-squares optimisation function 'lsqnonlin' to minimise the difference between the absorbance curve and the model curve. Our approach takes some minutes to reach a satisfactory fit, though this is perhaps not surprising given that the computation involves 96 transitions having 3 independent parameters, each with their own bounds, and a 1100+ point spectrum. We acknowledge that there may (if not *must*) be a more optimal fitting routine in terms of computational approach, time

taken, or elegance of code. We would be happy to see our work improved in this respect and will be publishing the code as part of the supporting information for an upcoming paper, and is included here in the appendix.

One feature of Nair's approach which is also present in our work is the assumption that all SWNT species present in the input information are represented in the absorbance spectrum also. In Nair's program the relative contributions were fixed in groups according to the location of peaks in the data, while we have relaxed this condition somewhat. Obviously if some absorbance is ascribed to a SWNT species which in fact is not present in the sample this will have an adverse effect on our measurement and may artificially increase the PLQY estimate for s-SWNTs with nearby E_{22}^S energies. In order to gain an estimate for the lower bound of the PLQY values, we repeat this last round of fitting—with the baseline corresponding to Nair's work as mentioned previously—and this time change the fit conditions. The bounds on energies and widths remain the same, but the bounds on amplitudes are modified. For those s-SWNTs identified in the PL map, the initial fit amplitude produced above becomes the lower bound, while the upper bound is removed; for the other s-SWNTs and the metallic tubes, the initial fit amplitude becomes the upper bound while the lower bound is reduced to zero and the starting amplitude value for the current fitting routine (i.e., the amplitude from the initial fit) is reduced by 75%. With this strong (and presumably overzealous) favouring of the s-SWNTs identified in the PL map, we aim to over-estimate the relevant absorbance values and thus give an estimate for the lower bound on the PLQY values.

The average and extrema of this fit plus the four fits using various backgrounds outlines earlier are presented in our work as the PLQY value and suggested error bars. The SWNT species with the greatest sensitivity to these variations in fitting approach—the (7,6) and (7,5) tubes—both

have very similar E_{22} values, suggesting that the other SWNT species (both semiconducting and metallic) with similar absorbance values are causing a good deal of uncertainty in the fit to the absorbance curve at that point.

5. Generate model PL emission spectra for each (n,m) species, representing $E_{11}^{(n,m)}$ and $E_{22}^{(n,m)}$ emissions. Fit each emission spectrum in the PL map in a similar fashion to the absorbance spectrum.

Using the input values for energies and widths, as modified after analysis of the PL map in step 2, we generate model emission curves for each semiconducting $E_{11}$and E_{22} transition. Again we use pseudo-Voigt profiles. The emission parameter values are first refined for each s-SWNT type identified with a peak in the PL map in turn. The emission spectrum closest to each tube type's excitation maximum is analysed, and values of $E_{11}^{(n,m)}$, $\alpha_{11}^{(n,m)}$ and $\Gamma_{11}^{(n,m)}$ are optimised for the relevant tube types, again carried out using the '`lsqnonlin`' routine, and the energy and width parameters for the peak in question are then fixed before moving on to the emission spectrum associated with the next species' peak emission.

With all parameters except amplitudes $\alpha_{11}^{(n,m)}$ now set, the emission lines in the PL map are fitted line-by-line using the '`quadprog`' quadratic programming function. Starting values for amplitudes for all $E_{11}^{(n,m)}$ emission peaks at a given excitation energy are calculated based on pseudo-Voigt shaped excitation profiles with a peak energy and width matching those obtained from our analysis of the PL map in step 2, and peak height for those identified s-SWNTs as estimated in the optimisation procedure above. Lower bounds are set at 0.8 times this starting fit, while no upper bounds are imposed. Modelled emission from semiconducting E_{22} and metallic E_{11} transitions is prohibited through the use of very low starting amplitudes and upper bounds. The fit is performed in two stages. In the first, only

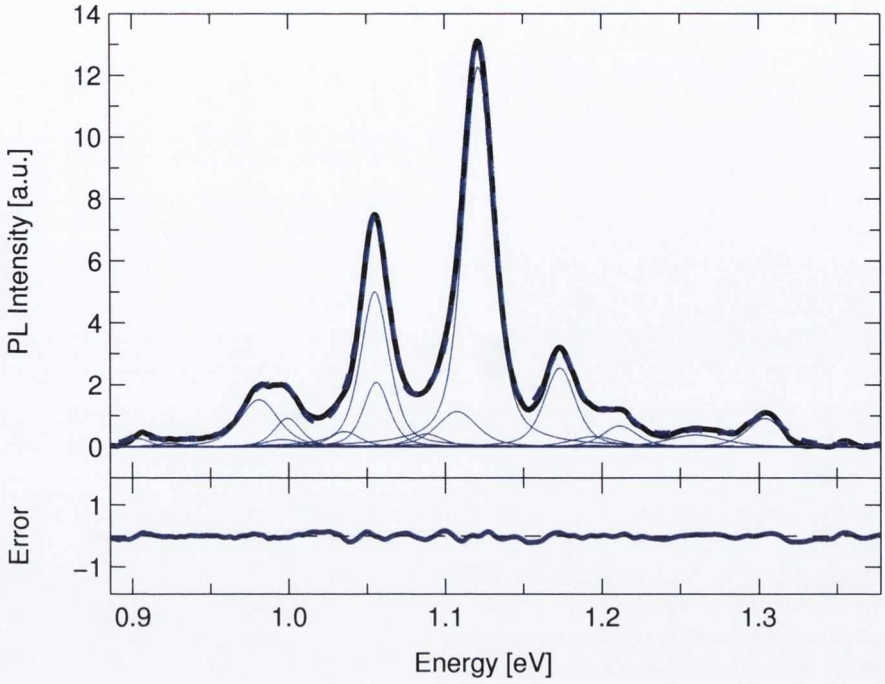

Figure 35: PL map emission spectrum (black solid line) from SWNTs in SDS-D_2O dispersion showing excitation at 1.722 eV, fitted as described in the text. Thin blue lines show component peaks while the dashed blue line show their sum. In the lower panel the difference between the PL emission spectrum and the sum of the fit peaks is plotted, with an identical vertical axis scale.

s-SWNTs with $E_{22}^{(n,m)}$ values within 0.1 eV of the excitation energy are involved. The fitted amplitude values obtained are then used as the starting values for the next stage. Here, the lower bounds are set to 0.9 times the results of the first stage, while unlimited upper bounds for $E_{11}^{(n,m)}$ emission are extended to all s-SWNTs with $E_{22}^{(n,m)}$ values within 1 eV of the excitation energy. In this way priority is given to those tubes at or near resonance with the excitation energy, with other tubes being added later on to 'fill in the gaps.' Figure 35 shows the final result of the PL fit for the emission line at 1.722 eV (= 720 nm) excitation. Each emission line is fitted without regard to the results of adjacent line fits.

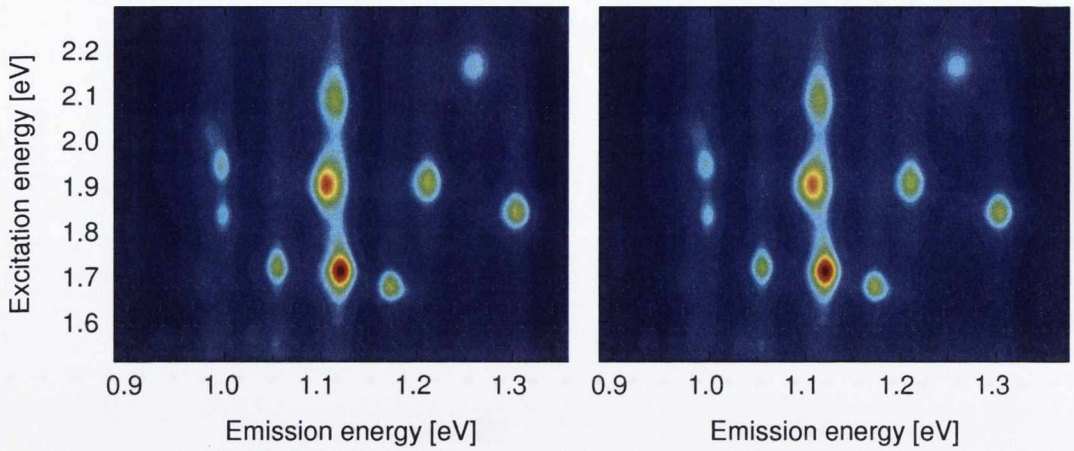

(a) (b)

Figure 36: (a) The input PL map data for SWNTs in SDS-D_2O and (b) the model PL map generated from E_{11} emission spectra during our fitting process.

The result of fitting each line of the PL map is a model map, both of which are shown in Figure 36. Differences between the two maps are minimal.

In fitting each of the emission spectra contained in the PL map, an 'excitation spectrum' is produced for each s-SWNT type, consisting of fitted amplitudes for the model $E_{11}^{(n,m)}$ emission curves versus excitation energy of the emission spectra. These generated excitation spectra are shown in Figure 37a, while 37b shows the PL map configured to show the emission peaks as a function of excitation energy. Our excitation spectra clearly match qualitatively the PL map, even where there is evidence of energy transfer between tubes or emission from phonon-assisted side bands, such as the secondary peak in (8,6) emission ($E_{11}^{(8,6)} = 1.054\,\text{eV}$, $E_{22}^{(8,6)} = 1.717\,\text{eV}$) at 1.907 eV excitation, indicating energy transfer from the (7,6) or (7,5) tube. Far away from the $E_{22}^{(n,m)}$ excitation energy, we see very noisy peaks, where the model $E_{11}^{(n,m)}$ emissions are used at low levels to fit what appears to be ill-defined 'background' PL emission from the dispersion.

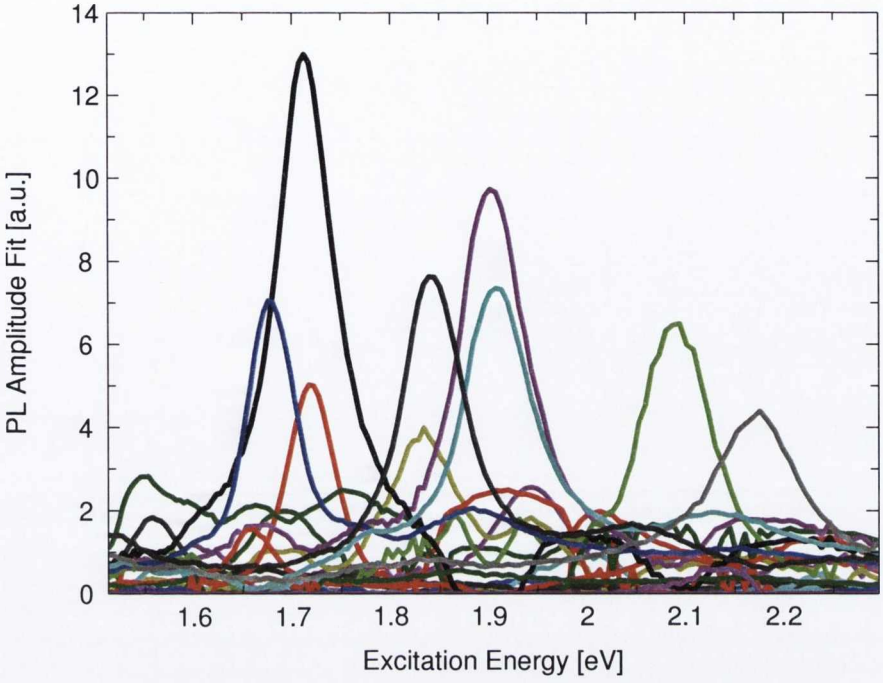

(a)

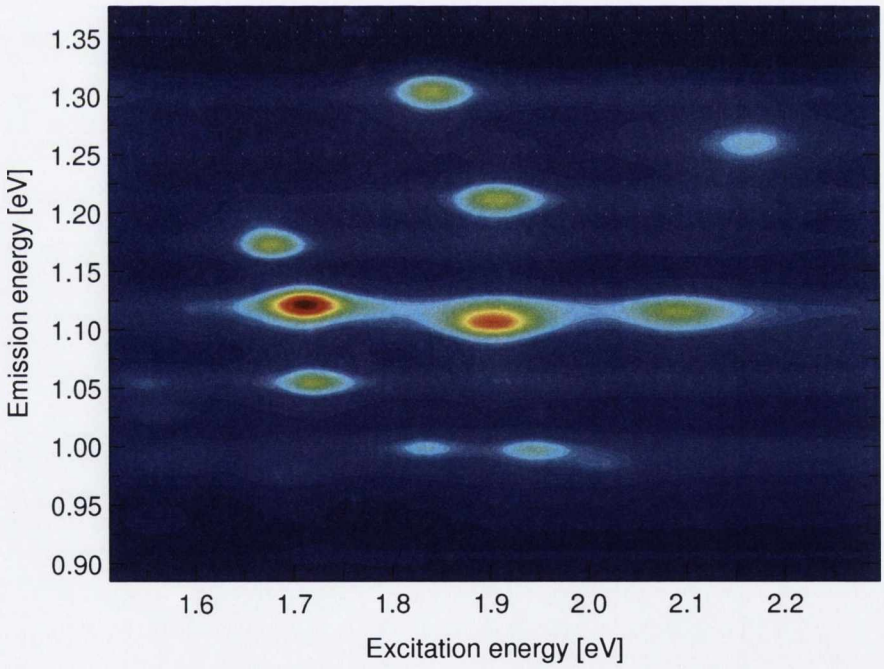

(b)

Figure 37: Model excitation spectra for SWNTs in SDS-D_2O dispersion. (a) Generated excitation spectra, showing the fitted $\alpha_{11}^{(n,m)}$ emission parameters for each s-SWNT as a function of excitation energy, and (b) the PL map for SWNTs in SDS-D_2O being fitted.

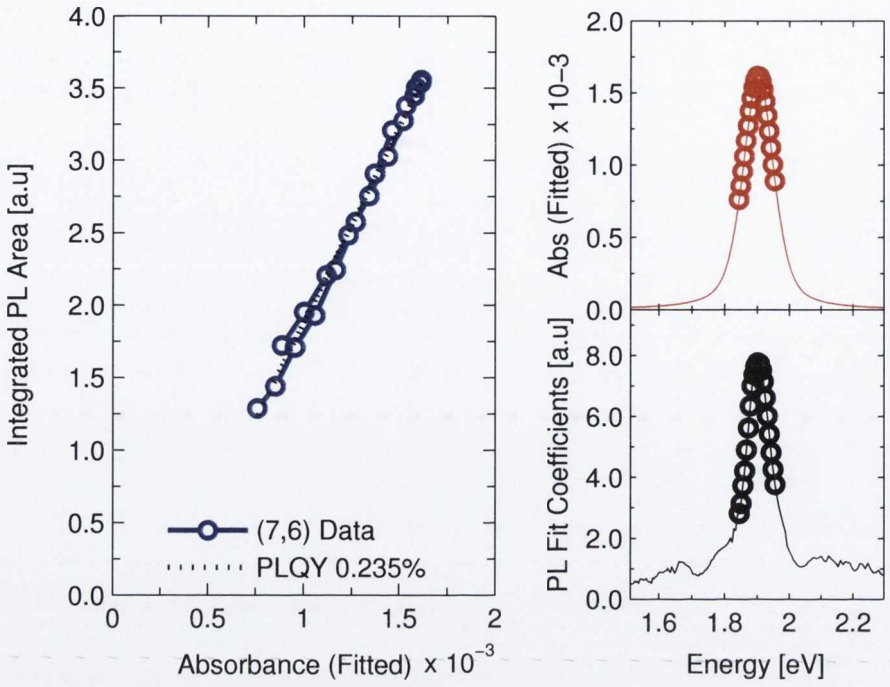

Figure 38: Analysis of the PL emission and absorbance for the (7,6) tube in an SDS-D_2O dispersion. Clockwise from main plot: Integrated fitted PL area as a function of fitted absorbance, model absorbance curve and fitted excitation spectrum, as a function of excitation energy.

6. Integrate the PL emission from each nanotube species in each fitted emission spectrum.

7. Calculate the ratio of integrated PL emission to absorbance for excitation energies near the $E_{22}^{(n,m)}$ absorbance peak for each semiconducting tube species identified in the PL map.

Once the values of $\alpha_{11}^{(n,m)}$ and $\Gamma_{11}^{(n,m)}$ have been identified for the emission curves in step 6 above, the spectrally integrated PL emission for each curve is easily calculated at each excitation energy.

In order to estimate PLQY values we need to correlate integrated emission with the absorbance of the material at the excitation wavelength. The absorbance value obtained from the fit procedure is here modified to account for the fact that only a certain fraction of tubes are likely to be

individualized and able to fluoresce, while others will be in bundles of varying size and will most likely have their excited states quenched via other mechanisms. An estimate of the mass fraction of individual tubes is obtained from atomic force microscopy (AFM) and used here to correct the fitted absorbance spectra for each tube type.

At energies near the $E_{22}^{(n,m)}$ absorbance peak we plot integrated PL emission as a function of absorbance for each tube type identified with a peak in the PL map. Figure 38 shows this analysis for the (7,6) tube. Also shown are the fitted E_{22} absorbance curve and the generated excitation spectrum.

We see that near the absorbance maximum the modelled absorbance and excitation spectrum correlate closely, and this is reflected in the linearity of the graph of integrated PL versus absorbance. While we typically obtain a good quality linear fit, we do not constrict the fit to pass through the origin. As indicated in the discussion of step 5 above, model curves are employed in small amounts to fit emission lines even relatively far from their $E_{22}^{(n,m)}$ maximum; this fit is noisy in places and may represent energy transfer or other higher-order effects. As our model absorbance curve does not account for anything other than a smooth and continuous fall to zero of the absorbance value away from the $E_{ii}^{(n,m)}$ peaks, we prefer to analyse only those points near the absorbance peaks and assume all other effects are relatively constant around these excitation energies.

In fitting the absorbance curve, we set the input values for energy and width for the E_{22}^{S} absorbance transitions to be equal (where possible) to those measured from the PL map, but there is considerable freedom allowed in the fit for the widths and amplitudes. Ideally, the profile shape of the E_{22}^{S} excitation spectrum and E_{22}^{S} absorbance spectrum for each s-SWNT species should coincide. Thus a plot of integrated emission—directly related to

the intensity of the excitation spectrum—and absorbance should be linear. When the two profiles do not coincide, we find deviations from linearity.

In Figure 39 we illustrate the cause of some of these deviations. In 39a we show a theoretical absorbance curve (black) and two theoretical excitation spectra (red and blue), each having the same peak centre but different widths. If we plot the value of the excitation spectra against that of the absorbance spectrum for a number of absorbance values (marked with dots on the absorbance curve), we see that the effect of unmatched peak widths is to bend or bow what would otherwise have been a straight line fit (red and blue curves, and dashed line in 39b). Similarly, from 39c and 39d we find that the effect of a shift in peak centre is to produce a loop or curve instead of a straight line fit. Lastly, 39e and 39f show the effect of a constant background PL emission, i.e. the excitation spectrum is shifted upwards somewhat, resulting in the plot of excitation spectrum against absorbance curve no longer passing through the origin.

Given that we allow some freedom in the fitting of absorbance energy and width, using the values derived from the PL map as a starting point only, we expect to see some of these effects in our graph of integrated PL versus absorbance. However, we find that the effects are generally small and do not increase greatly the uncertainty present in our results owing to the issues of background absorbance and the imposition of bounds on the amplitude in our absorbance fit, as discussed earlier. In theory one could use these results in a feedback loop to inform further the choice of values for peak centres and widths, particularly in the case where absorbance and fluorescence measurements are made using the same apparatus and set-up, but we have not implemented that here.

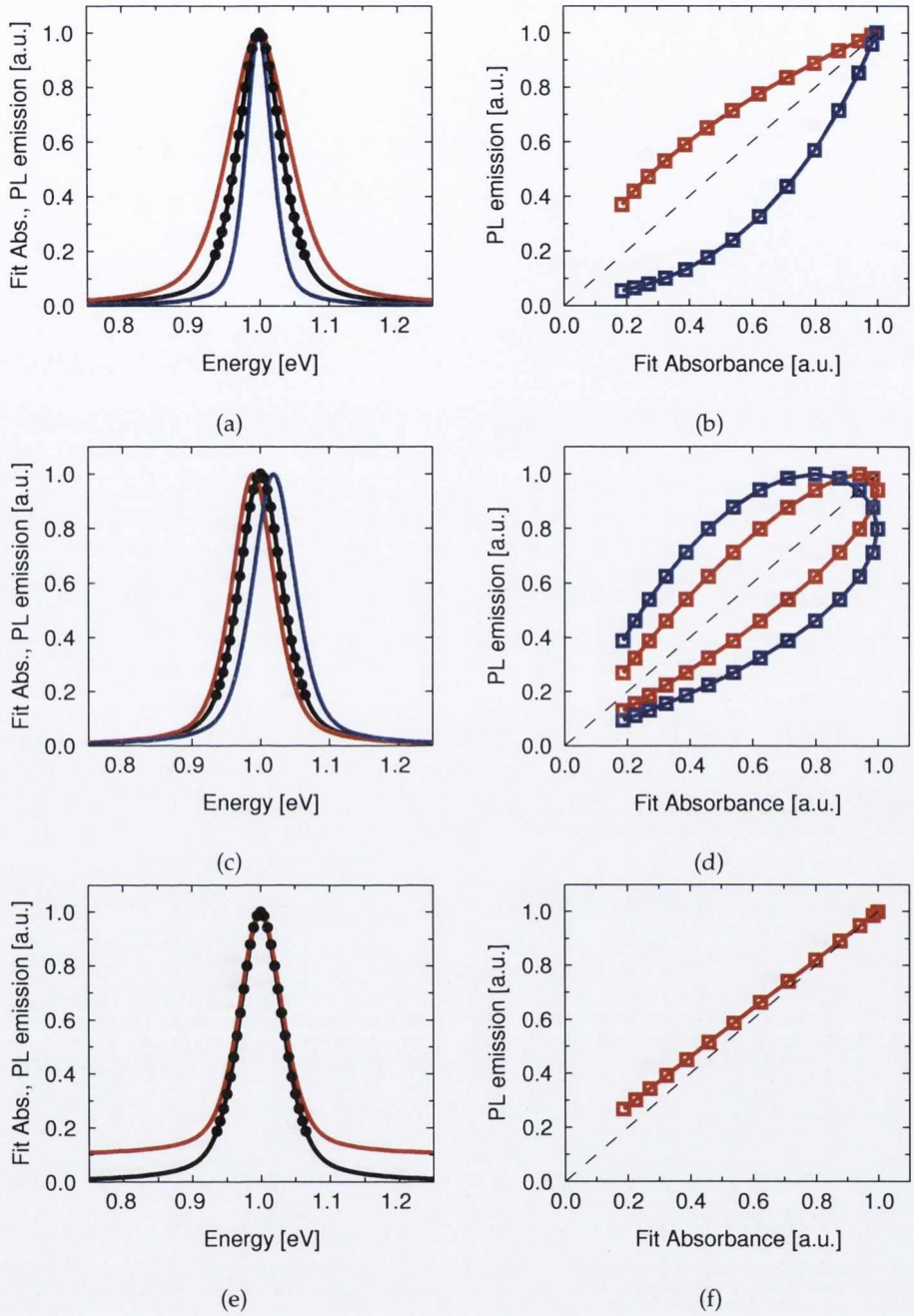

Figure 39: The effect of mismatched parameter values on plots of excitation spectra versus absorbance spectra. The black lines in (a), (c), and (e) represents the model absorbance curve and sampling points, while the coloured curves show hypothetical PL excitation spectra (which should ideally correspond to 'actual' absorbance curves). The resultant plots of PL intensity versus absorbance at these sampling points for mismatched peak widths, misaligned peak centres and unaccounted-for background are shown in (b), (d) and (f), respectively, with matching colours and data sample points.

8. Estimate the absolute PLQY value for each of these *(n,m)*-species, relative to a standard dye.

PL emission may be related simply to absorbance as follows:

$$I_{PL}/\eta_{det} = (I_{exc}\eta_{exc})A\phi K \tag{5.2}$$

where I_{PL}/η_{det} represents spectrally integrated PL emission, corrected for emission monochromator and detector efficiencies, $I_{exc}\eta_{exc}$ represents the intensity of the excitation beam at the excitation wavelength, corrected for lamp and monochromator performance, A is the absorbance of the material at the excitation wavelength, ϕ is the material PLQY and K is a constant which contains information regarding the set-up geometry and total fraction of emitted light collected. Both η_{det} and η_{exc} are normalised spectra, and so in practice we have the measured PL emission corrected as $I_{PL}/(\eta_{exc}\eta_{det})$.

We use a PL map which has been corrected for the spectral performance of the monochromators, lamp and detector, and thus our integrated PL values are proportional to absorbance, $I'_{PL} = A\phi K$. The slopes of the fit lines in our graph of I'_{PL} versus A in Figure 38 above are thus proportional to the PLQY values.

Using AFM data analysis, we correct the fitted absorbance to account for the presence of both small bundles and individual tubes. The presence of bundles of tubes can lead to energy transfer between semiconducting tubes, sometimes leading to luminescence from the acceptor tube [200], while the presence of metallic tubes in a bundle allows non-radiative recombination of excitons. These quenching mechanisms are very efficient, and the rate of luminescence from acceptor tubes is low—which explains the lack of observation of PL across the band gap of s-SWNTs before a suitable method

of isolating individual tubes was found. We thus assume that the large majority of observed PL near E_{22}^S–E_{11}^S resonance comes from individual nanotubes, and that only the fraction of absorbance attributable to individual nanotubes should be correlated with recorded PL to estimate PLQY values. From careful analysis of nanotube bundle length and diameter from AFM data, the number density of individual tubes in a given dispersion (N_{Ind}/V) can be estimated [198, 21]. This can be used to find the mass fraction of individual SWNTs, M_{Ind}/M_{Tot}. Briefly, the mass fraction is given by

$$\frac{M_{Ind}}{M_{Tot}} = M_{NT}\frac{N_{Ind}}{V}\left(\frac{M_{Tot}}{V}\right)^{-1} \tag{5.3}$$

where M_{Ind} and M_{Tot} refer to the mass of all individualized nanotubes and the total mass of all dispersed nanotubes and bundles respectively. In addition, M_{NT} is the average mass of an individual SWNT and M_{Tot}/V is the total nanotube (inc. bundles) mass per volume (i.e. the concentration, C). Writing M_{NT} in terms of the individual nanotube diameter and length and the mass per unit area of a graphene sheet (M/A), we get:

$$\frac{M_{Ind}}{M_{Tot}} = \left(\frac{M}{A}\right)\frac{\pi\langle D_{NT}\rangle\langle L_{NT}\rangle}{C}\frac{N_{Ind}}{V} \tag{5.4}$$

From the AFM data we calculate a value of $M_{Ind}/M_{Tot} = 0.35$ for sample D. Multiplying the absorbance by this value gives the absorbance due only to individual SWNTs. Implicit in this correction is the assumption that bundle formation is species-independent, as we did not have the means at our disposal to identify the chirality of each individual tube and small bundle identified in our AFM studies. We also assume the equivalence of absorbance contributed by isolated tubes and tubes in bundles, suggesting that once the larger bundles have been removed by

ultracentrifugation the broadening and red-shifting of absorbance peaks associated with bundling is negligible. While there is a large increase in the sharpness of absorbance peaks on going from the initial dispersion to the ultracentrifuged one, further increases may be attainable by optimising the amount of centrifugation (as will be discussed in Chapter 6).

As well as relative estimates of PLQY, we can estimate absolute PLQY values if we have absorbance and integrated quantum PL emission data for a substance of known quantum yield. Such data must be recorded under identical experimental conditions in order for the proportionality constant K to be eliminated. The absolute PLQY value, ϕ, can then be calculated from:

$$\phi_x = \phi_{St}\left(\frac{m_x}{m_{St}}\right)\left(\frac{n_x^2}{n_{St}^2}\right) \tag{5.5}$$

where m is the slope of the line fitting integrated PL emission versus absorbance (corrected for AFM data on individual bundles as above), n is the refractive index of the solution, and the subscripts x and St refer to the unknown material and the standard, respectively. The refractive index term is included to account for the effect of dispersion of light on the intensity of light recorded by the detector.

In order to ensure the accuracy of our standard materials, we obtained absorbance and PL data using identical instrument settings for rhodamine 6G and rhodamine B in ethanol, known to have PLQY values of 0.95 and 0.65 respectively [119]. When we take these PLQY values we can plot $Y = KA$ for each of these materials (see Figure 40), where $Y = I'_{PL}/\phi$ is the spectrally corrected, integrated PL emission divided by the PLQY. K being a constant for our experimental set-up, the co-linearity of these plots

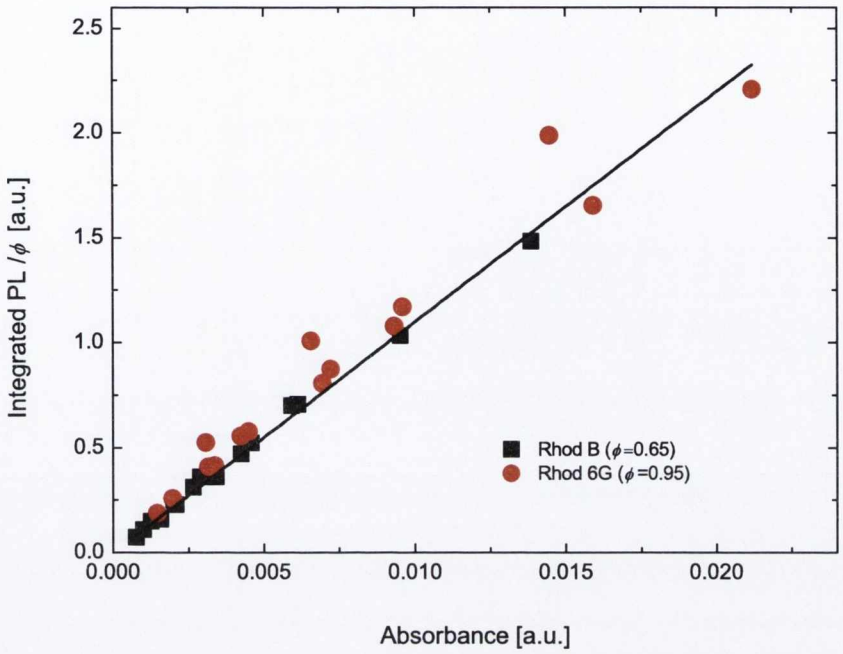

Figure 40: Cross-standardisation of our reference dyes. Data is plotted using the nominal PLQY values for each material, which should then produce linear plots with identical slope representing an instrument- and settings-specific constant, K.

indicates the combined accuracy of their nominal PLQY values and our experimental set-up.

Our PLQY results are provided with error bars indicating the range of values obtained when we use multiple backgrounds and when we set the parameters of the fit to favour those s-SWNTs detected in the PL map.

9. Plot results and write data to file.

Finally, the program saves the MATLAB figures it has generated and writes out data to a user-specified file. The output includes fit parameters for each transition, tables of individual fitted absorbance data, integrated emission area as a function of excitation wavelength and the calculated model PL map, as well as integrated emission as a function of absorbance for each tube. Most of the graphs produced during the analysis are saved by default.

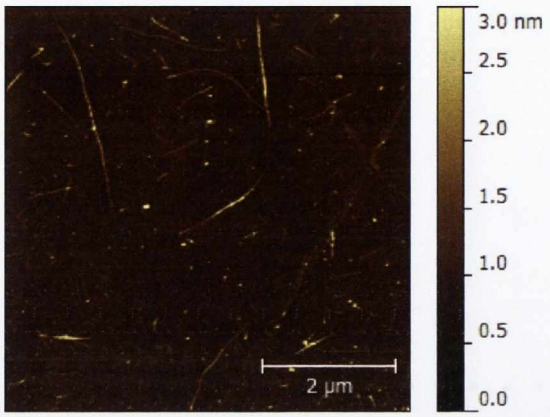

Figure 41: AFM image of tubes and bundles for SWNTs on a silicon substrate, from a SDS-D_2O dispersion, sample D. Length and diameter distributions are found from analysis of several such images.

5.4 RESULTS AND DISCUSSION

The prepared solutions consisted of well-dispersed individual SWNTs and small bundles as evidenced by AFM imaging (Figure 41). They showed good stability, with little or no decrease in absorbance over a period of weeks. Comparing the absorbance values for the original (uncentrifuged) solution of known concentration and for the other solutions, we estimate SWNT in SDS-D_2O concentrations $c = 0.161$, 0.080, 0.040, 0.020 and 0.008 $\mathrm{mg \cdot mL^{-1}}$ for samples A–E, respectively. See Figure 42 for absorbance curves of each solution.

To reduce complications arising from the inner-filter effect and from re-absorption, the effect of which on PL intensities was explored in detail in Chapter 4, we work in the concentration regime in which a linear relationship between absorbance (and thus concentration) and PL is maintained. Figure 43 illustrates the maximum peak height associated with three peaks identified in the PL map, measured using a 2×2 mm cuvette,

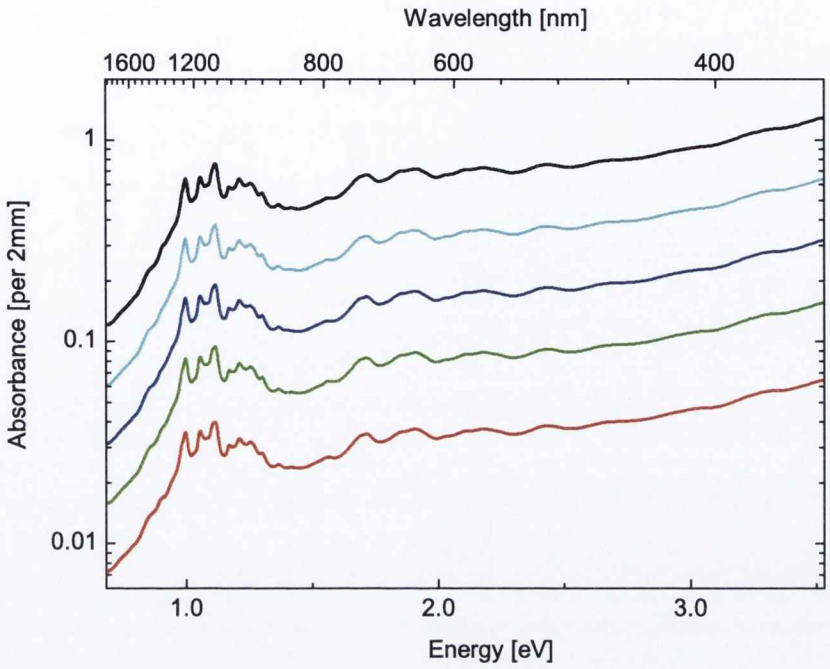

Figure 42: Absorbance spectra for dispersions of SWNTs in SDS-D_2O. Top to bottom: samples A–E, each a dilution of the previous dispersion with stock SDS-D_2O solution.

as a function of solution concentration. Inner-filter and re-absorption effects become important at concentrations above approximately 0.020 $mg \cdot mL^{-1}$, corresponding here to an average absorbance between 500 and 900 nm of 0.37 in a 1 cm absorbance cuvette. (If using a fluorescence cuvette of 1 cm pathlength, this concentration threshold would be lower. All later absorbance values given here relate to 2 mm pathlength absorbance, identical to our fluorescence cuvette pathlength.) We thus restrict our full analysis presented here to sample D. While of minimal concern to those utilizing micro-fluorescence apparatus to measure single-tube emissions, these effects would preclude any quantitative comparison of absorption and emission above a similar concentration threshold for common right-angled PL spectrometer geometries.

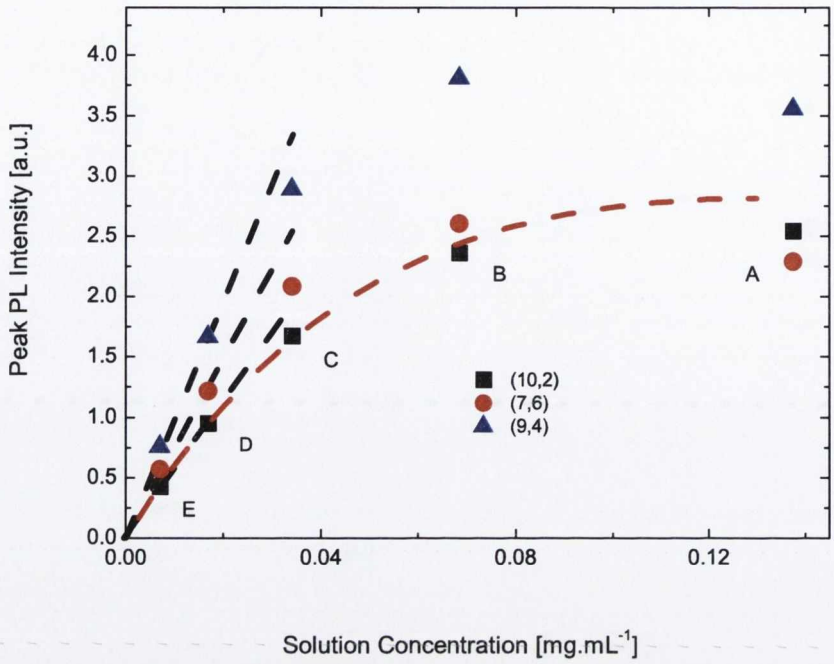

Figure 43: PL intensity as a function of concentration for a number of SWNTs in SDS-D_2O dispersions upon dilution. Successive dilutions from the starting concentration are required before a linear relationship between absorbance and detected PL intensity is established. The non-linearity is due to inner-filter effects as discussed in Chapter 4, which here become apparent above concentrations of approximately $0.02\,\mathrm{mg{\cdot}mL^{-1}}$. The red dashed line is a fit to the (10,2) data using Equation 4.1.

As previously outlined, the absorbance fit routine employed in the program is a modified version of that published by Nair *et al.* [152], with a different approach to the background and to the fitting of component peak parameters. The results of our fitting routine are shown for sample D ($c = 0.02\,\mathrm{mg{\cdot}mL^{-1}}$) in Figure 44.

Allowing more freedom to the fit parameters leads, inevitably, to a loss of uniqueness in the fit. To investigate the sensitivity of our program to small changes in the starting conditions, we examined the estimated individual absorbances when the non-resonant background is adjusted in a number of ways. We find that while the background can have a significant effect on the absorbance values it has a much less pronounced effect on the relative

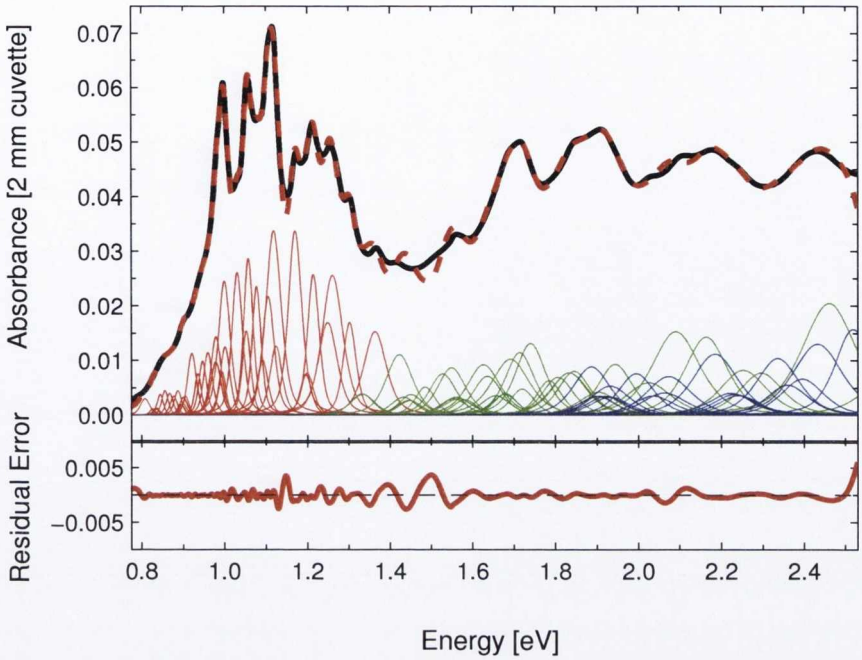

Figure 44: Fitted absorbance spectra for SWNTs in SDS-D_2O dispersion, sample D. Narrow red, green and blue lines indicate E_{11}^S, E_{22}^S and E_{11}^M transitions, respectively, while the dashed red line indicates the sum fit. The lower panel shows absolute error between the absorbance spectrum and model fit, to the same vertical scale.

absorbance values of different (n,m)-species. In order to produce a robust estimate for the lower bound for the PLQY value, we also performed the absorbance fit while favouring those s-SWNT species identified in the PL map at the expense of all other tube types. Where we produce comparative figures of PLQY values in Figure 46, we have shown the average PLQY values and included as error bounds the upper and lower extrema of PLQY values calculated under these various conditions as outlined Section 5.3.

Each of the emission spectra from the PL excitation-emission map is fitted using a similar routine to that used for the absorbance fit (see Figure 35). In all cases, extremely good fits are obtained, with R^2 values greater than 0.987. From the fits the integrated spectral emission as a function of individual mass-fraction corrected absorbance for each tube type can

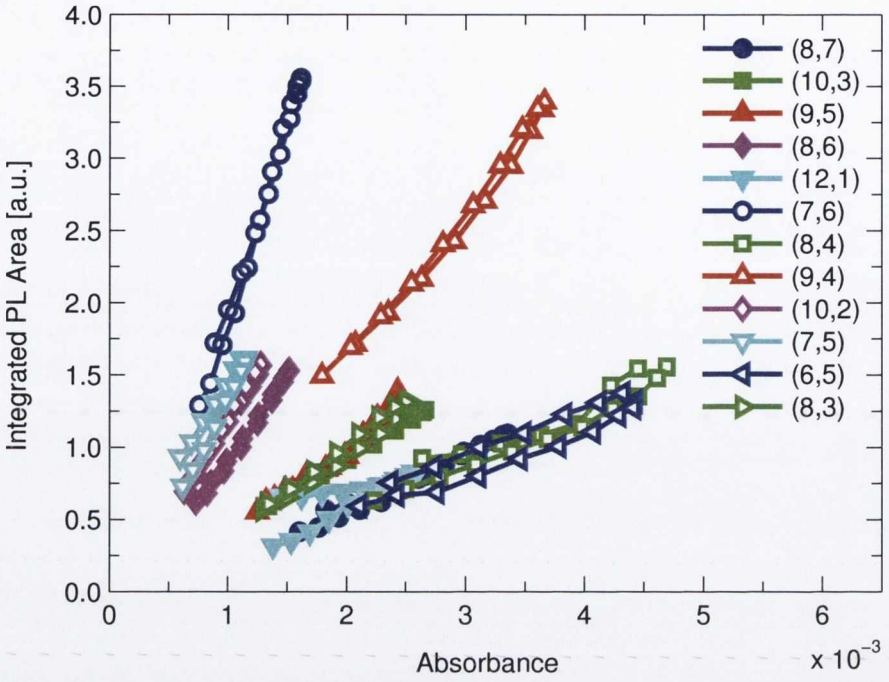

Figure 45: Integrated PL versus absorbance for a range of nanotubes observed in dispersions of SWNTs in SDS-D_2O. The curves show some of the features outlined in Figure 39 regarding the effects of mismatched peak parameters between the absorbance and PL excitation curves, but overall retain a near-linear shape.

then be calculated. We can now correlate integrated PL emission at each excitation wavelength with fitted absorbance values for each tube type, as shown in Figure 38. This information is calculated for each (n,m)-species identified by the MATLAB program in the PL map. In Figure 45 we illustrate the data for integrated emission versus absorbance for all the s-SWNTs analysed in this sample. We note that while the relationship between integrated emission and absorbance is broadly linear, the fit is not restricted to pass through the origin to allow for some background signal.

From Equation 5.2, it is clear that the slope of the PL versus absorbance fit is proportional to the PLQY of each tube type. Measuring the absorbance and integrated PL for our two reference dyes, rhodamine B and rhodamine 6G, under identical conditions allows us to eliminate the constant K and

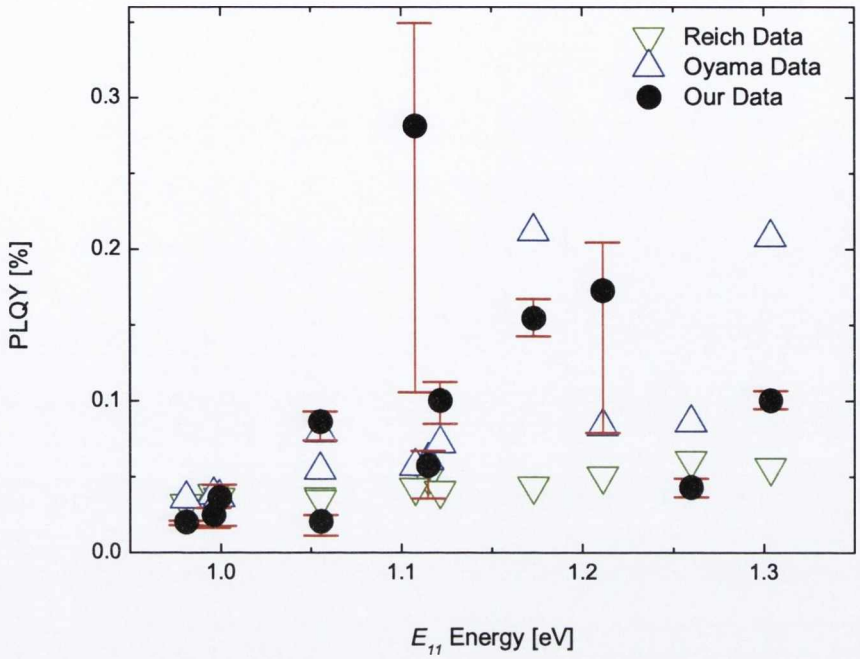

Figure 46: PLQY values for SWNT species observed in SDS-D_2O dispersion. Values estimated in this work are presented as red filled circles, while theoretical data from Reich *et al.* [173] and Oyama *et al.* [165] (as summarised by Luo *et al.* [140]), are shown as green downward and blue upward triangles, respectively. A general trend of increasing PLQY with increasing band gap is confirmed for all samples, in accordance with that suggested by Tsyboulski *et al.* [204].

estimate the absolute quantum yield, according to Equation 5.5. Figure 46 shows the PLQY data for several species of s-SWNT identified in our sample, with the information also provided in table form in Table 2, with the complete set of data provided in Table 3 and Table 4. Error bounds come from our manipulation of the non-resonant background, as mentioned previously. In general, the PLQY tends to increase with increasing band gap from $\sim 0.03\,\%$ to $\sim 0.15\,\%$. Two exceptions to this trend can be observed; the (6,5) and (8,3) tubes display PLQY values of $0.025\,\%$ and $0.05\,\%$ respectively, significantly below the trend line, while the (7,6) tube displays a relatively high PLQY of $0.28\,\%$. The (7,6) tube also displays the highest sensitivity to the changes in fit conditions, as indicated by the error bars.

Table 2: Table of PLQY values ϕ determined for various s-SWNTs in SDS-D_2O dispersion

(n,m)	d (nm)	E_{11} (eV)	γ_{11} (meV)	ϕ
(6,5)	0.757	1.260	58.8	0.043
(8,3)	0.782	1.302	36.8	0.100
(7,5)	0.829	1.214	33.4	0.173
(8,4)	0.840	1.118	44.2	0.058
(10,2)	0.884	1.170	38.9	0.154
(7,6)	0.895	1.106	34.8	0.281
(9,4)	0.916	1.124	28.9	0.100
(10,3)	0.936	1.000	33.3	0.025
(8,6)	0.966	1.058	26.0	0.086
(9,5)	0.976	1.002	27.0	0.036
(12,1)	0.995	1.054	23.7	0.021
(8,7)	1.032	0.980	21.9	0.020

Also shown are the values of PL/A (proportional to ϕ) calculated from the data provided by Luo *et al.* [140] in their work summarizing the models employed by Oyama *et al.* [165] and Reich *et al.* [173] The data has been normalized to our quantum yield value for the (8,7) tube. Both of these models show PL/A increasing with nanotube band gap in broad agreement with our results.

This relationship between increasing band gap and increasing PLQY can be related to the internal processes required for the recombination of the exciton generated in the SWNTs. Internal conversion of the exciton into multiple phonons in a single step becomes increasingly less

likely as the band gap—and hence the energy and number of phonons required—increases. The total non-radiative relaxation pathway (including phonon-mediated processes, Auger processes and recombination at defect sites) for s-SWNTs is highly efficient and so has a correspondingly short lifetime, measured in tens to hundreds of femtoseconds. The decrease in the availability of the multi-phonon relaxation pathway with increasing band gap will thus increase the non-radiative lifetime of the excited state and hence increase the PLQY as described in Section 2.1.5. The relationship between the non-radiative phonon decay route k and band gap was modelled by Tsyboulski *et al.* [204] as varying with $k \propto \exp(-\nu/C)$ where ν is the optical emission frequency. In addition, a recent publication by Hertel *et al.* [87] has suggested that the lifetime of the excited state in SWNTs—and hence the PLQY—is governed by the defect population, with the high mobility of excitons in SWNTs [187] allowing them to migrate along the length of the tube before recombining either at end points or defect sites.

While it has been estimated that PLQY values for surfactant-coated s-SWNTs can range up to $\sim 5\,\%$ or more[204] we measure PLQY values an order of magnitude lower. However, these higher values typically arise from studies of individual tubes, while here we are dealing with ensemble tube dispersions. It is to be expected that single-nanotube photometry will focus more on the brightest individual tubes, while the ensemble population will contain more defective tubes with lower PLQY values, thus reducing the average measured PLQY value. Thus, we expect the differences between our data and the models referred to above to contain information about the defect content of the tubes under study and on the effect of the local environment (e.g. surfactant coating).

Figure 47 plots these tubes in terms of their band gap and diameter, with marker size illustrating the relative PLQY value. The data points have been

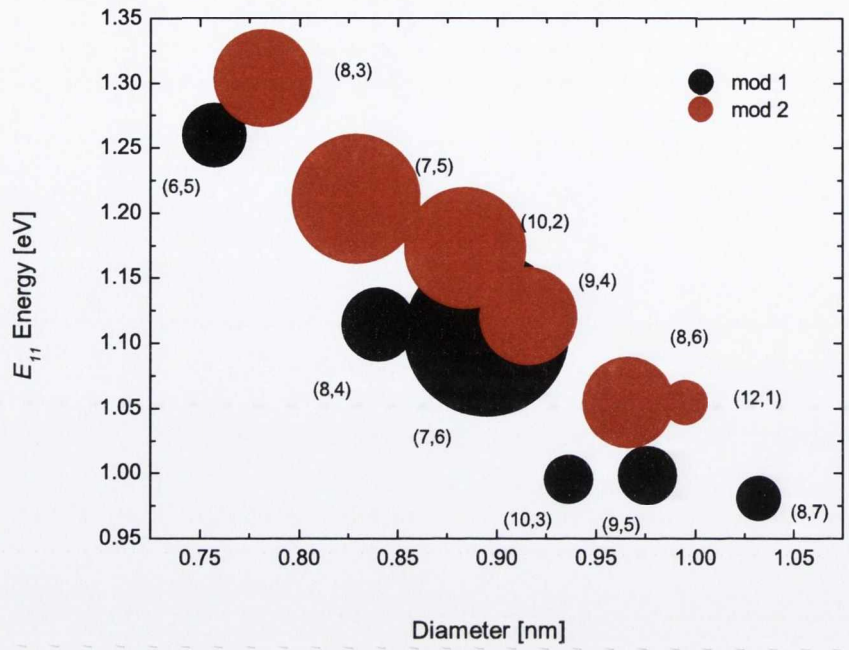

Figure 47: PLQY values expressed on a Kataura-like plot of E_{11} energy versus diameter. The data is coloured to show the difference between the mod 1 and mod 2 families. As suggested by Reich *et al.* [173], the PLQY values appear to be lower in general for mod 1 tubes.

coloured according to their $\mathrm{mod}(n-m,3)$ value. The data supports the theory of Reich *et al.* [173] which suggests that PLQY values are inherently weaker for the mod 1 family due to exciton resonances, whereby the value of E_{22}^S is sufficiently high to allow the E_{22}^S exciton to decay into two E_{11}^S excitons. Only one mod 2 tube—the (12,1) species—shows a lower PLQY value than any of the mod 1 tubes, while the only mod 1 tube with a PLQY value as high as any of the mod 2 tubes—the (7,6) species—is also the species with the largest uncertainty in Figure 46. The dependence on chirality (predicting lower PLQY values for tubes close to zig-zag in structure, i.e. having a small wrapping angle) is not shown quite as clearly, and would require more s-SWNT species to be identified in the sample to be tested in detail.

In terms of defect concentration as determined by the PLQY values, there appears to be a trend towards lower PLQY for the larger diameter tubes, though the limited sample size of (n,m)-species makes any strong link difficult to observe.

5.5 CONCLUSIONS

We have presented a method for measuring the PLQY of several species of semiconducting SWNT in liquid dispersions, using a reference standard dyes and taking into account several influencing factors such as concentration effects, nanotube bundling, and the reduction of the complex absorbance and emission spectra to their component parts. We suggest that other researchers adopt and adapt the MATLAB code in the supporting information to suit their needs. This would enable the relatively rapid assessment of PLQY values for multiple species of s-SWNT in various environments, in a standardised manner.

Our measurements indicate that HiPCO SWNTs in a surfactant-aided D_2O dispersion display PLQY values of the order of 0.1 %, showing clear support for the distinctive behaviour of mod 1 and mod 2 tubes proposed by Reich *et al.* [173] and the increase in PLQY with increasing band gap suggested by Tsyboulski *et al.* [204]. The PLQY values are in line with reported values for ensemble dispersions, though low compared to some recent reports for individual or chirality-separated tubes [130, 51].

Table 3: Fitted parameters for absorbance spectrum—metallic SWNTs in SDS-D_2O dispersion

(n,m)	d (nm)	Φ (deg)	E_{11} (eV)	γ_{11} (meV)	Abs. Area
(8,2)	0.73	10.9	2.519	105.1	0.524
(10,1)	0.84	4.7	2.337	121.2	0.400
(9,3)	0.86	13.9	2.362	119.1	0.210
(8,5)	0.90	22.4	2.396	119.7	0.253
(7,7)	0.96	30.0	2.186	126.7	0.474
(11,2)	0.96	8.2	2.433	140.8	0.586
(10,4)	0.99	16.1	2.224	125.7	0.164
(9,6)	1.04	23.4	2.244	118.8	0.138
(13,1)	1.07	3.7	1.995	102.2	0.256
(12,3)	1.09	10.9	2.036	118.8	0.135
(8,8)	1.10	30.0	2.234	122.9	0.151
(11,5)	1.13	17.8	2.064	126.8	0.167
(10,7)	1.17	24.2	2.074	126.6	0.307
(14,2)	1.20	6.6	1.932	111.4	0.204
(13,4)	1.22	13.0	1.932	110.4	0.122
(12,6)	1.26	19.1	1.921	108.6	0.124
(11,8)	1.31	24.8	1.901	105.6	0.121
(10,10)	1.38	30.0	1.887	104.2	0.306

Table 4: Fitted parameters for absorbance spectrum—semiconducting SWNTs in SDS-D_2O dispersion

(n,m)	d (nm)	Φ (deg)	E_{11} (eV)	γ_{11} (meV)	A Area	E_{22} (eV)	γ_{22} (meV)	A Area
(8,1)	0.68	5.8	1.199	35.6	0.094	2.628	160.0	0.462
(7,3)	0.71	17.0	1.249	54.2	0.290	2.461	155.6	1.000
(6,5)	0.76	27.0	1.260	58.8	0.533	2.165	121.2	0.558
(9,1)	0.76	5.2	1.364	65.6	0.319	1.785	72.6	0.153
(8,3)	0.78	15.3	1.302	36.8	0.214	1.845	91.4	0.243
(10,0)	0.79	0.0	1.077	25.2	0.200	2.297	125.1	0.308
(9,2)	0.81	9.8	1.091	30.7	0.113	2.254	131.0	0.331
(7,5)	0.83	24.5	1.214	33.4	0.302	1.905	92.4	0.109
(8,4)	0.84	19.1	1.118	44.2	0.488	2.091	136.3	0.668
(11,0)	0.87	0.0	1.196	32.7	0.083	1.678	73.1	0.094
(10,2)	0.88	8.9	1.170	38.9	0.443	1.680	68.1	0.090
(7,6)	0.89	27.5	1.106	34.8	0.276	1.904	112.4	0.161
(9,4)	0.92	17.5	0.980	28.9	0.095	2.025	130.9	0.231
(11,1)	0.92	4.3	1.124	35.0	0.156	1.714	82.8	0.304
(10,3)	0.94	12.7	1.000	33.3	0.276	1.944	98.2	0.295
(8,6)	0.97	25.3	1.058	26.0	0.254	1.720	67.1	0.108
(9,5)	0.98	20.6	1.002	27.0	0.120	1.834	107.9	0.277
(12,1)	0.99	4.0	1.054	23.7	0.132	1.549	79.5	0.222
(11,3)	1.01	11.7	1.031	30.1	0.268	1.561	86.7	0.097
(8,7)	1.03	27.8	0.900	21.9	0.015	1.834	101.3	0.260
(13,0)	1.03	0.0	0.980	29.0	0.149	1.692	106.9	0.390
(12,2)	1.04	7.6	0.902	23.8	0.025	1.807	87.4	0.202
(10,5)	1.05	19.1	0.995	20.1	0.055	1.581	67.3	0.062

(n,m)	d (nm)	Φ (deg)	E_{11} (eV)	γ_{11} (meV)	A Area	E_{22} (eV)	γ_{22} (meV)	A Area
(11,4)	1.07	14.9	0.907	18.7	0.020	1.740	85.5	0.371
(9,7)	1.10	25.9	0.937	19.2	0.049	1.566	85.2	0.083
(10,6)	1.11	21.8	0.897	19.2	0.013	1.636	81.0	0.172
(14,0)	1.11	0.0	0.961	25.3	0.100	1.433	73.9	0.085
(13,2)	1.12	7.1	0.948	22.5	0.074	1.447	73.1	0.065
(12,4)	1.14	13.9	0.922	25.1	0.092	1.451	69.3	0.080
(14,1)	1.15	3.4	0.827	15.4	0.005	1.656	81.4	0.096
(9,8)	1.17	28.1	0.828	15.8	0.005	1.627	93.7	0.285
(13,3)	1.17	10.2	0.876	22.6	0.025	1.528	76.8	0.187
(11,6)	1.19	20.4	0.887	21.2	0.030	1.449	69.2	0.060
(12,5)	1.20	16.6	0.832	17.2	0.006	1.555	74.7	0.073
(15,1)	1.23	3.2	0.867	22.5	0.025	1.338	72.2	0.092
(10,8)	1.24	26.3	0.844	17.5	0.020	1.423	76.5	0.260
(11,7)	1.25	22.7	0.813	19.6	0.016	1.486	58.1	0.096
(14,3)	1.25	9.5	0.856	19.2	0.025	1.332	67.3	0.087
(13,5)	1.28	15.6	0.837	15.4	0.006	1.332	69.0	0.089

PHOTOLUMINESCENCE QUANTUM YIELDS FROM SDS-AIDED DISPERSIONS

6

Using the approach outlined in the previous chapter for measuring the PLQY of a dispersion of SWNTs, this short chapter focuses on SWNTs suspended in D_2O using a single surfactant, SDS. The effect of prolonged ultracentrifugation on the sample as a purification step is investigated.

6.1 INTRODUCTION

The two key steps in the preparation of dispersions of SWNTs showing band-gap photoluminescence by O'Connell, Smalley and co-workers [159] were high-intensity sonication and ultracentrifugation. While reasonably stable suspensions of SWNTs in surfactant solutions can be achieved using such sonication and mild centrifugation [21], the optical properties (in terms of both clarity of absorbance spectra and intensity of PL peaks) are improved through ultracentrifugation.

In order to remove all but the smallest bundles, ultracentrifugation for a number of hours is common, typically at relative centrifugal forces in excess of 100,000 g. As outlined in Section 2.2, some research has been published on the dynamics of SWNTs in solution in a centrifugal field, and the sedimentation behaviour of SWNTs has been modelled. The sedimentation of particles in an ultracentrifuge is described by the Lamm equation, the solution of which gives the concentration of each sedimenting species as a

function of solution depth in the sample tube. However in our work we do not fractionate the supernatant, meaning that the continuous gradient of particles in the supernatant thus described is destroyed, and so the results here represent a simple supernatant/sediment system.

We employ ultracentrifugation at a consistent rotor speed for a series of increasing times to investigate the difference in optical properties of the resulting supernatants of SDS-assisted dispersions of SWNTs in D_2O. Absorbance and photoluminescence spectra of the supernatant solutions are recorded. The sample with the best optical properties is examined using the methods of analysis described in the previous chapter to fit the absorbance spectrum and produce an estimate of the PLQY of numerous (n,m) species of nanotube in a SWNT-SDS-D_2O dispersion.

6.2 EXPERIMENTAL PROCEDURE

HiPCO SWNTs were dispersed in a solution of SDS-D_2O using the previously outlined method of ice-cooled sonication with a high-powered sonic tip (Sonics Vibra-Cell VCX750; 750 W, 40 % amplitude, 5 min) followed by one hour in a sonic bath (Branson) and a repeat of the sonic tip treatment. The dispersion was made with 0.11 mg SWNT and 62.5 mg SDS in 10 mL D_2O.

The absorbance curve of the SWNT dispersion produced above was recorded using a Varian Cary 6000i spectrometer (1800–200 nm using a 1 mm quartz cuvette; dual beam mode with SDS-D_2O reference; bandpass 2 nm).

Samples were centrifuged in a Beckman Coulter ultracentrifuge for 2 h, 4 h, 6 h, 8 h, 12 h, 16 h and 30 h, using a SW-55 rotor (5 ml centrifuge tube

capacity) at a rotor speed of 35,500 rpm. The top 3 cm of supernatant was decanted, approximately 3 ml. This equates to a range of RCF values from $\sim 90,000$ g to 130,000 g from surface to maximum depth of the supernatant extracted from the centrifuge tube.

Absorbance spectra were taken for each supernatant solution using the same apparatus as for the original solution, with the exception of the cuvettes which were replaced by quartz cuvettes of 10 mm optical pathlength.

PL spectra were recorded using the Edinburgh Instruments FLS-920 NIR-PL spectrometer detailed in 3.2.2, using a 2 mm fluorescence cuvette. Excitation was 540–840 nm at 4 nm intervals, with the detector range from 900–1350 nm also at 4 nm intervals.

6.3 RESULTS

The absorbance data for our centrifuged range of samples is shown in Figure 48. Given that the density of surfactant-coated SWNTs is estimated to be in the region of 1.0–1.2 g·mL^{-1}, and that of D_2O is 1.105 g·mL^{-1}, we expect a combination of rate-zonal and isopycnic centrifugation (see 3.2.4). That is, we expect those surfactant-coated SWNTs with a density less than that of D_2O to remain in suspension (reaching isopycnic equilibrium) while the more dense SWNTs sediment over time according to their density and other characteristics (rate-zonal sedimentation). Both of these processes will be affected by the diffusion of SWNT species in the solution.

From Figure 48 it appears that the rate-zonal process dominates as there is a continual decrease in absorbance at all energies, indicating a continual sedimentation of all SWNT species. We expect the SDS-coated SWNTs

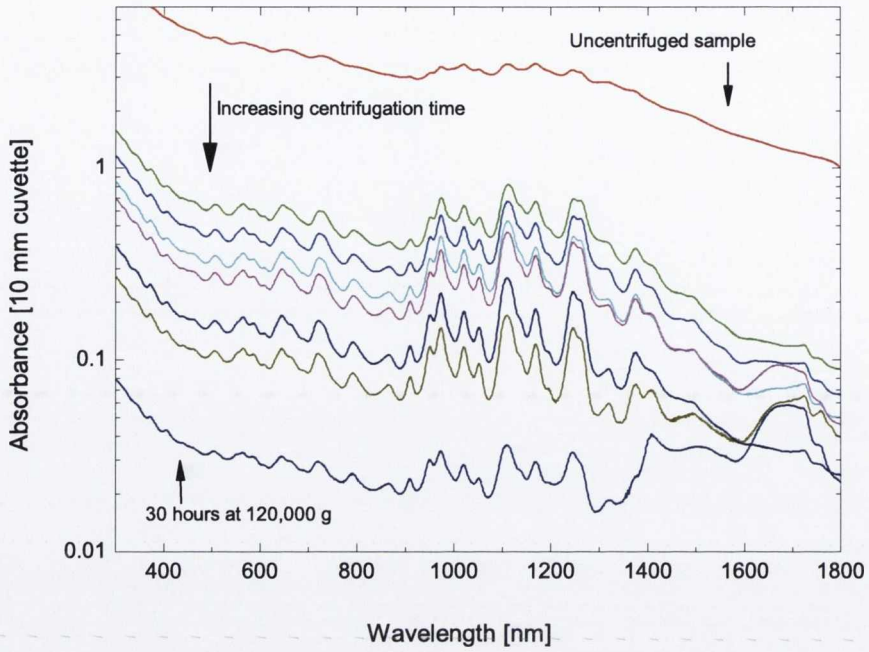

Figure 48: Absorbance curves for SDS-dispersed tubes, for a range of centrifugation times. The non-uniformity of the spectra at wavelengths greater than 1350 nm is due to the presence of water vapour absorbed by the D_2O from the air. This feature is removed prior to analysis.

to have a buoyant density close to that of D_2O, and the slow decay of absorbance suggests this is the case. Detailed analysis of sedimentation and diffusion constants are prohibited by our use of the bulk supernatant for analysis, which destroys any gradient in concentration that might have been present in the centrifuge tube.

The decrease in absorbance with increasing centrifugation time is illustrated in Figure 49, where we have shown the decay of the recorded absorbance at 100 nm intervals along the absorbance curve as a function of centrifugation time. Figure 49 shows a near-linear decay when plotted on a semi-log scale, corresponding to an exponential decay as suggested by Nicolosi *et al.* [155] with a time constant of 8–10 h for each of the sampled points.

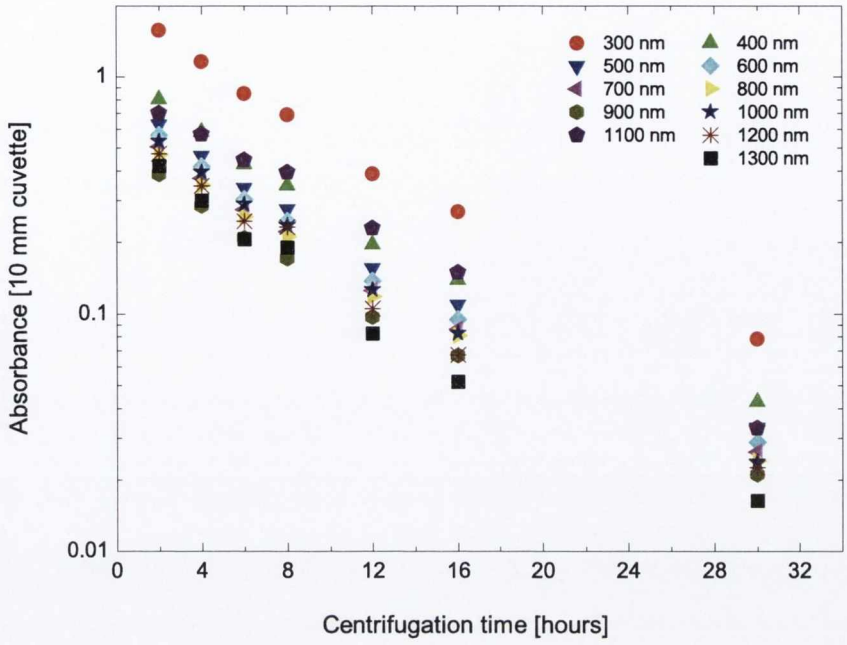

Figure 49: Decay of absorbance as function of centrifugation time for SDS-D_2O dispersions. A continuous decay is observed, without reaching a final equilibrium state.

Close inspection of the absorbance spectra reveals a change in the form of the absorbance curves, highlighted in Figure 50. Shown here are the same spectra as in Figure 48, but with their intensities normalised at 896 nm (1.384 eV), as indicated by a dot on each line. The spectra have been offset for clarity, with centrifugation time increasing from top to bottom. The increase in the relative peak heights as centrifugation time is increased from 0 h to 12 h is to be expected. As larger bundles and impurities in the as-prepared dispersion are removed, the presence of more individualised tubes will increase the relative height and resolution of the observed peaks through the removal of broadened peaks and non-resonant background absorbance. If individual tubes were to continue to be removed from solution by further centrifugation—as appears to be happening from the overall decrease in absorbance—the absorbance curve is expected to reach

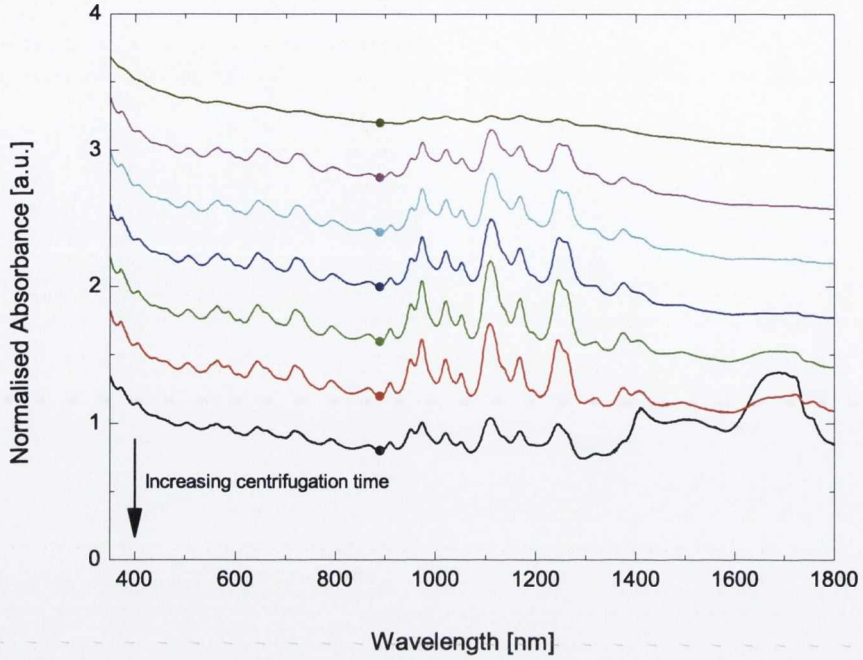

Figure 50: Absorbance curves, normalised and offset. The centrifugation times run from 2 h (top), through 4 h, 6 h, 8 h, 12 h (third from bottom), and 16 h, to 30 h (bottom).

an optimal spectrum dominated by individual tubes and at maximum resolution for the observed transitions, after which decreases in peak heights will occur according to the rates of sedimentation of the different SWNTs.

This relative peak height is plotted in Figure 51. Peak height has been measured at the energies indicated for the normalised spectra shown above, relative to the absorbance at 896 nm (1.384 eV) . A clear increase in peak height is shown for an initial increase in centrifugation time, which reaches a maximum for the samples presented here at a time of 12 h, before decreasing with further centrifugation. This degradation in peak intensity could be caused by the dominance in centrifuged samples of shorter tubes. As many of the shorter tubes may have been produced by nanotube scission during the sonication process, we can consider these

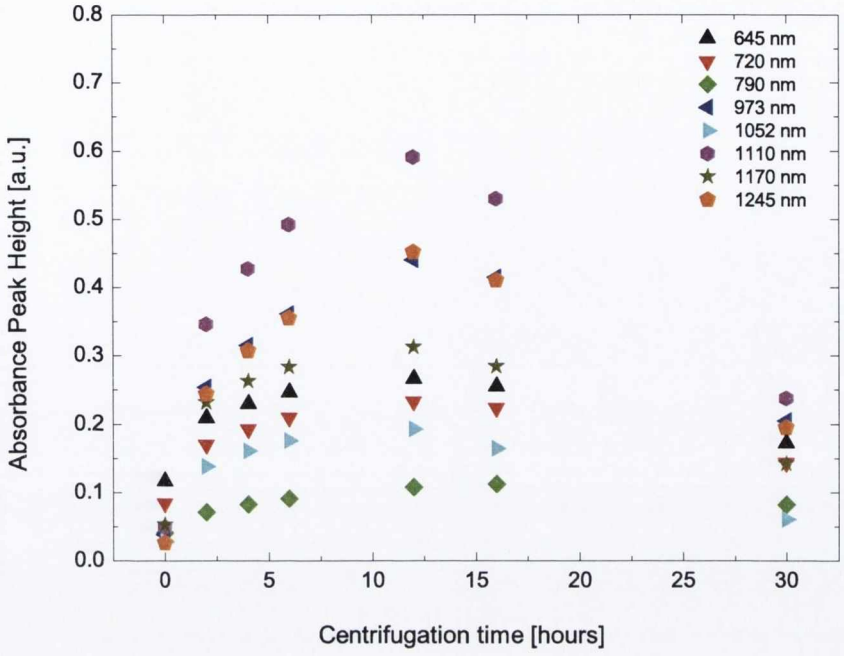

Figure 51: Relative absorbance peak heights as a function of centrifugation time for SDS-dispersed tubes. A maximum absorbance peak height is reached after approximately 12 h.

tubes to contain a higher concentration of defects, which may negatively affect the optical properties of the tubes. In terms of optimising the sample for absorbance analysis it appears that 12 h ultracentrifugation (at this particular rotor/speed combination) gives the best results.

PL and PLQY data

From our earlier work, we expect the effects of inner-filter behaviour to become apparent at solution absorbance values approaching 0.4 (measured using a 1 cm cuvette). Figure 52 shows a simple plot of emission peak intensity versus absorbance at the corresponding excitation energy. We can see that the relationship between absorbance and PL emission is not proportional across the range of samples. We suggest two reasons for this. At higher absorbances (that is, lower centrifugation times and therefore

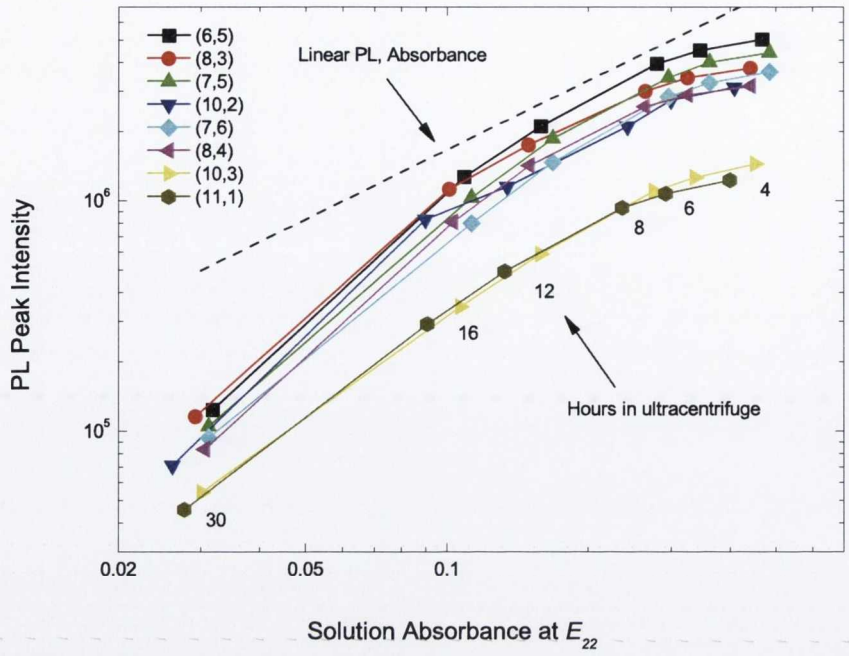

Figure 52: Intensity of PL map peaks as function of absorbance, for a range of centrifugation times. For high absorbance values, the relationship is sub-linear due to the inner-filter effects discussed in Chapter 4. At low absorbance values (for long centrifugation times) the PL emission is weaker than expected, most likely due to higher numbers of short tubes quenching the emission.

higher concentrations), we expect to find a distortion of the measured PL from the inner filter effect resulting in lower-than-expected emission. This is apparent in the graph for the samples centrifuged for 8 h or less. The solutions ultracentrifuged for 12 h, 16 h and 30 h fall below this threshold while the other solutions will require further dilution in order to make valid assessments of the PLQY values of the SWNTs involved. However, it is notable that the relationship is not strictly linear in this low-absorbance regime either. In this case, it is longer centrifugation times that produce lower-than-expected PL emission. The PL maps for these three samples which are free from inner-filter effects—the 12 h, 16 h, and 30 h samples—are shown in Figure 53. The PL maps for the 12 h and 16 h samples match

closely, while that of the 30 h sample shows a narrowing of the intensity range between the least and most intense peaks. (From an analysis of Figure 52, it would appear that the more intense peaks in the 12 h and 16 h sample appear comparatively weaker in the 30 h sample, as opposed to the weaker peaks gaining in relative intensity.)

One possible explanation for our observation that those SWNTs remaining in suspension after the longest ultracentrifugation period give suboptimal absorbance and PL spectra is that these tubes are either shorter or carry more defects. Both shortening of tubes through scission and an increase in the number of defects have been observed as a result of high-intensity sonication. Tubes with defects are liable to have enhanced exciton quenching mechanisms and thus a lower emission intensity and lower PLQY value. Short tubes are observed to have a lower PLQY value also, as the ends of tubes act like defects and short tubes thus have a higher defect-to-length ratio.

The 12 h sample is selected as having the optimal optical characteristics, showing both the highest relative absorbance peak height and strong PL emission. In order to ensure that this sample is truly below the absorbance threshold above which we can expect inner-filter and reabsorption effects, we dilute the sample and measure again the absorbance and PL emission. The relationship between absorbance at peak excitation energy and emission intensity is plotted in Figure 54, and confirms that this sample is free from such distorting effects.

The 12 h sample is analysed as per the steps outlined in the previous chapter to estimate the PLQY values of the SWNTs evident in the sample. A non-resonant background is subtracted as before, and our results are averaged over several such backgrounds as illustrated in Figure 55, while one other fit is performed favouring the identified SWNTs in order to

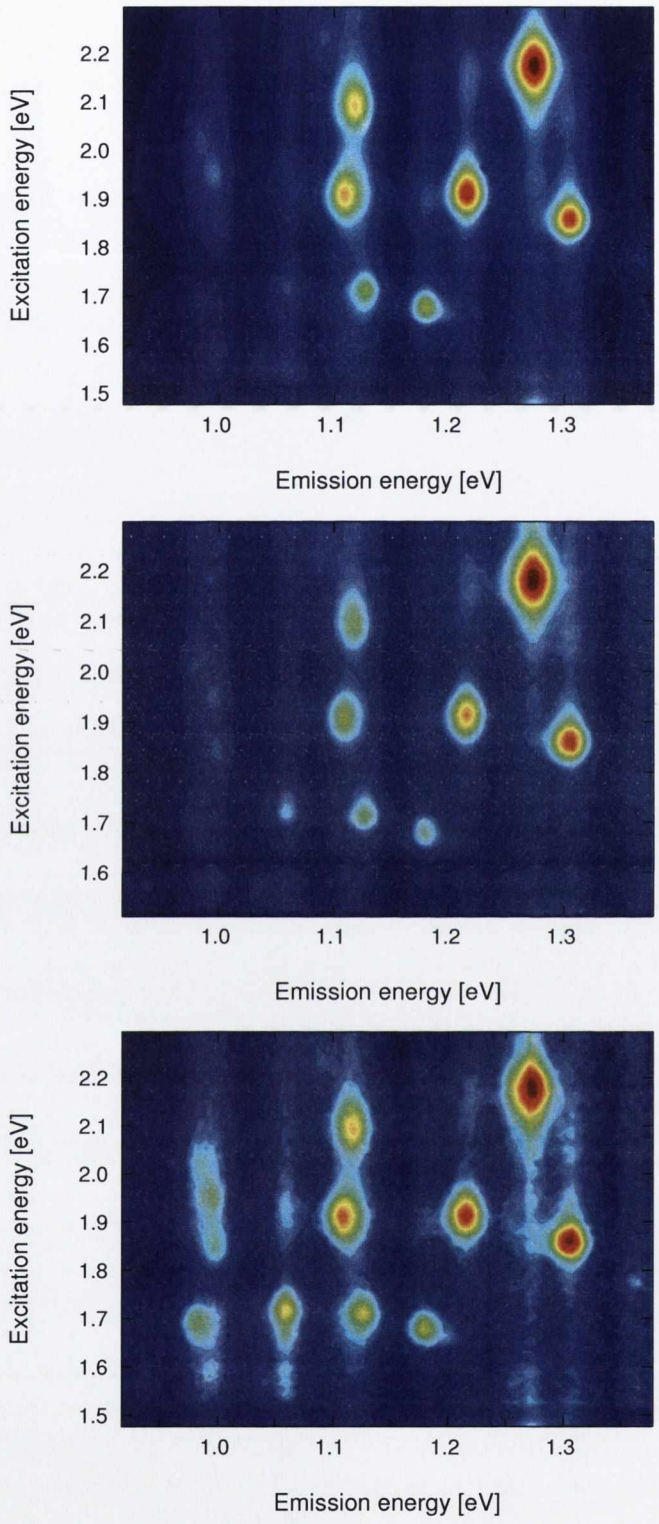

Figure 53: PL maps for SWNTs dispersed in SDS-D_2O as a function of centrifugation time, from top to bottom: 12 h, 16 h, and 30 h.

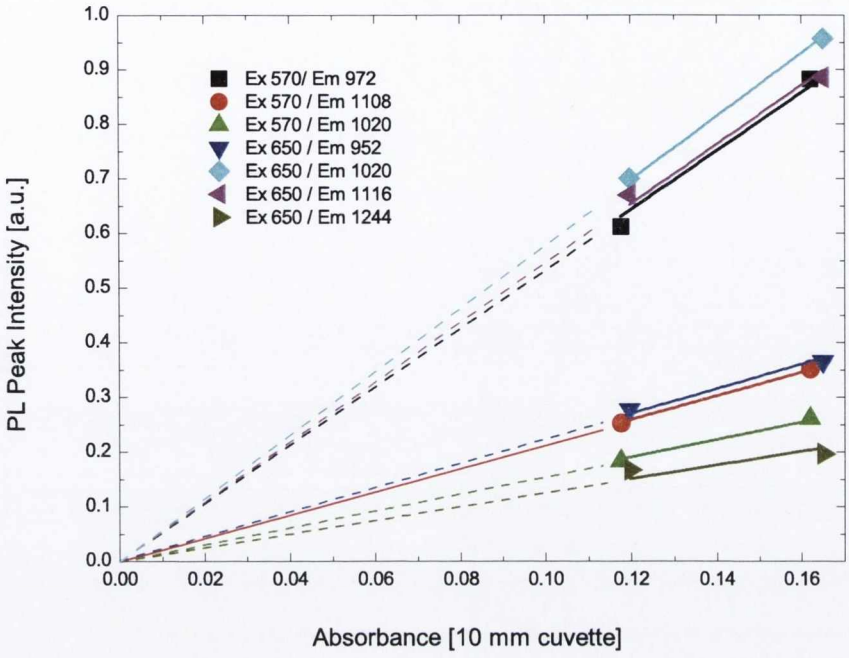

Figure 54: Linearity of PL intensity and absorbance for dilutions of sample SDS-12h. The use of a 2×2 mm microcuvette allows us to have linear PL and absorbance at concentrations exhibiting absorbance values of > 1 in 1 cm cuvettes.

estimate lower bounds for the PLQY values. The fitted absorbance and absolute error is shown in Figure 56.

PLQY values were estimated and are plotted in Figure 57. The trend noted in the previous chapter of increasing PLQY with increasing E_{11}^{S} value is again apparent, apart from the outlying behaviour of some small-diameter tubes and the high PLQY obtained from the (7, 6) nanotube. A comparison with our earlier work shows an increase in the maximum observed PL, from $\sim 0.25\,\%$ to $\sim 1\,\%$. Transition widths were comparatively unaffected, and match our previous analysis of SDS-dispersed tubes to within $\pm 10\,\%$. Given that the nanotubes used were the same for each sample, it is assumed that this difference must result from the difference in processing. There were two main differences here: one is that the initial

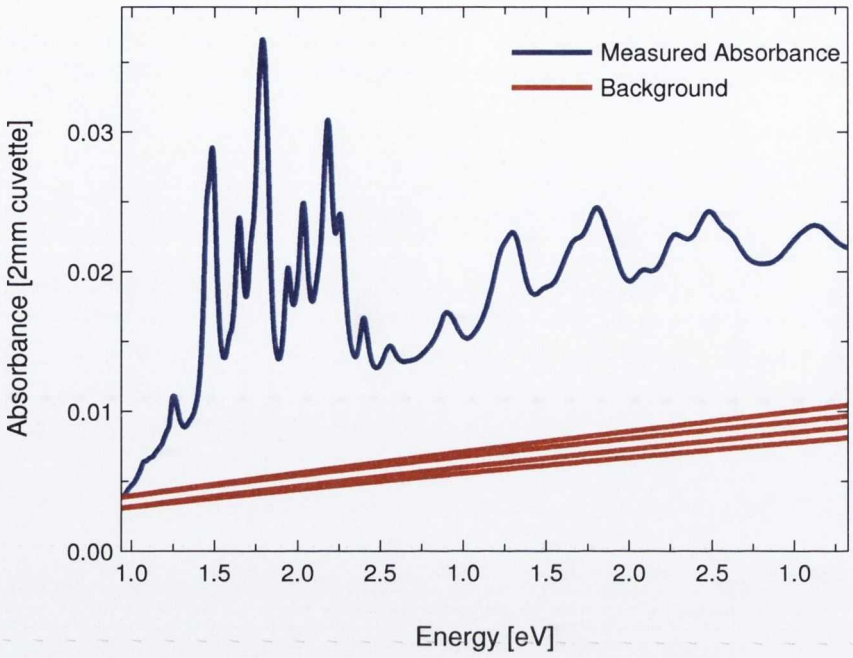

Figure 55: Absorbance spectrum of 12 h sample with multiple backgrounds. PLQY values were averaged over the results obtained using these backgrounds. The spectrum is sharper and more pronounced than the 4 h ultracentrifuged sample seen in Figure 32

concentration of tubes, without any centrifugation, was lower in the current set of samples. This means that for an equivalent amount of sonic energy from the tip, a higher proportion of bundles could be broken up leading to more individual tubes and thus a higher PLQY from the ensemble. The other factor is the centrifugation time. In this study we used increasing centrifugation times as a way of lowering the concentration, whereas in the work done to test the MATLAB program we had followed the common routine of centrifuging for 4 hr at approximately 120,000 g.

In order to examine the effect of the ultracentrifugation time on the estimated PLQY, we analysed the data for the 4 h, 8 h, and 16 h samples as well as the 12 h one which we had examined because of its sharper absorbance peaks. In this case each of the samples was diluted with stock

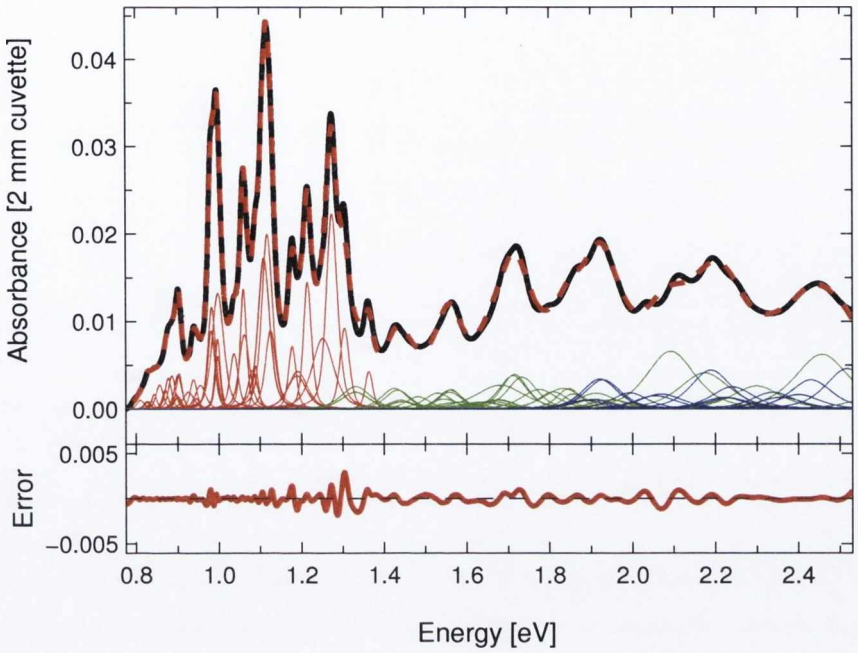

Figure 56: Fitted absorbance and residual error for SDS-SWNT-D_2O, ultracentrifuged for 12 h. The lower panel shows the residual error on the same vertical scale as the main plot.

SDS-D_2O solution until a linear relationship between absorbance and PL emission was reached. The PLQY values estimated are plotted in Figure 58 as a function of band gap, E_{11}.

From this analysis we can see that there is a clear effect of centrifugation. The 12 h solution showed among the highest PLQY values, which vindicates our choice of this sample as the one with the best optical properties, but is closely matched by the 8 h solution, both of which have PLQY values on average 100 % higher than the 4 h solution. The 16 h solution, however, had only slightly higher PLQY values than the 4 h solution on average, and several species showed lower PLQY values. The 4 h solution still displays higher average PLQY values than the previous SDS dispersion tested in Chapter 5, and so we suggest this is due to the difference in effective

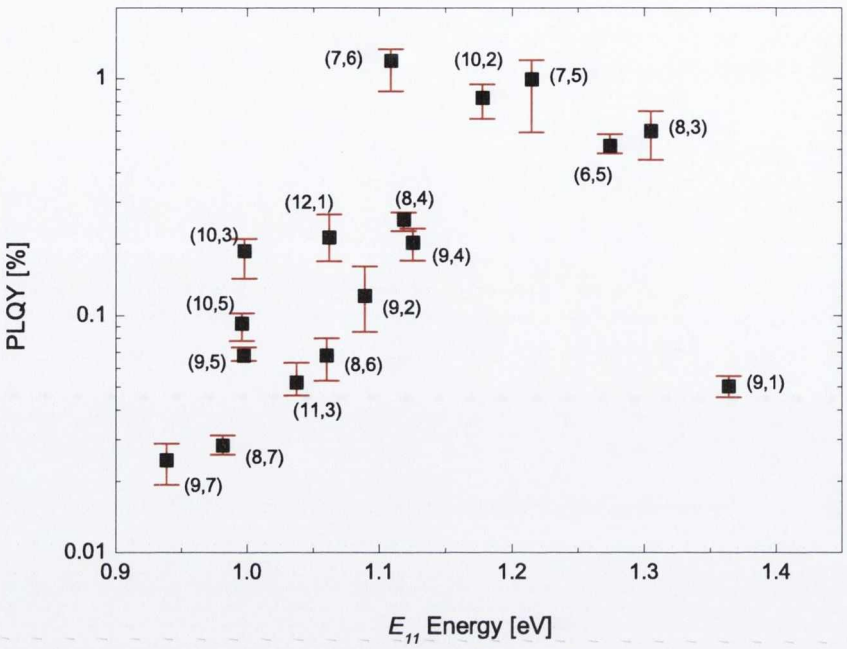

(a)

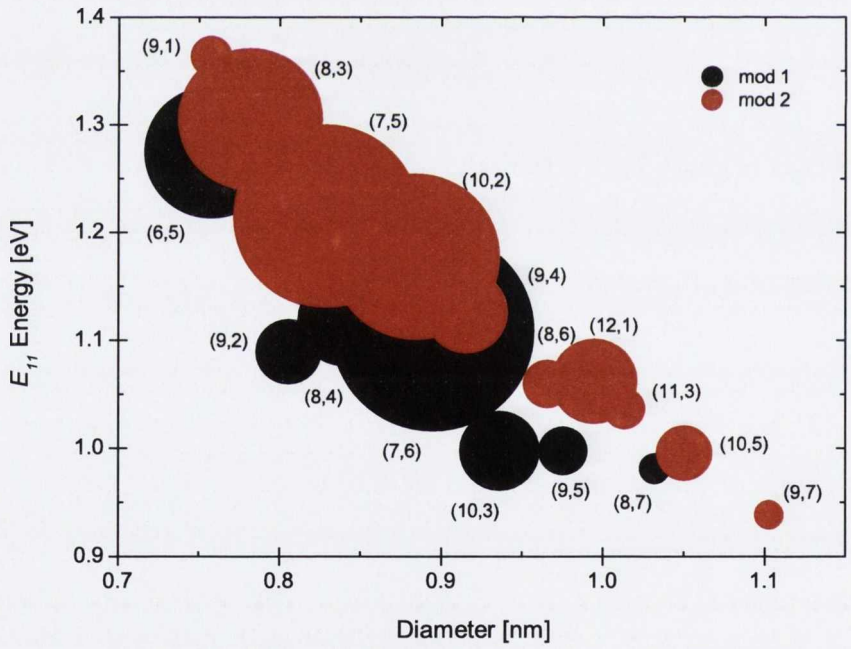

(b)

Figure 57: PLQY values for 12 h ultracentrifuged sample of SWNTs in SDS-D_2O. (a) PLQY values as a function of E_{11}, showing the increase with band gap, and (b) as a function of both wrapping angle and diameter (area of markers corresponds to PLQY value). As well as the difference in PLQY between mod 1 and mod 2 tubes discussed previously (see Figure Figure 47) we see a reduction in PLQY values for large diameter tubes.

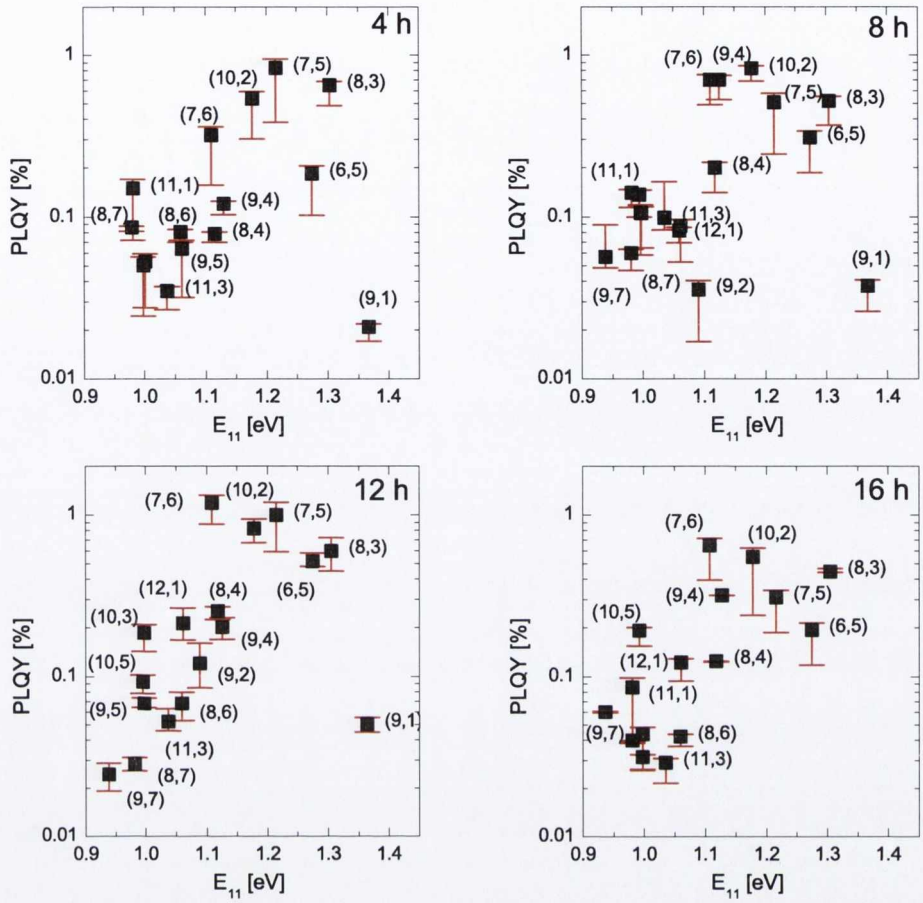

Figure 58: PLQY as a function of E_{11} energy for SDS-SWNT dispersions ultracentrifuged for 4 h, 8 h, 12 h and 16 h as indicated.

sonication energy arising from the lower original dispersion concentration used here.

We suggest that the ultracentrifugation process continues to remove small bundles of tubes, and the optimised time we describe here correlates to the highest ratio of good-quality unbundled tubes in the solution. That is, at lower centrifugation times the higher number of bundles decreases the average PLQY value while at longer centrifugation times there is a higher proportion of shorter tubes left in the supernatant, which again reduce the average PLQY as their endpoints act as defect sites for non-radiative

recombination of excitons. We aim to explore this further in future work through AFM and Raman studies.

It is notable that the highest PLQY observed was close to that reported (1.3 %) for density gradient separated tubes by Crochet *et al.* [51]. As our centrifugation does not selectively remove any particular species of tube it is possible that the remaining tubes provide outlets for energy transfer and other phenomena which reduce the overall PLQY value for the ensemble.

6.4 CONCLUSION

The PLQY of SDS-dispersed SWNTs was examined as a function of concentration, which was manipulated through the use of an extended series of ultracentrifugation times. It was found that an optimal ultracentrifugation time could be achieved, and that this was considerably higher (by a factor of 2–3) than centrifugation times commonly reported. From this optimally prepared solution we were able to estimate PLQY values for the ensemble dispersion of SWNTs that approached 1 %. This is close to the value of 1.3 % reported for density gradient separated SWNTs. It is suggested that the PLQY from a given dispersion could be optimised both through the centrifugation time and also through optimisation of the dispersion mechanism and effective sonication energy.

PLQY VALUES ESTIMATED FOR SWNTS IN DIFFERENT SURFACTANT ENVIRONMENTS

7

The routine developed over the last two chapters has been thus far applied solely to dispersions of SWNTs in SDS-D_2O solution. In this chapter dispersions created using a variety of surfactant or polymer stabilising agents are analysed. As well as PLQY values for ensemble dispersions, it is possible to compare transition energies and widths from the deconvoluted absorbance spectra.

7.1 INTRODUCTION

The analysis routine developed in Chapter 5 and Chapter 6 served several purposes. Primarily, it allowed the estimation of PLQY values for ensemble dispersions of SWNTs without the need to spectroscopically analyse the individual nanotubes, and in a relatively quick manner (although the computations performed in the MATLAB program, provided in Section A.1, could no doubt be optimised further to make the whole program faster). Also of importance in the design of the program was the standardisation of procedure and minimisation of subjective input from the analyst. As outlined in Section 2.2.5, there is little by way of accepted methodology in the measurement of PLQY values for dispersions, and several methods published so far require the researcher to choose values for transition energies, widths, or backgrounds which may bias the results from one im-

plementation to the next. In order to test the applicability of our approach to 'unseen' data recorded for similar but different measurements, we aim to use it to interpret the absorption and PL emission spectra from a further six surfactant- or polymer-aided dispersions.

In terms of the behaviour of the SWNT spectra, there are several features we expect to be of interest. The transition energies of the E_{11}^S and E_{22}^S transitions have been observed to shift on going from one surrounding medium to another, an effect termed the *solvatochromic shift*. While it has been established that this effect is related to the nanotube diameter, the value of E_{ii}^S in air, and the electronic properties of the immediate environment—the dielectric constant of the surrounding solvent or polarisation susceptibility, for example—the exact mechanism of this shift remains the subject of ongoing investigation [47]. In recording the energy values for the E_{11}^S and E_{22}^S transitions, our analysis provides us with an opportunity to test some of the proposed models for predicting the solvatochromic shift.

It has also been observed that the linewidth of individual transitions is narrower in air-suspended nanotube PL than for most emission observed from surfactant-dispersed tubes [128, 127]. As such we are interested to see the behaviour of transition widths in numerous environments, and to investigate any trends observed.

From the point of view of the program we have developed and the procedure for estimating PLQY values, it is important to verify that the custom-written MATLAB program functions from one instance to the next with only the bare minimum of input: details of expected transition energies and widths to identify PL map peaks, absorption and emission spectra, and some parameters relating to concentration and instrument functions.

Where our analytical routine functions as anticipated, it will then be possible to compare PLQY values estimated for different surfactant envi-

ronments and in the process demonstrate the feasibility of utilising our approach to investigate the optical properties of SWNT dispersions in any number of liquid-phase dispersion environments.

7.2 EXPERIMENTAL PROCEDURE

Following a similar path to the work detailed in Chapter 6, SWNTs were dispersed in four surfactant-D_2O solutions (sodium dodecylbenzenesulfonic acid (SDBS), sodium cholate (SC), polysorbate-80 or 'Tween-80' (T80), sodium taurodeoxycholate (TDOC)), and two polymer systems (flavin mononucleotide (FMN) in D_2O and poly(9,9-dioctylfluorenyl-2,7-diyl) (PFO) in toluene). SWNTs were dispersed using a combination of cooled ultrasonic tip and bath (tip: Sonics VibraCell VCX750, 750 W, 40 % amplitude, 5 min; bath: Branson 1510, frequency 42 kHz, power output 80 W, 60 min; repeat tip for 5 min). Bundles were removed using an ultracentrifuge (Beckman Coulter, rotor SW 55i, 35,500 rpm giving a relative centrifugal force of 90,000–130,000 g) for a series of timescales (2 h, 4 h, 6 h, 8 h, 12 h, 16 h, and 30 h), except for the PFO-dispersed tubes, for which much milder centrifugation was used (5,000 rpm giving $\sim$3,000 g RCF, for 5 min).

Absorbance spectra (Cary 6000i, dual beam, 1800–300 nm in a 10 mm quartz cuvette) were recorded for each solution in the centrifugation series, and by analogy with the work in SDS in the previous chapter the peak intensity of normalised absorbance spectra were examined to identify the solution with the optimal optical properties. This solution was diluted where necessary to ensure linearity between absorbance and photoluminescence intensity, and the PL excitation-emission map (Edinburgh Instru-

ments FLS 920 with liquid N_2-cooled Hamatsu 9957 photomultiplier tube detector; 2 × 2 mm fluorescence cuvette; excitation 540–820 nm, 4 nm steps, 15 nm slit widths; emission 900–1350 nm, 4 nm steps, 10 nm slit width) and corresponding absorption spectra were recorded.

Deconvolution of the absorbance spectra and estimation of PLQY values was performed using the MATLAB program outlined in Chapter 5 and provided in Section A.1. The initial transition energies and widths were as for the SDS samples (which is to say they were based on the information published in the articles and relevant supporting information in references 212 and 152, for SDS- and SDBS-encapsulated nanotubes), except in the case of the FMN-D_2O and PFO-toluene dispersions, where the size of the solvatochromic shift observed in the PL map necessitated the use of initial transition energy values based on those published by Ju *et al.* [105] for FMN-D_2O dispersions.

7.3 RESULTS AND DISCUSSION

7.3.1 *Absorbance Spectra*

Much like the results for SDS-stabilised tubes shown in Figure 48, absorption spectra showed a continual decrease over the range of centrifugation times explored. However, the rate of this decrease was not uniform. Figure 59 shows in the top panel the rate of decrease in the absorbance at the local minimum nearest 900 nm, normalised to the value recorded for the solution ultracentrifuged for 2 h, for each set of dispersions. The inset shows the absolute absorbance values of these points for the 2 h solution. This data illustrates the ability of the different stabilisation media to retain SWNTs in

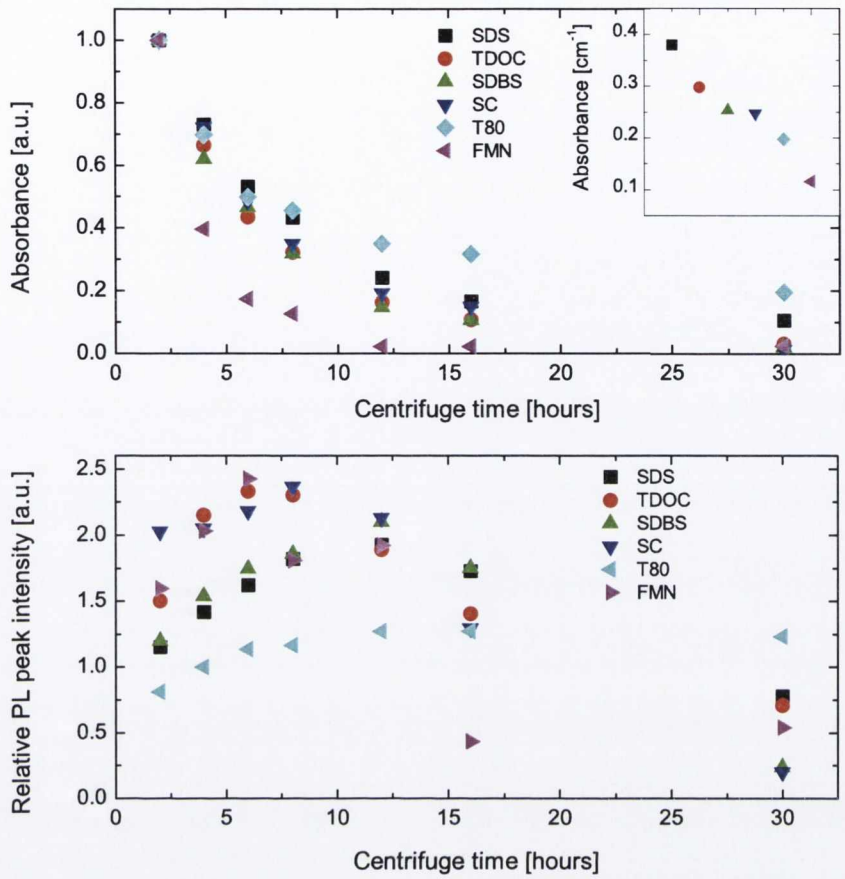

Figure 59: Absorbance and normalised absorption peak intensity as a function of centrifugation time for SWNTs stabilised with numerous surfactants and polymers. Top panel: Absorbance at local minimum near 900 nm as a function of centrifugation time. Lower panel: normalised peak intensity of local maximum near 1120 nm relative to minimum near 900 nm.

suspension under centrifugation, and we see that T80 shows the slowest rate of sedimentation of SWNTs while the FMN-stabilised dispersion is not as stable, with very little sign of any SWNTs remaining suspended after centrifugation times exceeding 8 h.

The relative intensity of peaks in the absorbance data compared to the minimum near 900 nm was investigated, and as for SDS-stabilised solutions it was found that each set of solutions—excluding PFO—showed an optimal

centrifugation time for which the relative intensity reached a maximum. This time was not uniform, and varied from 4 h for FMN-dispersed tubes to 16 h for those dispersed using Tween-80. The relative peak intensity for one representative peak (near 1120 nm) as a function of centrifugation time (cf. Figure 51) is plotted in Figure 59. The only set of dispersions for which the sample centrifuged for 30 h showed a comparable relative intensity to that of the samples centrifuged for 16 h (or less) was the T80 set, which may indicate that for this set of dispersions the suspended material sediments at an approximately uniform rate, while for the other materials there are several sedimentation (or dispersion) rates for different (n, m) species, bundles or types of bundle, leading to a change in form of the absorption spectrum over the course of the centrifugation.

No comparable data for the PFO-stabilised dispersion is available because, following the procedure outlined by Nish *et al.* [157], only a short period (5 min) of mild centrifugation was required to leave only a small amount of suspended nanotubes.

Where the optimal solution was found to be of too high a concentration (i.e. too high absorbance) to remain free of the inner filter effect it was diluted a number of times until a linear relationship between absorbance and PL was confirmed (cf. Figure 54).

Figure 60 shows the absorbance spectra for each of these optimally centrifuged solutions, normalised and offset for clarity. The samples have been diluted as necessary to provide a linear relationship between absorbance and PL emission. Two features are notable: there is a shift in absorbance peaks on going from one stabilising medium to another, and the non-resonant background in the PFO-dispersed sample has almost disappeared. The vertical dotted lines have been added to highlight the shift in energy for various peaks in the different dispersions. While this

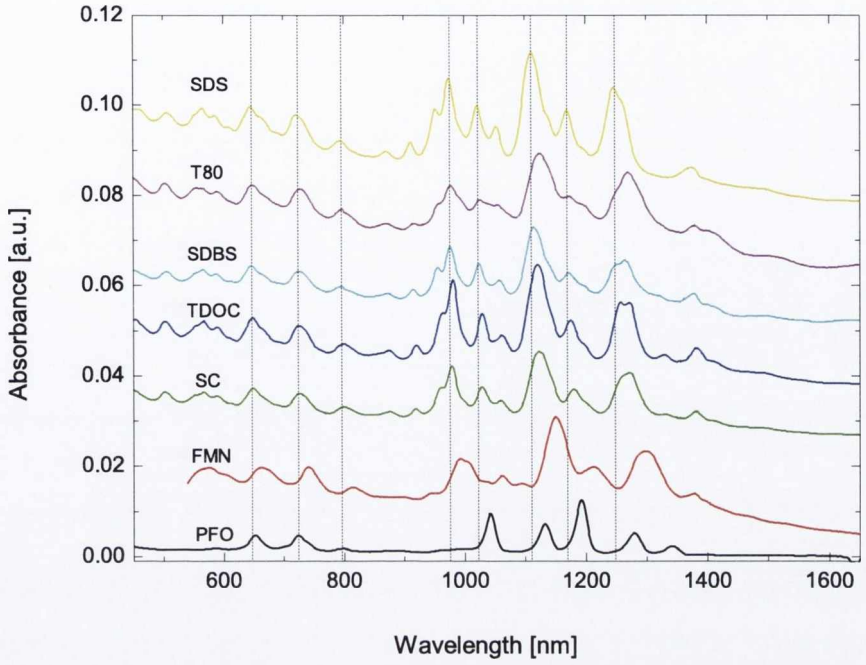

Figure 60: Absorbance spectra of various SWNT dispersions. From top to bottom: SDS, T80, SDBS, TDOC, SC, and FMN (all in D_2O) and PFO in toluene. The vertical dotted lines are a guide to the eye, highlighting the shift in various peak positions.

shifting of the absorbance peaks was to be expected and has been reported elsewhere [47] (and is dealt with further below), the apparent removal of the non-resonant background in the PFO-dispersed sample was not. In their paper dealing with the dispersion of SWNTs in aromatic polymers, Nish *et al.* [157] reported that nanotubes produced by the CoMoCAT method (supplied by Southwest Nanotech) suspended using PFO showed a similar sparse absorption spectrum with sharp peaks and very little background. However, both the CoMoCAT tubes when dispersed in SDBS and HiPCO nanotubes in both SDBS- and PFO-stabilised solutions displayed a much more 'typical' absorption behaviour with a large non-resonant background visible. Comparison of the intensity of the observed peaks also indicates a greater preference in our work for the suspension of the (7,5) tube, as

discussed below. They employed purified HiPCO nanotubes as opposed to our raw nanotubes. In other respects our preparation methods are broadly similar, including the use of mild centrifugation for a short time, and it is unclear how such differing spectra come about.

In attempting to fit the absorbance curves to their deconvoluted component spectra, this range of spectra posed challenges both due to the observed shift in peak energies and the difference in form between the spectrum of the PFO-dispersed tubes and that of any other material shown here.

The MATLAB code we have written utilises an initial set of transition energies, which may be corrected by reference to the transition energies measured from the PL map. It incorporates a small degree of flexibility: peaks in the PL map will be matched to the relevant (n, m) species if the values of E_{11} and E_{22} observed from the PL map are less than 15 meV and 40 meV, respectively, from their initial estimates. Both PFO- and FMN-stabilised solutions displayed larger shifts than this, as can be seen from both the absorbance spectra shown in Figure 60 and the PL maps shown in Figure 62. Increasing the allowed tolerance would lead to the misassignment of peaks for some species which appear close to each other on the PL map. However, the published transition energies for FMN-dispersed nanotubes given by Ju *et al.* [105] worked sufficiently well for both the FMN- and PFO-dispersed samples. In the absorbance fit, then, these energies were allowed to vary by up to 5 meV from their initial values to fit the absorbance data. Figure 61 shows the absorbance and residual fit for each of the six dispersion materials examined here. The spectra have been modified by subtraction of a background of the form $A_{bkg} = a\lambda^{-b}$, where a is chosen to match the spectra at low energies and $b = 0.7733$ as discussed in Section 5.3.

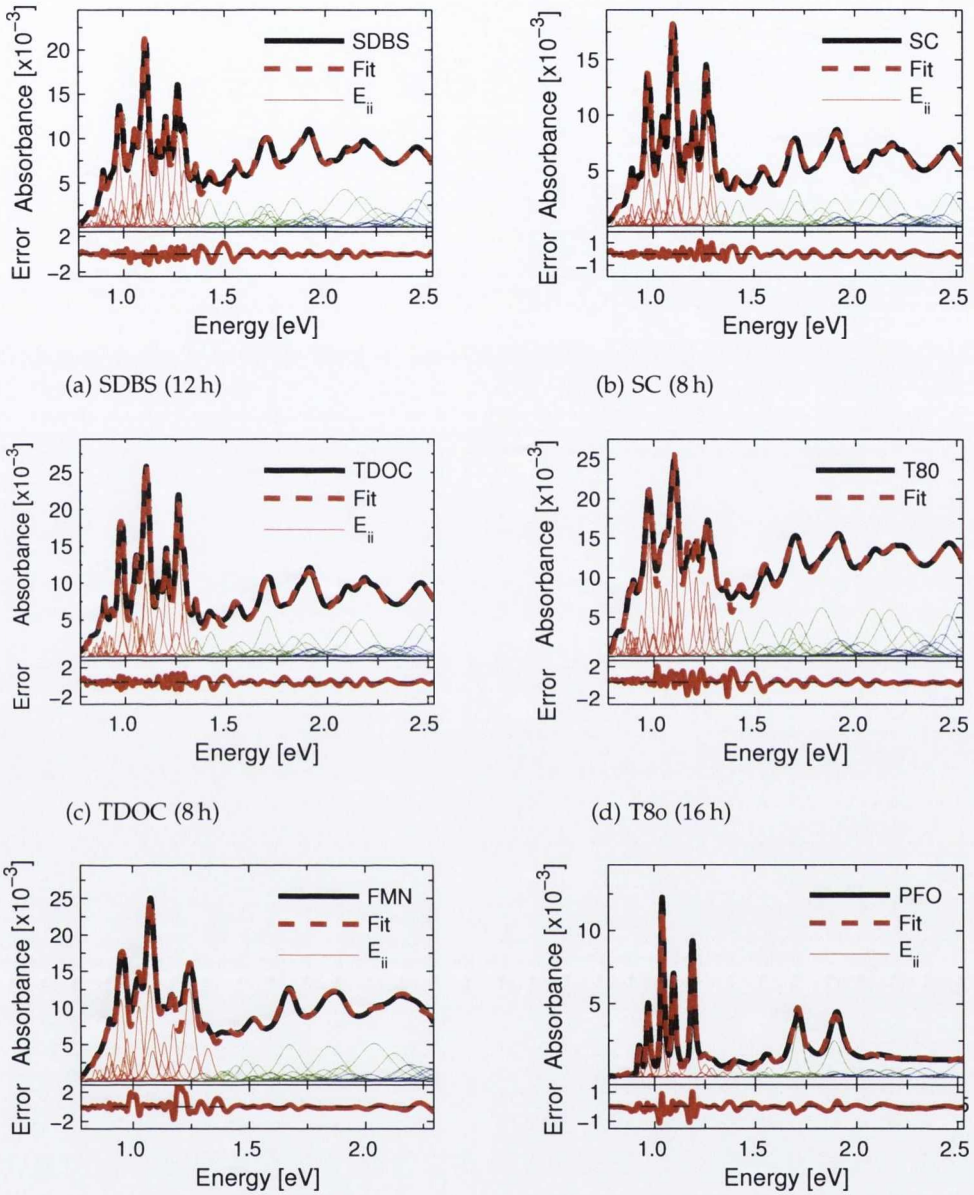

(a) SDBS (12 h)

(b) SC (8 h)

(c) TDOC (8 h)

(d) T8o (16 h)

(e) FMN (4 h)

(f) PFO (5 min)

Figure 61: Fitted absorbance data for SWNT dispersions, with the stabilising agent and time in the ultracentrifuge shown. Component transition peaks are shown as thin lines, with red corresponding to E_{11}^S, green to E_{22}^S, and blue to E_{11}^M. In each case the 'error' or residual has been plotted on a scale equal to that of the main panel.

The applicability of the code to various liquid-phase dispersions is largely verified by the quality of the fits achieved. The two cases where the fit deviates most from the measured spectrum occur in the FMN- and T80-stabilised solutions, in the regions around 1.2–1.5 eV. This appears to be related to the comparatively broad absorption spectra of these materials in this region, and the inability of the narrow component peaks present at this energy to accurately conform to this behaviour. It is notable that this region does not correspond to many prominent peaks in the PL map (see next section), and as such many of the transition widths at this energy will not have been confirmed from the PL data.

Absorbance fit widths and areas

The initial expected widths for both E_{11}^S and E_{22}^S transitions are based on those published by Ju *et al.* [105] for SWNTs dispersed in SDBS and in FMN. The FMN-dispersed tubes were reported to show a larger linewidth than those dispersed in SDBS. After the absorbance curves illustrated above have been fitted, we are able to examine the transition widths and see how they vary from one environment to the next. The average widths (using 12–15 tubes for each sample other than PFO, for which we use 5) for both E_{11}^S and E_{22}^S transitions are given in Table 6.

7.3.2 *PL Data and PLQY values*

PL excitation-emission maps

Illustrated in Figure 62 are the PL excitation-emission maps for the sample from each set of dispersions identified in the last section for its optimised absorbance spectra (and diluted where necessary). The range of the maps

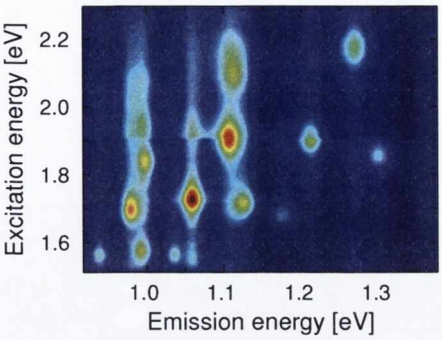

(a) SDBS (max 590,000 cps)

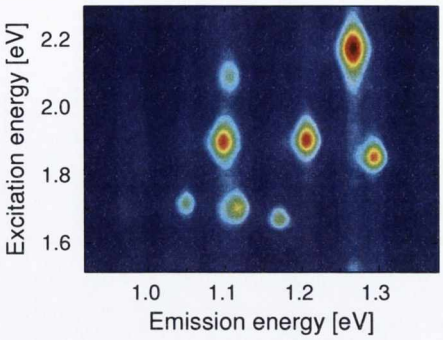

(b) SC (max 169,000 cps)

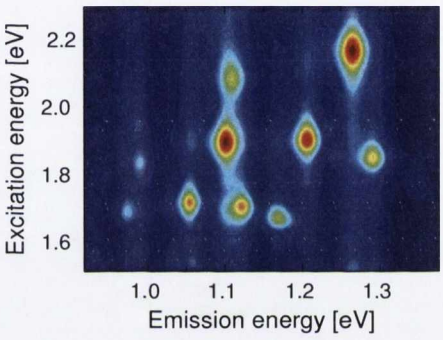

(c) TDOC (max 554,000 cps)

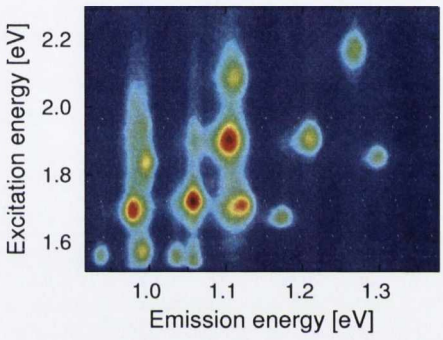

(d) T8o (max 114,000 cps)

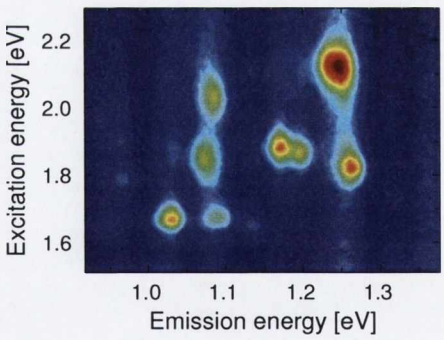

(e) FMN (max 80,000 cps)

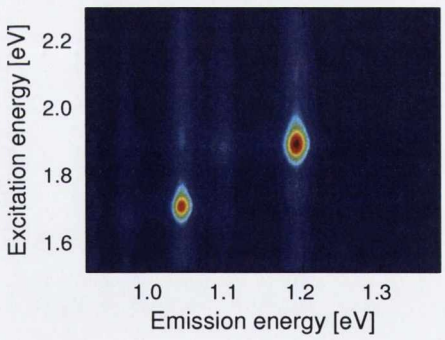

(f) PFO (max 305,000 cps)

Figure 62: PL excitation-emission maps for various surfactant and polymer dispersions. The maximum intensity is given for each map.

Table 6: Average fitted transition widths by stabilising agent

STABILISING AGENT	γ_{11} (meV)	γ_{22} (meV)
SDS	27.2	88.9
SDBS	28.8	95.8
SC	30.2	88.3
TDOC	28.3	87.0
T80	29.0	98.8
FMN	34.5	110.7
PFO	22.3	71.0

in terms of excitation and emission energies is identical, while the false colour height scale is normalised relative to the maximum peak height in each map. These maxima are given in the figure captions.

As in the absorption data, two notable features are the shifts in energy of some transitions in different media and the intriguing results from the PFO dispersion. Again comparing the PFO results to that published by Nish [157], we find that our results show features identified with both the CoMoCAT and HiPCO samples in PFO: where Nish reports the (8, 6) emission to be by far the most intense for HiPCO-PFO dispersions, with much weaker PL from other species, and reports the (7, 5) emission to be similarly prominent in CoMoCAT-PFO dispersions, we find that the (7, 5) peak is the most intense, closely followed by the (8, 6) peak. The general selectivity of PFO towards tubes of high wrapping angle is thus confirmed,

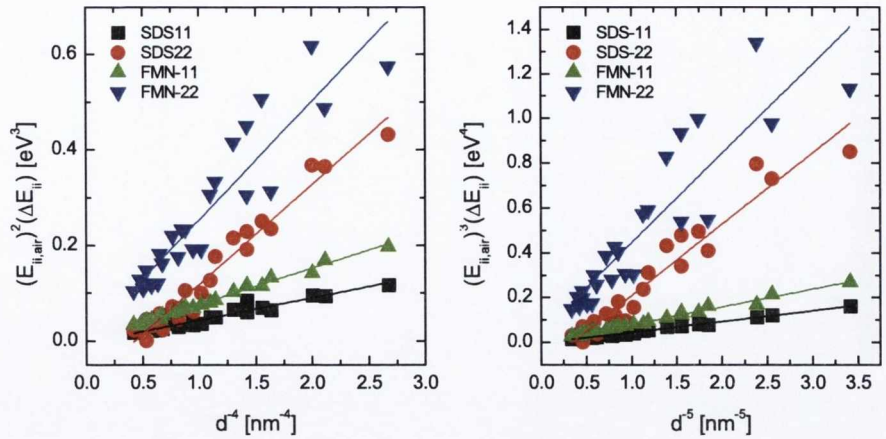

Figure 63: Solvatochromic shifts observed in the PL map, modelled as per the proposals of Choi (left) and Silvera-Batista (right).

although the details in terms of relative emission strength for our sample are somewhat surprising.

These discrepancies for our PFO-based results and those offered by Nish [157] are most likely based on batch differences between the nanotube samples. Our raw HiPCO samples thus provide a similar low-background absorbance to that obtained by Nish with CoMoCAT tubes, while his use of purified HiPCO tubes leads to the more typical nanotube absorbance background. Similarly, the relative abundances of the (8,6) and (7,5) tubes from one sample to another may explain the change in absolute emission intensity observed.

A clear shift in the transition energies is apparent, particularly for the PFO- and FMN-dispersed samples, as was noted in the absorbance spectra. This solvatochromic shift, ΔE_{ii}^S, has been modelled by Choi and Strano [47] for both ΔE_{11}^S and ΔE_{22}^S, and more recently by Silvera-Batista and co-workers [188] for ΔE_{11}^S.

While having no net dipole moment, SWNTs are highly polarizable, particularly along their long axis. In solution, there is a reaction field

formed by the effect of the SWNT on the solvent and the effect of the solvent on the SWNT, as the solvent molecules relax around and stabilise the SWNT. This reaction field is small for the SWNT in its ground state, but is much larger when the SWNT is in a photoexcited state with a resultant large dipole, forcing the solvent to rearrange to solvate the dipole and causing a difference in the solvation energy between the SWNT in its ground and excited states. This is then evidenced as a characteristic shift in the emission or absorption energies in different solvents, i.e. the solvatochromic shift.

Models of solvatochromic shift therefore involve the polarizability of the SWNT, α_{ii}. Its functional form is not precisely known, though it is generally taken to depend on the SWNT diameter d and band gap E_{ii}. (Several theoretical studies, each predicting a different relationship between α_{ii}, R and E_{ii} are summarised in the paper by Choi and Strano [47].) Also utilised to model the solvatochromic shift are the Onsager polarity functions, $f(\varepsilon,\eta) = [2(\varepsilon-1)/(2\varepsilon+1) - 2(\eta^2-1)/(2\eta^2+1)]$, involving the dielectric constant of the solvent medium, ε, and the refractive index η. Silvera-Batista and co-workers note that the PL intensity is dependent on ε, varying approximately as a function of $\varepsilon^{-0.5}$, while the solvatochromic shift can separately be linearly related to $f(\eta^2)$, to d^{-1}, and to ε.

Both models propose a relationship between ΔE_{ii} and d, and have been applied to our data for SDS (with a small solvatochromic shift) and FMN (large shift) in Figure 63. Most of the other surfactants have a similar shift to that found with SDS and are not shown. The formulation proposed by Choi,

$$\Delta E_{ii} \cdot E_{ii_{air}}^2 \propto d^{-4}$$

where ΔE_{ii} is the solvatochromic shift relative to the transition energy observed in air or a medium of dielectric constant $\epsilon \sim 1$, $E_{ii_{air}}$, and d is the nanotube diameter, holds well for the SDS-dispersed tubes. However, it does not accurately reflect the behaviour of the FMN-dispersed tubes for E_{22}. Although large, the solvatochromic shifts observed in FMN were not unexpected: our data matches that published by Ju *et al.* [105] for FMN dispersed SWNTs. The right-hand panel of Figure 63 shows the application of the model proposed by Silvera-Batista,

$$\Delta E_{11} \cdot E^3_{11_{air}} \propto d^{-5}$$

to the same data. (We have taken the liberty of applying the same form of equation to E_{22} also). Clearly the E_{22} data for FMN is not fully described by either of these models, and R^2 values for Choi and Silvera-Batista's models are 0.85 and 0.80, respectively.

The ability to modify the expected transition energies for the full set of SWNTs which we use to fit the absorption and PL data, based on the observation of the transition energies of a few species in the PL map and the use of a model like that proposed by Choi and Silvera-Batista, would significantly increase the applicability of our methodology to a wider range of potential dispersions. However, given the inability of both models to predict the behaviour of the transitions for FMN, as measured by us directly and verified against the energies published by Ju *et al.*, for this work we do not employ any such model and simply use those published values which most suit the dispersion in question. As long as the expected positions of the transition energies in a given environment are reasonably well known the automated MATLAB code will be able to proceed and analyse the data without any issues.

PLQY values

Previously in Chapter 5 we demonstrated the ability of our MATLAB code to estimate PLQY values for a SDS-stabilised dispersion of SWNTs, and showed in Chapter 6 that an appropriate level of ultracentrifugation could increase these PLQY values. In this chapter we have identified the 'optimal' solution in the same way as for the SDS dispersions, and can now compare PLQY values across the range of dispersions prepared here.

Since the sample dispersions to be analysed have been diluted, where necessary, to a level below that at which the inner-filter effect would cause interference, the absorption spectra for all samples (except PFO) are broadly similar in intensity, and a first approximation to the PLQY value can be made by comparing the maximum intensities for PL emission reported in Figure 62: SDBS and TDOC are expected to provide the highest PLQY values.

In the same manner as previously outlined, we perform the PLQY analysis multiple times with varying backgrounds in order to gain some insight into the sensitivity of our results to these small perturbations in what is an ill-defined background absorbance. Also, as before, one round of analysis was performed which strongly favoured semiconducting to metallic species in the absorbance fit, which should produce a lower PLQY value and indicate the sensitivity of the fit to the presence of metallic tubes, which are of course difficult to fit accurately due to their absence from the PL map.

AFM analysis (as outlined in 3.2.3) was carried out on three of the samples only as a result of time constraints, yielding values for mass fractions of individual tubes of 0.31, 0.35 and 0.42 for solutions stabilised with FMN, SDS and SC respectively. For other samples, an average value

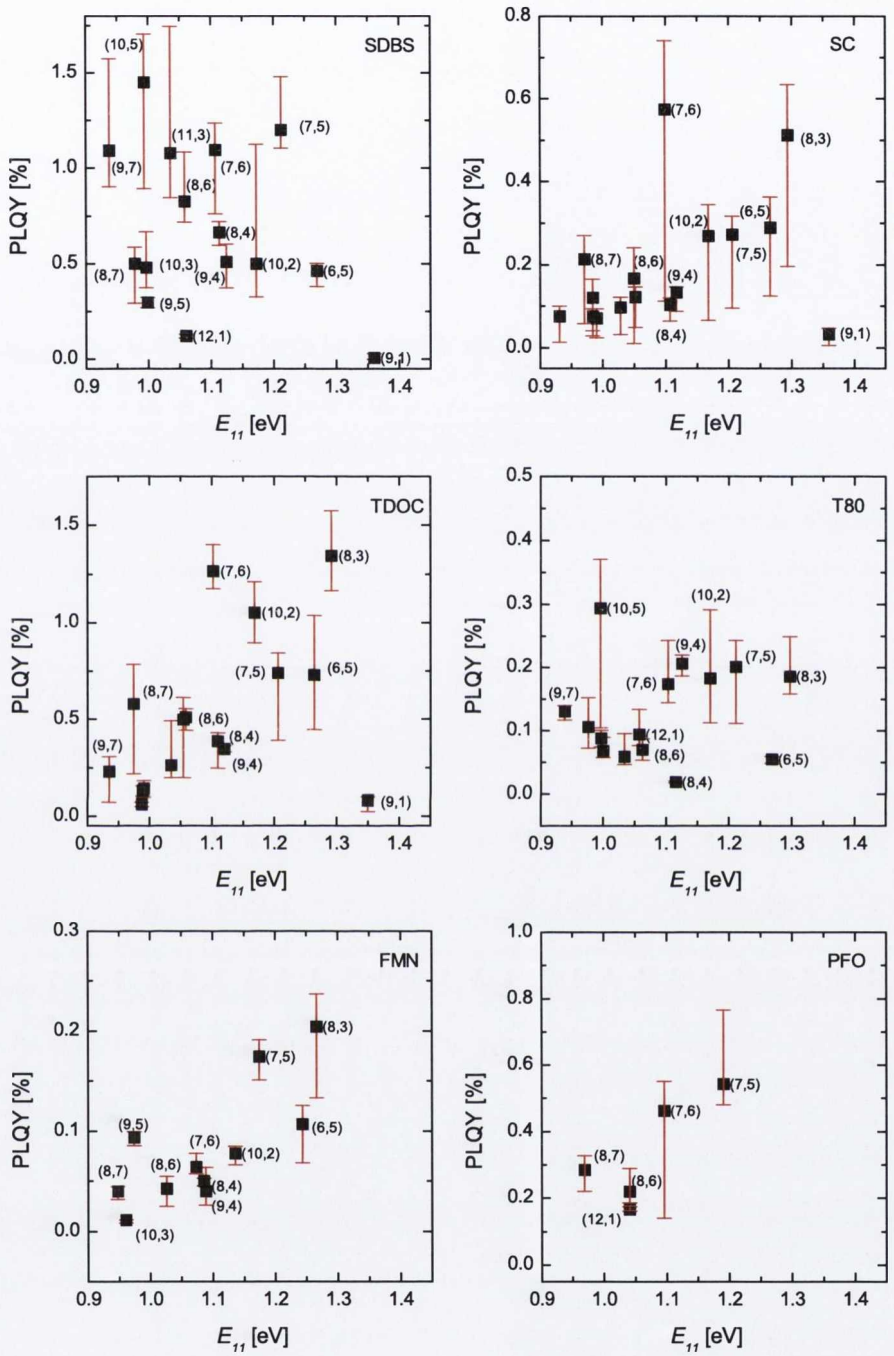

Figure 64: PLQY values for individual species of carbon nanotube in ensemble dispersions, using surfactants and polymers as indicated.

of 0.36 was employed. The full AFM analysis may be applied as part of future work.

PLQY values for the six dispersions prepared are shown in graphical form in Figure 64. We note that a number of (n, m) species, in particular the $(7,6)$, $(10,2)$, $(8,3)$ and $(7,5)$ tubes, consistently display the highest PLQY values in each ensemble. The trend observed previously of PLQY values generally increasing with increasing value of E_{11} is seen to hold loosely, with as before a tendency for small diameter tubes such as the $(9,1)$ and $(6,5)$ tubes to display lower PLQY values than might be expected. This is in line with the behaviour proposed by Tsyboulski *et al.* [204], although their work deals with the 'photoluminescence action cross section', i.e. the product of absorbance and PLQY, for individual tubes, and so their results are not directly comparable here.

PLQY values vary by close to an order of magnitude between dispersions, which is most likely due to a combination of the different wrapping conformations of the various stabilising agents and their ability to exclude oxygen, water and other molecules from the nanotube surface, where they would otherwise interact and cause the recombination of excitons, and the dispersion stability and the efficiency of the stabilising agent in producing individual, dispersed nanotubes. SDBS and TDOC produce the highest PLQY values, with the SDBS also displaying the highest average PLQY value for large diameter tubes.

The results for FMN-dispersed tubes, with the highest results in the range 0.001–0.002, can be compared with the results of Ju *et al.* [104], showing PLQY values for FMN-D_2O dispersed SWNTs of 0.8 %. However, the use of Styryl-13 as a fluorescence standard has been questioned [194], suggesting that these results are over-estimated by a factor or approximately 5.5. The highest results reported by Ju were for SWNTs dispersed in toluene using

a derivative of FMN, giving nominal PLQY values of 0.2. Even with the downward correction for the fluorescence standard, this would indicate a PLQY in the region of 0.04, which is still relatively high for ensemble dispersions but seems within reason. The explanation given by Ju *et al.* for this good performance is the exclusion of oxygen molecules from the surface of the nanotube by tight conformational arrangement of the molecule on the nanotube surface.

These observed PLQY values given here, of the order of 0.01, are among the higher values reported for ensemble dispersions of surfactant dispersions, and comparable to those PLQY values of approximately 0.013 recorded by Crochet *et al.* [51] for the brightest samples in a density-gradient separated dispersion (which was also subjected to 12 h in an ultracentrifuge at a similar RCF).

7.4 CONCLUSION

We have taken our program for analysing absorption and emission spectra and applied it to several dispersion environments, consisting of polymer- and surfactant-wrapped nanotubes in toluene and in D_2O. Given appropriate expected values for transition energies, which need to pay some regard to expected solvatochromic shifts on going from one medium to the next, we were able to deconvolute absorbance and PL emission spectra and hence estimate the PLQY of more than ten distinct (n, m) species in the dispersion.

Our estimates for the PLQY of various species approached 1.5 % in the highest case, though it is clear that the local environment plays a large part in determining the PLQY value and given a particularly suitable dispersing

agent this value could be surpassed. Our results are in good agreement with other studies of both ensembles and individual studies, which have suggested a PLQY value of between 0.01 and 0.1.

CONCLUSIONS AND FURTHER WORK

8

A review of the results presented in this thesis is given, along with a discussion outlining future work which would complement the experiments already undertaken.

8.1 CONCLUSIONS

This thesis aimed to estimate the photoluminescence quantum yield (PLQY) of ensemble dispersions of SWNTs through the analysis of absorbance and PL emission spectra.

Due to the high extinction coefficient ($> 30\,\mathrm{mL \cdot mg^{-1} \cdot cm^{-1}}$) of carbon nanotube solutions and their propensity to aggregate into bundles, it was necessary to examine the influence of these two characteristics on measured PL spectra. A model polymer, PFO, was chosen for use in a polymer/solvent system because of its well-known aggregation behaviour, observable via the appearance of a secondary peak in the absorbance at 435 nm.

PFO in toluene was investigated and showed very little sign of aggregation. The absorbance and PL emission characteristics of a range of samples varying in concentration were examined, from high concentration with obvious inner-filter effects down to low concentrations where the absorbance and PL emission were linear. The inner-filter effect, which typically affects recorded PL emission from solutions when the absorbance increases above

approximately 0.1 (as measured in a 1 cm cuvette), was modelled using our particular experimental set-up and used to predict the observed PL intensity recorded over our range of concentrations. The model was able to accurately predict the behaviour of the PL up to an absorbance value of approximately 10, maintaining an accuracy of $\pm 10\,\%$ when an appropriate micro-cuvette was used.

A change of solvents allowed us to alter the solubility of PFO, and again model the predicted PL emission. The degree of solubility related directly to the Hildebrand solubility parameters of the solvent, with solvents having such parameters in the range 18–19 $\mathrm{MPa}^{1/2}$ producing good dispersions as measured by the relative heights of the main absorbance peak and the secondary β-phase one. It was found that the model failed to accurately predict the emission behaviour when the degree of aggregation of PFO was increased, with the accuracy of the prediction failing to maintain 20 % accuracy at concentrations as low as $0.03\,\mathrm{mg{\cdot}mL^{-1}}$. We suggest that the primary cause of the discrepancy is the increase in energy transfer between the soluble and aggregate-phase PFO, due to the overlap of emission and absorbance spectra for the two material phases respectively.

Our model could thus be applied to solutions of absorbance less than ~ 10 (in a 1 cm cuvette) and used to distinguish between non-linear behaviour of PL with concentration caused by inner-filter effects and those caused by aggregation.

Satisfied that the PL emission observed from SWNT dispersions would be free from inner-filter effects (if the concentration was low enough) or could readily be corrected, the absorbance and photoluminescence spectra of a sample of SWNTs dispersed in D_2O were examined in detail. The SWNTs were dispersed using high power sonication and ultracentrifuged for 4 hrs at an average of 120,000 g to remove large bundles. The absorbance

spectrum was fitted using a modified version of a fitting routine published elsewhere, which was adapted to incorporate data from the PL map itself and to provide a fit with more independent flexibility regarding parameters such as width and amplitude of component peaks. A similar approach allowed the fitting of the PL emission map and thus the correlation of PL with absorbance for several species of SWNT simultaneously. Linear relationships between the deconvoluted component absorbance peaks and integrated PL emission were plotted, and we were able to investigate more than ten species of SWNT in one sample. Such an approach has not been shown elsewhere in the literature.

PLQY values were estimated by comparison with a study of rhodamine 6G and rhodamine B. PLQY values for the SDS-SWNT dispersion were found to vary up to $\sim 0.25\,\%$, with the (7,6) tube showing the highest value. The discrepancy between this and other comparatively high values reported for individual SWNT studies was ascribed to the difference in approach, with single-nanotube studies focusing on the brighter tubes while the ensemble displays the average PLQY, including contributions from short or defective with relatively low values. The PLQY values of the different (n,m) species were observed to increase with band gap energy E_{11}, except for some low diameter tubes. It is suggested that compared to published models, this failure of low-diameter tubes to observe the trend of increasing PLQY is the result of defects.

A further range of SDS-SWNT dispersions was prepared and tested, with different amounts of ultracentrifugation. Examination of the absorbance spectra showed a continual decrease in measured absorbance over all time scales up to 30 h ultracentrifugation. In contrast to the work of Ohmori *et al.* [160], analysis of the difference spectra did not reveal a consistent absorbance spectrum of the sedimenting material, and the shape and

intensity of the absorbance peaks were observed to change over time. The sample providing the sharpest peaks was then further investigated. It was found that higher PLQY values of close to 1.0 % could be achieved with optimised preparation, in terms of both effective sonication energy and ultracentrifugation time.

To test the applicability of our method of analysis to other liquid-phase environments, a number of SWNT dispersions were produced in a variety of surfactants and polymer stabilising agents. The difficulty of the solvatochromic shift observed was overcome through the use of published data for SWNT transition energies in various media; the possibility of modelling the observed shift to predict other transition energies was explored but no suitable model was found.

In the various dispersions tested, the PLQY recorded for most (n, m) species varied by up to an order of magnitude. This was related to both the varying efficiency of the dispersant and its ability to promote individualised nanotubes and also the different abilities to exclude interactions with the solvent, which might cause a quenching of photoluminescence.

We have been able to design a robust method for analysing SWNT absorption and PL emission data, and having investigated numerous issues regarding the accurate measurement of PL emission from nanotubes were apply this method to a variety of liquid-phase SWNT dispersions. It is hoped this will help both to generate a standardised approach to measuring nanotube PLQY values and also allow more research on the photophysics of SWNTs in ensemble dispersions.

8.2 OUTLOOK

The higher PLQY values reported here, on the order of 0.01, are in line with the highest values reported for ensemble dispersions of SWNTs outlined in the review of current literature. It is quite likely that improvements in the dispersion quality can increase this value towards 0.1, closer to the PLQY values shown for individual nanotubes. However, the presence of defects combined with the high exciton mobility will remain a source of non-radiative relaxation pathways, and in order for higher PLQY values to be achieved reductions in the defect population and an increase in the length of SWNTs (as endpoints act as defect sites) will be very beneficial. The idea of reducing the exciton diffusion mobility is also a possibility, though this may be counter-productive where possible applications such as sensors require the SWNT fluorescence to be quenched by an interaction anywhere along its length.

Such sensing applications may be the most important application of SWNT fluorescence, given the seemingly low intrinsic PLQY value but high sensitivity to environmental effects. Particularly, the NIR emission range of SWNTs makes them compatible with biological assays, as the emission to pass through tissue unimpeded. There are issues of toxicology remaining to be investigated before any biological applications are improved but the size and sensitivity of SWNTs makes them good candidates for future uses in this area.

For optoelectronic applications, it appears unlikely that sufficiently high PLQY values can be achieved (taking into account the necessary steps to isolate and separate tubes) in order to make SWNTs a commercially successful material, though research will no doubt continue towards specialist

applications for SWNTs and as a model system for other nanowire and nanotube devices.

8.3 FURTHER WORK

Our method of analysis lends itself to any liquid-phase dispersion of SWNTs where the transition energies of the suspended nanotubes are well known.

Combining our studies of the effect of centrifugation time on the PLQY values of SWNTs with those of inner-filter effects, it may be possible to estimate PLQY values for a range of (n,m) species in a dispersion as the concentration changes, to highlight any favourable bundling dynamics or concentrations.

The improved deconvolution of absorbance spectra presented here could be used to monitor populations of individual species in a variety of situations, for example comparing the number of SWNTs of each species suspended by different media, or the change in population as the sample undergoes a physical process or chemical reaction.

As well as a more detailed analysis of the concentration dependence in a single environment, we intend to examine this behaviour across a range of dispersing media. 'Selectivity' of dispersants and their ability to actively disperse certain species of SWNTs more than other species has been reported, but an analysis of the PLQY would be beneficial to highlight cases where selective quenching of emission competes with selective dispersion to change the intensity of emitted PL.

The MATLAB program written for this analysis could be modified to include some information based on the solvatochromic shifts of the peaks

in the PL map on going from one surfactant or solvent environment to another. Currently the transition energies must be supplied and must be close to those energies observed in the PL map for the program to function properly. Additionally, only those peaks identified in the map have their corresponding tubes' transition data updated to reflect what is observed in the PL map, while a calculation employing some semi-empirical solvatochromic shift could alter the transition energies and, if necessary, widths of the full SWNT population range, not just those observed in the PL map.

APPENDIX

A.1 MATLAB PROGRAM FOR ESTIMATING PLQY VALUES

MATLAB code for estimation of Photoluminescence Quantum Yields:

APLQY.m

```
function APLQY

%%%%%%%%%%%%%%%%%%%%%%%%%%%%%%%%%%%%%%%%%%%%%%%%%%%%%%%%%%%%%%%%%%%%%%%%%%%%
% A program designed to deconvolute the absorbance (A) and
% photoluminescence (PL) data for suspensions of single-walled carbon
% nanotubes and return estimates for their PLQY values by comparison
% with a standard reference material

% Written by the Coleman group at Trinity College Dublin.  The
% deconvolution of absorbance spectra builds on work published by the
% Strano group: Nair et al, Analytical Chemistry 78 (2006), 7689-7696

% Please feel free to expand and improve upon this work, giving fair
% attribution for any use.
%%%%%%%%%%%%%%%%%%%%%%%%%%%%%%%%%%%%%%%%%%%%%%%%%%%%%%%%%%%%%%%%%%%%%%%%%%%%

close all
clear all

global sub lsub ssc sm snt Outfile WL WU WU1 hc AU AL DetL DetL1 ...
DetE DetE1 DetSkip DetLamda ExcL ExcE ExcSkip ExcLamda AbsL AbsE ...
AbsSkip AbsLamda ROUND Sample

%Graph preferences
set(0,'DefaultFigureColor',[1 1 1])
set(0,'DefaultAxesFontSize',10)
set(0,'DefaultAxesFontName','Arial')
set(0,'DefaultAxesLineWidth',0.5)

tic
starttime=clock;
starttime=fix(starttime(4:5));

Get filenames and info therein
disp('-----------------------------------');
disp('Enter name of excel file containing data to be analyzed, ')
Infile=input...
    ('in sheets named "PLmap", "Abs" and "Parameters": ','s');
disp('-----------------------------------');
disp('Enter name of excel file containing SWNT information,');
```

```
SWNTfile=input('in sheet named "met" and "semic":  ','s');
disp('-----------------------------------');

SWNTfile='HiPCO';

% Comment these lines in/out to set new output filenames etc
% Outfile=input('Enter filename for program output: ','s');
Outfile=Infile;
disp('-----------------------------------');

Stds=xlsread(Infile,'Parameters','i10:i12');
hc=1239.84;
ExcLamda=xlsread(Infile,'Parameters','d4:d6');
ExcSkip=ExcLamda(3);
ExcL=ExcLamda(1):ExcSkip:ExcLamda(2);
ExcE=hc./ExcL;
DetLamda=xlsread(Infile,'Parameters','d8:d10');
DetSkip=DetLamda(3);
DetL=DetLamda(1):DetSkip:DetLamda(2);
DetL1=DetLamda(1):DetLamda(2);
DetE=hc./DetL;
DetE1=hc./DetL1;
AbsLamda=xlsread(Infile,'Parameters','I4:I6');
AbsSkip=AbsLamda(3);
AbsL=AbsLamda(1):AbsSkip:AbsLamda(2);
AbsE=hc./AbsL;
ROUND=1;
SCdata=xlsread(SWNTfile,'semic');
METdata=xlsread(SWNTfile,'met');

sm=size(METdata,1); ssc=size(SCdata,1); snt=sm+2*ssc;
[MET,SC,NT]=sortinfo(SCdata,METdata);
PLMap=xlsread(Infile,'PLMap')';
% Identify peaks in PL Map
[NT]=FindPeaks(PLMap,NT);

% Bounds on widths (for non- and identified SWNTs) and amplitudes
WL=0.5; WU=1.3; WU1=1.1;
AL=0.5; AU=2;

%For the repeat of the program with numerous backgrounds:
startval=1;
for ROUND=startval:5

close all
Infile
ROUND

% Fit absorbance as per Nair's work
spec=xlsread(Infile,'Abs');
[sub,lsub,bg]=bkgnd(spec,Infile);
[val,peak]=pkval(spec,bg);
[peak,AbsParams]=sortparams(peak,NT);
[weighting,grouppeaks,weightpeak,parameters]=...
parentvoigt(peak,AbsParams);
[AbsParams,Amax,Amin]=...
    areasolve(grouppeaks,parameters,peak,weighting,weightpeak);

% Adjust parameters for absorbance fit
AbsParams=adjustparams(AbsParams,Amax,Amin,peak);
drawgraphs(AbsParams);
[inABS]=trimABS(AbsParams);
```

```
% Fit PL map and calculate PLQY
[modelmap,PLMapint,coeffs,PLoutarea,AbsParams]=...
                            newplfit(PLMap,AbsParams);
graphslope(AbsParams,inABS,PLoutarea,coeffs,Stds);

disp('Start time:'); disp(starttime)
endtime=clock;
endtime=fix(endtime(4:5));
disp('End time: ')
disp(endtime)

% Maps and excitation profiles
plotres(modelmap,coeffs,PLMap);
end
end
disp('-----------------------------------');
disp('...done.')
disp('-----------------------------------');
end
%%%%%%%%%%%%%%%%%%%%%%%%%%%%%%%%%%%%%%%%%%%%%%%%%%%%%%%%%%%%%%%%%%%%%%%%%%%%

%%%%%%%%%%%%%%%%%%%%%%%%%%%%%%%%%%%%%%%%%%%%%%%%%%%%%%%%%%%%%%%%%%%%%%%%%%%%
function [MET,SC,NT]=sortinfo(SCdata,METdata)
%%%%%%%%%%%%%%%%%%%%%%%%%%%%%%%%%%%%%%%%%%%%%%%%%%%%%%%%%%%%%%%%%%%%%%%%%%%%
% Read in SWNT data and sort into parameter matrix to be used ...
% throughout this program. Separate semiconducting and metallic data.
%%%%%%%%%%%%%%%%%%%%%%%%%%%%%%%%%%%%%%%%%%%%%%%%%%%%%%%%%%%%%%%%%%%%%%%%%%%%
global sm ssc Sample

MET=zeros(sm,14); SC=zeros(2*ssc,14);
SCdata=sortrows(SCdata,5);
METdata=sortrows(METdata,5);
Factor=1;
if Sample==7
    Factor=0.9725;
elseif Sample==10
    Factor=0.985;
end
METdata(:,5)=METdata(:,5)*Factor;
SCdata(:,5)=SCdata(:,5)*Factor;
SCdata(:,7)=SCdata(:,7)*Factor;
for l=1:sm
    MET(l,:)=[METdata(l,1:6) METdata(l,5:6) zeros(1,5) l];
end
for l=1:ssc
    SC(l,:)=[SCdata(l,1:6) SCdata(l,5:6) 0 SCdata(l,5:6) 0 0 l+sm];
    SC(l+ssc,:)=[SCdata(l,1:4)...
    SCdata(l,7:8) SCdata(l,7:8) 0 SCdata(l,7:8) 0 0 l+sm+ssc];
end
NT=[MET;SC];
NT(:,6)=NT(:,6)/1000;
NT(:,8)=NT(:,8)/1000;
NT(:,11)=NT(:,11)/1000;
end
%%%%% end of 'sortinfo' %%%%%%%%%%%%%%%

%%%%%%%%%%%%%%%%%%%%%%%%%%%%%%%%%%%%%%%%%%%%%%%%%%%%%%%%%%%%%%%%%%%%%%%%%%%%
function [NT]=FindPeaks(PLMap,NT)
%%%%%%%%%%%%%%%%%%%%%%%%%%%%%%%%%%%%%%%%%%%%%%%%%%%%%%%%%%%%%%%%%%%%%%%%%%%%
% Local maxima (above a user-defined level) are identified and the
% immediate environment interpolated to find 'real' maxima.
%%%%%%%%%%%%%%%%%%%%%%%%%%%%%%%%%%%%%%%%%%%%%%%%%%%%%%%%%%%%%%%%%%%%%%%%%%%%
global DetSkip ExcSkip DetL ExcL Outfile hc sm snt ssc PLav DetE ExcE Sample
```

```
LDetL=length(DetL); LExcL=length(ExcL);
figure()
    contourf(DetE,ExcE,PLMap,50,'linestyle','none')
    box on; hold on
    set(gcf,'name','Input PL Map')
    xlabel('Emission energy [eV]')
    ylabel('Excitation energy [eV]')
disp('Please examine the displayed PL map, and enter')
Threshold=input('minimum PL intensity for QY calculation: ','s');
Threshold=sscanf(Threshold,'%i');
disp('-----------------------------------');

r=0; s=3;
% Criteria for assigment of identified peak to particular SWNT here
Tol11=0.012; Tol22=0.04;
for i=2:LExcL-1
    for j=2:LDetL-1
        localmax=max(max(PLMap(max(i-s,1):min(i+s,LExcL),...
            max(j-s,1):min(j+s,LDetL))));
        if PLMap(i,j)>Threshold && PLMap(i,j)==localmax
            r=r+1;
            DataPeaks(r,:)=[DetL(j) ExcL(i) PLMap(i,j)];
            InterpMap=...
            interp2(
          hc./(DetL(max(j-s,1)):DetSkip:DetL(min(j+s,LDetL))),...
          hc./(ExcL(max(i-s,1)):ExcSkip:ExcL(min(i+s,LExcL))),...
            PLMap(max(i-s,1):min(i+s,LExcL),
                max(j-s,1):min(j+s,LDetL)),...
        hc./(DetL(max(j-s,1)):DetSkip/8:DetL(min(j+s,LDetL)))',...
        hc./(ExcL(max(i-s,1)):ExcSkip/8:ExcL(min(i+s,LExcL))),...
                                        'spline');
            for k=1:size(InterpMap,1)
                for l=1:size(InterpMap,2)
                    if (InterpMap(k,l)>=max(InterpMap))
            Peak(r,:)=[hc./(DetL(max(j-s,1))+(l-1)*DetSkip/8)...
                       hc./(ExcL(max(i-s,1))+(k-1)*ExcSkip/8)...
                                    InterpMap(k,l)];
                    end
                end
            end
        end
    end
end
Diffw11=[]; Diffw22=[];
PLav=mean(mean(PLMap));
for j=1+sm:sm+ssc
    k=j+ssc;
    for i=1:size(Peak,1)
        if abs(NT(j,10)-Peak(i,1))<=Tol11 && abs(NT(k,7)-Peak(i,2))<=Tol22
            NT(j,10)=Peak(i,1); NT(j,7)=Peak(i,1);
            NT(k,7)=Peak(i,2); NT(k,10)=Peak(i,2);
            NT(j,12)=Peak(i,3);
            [w11,w22]=findwidths(DataPeaks(i,1:2),Peak(i,1:2),PLMap);
            Diffw11=[Diffw11 w11/NT(j,11)];
            Diffw22=[Diffw22 w22/NT(k,8)];
            NT(j,13)=1; NT(k,13)=1;
            NT(j,11)=w11; NT(j,8)=w11;
            NT(k,8)=w22; NT(k,11)=w22;
            NT(j,12)=Peak(i,3)/PLav;
            Peak(i,1:2)
       end
    end
```

```
end
for j=1+sm:sm+ssc
    k=j+ssc;
    if NT(j,13)~=1
        NT(j,11)=NT(j,6)*mean(Diffw11);
        NT(j,8)=NT(j,11);
        NT(k,8)=NT(k,6)*mean(Diffw22);
        NT(k,11)=NT(k,8);
    end
end
    plot(Peak(:,1),Peak(:,2),...
'marker','o','markeredgecolor','w','linestyle','none','markersize',6)
    plot(NT(1+sm:sm+ssc,5),NT(1+sm+ssc:snt,5),...
'marker','o','markeredgecolor','r','linestyle','none','markersize',6)
    plot(NT(1+sm:sm+ssc,10),NT(1+sm+ssc:snt,7),...
'marker','o','linestyle','none','markerfacecolor','w','markersize',6);
    xlabel('Emission energy [eV]')
    ylabel('Excitation energy [eV]')
    set(gcf,'name','PL Map and E11 & E22 Data');
    saveas(gcf,[Outfile ' Eii Data'],'fig')
    close

tempxlfile(NT);
disp('-----------------------------------');
disp('Please check the file TempSCData.xls for any erroneous')
disp('assignments that have been made. Use "Save As" and use')
newfile=input('Sheet1, and enter corrected file name here:  ','s');
disp('-----------------------------------');
NT=xlsread(newfile,'Sheet1');
end
%%%%% end of 'FindPeaks' %%%%%%%%%%%%%%%%%%%%%%%%%%%%%%%%%%%%%%%%%%%%%%%%

%%%%%%%%%%%%%%%%%%%%%%%%%%%%%%%%%%%%%%%%%%%%%%%%%%%%%%%%%%%%%%%%%%%%%%%%%%
function [w11,w22]=findwidths(dpks,Peak,PLMap)
%%%%%%%%%%%%%%%%%%%%%%%%%%%%%%%%%%%%%%%%%%%%%%%%%%%%%%%%%%%%%%%%%%%%%%%%%%
% Routine for finding the FWHM of peaks in the PL map.  Widths are
% converted from wavelengths to energies and averaged for each SWNT.
% Resulting widths are plotted as red crosses on the corrected PL map.
% This routine seems pretty messy, hopefully will get cleaned up.
%%%%%%%%%%%%%%%%%%%%%%%%%%%%%%%%%%%%%%%%%%%%%%%%%%%%%%%%%%%%%%%%%%%%%%%%%%
global DetLamda DetSkip ExcLamda ExcSkip hc

[lex,lem]=size(PLMap);
emcol=(dpks(1)-DetLamda(1))/DetSkip+1;
excrow=(dpks(2)-ExcLamda(1))/ExcSkip+1;
excdataA=PLMap(excrow:lex,emcol); excdataB=PLMap(1:excrow,emcol);
emdataA=PLMap(excrow,emcol:lem); emdataB=PLMap(excrow,1:emcol);
excwidth1=datawidth(excdataA,excdataB,ExcSkip);
excwidth=excwidth1-1;
emwidth1=datawidth(emdataA,emdataB,DetSkip);
emwidth=emwidth1-1;
w11=2*mean([abs((hc/dpks(1)-hc/(dpks(1)+emwidth))), ...
    abs((hc/dpks(1)-hc/(dpks(1)-emwidth)))],2);
w22=2*mean([abs((hc/dpks(2)-hc/(dpks(2)+excwidth))) ...
    abs((hc/dpks(2)-hc/(dpks(2)-excwidth)))],2);
ExcWidthXData=(Peak(1))*(ones(1,3));
EmWidthYData=(Peak(2))*(ones(1,3));
ExcWidthYData=[Peak(2)-w22/2, Peak(2),Peak(2)+w22/2];
EmWidthXData=[Peak(1)-w11/2, Peak(1),Peak(1)+w11/2];
    plot(EmWidthXData,EmWidthYData,'r+-')
    plot(ExcWidthXData,ExcWidthYData,'r+-')
end
%%%%% end of 'findwidths'%%%%%%%%%%%%%%%%%%%%%%%%%%%%%%%%%%%%%%%%%%%%%%%%
```

```
%%%%%%%%%%%%%%%%%%%%%%%%%%%%%%%%%%%%%%%%%%%%%%%%%%%%%%%%%%%%%%%%%%%%%%%%
function hwhm=datawidth(side1,side2,Skip)
%%%%%%%%%%%%%%%%%%%%%%%%%%%%%%%%%%%%%%%%%%%%%%%%%%%%%%%%%%%%%%%%%%%%%%%%
% Calculates the HWHM, in terms of (number of data points)*(units per
% data point).  Criteria for determining HWHM: data value falls below
% 3/4 of max. (Some peaks are too close together to allow the data to
% fall to % 1/2 maximum value!) (in which case Voigt HWHM is approx
% 5/3*measured width); edge of the PL map reached; minimum in the
% data reached.
%%%%%%%%%%%%%%%%%%%%%%%%%%%%%%%%%%%%%%%%%%%%%%%%%%%%%%%%%%%%%%%%%%%%%%%%

gr1=gradient(side1);
gr2=gradient(side2);
hm=side1(1)/2;

for i=2:length(side1)-1
    if ((gr1(i-1)<0 && gr1(i+1)>0) || i==length(side1)-1)
        hwhm1=(i-1)*Skip;
        break
    elseif side1(i)<1.5*hm
        hwhm1=(i-1)*Skip*5/3;
        break
    end
end
for i=length(side2)-1:-1:2
    if ((gr2(i-1)<0 && gr2(i+1)>0) || i==2)
        hwhm2=(length(side2)-i)*Skip;
        break
    elseif side2(i)<1.5*hm
        hwhm2=(length(side2)-i)*Skip*5/3;
        break
    end
end
hwhm=min([abs(hwhm1) abs(hwhm2)]);
end
%%%%% end of 'datawidth'%%%%%%%%%%%%%%%%%%%%%%%%%%%%%%%%%%%%%%%%%%%%%%%%%

%%%%%%%%%%%%%%%%%%%%%%%%%%%%%%%%%%%%%%%%%%%%%%%%%%%%%%%%%%%%%%%%%%%%%%%%
function [sub,lsub,bg]=bkgnd(spec,Infile)
%%%%%%%%%%%%%%%%%%%%%%%%%%%%%%%%%%%%%%%%%%%%%%%%%%%%%%%%%%%%%%%%%%%%%%%%
% Background subtraction, using a value obtained from Nair et al
% unless the user provides a suitable alternative.
%%%%%%%%%%%%%%%%%%%%%%%%%%%%%%%%%%%%%%%%%%%%%%%%%%%%%%%%%%%%%%%%%%%%%%%%
global AbsLamda ExcLamda AbsSpec hc AbsL AbsE

s1=spec(1,1);
counter=0;

disp('Do you have a suitable absorbance');
disp('background (b), or would you like to');
opt=input('calculate a new one (c)? (b/c):  ','s' );
disp('-----------------------------------');
if opt=='b';
    bg=xlsread(Infile,'Bkg');
    bg1=bg(1,1);
    bg=bg(AbsL-bg1+1,2);
    spec=spec(AbsL-s1+1,:);
    sub=spec(:,1);
    sub(:,2)=spec(:,2)-bg;
    s=sub(1:2,:);
    k=2;
    for i=3:length(sub)-2
```

```
        k=k+1;
        s(k,1)=sub(i,1);
        s(k,2)=(sub(i-2,2)+2*sub(i-1,2)+3*sub(i,2)+2*sub(i+1,2)+...
                                                    sub(i+2,2))/9;
    end
    s=[s;sub(length(sub)-1:length(sub),:)];
    sub=s;
    lsub=length(sub);
else
    while 1>0
    if counter>0
        AbsE=input('Enter absorption energy limits: ','s');
        disp('-----------------------')
        AbsE=sscanf(AbsE,'%f');
        AbsLamda=hc./AbsE;
        AbsLamda=round(sortrows(AbsLamda));
        c=0; d=0;
        for i=1:length(AbsL)
            if c==0;
            if AbsL(i)>=AbsLamda(1)
                AbsLamda(1)=AbsL(i);
                c=c+1;
            end
            end
            if d==0;
                if AbsL(i)>=AbsLamda(2)
                    AbsLamda(2)=AbsL(i);
                    d=d+1;
                end
            end
        end
        AbsL=AbsLamda(1):AbsLamda(2);
        AbsE=hc./AbsL;
    end
    if AbsLamda(1)>ExcLamda(1)
        error('Incompatible absorption and excitation range');
    end;
    if AbsLamda(2)<ExcLamda(2)
        error('Incompatible absorption and excitation range');
    end;
     figure()
    plot(hc./spec(AbsLamda(1)-spec(1,1)+1:...
         AbsLamda(2)-spec(1,1)+1,1),spec(AbsLamda(1)-spec(1,1)+1:...
                        AbsLamda(2)-spec(1,1)+1,2),'LineWidth',2)
    hold on
    [temp,bg]=bkg(spec(AbsLamda(1)-s1+1:AbsLamda(2)-s1+1,:),...
                                        AbsLamda(2)-AbsLamda(1)+1);

    sub=temp;
    axis([hc/sub(length(sub),1) hc/sub(1,1) 0 ...
        1.1*max(spec(AbsLamda(1)-spec(1,1)+1:AbsLamda(2)-spec(1,1)+1,2))])
    plot(hc./spec(AbsLamda(1)-spec(1,1)+1:...
                    AbsLamda(2)-spec(1,1)+1,1),bg','r','LineWidth',2)
    ylabel('Absorbance')
    xlabel('Energy [eV]');
    legend('Measured Absorbance','Calculated Background',4)
    set(gcf,'name','Measured Absorbance and Calculated Background');
    legend('boxoff')
    hold off
%     close
    disp('-----------------------')
%     opt=input('Are you satisfied with the background (y/n)? ','s');
opt='y';
```

```
    if opt=='y'
        break
    end
    counter=counter+1;
    end
    sub=temp;
    lsub=length(sub);
end
AbsSpec=sub(:,2);
end
%%%%% end of 'bkgnd' %%%%%%%%%%%%%%%%%%

%%%%%%%%%%%%%%%%%%%%%%%%%%%%%%%%%%%%%%%%%%%%%%%%%%%%%%%%%%%%%%%%%%%%%%%%%%%
function [sub,bg]=bkg(spec,lspec)
%%%%%%%%%%%%%%%%%%%%%%%%%%%%%%%%%%%%%%%%%%%%%%%%%%%%%%%%%%%%%%%%%%%%%%%%%%%
% Calculates the background, using the exponent derived from Nair
% et al's work and maximising the value of the constant term in the
% low-energy limit.  Subtracts background.
%%%%%%%%%%%%%%%%%%%%%%%%%%%%%%%%%%%%%%%%%%%%%%%%%%%%%%%%%%%%%%%%%%%%%%%%%%%

global data ldata col ROUND Sample

data=spec;
ldata=lspec;
col=2;
kb=[200 0.9];
log_kb=[log(kb(1)) kb(2)];
A=[ones(ldata,1) -log(data(:,1))];
B=log(data(:,col));
log_kopt=fmincon(@fit3,log_kb,A,B);
kopt=[exp(log_kopt(1)) log_kopt(2)];
bg=kopt(1)./(data(:,1).^kopt(2));
% % If you have a known exponent, enter it in the next two lines:
% Temp1=(data(ldata,2))*(data(ldata,1).^(0.77327));
% bg1=Temp1./(data(:,1).^(0.77327));
% Tenperc=data(ldata,2)*0.2;
% bg2=Temp1./(data(:,1).^(0.77327))-Tenperc;
%
% kopt(2)=log(bg1(ldata)/(bg1(1)+Tenperc))/log(data(ldata)/data(1));
% kopt(1)=(bg1(1)+Tenperc)/(data(1)^kopt(2));
% bg3=kopt(1).*(data(:,1).^(kopt(2)));
%
% kopt(2)=log((bg1(ldata)-Tenperc)/(bg1(1)-2*Tenperc))/...
%                                 log(data(ldata)/data(1));
% kopt(1)=(bg1(1)-2*Tenperc)/(data(1)^kopt(2));
% bg4=kopt(1).*(data(:,1).^(kopt(2)));


Temp1=(data(ldata,2))*(data(ldata,1).^(kopt(2)));
bg1=bg;
Tenperc=data(ldata,2)*0.2;
bg2=Temp1./(data(:,1).^(kopt(2)))-Tenperc;

kopt(2)=log(bg1(ldata)/(bg1(1)+Tenperc))/log(data(ldata)/data(1));
kopt(1)=(bg1(1)+Tenperc)/(data(1)^kopt(2));
bg3=kopt(1).*(data(:,1).^(kopt(2)));

kopt(2)=log((bg1(ldata)-Tenperc)/(bg1(1)-2*Tenperc))/...
                                log(data(ldata)/data(1));
kopt(1)=(bg1(1)-2*Tenperc)/(data(1)^kopt(2));
bg4=kopt(1).*(data(:,1).^(kopt(2)));
```

```
if ROUND==1
% Just to get all the backgrounds on one graph
    bg=[bg1 bg2 bg3 bg4];
elseif ROUND==2
    bg=bg2;
elseif ROUND==3
    bg=bg3;
elseif ROUND==4
    bg=bg4;
elseif ROUND==5
    bg=bg1;
end
sub=data(:,1);
if ROUND==1
sub(:,2)=data(:,2)-bg1;
else sub(:,2)=data(:,2)-bg;
end

s=sub(1:2,:);
k=2;
for i=3:length(sub)-2
    k=k+1;
    s(k,1)=sub(i,1);
    s(k,2)=(sub(i-2,2)+2*sub(i-1,2)+3*sub(i,2)+...
                            2*sub(i+1,2)+sub(i+2,2))/9;
end
s=[s;sub(length(sub)-1:length(sub),:)];
sub=s;
end
%%%% end of 'bkg' %%%%%%%%%%%%%%%%%%%%%%%%%%%%%%%%%%%%%%%%%%%%%%%%%%%%%%%%

%%%%%%%%%%%%%%%%%%%%%%%%%%%%%%%%%%%%%%%%%%%%%%%%%%%%%%%%%%%%%%%%%%%%%%%%%
function err=fit3(log_kb)
%Function that is minimised by the optimiser "fmincon" in Nair's work.
%%%%%%%%%%%%%%%%%%%%%%%%%%%%%%%%%%%%%%%%%%%%%%%%%%%%%%%%%%%%%%%%%%%%%%%%%
global data ldata col

log_data=log(data);
log_bkg=log_kb(1)*ones(ldata,1)-log_kb(2)*log_data(:,1);
F=log_data(:,col)-log_bkg;
err=F'*F;
end
%%%%%%%%%%%%%%%% end of 'fit3' %%%%%%%%%%%%%%%%%%%%%%%%%%%%%%%%%%%%%%%%%%

%%%%%%%%%%%%%%%%%%%%%%%%%%%%%%%%%%%%%%%%%%%%%%%%%%%%%%%%%%%%%%%%%%%%%%%%%
function [val,peak]=pkval(spec,bg)
%%%%%%%%%%%%%%%%%%%%%%%%%%%%%%%%%%%%%%%%%%%%%%%%%%%%%%%%%%%%%%%%%%%%%%%%%
%Locates peaks and valleys in the spectrum and seeks user input
%on any peaks/valleys that have been missed out
%%%%%%%%%%%%%%%%%%%%%%%%%%%%%%%%%%%%%%%%%%%%%%%%%%%%%%%%%%%%%%%%%%%%%%%%%
global AbsLamda sub lsub Outfile hc ROUND

s1=sub(1,1);
pwav=[];
vwav=[];
gr=gradient(sub(:,2));
q=0;
for i=2:(lsub-100)
    if (gr(i-1)<0 && gr(i+1)>0)
        q=q+1;
        s(q,1)=sub(i,1);
        s(q,2)=sub(i,2);
    end
```

```
    end
546 len_s=q;
    val(1,1)=sub(1,1);
    val(1,2)=sub(1,2);
    val(2,1)=s(1,1);
    val(2,2)=s(1,2);
551 i=1;
    k=2;
    while i<(len_s-2)
        k=k+1;
        j=i+1;
556     j_in=j;
        while (s(j,1)-s(i,1))<9
            j=j+1;
        end
        j_fin=j;
561     val(k,1)=s(j,1);
        val(k,2)=s(j,2);
        i=i+(j_fin-j_in+1);
    end
    val(length(val)+1,:)=sub(lsub,:);
566 q=0;
    for i=1:length(val)-1
        q=q+1;
        L1=val(i,1);
        L2=val(i+1,1);
571     m=max(sub(L1-s1+1:L2-s1+1,2));
        for L=L1:L2
            if sub(L-s1+1,2)==m
                wav=sub(L-s1+1,1);
            end
576     end
        peak(q,1)=hc/wav;
        peak(q,2)=m;

    end
581 val(:,1)=hc./val(:,1);
    figure()
    subplot('position',[0.12 0.55 0.76 0.4])
        plot(hc./spec(AbsLamda(1)-spec(1,1)+1:...
            AbsLamda(2)-spec(1,1)+1,1),spec((AbsLamda(1)-spec(1,1)+1):...
586                                 (AbsLamda(2)-spec(1,1)+1),2),'LineWidth',2)
        hold on
        axis([hc/sub(lsub,1) hc/sub(1,1) 0 ...
            1.1*max(spec(AbsLamda(1)-spec(1,1)+1:AbsLamda(2)-spec(1,1)+1,2))])
        plot(hc./spec(AbsLamda(1)-spec(1,1)+1:...
591                             AbsLamda(2)-spec(1,1)+1,1),bg,'r','LineWidth',2)
        set(gca,'XTickLabel','')
        ylabel('Absorbance')
        legend('Measured Absorbance','Calculated Background',4)
        legend('boxoff')
596 subplot('position',[0.12 0.15 0.76 0.4])
        plot(hc./sub(:,1),sub(:,2),'LineWidth',2)
        hold on
        axis([hc/sub(lsub,1) hc/sub(1,1) 0 1.1*max(sub(:,2))])
        plot(peak(:,1),peak(:,2),'or')
601     plot(val(:,1),val(:,2),'sk')
        set(gcf,'name','Located Peak and Valley Points');
        xlabel('Energy [eV]')
        ylabel('Absorbance')
        legend('Absorbance','Identified peaks','Identified valleys')
606     legend('boxoff')
        saveas(gcf,[Outfile num2str(ROUND) ' Abs Pks and Vals'],'fig')
```

```
    close

op=input('Do you wish to add more peaks and valleys (y/n)? ','s');
if op=='y'
    pwav=input('Enter energies of additional peaks: ','s');
    vwav=input('Enter energies of additional valleys: ','s');
    pwav=sscanf(pwav,'%f');
    vwav=sscanf(vwav,'%f');
    pwav=round(hc./pwav);
    pnum=pwav-sub(1,1)+1;
    pwav=[pwav sub(pnum,2)];
    pwav(:,1)=hc./pwav(:,1);
    vwav=round(hc./vwav);
    vnum=vwav-sub(1,1)+1;
    vwav=[vwav sub(vnum,2)];
    vwav(:,1)=hc./vwav(:,1);
end
peak=[peak;pwav];
peak=sortrows(peak,1);
val=[val;vwav];
val=sortrows(val,1);

% Commented out - didn't seem to be an issue

% Used during instances of multiple valleys and no
% intermediate peak at the start of the spectrum.
% Could also be used to remove 'unhelpful' peaks
% in the spectrum with a bit of extra code around here.

% op=input('Are there extraneous peaks or valleys (y/n)? ','s');
op='n';
if op=='y'
    wstart=input('Enter new high energy limit: ');
    for i=length(val)-1:-1:2
        if peak(i,1)>wstart
            peak(i,:)=[];
        end
        if val(i+1,1)>wstart
            val(i+1,:)=[];
        end
        if val(length(val),1)<wstart
            val=[val; wstart sub(round(hc/wstart)-sub(1,1)+1,2)];
            break
        end
    end
    wstart=round(hc/wstart)-sub(1,1)+1;
    sub=sub(wstart:length(sub),:);
    lsub=length(sub);
else
    sub=sub;
    lsub=lsub;
end
for q=1:size(peak,1)
    peak(q,3)=val(q,1);
    peak(q,4)=val(q+1,1);
end
s1=sub(1,1);
hold off
    plot(hc./sub(:,1),sub(:,2),'LineWidth',2)
    hold on
    axis([hc/sub(lsub,1) hc/sub(1,1) 0 1.1*max(sub(:,2))])
    plot(peak(:,1),sub(round(hc./peak(:,1))-s1+1,2),'ob')
    plot(val(:,1),sub(round(hc./val(:,1))-s1+1,2),'sk')
```

```
    xlabel('Energy [eV]')
    ylabel('Absorbance')
    legend('Absorbance','Identified peaks','Identified valleys')
    legend('boxoff')
    set(gcf,'name','Updated Peak and Valley Points');
    saveas(gcf,[Outfile num2str(ROUND) ' Pks and Vals'],'fig')
    close
end
%%%%% end of 'pkval' %%%%%%%%%%%%%%%%%%%%%%%%%%%%%%%%%%%%%%%%%%%%%%%%

%%%%%%%%%%%%%%%%%%%%%%%%%%%%%%%%%%%%%%%%%%%%%%%%%%%%%%%%%%%%%%%%%%%%%%
function [peak,AbsParams]=sortparams(peak,NT)
%%%%%%%%%%%%%%%%%%%%%%%%%%%%%%%%%%%%%%%%%%%%%%%%%%%%%%%%%%%%%%%%%%%%%%

global havepeaks snt

AbsParams=[];
havepeaks=zeros(size(peak,1),1);
for i=1:size(peak,1)
    for j=1:snt
        if peak(i,4)>NT(j,7) && NT(j,7)>=peak(i,3)
            AbsParams=[AbsParams;NT(j,:)];
            havepeaks(i)=havepeaks(i)+1;
        elseif peak(i,4)==min(peak(:,4)) && NT(j,7)<peak(i,4)
            AbsParams=[AbsParams;NT(j,:)];
            havepeaks(i)=havepeaks(i)+1;
        elseif peak(i,3)==max(peak(:,3)) && NT(j,7)>=peak(i,3)
            AbsParams=[AbsParams;NT(j,:)];
            havepeaks(i)=havepeaks(i)+1;
        end
    end

% The 'quadprog' program may throw up an error if there is a zero
% entry, i.e. if there is a parent peak with no matching child peak
% to fit. This ought to warn you about the problem.
    if havepeaks(i)==0
        R1=sprintf('Potential Error? – No matching absorbances');
        R2=sprintf('between %1.4f',' and %1.4f','eV',...
                                    peak(i,3),peak(i,4));
        disp(R1);
        disp(R2);
        pks=NT(:,7); pksu=sortrows(pks,1); pksd=sortrows(pks,-1);
        for k=1:length(pks)
            if pksu(k)>peak(i,4)
                pku=pksu(k);
              Try=sprintf(['Nearest peak above is %1.4f','eV'],pku);
                disp(Try);
                break
            end
            if pksd(k)<peak(i,3)
                pkd=pksd(k);
              Try=sprintf(['Nearest peak below is %1.4f','eV'],pkd);
                disp(Try);
                break
            end
        end
    end
end
peak=[peak havepeaks];
end
%%%%% end of 'sortparams'%%%%%%%%%%%%%%%%%%%%%%%%%%%%%%%%%%%%%%%%%%%%%

%%%%%%%%%%%%%%%%%%%%%%%%%%%%%%%%%%%%%%%%%%%%%%%%%%%%%%%%%%%%%%%%%%%%%%
```

```
function [weighting,grouppeaks,weightpeak,AbsParams]=...
          parentvoigt(peak,AbsParams)
%%%%%%%%%%%%%%%%%%%%%%%%%%%%%%%%%%%%%%%%%%%%%%%%%%%%%%%%%%%%%%%%%%%%%%%%%%%%
% Calculates the 'parent' Voigt profiles formed by grouping the
% individual model peaks according to the peaks identified in the
% absorbance curve. Also calculates the equivalent
%%%%%%%%%%%%%%%%%%%%%%%%%%%%%%%%%%%%%%%%%%%%%%%%%%%%%%%%%%%%%%%%%%%%%%%%%%%%
global havepeaks AbsE AbsSpec

weighting=[];
temp=[];
k=1;
for i=1:size(peak,1)
    for j=k:sum(havepeaks(1:i))
        AbsParams(j,9)=peak(i,2)/havepeaks(i);
        temp(j,1)=abs(peak(i,1)-AbsParams(j,7))/...
                                            (peak(i,4)-peak(i,3));
    end
    denom=sum(exp(-temp(k:j,1)));
    for j=k:sum(havepeaks(1:i))
        weighting(j,1)=exp(-temp(j,1))/denom;
    end
    k=k+havepeaks(i);
end

[startabs,startabsind]=findcurve(AbsParams(:,7:9),AbsE);

for i=1:size(startabsind,2)
    weightpeak(:,i)=weighting.*startabsind(:,i);
end
k=1;
for i=1:size(peak,1)
    t=sum(havepeaks(1:i));
    grouppeaks(i,:)=sum(weightpeak(k:t,:),1);
    k=k+havepeaks(i);
end
% figure()
% hold on
% plot(AbsE,grouppeaks,'b')
% plot(AbsE,AbsSpec,'k')
% plot(AbsE,startabsind,'r:')
% plot(AbsE,weightpeak,'g--')
% close
end
%%%%% end of 'parentvoigt'%%%%%%%%%%%%%%%%%%%%%%%%%%%%%%%%%%%%%%%%%%%%%%%%%

%%%%%%%%%%%%%%%%%%%%%%%%%%%%%%%%%%%%%%%%%%%%%%%%%%%%%%%%%%%%%%%%%%%%%%%%%%%%
function [AbsParams,Amax,Amin]=...
    areasolve(grouppeaks,AbsParams,peak,weighting,weightpeak)
%%%%%%%%%%%%%%%%%%%%%%%%%%%%%%%%%%%%%%%%%%%%%%%%%%%%%%%%%%%%%%%%%%%%%%%%%%%%
% Given the parent peaks calculated above, the absorbance curve is
% fitted using quadratic programming, as per Nair's work.  This then
% provides the upper and lower bound on amplitudes for the rest of
% the fit when multiplied by the AU and UL factors defined at the
% beginning.  The fit is then repeated using these bounds, relaxing
% the rule on relative amplitudes within a parent peak used before.
%%%%%%%%%%%%%%%%%%%%%%%%%%%%%%%%%%%%%%%%%%%%%%%%%%%%%%%%%%%%%%%%%%%%%%%%%%%%
global havepeaks AbsSpec AU AL AbsE

lb=zeros(1,size(grouppeaks,1));
lb=(peak(:,2)./peak(:,5))./max(grouppeaks,[],2);
% lb=ones(1,size(grouppeaks,1))*1;
ub=repmat(Inf,1,size(grouppeaks,1));
```

```
options=optimset('TolFun',1e-20,'MaxIter',100000000);

H=grouppeaks*grouppeaks';
f=-grouppeaks*AbsSpec;
[C]=quadprog(H,f,[],[],[],[],lb,ub,[],options);

k=1;
for i=1:size(peak,1)
    t=sum(havepeaks(1:i));
    for j=k:t
        CA(j,1)=C(i);
        CAmax(j,1)=AU*C(i);
        CAmin(j,1)=AL*C(i);
    end
    k=k+havepeaks(i);
end

H=weightpeak*weightpeak';
f=-weightpeak*AbsSpec;
[Cadj]=quadprog(H,f,[],[],[],[],CAmin,CAmax,CA,options);
Astart=CA.*weighting.*AbsParams(:,9);
Aadj=Cadj.*weighting.*AbsParams(:,9);
Amax=CAmax.*weighting.*AbsParams(:,9);
Amin=CAmin.*weighting.*AbsParams(:,9);
AbsParams(:,9)=Aadj;
AbsParams(:,15)=Astart;

end
%%%%% end of 'areasolve'%%%%%%%%%%%%%%%%%%%%%%%%%%%%%%%%%%%%%%%%%%%%%%%%%%%%

%%%%%%%%%%%%%%%%%%%%%%%%%%%%%%%%%%%%%%%%%%%%%%%%%%%%%%%%%%%%%%%%%%%%%%%%%%%
function AbsParams=adjustparams(AbsParams,Amax,Amin,peak)
%%%%%%%%%%%%%%%%%%%%%%%%%%%%%%%%%%%%%%%%%%%%%%%%%%%%%%%%%%%%%%%%%%%%%%%%%%%
% Taking the amplitudes found above as starting values, adjust the
% parameters of each absorption peak. We fit the peaks in order, from
% low to high energy, incorporating subpeaks within a small range of
% the peak in question into the fit
%%%%%%%%%%%%%%%%%%%%%%%%%%%%%%%%%%%%%%%%%%%%%%%%%%%%%%%%%%%%%%%%%%%%%%%%%%%
global havepeaks sub ib1 otherparas spectrum AbsE energyrange...
     AbsSpec ib2 Outfile snt WL WU WU1 hc T ROUND

InAbsParams=AbsParams;
peak=sortrows(peak,3);

% Just some weightings to make energy, width and amplitude fit
% a little more sensitive
T=[1 0.000001 0.0001];

energyrange=AbsE;
spectrum=AbsSpec';
maxw=[]; minw=[];

% Set bounds on energy, width and amplitude here
for s=1:snt
% Minimum widths:
    minw(:,1)=WL*min(AbsParams(:,6),AbsParams(:,8));
% Energy and maximum widths depend on whether the s-SWNT is
% identified in the PL Map; max/min amplitudes come from previous
% function:
    if AbsParams(s,13)==1
        maxw(s,1)=WU1*max(AbsParams(s,6),AbsParams(s,8));
        LB(s,:)=[AbsParams(s,7)-0.0025 minw(s,1) Amin(s,1)];
        UB(s,:)=[AbsParams(s,7)+0.0025 maxw(s,1) Amax(s,1)];
```

```
    else
        maxw(s,1)=WU*max(AbsParams(s,6),AbsParams(s,8));
        LB(s,:)=[AbsParams(s,7)-0.005 minw(s,1) Amin(s,1)];
        UB(s,:)=[AbsParams(s,7)+0.005 maxw(s,1) Amax(s,1)];
    end
end

if ROUND==5
% Interesting amplitude bounds for this round
for s=1:snt
    if AbsParams(s,13)==1
        LB(s,3)=AbsParams(s,9)*0.75;
        UB(s,3)=10*AbsParams(s,9);
    else
        LB(s,3)=0;
        UB(s,3)=AbsParams(s,9);
        AbsParams(s,9)=AbsParams(s,9)*0.5;
    end
end
end

for i=1:size(peak,1)
    Progress=sprintf(...
    'Adjusting parameters for %i subpeaks in peak %i ...
    (of %i peaks total)', havepeaks(i),i,size(peak,1));
    disp(Progress)
    tic
    inputLB=[]; inputUB=[]; inputs=[];

% Define an 'inner bound' and an 'outer bound'.  The inner bound is
% the range over which the curve is fitted, the outer bound defines
% those sub-peaks which are involved in the fit

    i1=peak(i,4)*1.0; o1=peak(i,4)*1.2;
    ib1=max(1,round(hc/i1)-sub(1,1)+1);
    ib2=size(sub,1);
    otherparas=[];
    paramnumber=[];
    k=0;
    for j=1:snt
        if peak(i,3)-0.5<AbsParams(j,7) && AbsParams(j,7)<=o1
            k=k+1;
            paramnumber=[paramnumber;j];
            inputs(k,:)=[AbsParams(j,7)/T(1)...
                AbsParams(j,8)/T(2) AbsParams(j,9)/T(3)];
            inputLB(k,:)=[LB(j,1)/T(1) LB(j,2)/T(2) LB(j,3)/T(3)];
            inputUB(k,:)=[UB(j,1)/T(1) UB(j,2)/T(2) UB(j,3)/T(3)];
        else
            otherparas=[otherparas; AbsParams(j,7)/T(1) ...
                 AbsParams(j,8)/T(2) AbsParams(j,9)/T(3)];
        end
    end
    [incurve,incurves]=findcurveT(inputs,AbsE);
    other=findcurveT(otherparas,AbsE);

% If you want to see the peak-by-peak fitting:
%     figure()
%     hold on
%         plot(energyrange,spectrum,'k','LineWidth',2)
%         plot(AbsE,incurve,'r')
%         plot(AbsE,incurves,'r--')
%         plot(AbsE,other+incurve,'r','LineWidth',2)
```

```
    options=optimset('TolFun',1e-6,'TolCon',1e-6,'TolX',1e-4,...
    'MaxIter',10000,'MaxFunEvals',10000);
    if ROUND==5
926   options=optimset('TolFun',1e-4);
    end
    fitparams=lsqnonlin(@fit_spec,inputs,inputLB,inputUB,options);

% Those peaks within the inner bound have their parameters updated:
931 for j=1:size(fitparams)
        k=paramnumber(j);
        if AbsParams(k,7)<=peak(i,4)*1.2
            AbsParams(k,7:9)=[fitparams(j,1)*T(1) ...
                        fitparams(j,2)*T(2) fitparams(j,3)*T(3)];
936     end
    end
    toc
    [outcurve,outcurves]=findcurveT(fitparams,AbsE);

941 % Again, uncomment to see individual fits
%     plot(AbsE,outcurve,'b')
%     plot(AbsE,outcurves,'b--')
%     plot(AbsE,other+outcurve,'b','LineWidth',2)
%     plot(AbsE(ib1),AbsSpec(ib1),'b<')
946 %     plot(AbsE(ib2),AbsSpec(ib2),'b>')
%     pkcentre=sprintf('Fitting peak at %1.3f eV', peak(i,1));
%     set(gcf,'name',pkcentre);

c=fix(clock);
951 time=c(4:5)
otherabs=[];
end
Changes=(AbsParams(:,7:9)-LB)./(UB-LB);
% figure()
956 % hold on
% plot([1:3],Changes)
%     saveas(gcf,[Outfile num2str(ROUND) ' Changes'],'fig')


961 % If you want to see the starting, initial fit and modified fits
% displayed together, uncomment here and after the optimisation:

startcurve=findcurve([AbsParams(:,7:8) AbsParams(:,15)],AbsE);
[adjcurve]=findcurve(AbsParams(:,7:9),AbsE);
966 % figure()
% hold on
%     plot(AbsE,AbsSpec,'k','LineWidth',2)
%     plot(AbsE,startcurve,'g:','LineWidth',2)
%     plot(AbsE,adjcurve,'b:','LineWidth',2)
971 %     axis([AbsE(length(AbsE)) AbsE(1) 0 1.1*max(AbsSpec)])
%     set(gcf,'name','Final Absorbance Fit')
%     set(gca,'box','on')

% All peaks and peak components optimised concurrently:
976 otherparas=[];
ib1=1; ib2=size(sub,1);
    options=optimset('TolFun',1e-7,'TolCon',1e-6,'TolX',1e-6,...
            'MaxIter', 100000,'MaxFunEvals',100000);
    if ROUND==5
981 % Because this round is a bit tricky
        options=optimset('TolFun',1e-6,'MaxFunEvals',50000);
    end
disp('-----------------------------------');
disp('Now optimising all peak parameters.  Patience please...')
```

```
[finalfitparams,resnorm]=lsqnonlin(@fit_spec,[AbsParams(:,7)/T(1) ...
    AbsParams(:,8)/T(2) AbsParams(:,9)/T(3)],...
            [LB(:,1)/T(1) LB(:,2)/T(2) LB(:,3)/T(3)],...
            [UB(:,1)/T(1) UB(:,2)/T(2) UB(:,3)/T(3)],options);
disp('------------------------------------');
AbsParams(:,7:9)=[finalfitparams(:,1)*T(1) finalfitparams(:,2)*T(2) finalfitparams(:,3)*
    T(3)];
c=fix(clock); time=c(4:5)
t=toc; t=t/60
figure()
hold on
    [finalcurve,finalcurves]=findcurveT(finalfitparams,AbsE);
    plot(AbsE,finalcurve,'r-','LineWidth',2)
    plot(AbsE,finalcurves,'r--')
    legend('Absorbance','Start Fit','Init. Fit','Final Fit',1)
    legend('boxoff')
    saveas(gcf,[Outfile num2str(ROUND) ' Abs Fit'],'fig')
    close
end
%%%% end of 'adjustparams'%%%%%%%%%%%%%%%%%%%%%%%%%%%%%%%%%%%%%%%%%%%%%%%%%%%%%%%%

%%%%%%%%%%%%%%%%%%%%%%%%%%%%%%%%%%%%%%%%%%%%%%%%%%%%%%%%%%%%%%%%%%%%%%%%%%%%%%%%
function drawgraphs(AbsParams)
%%%%%%%%%%%%%%%%%%%%%%%%%%%%%%%%%%%%%%%%%%%%%%%%%%%%%%%%%%%%%%%%%%%%%%%%%%%%%%%%
% Plot the final fit data, with individual peaks and errors.
%%%%%%%%%%%%%%%%%%%%%%%%%%%%%%%%%%%%%%%%%%%%%%%%%%%%%%%%%%%%%%%%%%%%%%%%%%%%%%%%
global AbsSpec AbsE Outfile sub lsub sm snt ssc hc ROUND

AbsParams=sortrows(AbsParams,14);
[finalfitcurve,finalfitcurves]=findcurve(AbsParams(:,7:9),AbsE);

Mind=finalfitcurves(1:sm,:);
E11ind=finalfitcurves(sm+1:sm+ssc,:);
E22ind=finalfitcurves(sm+ssc+1:snt,:);
writeoutcol={'Energy','Measured','Model'};
for i=1:snt
    if i<=sm
    writeoutcol(1,i+3)={['(' num2str(AbsParams(i,1)) ',' ...
        num2str(AbsParams(i,2)) ') E11(M)']};
    elseif i<=sm+ssc
    writeoutcol(1,i+3)={['(' num2str(AbsParams(i,1)) ',' ...
        num2str(AbsParams(i,2)) ') E11']};
    elseif i<=snt
    writeoutcol(1,i+3)={['(' num2str(AbsParams(i,1)) ',' ...
        num2str(AbsParams(i,2)) ') E22']};
    end
end

writeout=[AbsE' AbsSpec finalfitcurve' finalfitcurves'];

xlswrite([Outfile num2str(ROUND)],writeoutcol,'Absorbance Fits');
xlswrite([Outfile num2str(ROUND)],writeout,'Absorbance Fits','A2');

figure();
        subplot('position',[0.12 0.31 0.76 0.64])
            hold on
            plot(AbsE,AbsSpec,'k-','LineWidth',2);
            plot(AbsE,finalfitcurve,'r--','LineWidth',2);
            plot(AbsE,E11ind,'r:','LineWidth',0.25)
            plot(AbsE,E22ind,'g:','LineWidth',0.25)
            plot(AbsE,Mind,'b:','LineWidth',0.25)
            axis([hc/sub(lsub,1) hc/sub(1,1) 0 1.1*max(AbsSpec)])
            axscaleA=axis;
```

```
            legend('Absorbance','Model Fit','Fit Components',1)
            legend('boxoff')
            set(gca,'XTickLabel','','Box','on')
            ylabel('Absorbance','FontSize',14)
        subplot('position',[0.12 0.15 0.76 0.16])
            hold on
            plot(AbsE,(AbsSpec-finalfitcurve'),'r','LineWidth',2)
            axis([hc/sub(lsub,1) hc/sub(1,1) ...
                 0-((axscaleA(4)-axscaleA(3))/4)/2 ...
                  0+((axscaleA(4)-axscaleA(3))/4)/2])
            xlabel('Energy [eV]','FontSize',14)
            ylabel('Error','FontSize',14)
            set(gcf,'name','Absorbance Fit and Error');
            saveas(gcf,[Outfile num2str(ROUND) ...
                                ' A Fit and Error'],'fig')
            close
end
%%%%% end of 'drawgraphs' %%%%%%%%%%%%%%%%%%%%%%%%%%%%%%%%%%%%%%%%%%%%%%%%

%%%%%%%%%%%%%%%%%%%%%%%%%%%%%%%%%%%%%%%%%%%%%%%%%%%%%%%%%%%%%%%%%%%%%%%%%%
function [inABS]=trimABS(AbsParams)
%%%%%%%%%%%%%%%%%%%%%%%%%%%%%%%%%%%%%%%%%%%%%%%%%%%%%%%%%%%%%%%%%%%%%%%%%%
%Trims the input absorbance data to suit the given excitation
%wavelengths.
%%%%%%%%%%%%%%%%%%%%%%%%%%%%%%%%%%%%%%%%%%%%%%%%%%%%%%%%%%%%%%%%%%%%%%%%%%
global AbsLamda ExcLamda ExcSkip AbsE

AbsParams=sortrows(AbsParams,14);
[absfit,indabsfits]=findcurve(AbsParams(:,7:9),AbsE);
absstart=(ExcLamda(1)-AbsLamda(1))+1;
absend=(ExcLamda(2)-AbsLamda(1))+1;
inABS=indabsfits(:,absstart:ExcSkip:absend)';
end
%%%%% end of 'trimABS' %%%%%%%%%%%%%%%%%%%%%%%%%%%%%%%%%%%%%%%%%%%%%%%%%%

%%%%%%%%%%%%%%%%%%%%%%%%%%%%%%%%%%%%%%%%%%%%%%%%%%%%%%%%%%%%%%%%%%%%%%%%%%
function [modelmap,PLMapint,coeffs,PLoutarea,AbsParams]=...
    newplfit(PLMap,AbsParams)
%%%%%%%%%%%%%%%%%%%%%%%%%%%%%%%%%%%%%%%%%%%%%%%%%%%%%%%%%%%%%%%%%%%%%%%%%%
% Take each PL emission line in turn and fit PL emission curves to it.
% Only amplitudes are fitted for speed of calculation.  Thus, peak
% energies and widths and lineshape are fixed for each SWNT identified in
% the PL map in turn, at the excitation nearest their E22 max.
%%%%%%%%%%%%%%%%%%%%%%%%%%%%%%%%%%%%%%%%%%%%%%%%%%%%%%%%%%%%%%%%%%%%%%%%%%
global snt DetL DetL1 ExcL Outfile sm ssc PLav DetE1 ExcE hc ...
DetLamda ROUND

AbsParams=sortrows(AbsParams,14);
PLMapint=interp2(DetL,ExcL',PLMap,DetL1,ExcL','spline');
PLMapint=(PLMapint+abs(PLMapint))/2;

% For each peak identified in the PL map, optimise and set the energy
% and width parameters:
for i=sm+ssc+1:snt
    if AbsParams(i,13)==1
        nmtype=sprintf('Setting parameters for (%i,%i) tube.',...
                                    AbsParams(i,1), AbsParams(i,2));
        disp(nmtype);
        [AbsParams]=maxplfit(i,PLMapint,AbsParams);
    end
end

% For fitting PL emission curves, we start with a generic large
```

```
% amplitude, defined as the average of the PL map, and thus fit in
% terms  of 'coefficients', occasionally converting back and forth.
[PLtotal,PLem]=findcurve([AbsParams(:,10:11) PLav*ones(snt,1)],DetE1);
coeffs=[]; modelmap=[]; PLoutarea=[]; Line=1:size(PLMapint,1);

for i=1:size(PLMapint,1)
    progress=sprintf('Fitting PL emission line %i of %i',i,max(Line));
    disp('------------------------------------');
    disp(progress)
    disp('------------------------------------');
    E22=ExcE(i);
    spectrum=PLMapint(i,:);
    H=PLem*PLem';
    f=-(PLem*spectrum');
    lb=zeros(snt,1);    ub=Inf*ones(snt,1);    x0=lb;
    A=qpfit(H,f,lb,ub,x0,E22,0.1,AbsParams);
    B=qpfit(H,f,A*0.9,ub,A,E22,1,AbsParams);
    coeffs=[coeffs (B*PLav)];
    plmodelcurve=B'*PLem;
    modelmap=[modelmap; plmodelcurve];
    for j=1:size(PLem,2)
        IndPLoutB(:,j)=B.*PLem(:,j);
    end
    Remain=spectrum-plmodelcurve;
% For each fitted PL emission line, calculate the emission area from
% each s-SWNT
    IndArea=-trapz(DetE1,IndPLoutB,2)';
    PLoutarea=[PLoutarea; IndArea];

% Uncomment to see the fits or to specify which lines to fit...
    if i==91
    figure();
        subplot('position',[0.12 0.35 0.76 0.60])
            hold on
            plot(DetE1,spectrum,'k-','LineWidth',2);
            plot(DetE1,plmodelcurve,'b--','LineWidth',2);
            plot(DetE1,IndPLoutB,'b:')
            xlim([hc/DetLamda(2) hc/DetLamda(1)])
            axscaleA=axis;
            legend('Experimental PL Data','Model Fit',...
                                'Fit Components',2)
            legend('boxoff')
            set(gca,'XTickLabel','','Box','on')
            ylabel('PL Intensity','FontSize',14)
        subplot('position',[0.12 0.15 0.76 0.20])
            plot(DetE1,Remain,'LineWidth',2)
            axis([hc/DetLamda(2) hc/DetLamda(1) ...
                            0-((axscaleA(4)-axscaleA(3))/3)/2 ...
                            0+((axscaleA(4)-axscaleA(3))/3)/2])
            xlabel('Energy [eV]','FontSize',14)
            ylabel('Error','FontSize',14)
            set(gca,'YAxisLocation','right')
            Title=sprintf('Fits and errors, ...
                Exc = %i nm (%1.3f eV)',ExcL(i),ExcE(i));
        set(gcf,'name',Title);
        saveas(gcf,[Outfile num2str(ROUND) ' PL Fits and Err'],'fig')
        close
    end
end
xlswrite([Outfile num2str(ROUND)],modelmap','Model PL Map');
AbsParams(:,12)=AbsParams(:,12)*PLav;
end
%%%%% end of 'newplfit'%%%%%%%%%%%%%%%%%%%%%%%%%%%%%%%%%%%%%%%%%%%%%%%%%%%%
```

```
%%%%%%%%%%%%%%%%%%%%%%%%%%%%%%%%%%%%%%%%%%%%%%%%%%%%%%%%%%%%%%%%%%%%%%%%%%%%
function [AbsParams]=maxplfit(i,PLMapint,AbsParams)
%%%%%%%%%%%%%%%%%%%%%%%%%%%%%%%%%%%%%%%%%%%%%%%%%%%%%%%%%%%%%%%%%%%%%%%%%%%%
% Optimises the parameters for each individual SWNT.  The PL emission
% line being examined corresponds to the emission maximum of one
% s-SWNT. Amplitudes are first fitted using 'quadprog', first fitting
% only peaks with an E22 energy near to the excitation energy, then
% allowing more peaks to be involved.  The parameters (energy, width
% and amplitude) are then fitted using the 'lsqnonlin' routine and
% saved for the peak in question.
%%%%%%%%%%%%%%%%%%%%%%%%%%%%%%%%%%%%%%%%%%%%%%%%%%%%%%%%%%%%%%%%%%%%%%%%%%%%
global ExcLamda ExcSkip snt hc ssc sm ib1 ib2 spectrum...
    energyrange otherparas PLav DetE1

E22=AbsParams(i,7);
E11=AbsParams(i-ssc,10);
excl=hc/E22;
PLexc=round((excl-ExcLamda(1))/ExcSkip)+1;
energyrange=DetE1;
spectrum=PLMapint(PLexc,:);
[PLtotal,PLem]=findcurve([AbsParams(:,10:11) PLav*ones(snt,1)],energyrange);
ib1=1; ib2=length(energyrange);

% Fit amplitudes:
H=PLem*PLem';
f=-(PLem*spectrum');
lb=zeros(snt,1);
x0=lb;
ub=Inf*ones(snt,1);
zeroorder=qpfit(H,f,lb,ub,x0,E22,0.1,AbsParams);
E=qpfit(H,f,zeroorder*0.8,ub,zeroorder,E22,1,AbsParams);
E=E*PLav;
tic

% Set bounds and fit parameters:
otherparas=[];
q=0; r=0;
for j=sm+1:snt
    if E(j)>0.1
        if (abs(AbsParams(j,10)-E11)<0.15) || j==(i-ssc)
            q=q+1;
            maxw=max(1.1*AbsParams(j,6),1.1*AbsParams(j,11));
            minw=min(0.75*AbsParams(j,6),0.75*AbsParams(j,11));
            inputs(q,:)=[AbsParams(j,10:11) E(j)];
            lower(q,:)=[AbsParams(j,10)-0.0025 minw 0.9*E(j)];
            upper(q,:)=[AbsParams(j,10)+0.0025 maxw max(1.1*E(j),1)];
            if j==(i-ssc)
                r=q;
            end
        else
            otherparas=[otherparas; AbsParams(j,10:11) E(j)];
        end
    end
end
options=optimset('TolFun',1e-2,'MaxIter',1e20,'MaxFunEvals',1e20,...
    'TolCon',1e-2,'TolX',1e-1);
fitplparas=lsqnonlin(@fit_spec,inputs,lower,upper,options);
AbsParams(i-ssc,10:12)=[fitplparas(r,1:2) fitplparas(r,3)/PLav];
toc

% Uncomment if you want to see the optimising of the bounds.
```

```
% Tubetype=sprintf('(%i,%i) PL parameters, Exc %1.3f eV',...
%     AbsParams(i,1),AbsParams(i,2),E22);
% figure()
% hold on
% plot(energyrange,spectrum,'k','LineWidth',2)
% [incurve,incurves]=findcurve([AbsParams(:,10:11) E],energyrange);
% indincurve=findcurve([AbsParams(r,10:11) E(r)],energyrange);
% plot(energyrange,incurve,'b')
% plot(energyrange,incurves,'b--','LineWidth',0.5)
% plot(energyrange,indincurve,'b--','LineWidth',2)
% [outcurve,indoutcurves]=findcurve(fitplparas,energyrange);
% plot(energyrange,outcurve,'r')
% plot(energyrange,indoutcurves,'r--','LineWidth',0.5)
% plot(energyrange,indoutcurves(r,:),'r--','LineWidth',2)
% set(gca,'Box','on')
% set(gcf,'name',Tubetype);
end
%%%%% end of 'maxplfit' %%%%%%%%%%%%%%%%%%%%%%%%%%%%%%%%%%%%%%%%%%%%%

%%%%%%%%%%%%%%%%%%%%%%%%%%%%%%%%%%%%%%%%%%%%%%%%%%%%%%%%%%%%%%%%%%%%%
function [Sol]=qpfit(H,f,lb,ub,x0,E22,lim,pars)
%%%%%%%%%%%%%%%%%%%%%%%%%%%%%%%%%%%%%%%%%%%%%%%%%%%%%%%%%%%%%%%%%%%%%
% Back-end routine for any quadratic programming.  Includes E22, the
% excitation energy and 'lim', which dictates the range of energies
% either side of E22 for which different SWNTs are used in the fit.
%%%%%%%%%%%%%%%%%%%%%%%%%%%%%%%%%%%%%%%%%%%%%%%%%%%%%%%%%%%%%%%%%%%%%
global sm snt ssc

explor=zeros(snt,1);
E22in=pars(:,10);
W22in=pars(:,11);%./1000;
for j=1:sm
    ub(j,1)=1e-4;
end
for j=(sm+ssc+1):snt
    Gcurve(j)=exp(-4*log(2)*(E22-E22in(j))^2/W22in(j)^2);
    Lcurve(j)=(0.5*W22in(j))^2/((E22-E22in(j))^2+(0.5*W22in(j))^2);
    explor(j)=0.5*Gcurve(j)+0.5*Lcurve(j);
    k=j-ssc;
    ub(j,1)=1e-4;
    if (E22in(j)-E22>lim || ...
        E22-E22in(j)>1.5*lim)
        if x0(k,1)==0
            x0(k,1)=pars(k,12)*explor(j);
        end
    elseif (E22in(j)-E22<=lim || ...
        E22-E22in(j)<=1.5*lim)
        if x0(k,1)==0
            x0(k,1)=pars(k,12)*explor(j);
        end
        if (lb(k,1)==0 && pars(k,13)==1)
            lb(k,1)=0.8*pars(k,12)*explor(j);
        end
    end
end
options=optimset('TolFun',1e-20,'MaxIter',10000);
Sol=quadprog(H,f,[],[],[],[],lb,ub,x0,options);
end
%%%%% end of 'qpfit' %%%%%%%%%%%%%%%%%%%%%%%%%%%%%%%%%%%%%%%%%%%%%%%%

%%%%%%%%%%%%%%%%%%%%%%%%%%%%%%%%%%%%%%%%%%%%%%%%%%%%%%%%%%%%%%%%%%%%%
function [AbsParams]=graphslope(AbsParams,inABS,PLoutarea,coeffs,Stds)
%%%%%%%%%%%%%%%%%%%%%%%%%%%%%%%%%%%%%%%%%%%%%%%%%%%%%%%%%%%%%%%%%%%%%
```

```
% Calculate the ratio of emitted PL to absorbance and display the
% results. Absorbance is corrected for the mass fraction of
% individual tubes.  PLvA fits are not through zero, this is easily
% changed: use 'Slope(j)=C\d'
%%%%%%%%%%%%%%%%%%%%%%%%%%%%%%%%%%%%%%%%%%%%%%%%%%%%%%%%%%%%%%%%%%%%%%%%%%%%
global ExcLamda snt Outfile hc sm ssc ExcE ExcL ROUND
persistent legs

MassFrac=Stds(1);   StQY=Stds(2);   nsqrd=Stds(3);
ABS=inABS(1:size(inABS,1),:)*MassFrac;
sabs=size(ABS,1);
Slope=zeros(snt,1); QY=zeros(snt,1); total=0;
figure();
PLvAfig=gcf;
hold on
ColOrd=[0 0 1; 0 1 0; 1 0 0; 1 0 1; 0 1 1];
[m]=size(ColOrd,1);
MarkerOrd='osx+v';
set(gca,'ColorOrder',ColOrd)
set(gca,'LineStyleOrder','-|--|:|-.')
LineOrd=get(gca,'LineStyleOrder');

for i=1+sm+ssc:snt
    j=i-ssc;
    if AbsParams(i,13)==1
        total=total+1;
        ColRow=rem(total,m);
        if ColRow==0
            ColRow=m;
        end
        Col=ColOrd(ColRow,:);
        LineRow=floor(total/m)+1;
        if rem(total,m)==0
            LineRow=LineRow-1;
        end
        LinSty=LineOrd(LineRow,:);
        Tubetype=sprintf('(%i,%i) SWNT',AbsParams(i,1),...
                                              AbsParams(i,2));
        disp(sprintf('Now fitting %s...',Tubetype))
        Eo=AbsParams(i,7);
        gamma=AbsParams(i,8);
        [energy,range,wlength]=getenergy(Eo,gamma,sabs);
        C=ABS(range,i);
        d=PLoutarea(range,j);
        SlopeData=polyfit(C,d,1);
        Slope(j)=SlopeData(1);
        QY(j)=(Slope(j)/StQY)*nsqrd;
        Inter=SlopeData(2);
        colname={'Abs',['(' num2str(AbsParams(i,1))...
            ',' num2str(AbsParams(i,2)) ') PL']};
        if total<=13
            firstcol=char(double('A')+(total-1)*2);
            secondcol = char(firstcol+1);
            coloutname= sprintf('%s1:%s1',firstcol,secondcol);
        elseif total>13
            nalpha=floor(total/13)-1;
            remain=rem(total,13);
            if rem(total,13)==0
                remain=13;
            end
            FColFirstLetter = char(double('A') + nalpha);
            FColSecondLetter = char(double('A') + 2*(remain-1));
            firstcol = [FColFirstLetter FColSecondLetter];
```

```
            secondcol = [FColFirstLetter ...
                         char(double(FColSecondLetter)+1)];
            coloutname=sprintf('%s1:%s1',firstcol,secondcol);
        end
        ldata=length(C);
        dataout=[C d];
        dataoutname=sprintf('%s%i:%s%i',...
                            firstcol,2,secondcol,ldata+1);
        xlswrite([Outfile num2str(ROUND)],colname,'PL v A',coloutname);
        xlswrite([Outfile num2str(ROUND)],dataout,'PL v A',dataoutname);

        figure(PLvAfig)
            plot(C,d,'LineStyle',LinSty,'Color',Col,...
                     'LineWidth',2,'Marker',MarkerOrd(ColRow));
            xlabel('Absorbance','FontSize',14);
            ylabel('Integrated PL Area','FontSize',14)
            set(gcf,'name','PL v A for All Tubes');
            set(gca,'box','on')
            legall{total,1}=sprintf('(%i,%i)',...
                         AbsParams(i,1),AbsParams(i,2));
            legend(legall,'FontSize',12,4)
            legend('boxoff')
            saveas(gcf,[Outfile num2str(ROUND) ' PLvA all'],'fig')

        figure();
        subplot(2,3,[1 5]);
            hold on
            plot(C,d,'ko-','LineWidth',2);
            plot(C,Slope(j)*C+Inter,'k:','LineWidth',2)
            set(gca,'box','on')
            xlabel('Absorbance (Fitted)');
            ylabel('Integrated PL Area')
            legs{1,i}=('Model Data');
            legs{2,i}=sprintf('Q.Y. = %1.4f',QY(j));
            legend(legs(:,i),'Location','NorthWest')
            legend('boxoff')
        subplot(2,3,6);
            hold on
            plot(ExcE,coeffs(j,:),'b-');
            plot(hc./wlength,coeffs(j,range),'bo','LineWidth',2)
            set(gca,'box','on')
            xlim([hc/ExcLamda(2) hc/ExcLamda(1)]);
            xlabel('Energy [eV]');
            ylabel('PL Amplitude Fits');
        subplot(2,3,3);
            hold on
            plot(ExcE,ABS(:,i),'r-');
            plot(hc./wlength,ABS(range,i),'ro','LineWidth',2)
            set(gca,'box','on')
            xlim([hc./ExcLamda(2) hc./ExcLamda(1)]);
            xlabel('Energy [eV]');
            ylabel('Absorbance (Fitted)');
            set(gcf,'name',[Tubetype ' PL v A']);
            saveas(gcf,[Outfile num2str(ROUND) Tubetype],'fig')
            hold off
            close
    end
end
disp('-----------------------------------');
disp('Writing out results to file...')
disp('-----------------------------------');
for i=1+sm:sm+ssc
   NT(i-sm)={['(' num2str(AbsParams(i,1)) ',' ...
```

```
       num2str(AbsParams(i,2)) ')  [' ...
       num2str(AbsParams(i,5)) ']']};
end
xlswrite([Outfile num2str(ROUND)],NT,'PL Amp Fits','B1');
xlswrite([Outfile num2str(ROUND)],NT,'Model PL Areas','B1');
xlswrite([Outfile num2str(ROUND)],ExcL','PL Amp Fits','A2');
xlswrite([Outfile num2str(ROUND)],ExcL','Model PL Areas','A2');
AbsParams=[AbsParams(:,1:14) Slope QY];
colfap={'n','m','Dia(nm)','Phi (rad)','E|Orig [eV]','W|Orig [meV]',...
    'E|Abs (eV)','W|Abs [meV]','A|Abs','E|Em (eV)','W|Em (meV)',...
                     'A|Em','Inc','Order','Slope','QY'};
range2=sprintf('A2:P%i',snt+1);
xlswrite([Outfile num2str(ROUND)],colfap,'Fit Params','A1:P1');
xlswrite([Outfile num2str(ROUND)],AbsParams,'Fit Params',range2);
xlswrite([Outfile num2str(ROUND)],round(coeffs(sm+1:sm+ssc,:)'),...
                                              'PL Amp Fits','B2');
xlswrite([Outfile num2str(ROUND)],round(PLoutarea(:,sm+1:sm+ssc)),...
                                     'Model PL Areas','B2');
close all
end
%%%%% end of 'graphslope' %%%%%%%%%%%%%%%%%%%%%%%%%%%%%%%%%%%%%%%%%%%%%

%%%%%%%%%%%%%%%%%%%%%%%%%%%%%%%%%%%%%%%%%%%%%%%%%%%%%%%%%%%%%%%%%%%%%%
function [energy,range,wlength]=getenergy(Eo,gamma,sabs)
%%%%%%%%%%%%%%%%%%%%%%%%%%%%%%%%%%%%%%%%%%%%%%%%%%%%%%%%%%%%%%%%%%%%%%
% Back-end function to get the right range of energies/wavelength for
% comparing PL to A.
%%%%%%%%%%%%%%%%%%%%%%%%%%%%%%%%%%%%%%%%%%%%%%%%%%%%%%%%%%%%%%%%%%%%%%
global ExcLamda ExcSkip hc

EMstart=hc/(Eo+0.35*gamma);
EMend=hc/(Eo-0.35*gamma);
range=((EMstart-ExcLamda(1))/ExcSkip:(EMend-ExcLamda(1))/ExcSkip)+1;
range=fix(range);
temp=[];
for j=1:length(range)
    if (range(1,j)>=0 && range(1,j)<sabs)
        temp=[temp range(1,j)];
    end
end
range=temp+1;
wlength=ExcLamda(1)+(temp)*ExcSkip;
energy=(hc./wlength)';
end
%%%%% end of 'getenergy' %%%%%%%%%%%%%%%%%%%%%%%%%%%%%%%%%%%%%%%%%%%%%%

%%%%%%%%%%%%%%%%%%%%%%%%%%%%%%%%%%%%%%%%%%%%%%%%%%%%%%%%%%%%%%%%%%%%%%
function tempxlfile(Tempnt)
%%%%%%%%%%%%%%%%%%%%%%%%%%%%%%%%%%%%%%%%%%%%%%%%%%%%%%%%%%%%%%%%%%%%%%
% Write out the data after comparing the PL map to input values for
% checking by the user
%%%%%%%%%%%%%%%%%%%%%%%%%%%%%%%%%%%%%%%%%%%%%%%%%%%%%%%%%%%%%%%%%%%%%%
global snt

colnt={'n','m','Dia(nm)','Phi (rad)','E|In (eV)','W|In (meV)',...
    'E|Abs (eV)','W|Abs (meV)','A|Abs','E|Em (eV)', 'W|Em (meV)',...
    'A|Em','Inc 1/0','Order'};
range2=sprintf('A2:O%i',snt+1);
xlswrite('TempSCData',colnt,'Sheet1','A1:O1');
xlswrite('TempSCData',Tempnt,'Sheet1',range2);
end
%%%%% end of 'tempxlfile' %%%%%%%%%%%%%%%%%%%%%%%%%%%%%%%%%%%%%%%%%%%%%
```

```
%%%%%%%%%%%%%%%%%%%%%%%%%%%%%%%%%%%%%%%%%%%%%%%%%%%%%%%%%%%%%%%%%%%%%%%%
function plotres(modelmap,coeffs,PLMap)
%%%%%%%%%%%%%%%%%%%%%%%%%%%%%%%%%%%%%%%%%%%%%%%%%%%%%%%%%%%%%%%%%%%%%%%%
global DetLamda ExcLamda Outfile hc ExcE DetE DetE1 ROUND

figure()
    axis(hc./[DetLamda(2) DetLamda(1) ExcLamda(2) ExcLamda(1)]);
    set(gca,'color',[0 0 0.6]);
    hold on
    contourf(DetE,ExcE,PLMap,50,'linestyle','none');%...
    xlabel('Emission energy [eV]','FontSize',14)
    ylabel('Excitation energy [eV]','FontSize',14)
    set(gcf,'name','Input PL Map');
    saveas(gcf,[Outfile num2str(ROUND) ' Input'],'fig')
    close

figure()
    hold on
    set(gca,'Color',[0 0 0.6])
    contourf(DetE1,ExcE,modelmap,50,'linestyle','none')
    set(gcf,'name','Model PL Map');
    xlabel('Emission energy [eV]','FontSize',14)
    ylabel('Excitation energy [eV]','FontSize',14)
    zlabel('PL Intensity','FontSize',14)
    saveas(gcf,[Outfile num2str(ROUND) ' Model'],'fig')
    close

figure()
    plot(ExcE,coeffs','LineWidth',2)
    set(gcf,'name','Generated Excitation Profiles')
    xlabel('Excitation Energy [eV]','FontSize',14)
    ylabel('PL Amplitude Fit','FontSize',14)
    xlim([hc/ExcLamda(2) hc/ExcLamda(1)]);
    saveas(gcf,[Outfile num2str(ROUND) ' ExcProf'],'fig')
    close
end
%%%%% end of 'PlotRes' %%%%%%%%%%%%%%%%%%%%%%%%%%%%%%%%%%%%%%%%%%%%%%%%%%

%%%%%%%%%%%%%%%%%%%%%%%%%%%%%%%%%%%%%%%%%%%%%%%%%%%%%%%%%%%%%%%%%%%%%%%%
function [curve,curves]=findcurve(parameters,energy)
%%%%%%%%%%%%%%%%%%%%%%%%%%%%%%%%%%%%%%%%%%%%%%%%%%%%%%%%%%%%%%%%%%%%%%%%

lenergy=length(energy);
curve=zeros(1,lenergy);
curves=[];
parameters(:,2)=parameters(:,2);%/1000;
for i=1:(size(parameters,1))
    for j=1:lenergy
        Gcurve(j)=parameters(i,3)*exp(-4*log(2)*...
                    (energy(j)-parameters(i,1))^2/parameters(i,2)^2);
        Lcurve(j)=(parameters(i,3)*(0.5*parameters(i,2))^2/...
            ((energy(j)-parameters(i,1))^2+(0.5*parameters(i,2))^2));
    end
    curvecomponent=0.5*Lcurve+0.5*Gcurve;
    curve=curve+curvecomponent;
    curves=[curves; curvecomponent];
end
end
%%%%% end of 'findcurve' %%%%%%%%%%%%%%%%%%%%%%%%%%%%%%%%%%%%%%%%%%%%%%%%%

%%%%%%%%%%%%%%%%%%%%%%%%%%%%%%%%%%%%%%%%%%%%%%%%%%%%%%%%%%%%%%%%%%%%%%%%
function [curve,curves]=findcurveT(parameters,energy)
%%%%%%%%%%%%%%%%%%%%%%%%%%%%%%%%%%%%%%%%%%%%%%%%%%%%%%%%%%%%%%%%%%%%%%%%
```

```
global T

lenergy=length(energy);
curve=zeros(1,lenergy);
curves=[];
parameters(:,1)=parameters(:,1)*T(1);
parameters(:,2)=parameters(:,2)*T(2);
parameters(:,3)=parameters(:,3)*T(3);
for i=1:(size(parameters,1))
    for j=1:lenergy
        Gcurve(j)=parameters(i,3)*exp(-4*log(2)*...
                    (energy(j)-parameters(i,1))^2/parameters(i,2)^2);
        Lcurve(j)=(parameters(i,3)*(0.5*parameters(i,2))^2/...
            ((energy(j)-parameters(i,1))^2+(0.5*parameters(i,2))^2));
    end
    curvecomponent=0.5*Lcurve+0.5*Gcurve;
    curve=curve+curvecomponent;
    curves=[curves; curvecomponent];
end
end
%%%%% end of 'findcurveT' %%%%%%%%%%%%%%%%%%%%%%%%%%%%%%%%%%%%%%%%%%%%%%%%

%%%%%%%%%%%%%%%%%%%%%%%%%%%%%%%%%%%%%%%%%%%%%%%%%%%%%%%%%%%%%%%%%%%%%%%%%%%
function diff = fit_spec(inputs)
%%%%%%%%%%%%%%%%%%%%%%%%%%%%%%%%%%%%%%%%%%%%%%%%%%%%%%%%%%%%%%%%%%%%%%%%%%%
global spectrum otherparas energyrange ib1 ib2

if size(otherparas,1)>0
    static=findcurveT(otherparas,energyrange);
else
    static=0;
end
change=findcurveT(inputs,energyrange);
modelfit=static+change;
diff=spectrum(ib1:ib2)-modelfit(ib1:ib2);
end
%%%%% end of 'fit_spec' %%%%%%%%%%%%%%%%%%%%%%%%%%%%%%%%%%%%%%%%%%%%%%%%%
```

[1] Anantram, M.P. and Leonard, F. Physics of carbon nanotube electronic devices. *Reports on Progress in Physics*, 69 (3), 507–561 (**2006**)

[2] Ando, T. Theory of electronic states and transport in carbon nanotubes. *Journal of the Physics Society Japan*, 74 (3), 777–817 (**2005**)

[3] Andrews, R., Jacques, D., Rao, A.M., Rantell, T., Derbyshire, F., Chen, Y., Chen, J. and Haddon, R.C. Nanotube composite carbon fibers. *Applied Physics Letters*, 75 (9), 1329–1329 (**1999**)

[4] Aprile, C., Martín, R., Alvaro, M., Scaiano, J.C. and Garcia, H. Near-infrared emission quantum yield of soluble short single-walled carbon nanotubes. *ChemPhysChem*, 10 (8), 1305–1310 (**2009**)

[5] Ariu, M., Lidzey, D.G., Sims, M., Cadby, A.J., Lane, P.A. and Bradley, D.D.C. The effect of morphology on the temperature-dependent photoluminescence quantum efficiency of the conjugated polymer poly(9, 9-dioctylfluorene). *Journal of Physics: Condensed Matter*, 14 (42), 9975–9986 (**2002**)

[6] Ariu, M., Sims, M., Rahn, M.D., Hill, J., Fox, A.M., Lidzey, D.G., Oda, M., Cabanillas-Gonzalez, J. and Bradley, D.D.C. Exciton migration in β -phase poly(9,9-dioctylfluorene). *Physical Review B*, 67 (19), 195333/1–11 (**2003**)

[7] Arnold, K., Hennrich, F., Krupke, R., Lebedkin, S. and Kappes, M.M. Length separation studies of single walled carbon nanotube dispersions. *physica status solidi (b)*, 243 (13), 3073–3076 (**2006**)

[8] Arnold, M.S., Green, A.A., Hulvat, J.F., Stupp, S.I. and Hersam, M.C. Sorting carbon nanotubes by electronic structure using density differentiation. *Nature Nanotechnology*, 1 (1), 60–65 (**2006**)

[9] Arnold, M.S., Stupp, S.I. and Hersam, M.C. Enrichment of single-walled carbon nanotubes by diameter in density gradients. *Nano Letters*, 5 (4), 713–718 (**2005**)

[10] Arnold, M.S., Suntivich, J., Stupp, S.I. and Hersam, M.C. Hydrodynamic characterization of surfactant encapsulated carbon nanotubes using an analytical ultracentrifuge. *ACS Nano*, 2 (11), 2291–2300 (**2008**)

[11] Ashcroft, N.W. and Mermin, N.D. *Solid State Physics*. Brooks Cole (**1976**). ISBN 0030839939

[12] Atkins, P. and de Paula, J. *Physical Chemistry*. W. H. Freeman (**2006**). ISBN 0716787598

[13] Ausman, K.D., Piner, R., Lourie, O., Ruoff, R.S. and Korobov, M. Organic solvent dispersions of single-walled carbon nanotubes: Toward solutions of pristine nanotubes. *The Journal of Physical Chemistry B*, 104 (38), 8911–8915 (**2000**)

[14] Avouris, P., Freitag, M. and Perebeinos, V. Carbon-nanotube photonics and optoelectronics. *Nature Photonics*, 2 (6), 341–350 (**2008**)

[15] Bachilo, S.M., Strano, M.S., Kittrell, C., Hauge, R.H., Smalley, R.E. and Weisman, R.B. Structure-assigned optical spectra of single-walled carbon nanotubes. *Science*, 298 (5602), 2361–2366 (**2002**)

[16] Bahr, J.L., Mickelson, E.T., Bronikowski, M.J., Smalley, R.E. and Tour, J.M. Dissolution of small diameter single-wall carbon nanotubes in organic solvents? *Chemical Communications*, (2), 193–194 (**2001**)

[17] Barros, E.B., Jorio, A., Samsonidze, G.G., Capaz, R.B., Souza Filho, A.G., Mendes Filho, J., Dresselhaus, G. and Dresselhaus, M.S. Review on the symmetry-related properties of carbon nanotubes. *Physics Reports*, 431 (6), 261–302 (**2006**)

[18] Baughman, R.H. Carbon nanotubes—the route toward applications. *Science*, 297 (5582), 787–792 (**2002**)

[19] Berber, S., Kwon, Y.K. and Tomanek, D. Unusually high thermal conductivity of carbon nanotubes. *Physical Review Letters*, 84 (20), 4613–4613 (**2000**)

[20] Berciaud, S., Cognet, L. and Lounis, B. Luminescence decay and the absorption cross section of individual single-walled carbon nanotubes. *Physical Review Letters*, 101 (7), 077402/1–4 (**2008**)

[21] Bergin, S.D., Nicolosi, V., Cathcart, H., Lotya, M., Rickard, D., Sun, Z., Blau, W.J. and Coleman, J.N. Large populations of individual nanotubes in surfactant-based dispersions without the need for ultracentrifugation. *Journal of Physical Chemistry C*, 112 (4), 972–977 (**2008**)

[22] Bergin, S.D., Nicolosi, V., Giordani, S., Gromard, A.d., Carpenter, L., Blau, W.J. and Coleman, J.N. Exfoliation in ecstasy: liquid crystal formation and concentration-dependent debundling observed for single-wall nanotubes dispersed in the liquid drug γ-butyrolactone. *Nanotechnology*, 18 (45), 455705–455705 (**2007**)

[23] Bergin, S.D., Nicolosi, V., Streich, P.V., Giordani, S., Sun, Z., Windle, A.H., Ryan, P., Niraj, N.P.P., Wang, Z.T.T., Carpenter, L., Blau, W.J., Boland, J.J., Hamilton, J.P. and Coleman, J.N. Towards solutions of single-walled carbon nanotubes in common solvents. *Advanced Materials*, 20 (10), 1876–1881 (**2008**)

[24] Bergin, S.D., Sun, Z., Rickard, D., Streich, P.V., Hamilton, J.P. and Coleman, J.N. Multicomponent solubility parameters for single-walled carbon nanotube–solvent mixtures. *ACS Nano*, 3 (8), 2340–2350 (**2009**)

[25] Bergin, S.D., Sun, Z., Streich, P., Hamilton, J. and Coleman, J.N. New solvents for nanotubes: Approaching the dispersibility of surfactants. *The Journal of Physical Chemistry C*, 114 (1), 231–237 (**2010**)

[26] Bernius, M.T., Inbasekaran, M., O'Brien, J. and Wu, W. Progress with light-emitting polymers. *Advanced Materials*, 12 (23), 1737–1750 (**2000**)

[27] Bethune, D.S., Klang, C.H., de Vries, M.S., Gorman, G., Savoy, R., Vazquez, J. and Beyers, R. Cobalt-catalysed growth of carbon nanotubes with single-atomic-layer walls. *Nature*, 363 (6430), 605–607 (**1993**)

[28] Biercuk, M.J., Llaguno, M.C., Radosavljevic, M., Hyun, J.K., Johnson, A.T. and Fischer, J.E. Carbon nanotube composites for thermal management. *Applied Physics Letters*, 80 (15), 2767–2769 (**2002**)

[29] Blackburn, J.L., McDonald, T.J., Metzger, W.K., Engtrakul, C., Rumbles, G. and Heben, M.J. Protonation effects on the branching ratio in photoexcited single-walled carbon nanotube dispersions. *Nano Letters*, 8 (4), 1047–1054 (**2008**)

[30] Blake, R., Gun'ko, Y.K., Coleman, J., Cadek, M., Fonseca, A., Nagy, J.B. and Blau, W.J. A generic organometallic approach toward ultra-strong carbon nanotube polymer composites. *Journal of the American Chemical Society*, 126 (33), 10226–10227 (**2004**)

[31] Boehm, H.P. The first observation of carbon nanotubes. *Carbon*, 35 (4), 581–584 (**1997**)

[32] Bonaccorso, F. Debundling and selective enrichment of swnts for applications in dye-sensitized solar cells. *International Journal of Photoenergy*, (Art. No. 727134), 1–14 (**2010**)

[33] Boul, P., Liu, J., Mickelson, E., Huffman, C., Ericson, L., Chiang, I., Smith, K., Colbert, D., Hauge, R., Margrave, J. and Smalley, R. Reversible sidewall functionalization of buckytubes. *Chemical Physics Letters*, 310 (3-4), 367–372 (**1999**)

[34] Burroughes, J.H., Bradley, D.D.C., Brown, A.R., Marks, R.N., Mackay, K., Friend, R.H., Burns, P.L. and Holmes, A.B. Light-emitting diodes based on conjugated polymers. *Nature*, 347 (6293), 539–541 (**1990**)

[35] Cadby, A.J., Lane, P.A., Mellor, H., Martin, S.J., Grell, M., Giebeler, C., Bradley, D.D.C., Wohlgenannt, M., An, C. and Vardeny, Z.V. Film morphology and photophysics of polyfluorene. *Physical Review B*, 62 (23), 15604–15604 (**2000**)

[36] Cadek, M., Coleman, J.N., Ryan, K.P., Nicolosi, V., Bister, G., Fonseca, A., Nagy, J.B., Szostak, K., Béguin, F. and Blau, W.J. Reinforcement of polymers with carbon nanotubes: The role of nanotube surface area. *Nano Letters*, 4 (2), 353–356 (**2004**)

[37] Cai, L., Bahr, J., Yao, Y. and Tour, J. Ozonation of single-walled carbon nanotubes and their assemblies on rigid self-assembled monolayers. *Chemistry of Materials*, 14 (10), 4235–4241 (**2002**)

[38] Carlson, L.J., Maccagnano, S.E., Zheng, M., Silcox, J. and Krauss, T.D. Fluorescence efficiency of individual carbon nanotubes. *Nano Letters*, 7 (12), 3698–3703 (**2007**)

[39] Caruso, M.E., Lattante, S., Cingolani, R. and Anni, M. Microscopic investigation of the poly(9,9-dioctylfluorene) photoluminescence dependence on the deposition conditions by confocal laser microscopy. *Applied Physics Letters*, 88 (18), 181906/1–3 (**2006**)

[40] Casey, J.P., Bachilo, S.M., Moran, C.H. and Weisman, R.B. Chirality-resolved length analysis of single-walled carbon nanotube samples through shear-aligned photoluminescence anisotropy. *ACS Nano*, 2 (8), 1738–1746 (**2008**)

[41] Cassell, A.M., Raymakers, J.A., Kong, J. and Dai, H. Large scale cvd synthesis of single-walled carbon nanotubes. *The Journal of Physical Chemistry B*, 103 (31), 6484–6492 (**1999**)

[42] Cathcart, H. and Coleman, J.N. Quantitative comparison of ultracentrifuged and diluted single walled nanotube dispersions; differences in dispersion quality. *Chemical Physics Letters*, 474 (1-3), 122–126 (**2009**)

[43] Chen, J., Hamon, M.A., Hu, H., Chen, Y., Rao, A.M., Eklund, P.C. and Haddon, R.C. Solution properties of single-walled carbon nanotubes. *Science*, 282 (5386), 95–98 (**1998**)

[44] Chen, S.H., Su, A.C., Su, C.H. and Chen, S.A. Crystalline forms and emission behavior of poly(9,9-di-n-octyl-2,7-fluorene). *Macromolecules*, 38 (2), 379–385 (**2005**)

[45] Chen, Y., Haddon, R., Fang, S., Rao, A., Lee, W., Dickey, E., Grulke, E., Pendergrass, J., Chavan, A., Haley, B. and Smalley, R. Chemical attachment of organic functional groups to single-walled carbon nanotube material. *Journal of Materials Research*, 13 (9), 2423–2431 (**1998**)

[46] Cheng, H.M., Li, F., Su, G., Pan, H.Y., He, L.L., Sun, X. and Dresselhaus, M.S. Large-scale and low-cost synthesis of single-walled carbon nanotubes by the catalytic pyrolysis of hydrocarbons. *Applied Physics Letters*, 72 (25), 3282–3284 (**1998**)

[47] Choi, J.H. and Strano, M.S. Solvatochromism in single-walled carbon nanotubes. *Applied Physics Letters*, 90 (22), 223114/1–3 (**2007**)

[48] Cognet, L., Tsyboulski, D.A., Rocha, J.D.R., Doyle, C.D., Tour, J.M. and Weisman, R.B. Stepwise quenching of exciton fluorescence in carbon nanotubes by single-molecule reactions. *Science*, 316 (5830), 1465–1468 (**2007**)

[49] Coleman, J.N., Khan, U., Blau, W.J. and Gun'ko, Y.K. Small but strong: A review of the mechanical properties of carbon nanotube-polymer composites. *Carbon*, 44 (9), 1624–1652 (**2006**)

[50] Crochet, J., Clemens, M. and Hertel, T. Optical properties of structurally sorted single-wall carbon nanotube ensembles. *Physica Status Solidi (b)*, 244 (11), 3964–3968 (**2007**)

[51] Crochet, J., Clemens, M. and Hertel, T. Quantum yield heterogeneities of aqueous single-wall carbon nanotube suspensions. *Journal of the American Chemical Society*, 129, 8058–8059 (**2007**)

[52] Dai, H., Rinzler, A.G., Nikolaev, P., Thess, A., Colbert, D.T. and Smalley, R.E. Single-wall nanotubes produced by metal-catalyzed disproportionation of carbon monoxide. *Chemical Physics Letters*, 260 (3-4), 471–475 (**1996**)

[53] Dalton, A.B., Collins, S., Munoz, E., Razal, J.M., Ebron, V.H., Ferraris, J.P., Coleman, J.N., Kim, B.G. and Baughman, R.H. Super-tough carbon-nanotube fibres. *Nature*, 423 (6941), 703–703 (**2003**)

[54] Datta, S. *Quantum Transport: Atom to Transistor*. Cambridge University Press (**2005**). ISBN 0521631459

[55] Detriche, S., Zorzini, G., Colomer, J., Fonseca, A. and Nagy, J. Application of the hansen solubility parameters theory to carbon nanotubes. *Journal of Nanoscience and Nanotechnology*, 8 (11), 6082–6092 (**2008**)

[56] Di Ventra, M., Evoy, S. and Heflin, J.R. *Introduction to nanoscale science and technology*. Springer (**2004**). ISBN 9781402077203

[57] Dresselhaus, M.S., Dresselhaus, G. and Saito, R. Physics of carbon nanotubes. *Carbon*, 33 (7), 883–891 (**1995**)

[58] Dresselhaus, M.S., Dresselhaus, G., Saito, R. and Jorio, A. Raman spectroscopy of carbon nanotubes. *Physics Reports*, 409 (2), 47–99 (**2005**)

[59] Dresselhaus, M.S., Dresselhaus, G., Saito, R. and Jorio, A. Exciton photophysics of carbon nanotubes. *Annual Review of Physical Chemistry*, 58, 719–747 (**2007**)

[60] Duesberg, G.S., Burghard, M., Muster, J. and Philipp, G. Separation of carbon nanotubes by size exclusion chromatography. *Chemical Communications*, 1998 (3), 435–436 (**1998**)

[61] Duque, J.G., Pasquali, M., Cognet, L. and Lounis, B. Environmental and synthesis-dependent luminescence properties of individual single-walled carbon nanotubes. *ACS Nano*, 3 (8), 2153–2156 (**2009**)

[62] Fagan, J.A., Landi, B.J., Mandelbaum, I., Simpson, J.R., Bajpai, V., Bauer, B.J., Migler, K., Hight Walker, A.R., Raffaelle, R. and Hobbie, E.K. Comparative measures of single-wall carbon nanotube dispersion. *The Journal of Physical Chemistry B*, 110 (47), 23801–23805 (**2006**)

[63] Fagan, J.A., Becker, M.L., Chun, J. and Hobbie, E.K. Length fractionation of carbon nanotubes using centrifugation. *Advanced Materials*, 20 (9), 1609–1613 (**2008**)

[64] Fermi, E. *Nuclear Physics : A Course Given By Enrico Fermi : Revised Edition*. University of Chicago Press (**1958**)

[65] Förster, T. Zwischenmolekulare energiewanderung und fluoreszenz. *Annalen der Physik*, 437 (1-2), 55–75 (**1948**)

[66] Fox, M. *Optical Properties of Solids*. Oxford University Press, USA (**2010**). ISBN 0199573360

[67] Friend, R.H., Gymer, R.W., Holmes, A.B., Burroughes, J.H., Marks, R.N., Taliani, C., Bradley, D.D.C., Santos, D.A.D., Bredas, J.L., Logdlund, M. and Salaneck, W.R. Electroluminescence in conjugated polymers. *Nature*, 397 (6715), 121–128 (**1999**)

[68] Furtado, C.A., Kim, U.J., Gutierrez, H.R., Pan, L., Dickey, E.C. and Eklund, P.C. Debundling and dissolution of single-walled carbon nanotubes in amide solvents. *Journal of the American Chemical Society*, 126 (19), 6095–6105 (**2004**)

[69] Giordani, S., Bergin, S.D., Nicolosi, V., Lebedkin, S., Kappes, M.M., Blau, W.J. and Coleman, J.N. Debundling of single-walled nanotubes by dilution: Observation of large populations of individual nanotubes in amide solvent dispersions. *The Journal of Physical Chemistry B*, 110 (32), 15708–15718 (**2006**)

[70] Gong, X., Liu, J., Baskaran, S., Voise, R.D. and Young, J.S. Surfactant-assisted processing of carbon nanotube/polymer composites. *Chemistry of Materials*, 12 (4), 1049–1052 (**2000**)

[71] Grell, M., Bradley, D.D.C., Long, X., Chamberlain, T., Inbasekaran, M., Woo, E.P. and Soliman, M. Chain geometry, solution aggregation and enhanced dichroism in the liquidcrystalline conjugated polymer poly (9, 9-dioctylfluorene). *Acta Polymerica*, 49 (8), 439–444 (**1998**)

[72] Grell, M., Bradley, D.D.C., Ungar, G., Hill, J. and Whitehead, K.S. Interplay of physical structure and photophysics for a liquid crystalline polyfluorene. *Macromolecules*, 32 (18), 5810–5817 (**1999**)

[73] Grell, M., Knoll, W., Lupo, D., Meisel, A., Miteva, T., Neher, D., Nothofer, H.G., Scherf, U. and Yasuda, A. Blue polarized electroluminescence from a liquid crystalline polyfluorene. *Advanced Materials*, 11 (8), 671–675 (**1999**)

[74] Grice, A.W., Bradley, D.D.C., Bernius, M.T., Inbasekaran, M., Wu, W.W. and Woo, E.P. High brightness and efficiency blue light-emitting polymer diodes. *Applied Physics Letters*, 73 (5), 629–631 (**1998**)

[75] Haddon, R.C., Sippel, J., Rinzler, A.G. and Papa, F. Purification and separation of carbon nanotubes. *MRS Bulletin*, 29 (4), 252–259 (**2004**)

[76] Hagen, A. and Hertel, T. Quantitative analysis of optical spectra from individual single-wall carbon nanotubes. *Nano Letters*, 3 (3), 383–388 (**2003**)

[77] Hagen, A., Steiner, M., Raschke, M.B., Lienau, C., Hertel, T., Qian, H., Meixner, A.J. and Hartschuh, A. Exponential decay lifetimes of excitons in individual single-walled carbon nanotubes. *Physical Review Letters*, 95 (19), 197401/1–4 (**2005**)

[78] Haggenmueller, R., Rahatekar, S.S., Fagan, J.A., Chun, J., Becker, M.L., Naik, R.R., Krauss, T., Carlson, L., Kadla, J.F., Trulove, P.C., Fox, D.F., DeLong, H.C., Fang, Z., Kelley, S.O. and Gilman, J.W. Comparison of the quality of aqueous dispersions of single wall carbon nanotubes using surfactants and biomolecules. *Langmuir*, 24 (9), 5070–5078 (**2008**)

[79] Harris, P.J.F. *Carbon Nanotube Science: Synthesis, Properties and Applications*. Cambridge University Press (**2009**). ISBN 0521828953

[80] Hayer, A., Khan, A.L.T., Friend, R.H. and Köhler, A. Morphology dependence of the triplet excited state formation and absorption in polyfluorene. *Physical Review B*, 71 (24), 241302/1–4 (**2005**)

[81] Hazani, M., Naaman, R., Hennrich, F. and Kappes, M.M. Confocal fluorescence imaging of dna-functionalized carbon nanotubes. *Nano Letters*, 3 (2), 153–155 (**2003**)

[82] Heller, D.A., Baik, S., Eurell, T.E. and Strano, M.S. Single-walled carbon nanotube spectroscopy in live cells: Towards long-term labels and optical sensors. *Advanced Materials*, 17 (23), 2793–2799 (**2005**)

[83] Heller, D.A., Barone, P.W. and Strano, M.S. Sonication-induced changes in chiral distribution: A complication in the use of single-walled carbon nanotube fluorescence for determining species distribution. *Carbon*, 43 (3), 651–653 (**2005**)

[84] Heller, D.A., Mayrhofer, R.M., Baik, S., Grinkova, Y.V., Usrey, M.L. and Strano, M.S. Concomitant length and diameter separation of single-walled carbon nanotubes. *Journal of the American Chemical Society*, 126 (44), 14567–14573 (**2004**)

[85] Hennrich, F., Krupke, R., Arnold, K., Rojas Stütz, J.A., Lebedkin, S., Koch, T., Schimmel, T. and Kappes, M.M. The mechanism of cavitation-induced scission of single-walled carbon nanotubes. *The Journal of Physical Chemistry B*, 111 (8), 1932–1937 (**2007**)

[86] Hertel, T., Hagen, A., Talalaev, V., Arnold, K., Hennrich, F., Kappes, M., Rosenthal, S., McBride, J., Ulbricht, H. and Flahaut, E. Spectroscopy of single- and double-wall carbon nanotubes in different environments. *Nano Letters*, 5 (3), 511–514 (**2005**)

[87] Hertel, T., Himmelein, S., Ackermann, T., Stich, D. and Crochet, J. Diffusion limited photoluminescence quantum yields in 1-d semiconductors: Single-wall carbon nanotubes. *ACS Nano*, 4 (12), 7161–7168 (**2010**)

[88] Hildebrand, J. *Regular and Related Solutions: The Solubility of Gases, Liquids, and Solids*. Krieger Publishing Company (**1970**). ISBN 0442156650

[89] Huang, H., Kajiura, H., Maruyama, R., Kadono, K. and Noda, K. Relative optical absorption of metallic and semiconducting single-walled carbon nanotubes. *The Journal of Physical Chemistry B*, 110 (10), 4686–4690 (**2006**)

[90] Huang, L., Pedrosa, H. and Krauss, T. Ultrafast ground-state recovery of single-walled carbon nanotubes. *Physical Review Letters*, 93 (1), 017403/1–4 (**2004**)

[91] Huang, L., Zhang, H., Wu, B., Liu, Y., Wei, D., Chen, J., Xue, Y., Yu, G., Kajiura, H. and Li, Y. A generalized method for evaluating the metallic-to-semiconducting ratio of separated single-walled carbon nanotubes by UV-Vis-NIR characterization. *The Journal of Physical Chemistry C*, 114 (28), 12095–12098 (**2010**)

[92] Huang, S., Cai, X. and Liu, J. Growth of millimeter-long and horizontally aligned single-walled carbon nanotubes on flat substrates. *Journal of the American Chemical Society*, 125 (19), 5636–5637 (**2003**)

[93] Hwang, J.Y., Nish, A., Doig, J., Douven, S., Chen, C.W., Chen, L.C. and Nicholas, R.J. Polymer structure and solvent effects on the selective dispersion of single-walled carbon nanotubes. *Journal of the American Chemical Society*, 130, 3543–3553 (**2008**)

[94] Iijima, S. Helical microtubules of graphitic carbon. *Nature*, 354, 56–58 (**1991**)

[95] Iijima, S. and Ichihashi, T. Single-shell carbon nanotubes of 1-nm diameter. *Nature*, 363, 603–605 (**1993**)

[96] Iijima, S., Ichihashi, T. and Ando, Y. Pentagons, heptagons and negative curvature in graphite microtubule growth. *Nature*, 356 (6372), 776–778 (**1992**)

[97] Itkis, M.E., Perea, D.E., Niyogi, S., Rickard, S.M., Hamon, M.A., Hu, H., Zhao, B. and Haddon, R.C. Purity evaluation of as-prepared single-walled carbon nanotube soot by use of solution-phase near-ir spectroscopy. *Nano Letters*, 3 (3), 309–314 (**2003**)

[98] Itkis, M.E., Perea, D.E., Jung, R., Niyogi, S. and Haddon, R.C. Comparison of analytical techniques for purity evaluation of single-walled carbon nanotubes. *Journal of the American Chemical Society*, 127 (10), 3439–3448 (**2005**)

[99] Javey, A. and Kong, J. *Carbon Nanotube Electronics*. Springer (**2009**). ISBN 0387368337

[100] Jones, M., Engtrakul, C., Metzger, W.K., Ellingson, R.J., Nozik, A.J., Heben, M.J. and Rumbles, G. Analysis of photoluminescence from solubilized single-walled carbon nanotubes. *Physical Review B*, 71 (11), 115426/1–9 (**2005**)

[101] Jones, M., Metzger, W.K., McDonald, T.J., Engtrakul, C., Ellingson, R.J., Rumbles, G. and Heben, M.J. Extrinsic and intrinsic effects on the excited-state kinetics of single-walled carbon nanotubes. *Nano Letters*, 7 (2), 300–306 (**2007**)

[102] Jorio, A., Fantini, C., Pimenta, M.A., Heller, D.A., Strano, M.S., Dresselhaus, M.S., Oyama, Y., Jiang, J. and Saito, R. Carbon nanotube population analysis from raman and photoluminescence intensities. *Applied Physics Letters*, 88 (2), 023109/1–3 (**2006**)

[103] Journet, C. and Maser, W.K. Large-scale production of single-walled carbon nanotubes by the electric-arc technique. *Nature*, 388 (6644), 756–758 (**1997**)

[104] Ju, S.Y., Kopcha, W.P. and Papadimitrakopoulos, F. Brightly fluorescent single-walled carbon nanotubes via an oxygen-excluding surfactant organization. *Science*, 323 (5919), 1319–1323 (**2009**)

[105] Ju, S.Y., Doll, J., Sharma, I. and Papadimitrakopoulos, F. Selection of carbon nanotubes with specific chiralities using helical assemblies of flavin mononucleotide. *Nature Nanotechnology*, 3 (6), 356–362 (**2008**)

[106] Kane, C.L. and Mele, E.J. Ratio problem in single carbon nanotube fluorescence spectroscopy. *Physical Review Letters*, 90 (20), 207401/1–4 (**2003**)

[107] Kataura, H., Kumazawa, Y., Maniwa, Y., Umezu, I., Suzuki, S., Ohtsuka, Y. and Achiba, Y. Optical properties of single-wall carbon nanotubes. *Synthetic Metals*, 103 (1-3), 2555–2558 (**1999**)

[108] Kato, T. and Hatakeyama, R. Exciton energy transfer-assisted photoluminescence brightening from freestanding single-walled carbon nanotube bundles. *Journal of the American Chemical Society*, 130 (25), 8101–8107 (**2008**)

[109] Kelly, K., Chiang, I., Mickelson, E., Hauge, R., Margrave, J., Wang, X., Scuseria, G., Radloff, C. and Halas, N. Insight into the mechanism of sidewall functionalization of single-walled nanotubes: an stm study. *Chemical Physics Letters*, 313 (3-4), 445–450 (**1999**)

[110] Khan, A.L.T., Banach, M.J. and Köhler, A. Control of β-phase formation in polyfluorene thin films via franck-condon analysis. *Synthetic Metals*, 139 (3), 905–907 (**2003**)

[111] Khan, A.L.T., Sreearunothai, P., Herz, L.M., Banach, M.J. and Köhler, A. Morphology-dependent energy transfer within polyfluorene thin films. *Physical Review B*, 69 (8), 085201/1–8 (**2004**)

[112] Kilbride, B.E., Coleman, J.N., Fraysse, J., Fournet, P., Cadek, M., Drury, A., Hutzler, S., Roth, S. and Blau, W.J. Experimental observation of scaling laws for alternating current and direct current conductivity in polymer-carbon nanotube composite thin films. *Journal of Applied Physics*, 92 (7), 4024–4030 (**2002**)

[113] Kinder, J.M. and Mele, E.J. Nonradiative recombination of excitons in carbon nanotubes mediated by free charge carriers. *Physical Review B*, 78 (15), 155429–155429 (**2008**)

[114] Kong, J., Franklin, N.R., Zhou, C., Chapline, M.G., Peng, S., Cho, K. and Dai, H. Nanotube molecular wires as chemical sensors. *Science*, 287 (5453), 622–625 (**2000**)

[115] Kopainsky, B., Qiu, P., Kaiser, W., Sens, B. and Drexhage, K.H. Lifetime, photostability, and chemical structure of ir heptamethine cyanine dyes absorbing beyond 1 μm. *Applied Physics B: Lasers and Optics*, 29 (1), 15–18 (**1982**)

[116] Kose, M.E., Harruff, B.A., Lin, Y., Veca, L.M., Lu, F. and Sun, Y.P. Efficient quenching of photoluminescence from functionalized single-walled carbon nanotubes by nitroaromatic molecules. *The Journal of Physical Chemistry B*, 110 (29), 14032–14034 (**2006**)

[117] Kratschmer, W., Lamb, L.D., Fostiropoulos, K. and Huffman, D.R. Solid c60: a new form of carbon. *Nature*, 347 (6291), 354–358 (**1990**)

[118] Kroto, H.W., Heath, J.R., O'Brien, S.C., Curl, R.F. and Smalley, R.E. C60: Buckminsterfullerene. *Nature*, 318, 162–163 (**1985**)

[119] Kubin, R.F. and Fletcher, A.N. Fluorescence quantum yields of some rhodamine dyes. *Journal of Luminescence*, 27 (4), 455–462 (**1982**)

[120] Kubista, M., Sjoback, R., Eriksson, S. and Albinsson, B. Experimental correction for the inner-filter effect in fluorescence spectra. *The Analyst*, 119 (3), 417–419 (**1994**)

[121] Kuwahara, S., Sugai, T. and Shinohara, H. Determining exact molar absorbance coefficients of single-wall carbon nanotubes. *Physical Chemistry Chemical Physics*, 11 (7), 1091–1097 (**2009**)

[122] Lakowicz, J.R. *Principles of fluorescence spectroscopy*. Springer (**2006**). ISBN 9780387312781

[123] Landi, B.J., Ruf, H.J., Worman, J.J. and Raffaelle, R.P. Effects of alkyl amide solvents on the dispersion of single-wall carbon nanotubes. *The Journal of Physical Chemistry B*, 108 (44), 17089–17095 (**2004**)

[124] Lebedkin, S., Arnold, K., Hennrich, F., Krupke, R., Renker, B. and Kappes, M.M. Ftir-luminescence mapping of dispersed single-walled carbon nanotubes. *New Journal of Physics*, 5, 140.1–140.11 (**2003**)

[125] Lebedkin, S., Hennrich, F., Kiowski, O. and Kappes, M.M. Photophysics of carbon nanotubes in organic polymer-toluene dispersions: Emission and excitation satellites and relaxation pathways. *Physical Review B*, 77 (16) (**2008**)

[126] Lebedkin, S., Hennrich, F., Skipa, T. and Kappes, M.M. Near-infrared photoluminescence of single-walled carbon nanotubes prepared by the laser vaporization method. *The Journal of Physical Chemistry B*, 107 (9), 1949–1956 (**2003**)

[127] Lefebvre, J., Fraser, J.M., Finnie, P. and Homma, Y. Photoluminescence from an individual single-walled carbon nanotube. *Physical Review B*, 69 (7), 075403/1–5 (**2004**)

[128] Lefebvre, J., Fraser, J.M., Homma, Y. and Finnie, P. Photoluminescence from single-walled carbon nanotubes: a comparison between suspended and micelle-encapsulated nanotubes. *Applied Physics A: Materials Science & Processing*, 78 (8), 1107–1110 (**2004**)

[129] Lefebvre, J., Maruyama, S. and Finnie, P. Photoluminescence: science and applications. *Topics in Applied Physics*, 111, 287–319 (**2008**)

[130] Lefebvre, J., Austing, D.G., Bond, J. and Finnie, P. Photoluminescence imaging of suspended single-walled carbon nanotubes. *Nano Letters*, 6 (8), 1603–1608 (**2006**)

[131] Li, L.J., Nicholas, R.J., Chen, C.Y., Darton, R.C. and Baker, S.C. Comparative study of photoluminescence of single-walled carbon nanotubes wrapped with sodium dodecyl sulfate, surfactin and polyvinylpyrrolidone. *Nanotechnology*, 16 (5), S202–S205 (**2005**)

[132] Li, W.Z., Xie, S.S., Qian, L.X., Chang, B.H., Zou, B.S., Zhou, W.Y., Zhao, R.A. and Wang, G. Large-scale synthesis of aligned carbon nanotubes. *Science*, 274 (5293), 1701–1703 (**1996**)

[133] Li, X., Tu, X., Zaric, S., Welsher, K., Seo, W.S., Zhao, W. and Dai, H. Selective synthesis combined with chemical separation of single-walled carbon nanotubes for chirality selection. *Journal of the American Chemical Society*, 129 (51), 15770–15771 (**2007**)

[134] Li, Y., Kim, W., Zhang, Y., Rolandi, M., Wang, D. and Dai, H. Growth of single-walled carbon nanotubes from discrete catalytic nanoparticles of various sizes. *The Journal of Physical Chemistry B*, 105 (46), 11424–11431 (**2001**)

[135] Lian, Y., Maeda, Y., Wakahara, T., Akasaka, T., Kazaoui, S., Minami, N., Choi, N. and Tokumoto, H. Assignment of the fine structure in the optical absorption spectra of soluble single-walled carbon nanotubes. *The Journal of Physical Chemistry B*, 107 (44), 12082–12087 (**2003**)

[136] Liang, W., Bockrath, M., Bozovic, D., Hafner, J.H., Tinkham, M. and Park, H. Fabry-Perot interference in a nanotube electron waveguide. *Nature*, 411 (6838), 665–669 (**2001**)

[137] Lin, Y., Zhou, B., Martin, R.B., Henbest, K.B., Harruff, B.A., Riggs, J.E., Guo, Z.X., Allard, L.F. and Sun, Y.P. Visible luminescence of carbon nanotubes and dependence on functionalization. *Journal of Physical Chemistry B*, 109 (31), 14779–14782 (**2005**)

[138] Liu, J., Rinzler, A., Dai, H., Hafner, J., Bradley, R., Boul, P., Lu, A., Iverson, T., Shelimov, K., Huffman, C., Rodriguez-Macias, F., Shon, Y., Lee, T., Colbert, D. and Smalley, R. Fullerene pipes. *Science*, 280 (5367), 1253–1256 (**1998**)

[139] Lucas, A., Zakri, C., Maugey, M., Pasquali, M., Schoot, P.v.d. and Poulin, P. Kinetics of nanotube and microfiber scission under sonication. *The Journal of Physical Chemistry C*, 113 (48), 20599–20605 (**2009**)

[140] Luo, Z., Pfefferle, L.D., Haller, G.L. and Papadimitrakopoulos, F. (*n*,*m*) abundance evaluation of single-walled carbon nanotubes by fluorescence and absorption spectroscopy. *Journal of the American Chemical Society*, 128 (48), 15511–15516 (**2006**)

[141] Ma, Y., Hertel, T., Vardeny, Z.V., Fleming, G.R. and Valkunas, L. Ultrafast spectroscopy of carbon nanotubes. *Topics in Applied Physics*, 111, 321–353 (**2008**)

[142] Maeda, Y., Kanda, M., Hashimoto, M., Hasegawa, T., Kimura, S.i., Lian, Y., Wakahara, T., Akasaka, T., Kazaoui, S., Minami, N., Okazaki, T., Hayamizu, Y., Hata, K., Lu, J. and Nagase, S. Dispersion and separation of small-diameter single-walled carbon nanotubes. *Journal of the American Chemical Society*, 128 (37), 12239–12242 (**2006**)

[143] Maeda, Y., Kimura, S.i., Hirashima, Y., Kanda, M., Lian, Y., Wakahara, T., Akasaka, T., Hasegawa, T., Tokumoto, H., Shimizu, T., Kataura, H., Miyauchi, Y., Maruyama, S., Kobayashi, K. and Nagase, S. Dispersion of single-walled carbon nanotube bundles in nonaqueous solution. *The Journal of Physical Chemistry B*, 108 (48), 18395–18397 (**2004**)

[144] Maultzsch, J., Pomraenke, R., Reich, S., Chang, E., Prezzi, D., Ruini, A., Molinari, E., Strano, M.S., Thomsen, C. and Lienau, C. Exciton binding energies in carbon nanotubes from two-photon photoluminescence. *Physical Review B*, 72 (24), 241402/1–4 (**2005**)

[145] Miller, J.N. *Standards in Fluorescence Spectroscopy*. Chapman (**1981**). ISBN 041222500X

[146] Minami, N., Kim, Y., Miyashita, K., Kazaoui, S. and Nalini, B. Cellulose derivatives as excellent dispersants for single-wall carbon nanotubes as demonstrated by absorption and photoluminescence spectroscopy. *Applied Physics Letters*, 88 (9), 093123/1–3 (**2006**)

[147] Miteva, T., Meisel, A., Knoll, W., Nothofer, H.G., Scherf, U., Müller, D.C., Meerholz, K., Yasuda, A. and Neher, D. Improving the performance of polyfluorene-based organic light-emitting diodes via end-capping. *Advanced Materials*, 13 (8), 565–570 (**2001**)

[148] Miyauchi, Y., Saito, R., Sato, K., Ohno, Y., Iwasaki, S., Mizutani, T., Jiang, J. and Maruyama, S. Dependence of exciton transition energy of single-walled carbon nanotubes on surrounding dielectric materials. *Chemical Physics Letters*, 442, 394–399 (**2007**)

[149] Miyauchi, Y., Oba, M. and Maruyama, S. Cross-polarized optical absorption of single-walled nanotubes by polarized photoluminescence excitation spectroscopy. *Physical Review B*, 74 (20) (**2006**)

[150] Monthioux, M. and Kuznetsov, V.L. Who should be given the credit for the discovery of carbon nanotubes? *Carbon*, 44 (9), 1621–1623 (**2006**)

[151] Moore, V.C., Strano, M.S., Haroz, E.H., Hauge, R.H., Smalley, R.E., Schmidt, J. and Talmon, Y. Individually suspended single-walled carbon nanotubes in various surfactants. *Nano Letters*, 3 (10), 1379–1382 (**2003**)

[152] Nair, N., Usrey, M.L., Kim, W.J., Braatz, R.D. and Strano, M.S. Estimation of the (n,m) concentration distribution of single-walled carbon nanotubes from photoabsorption spectra. *Analytical Chemistry*, 78, 7689–7696 (**2006**)

[153] Nair, N., Kim, W.J., Braatz, R.D. and Strano, M.S. Dynamics of surfactant-suspended single-walled carbon nanotubes in a centrifugal field. *Langmuir*, 24 (5), 1790–1795 (**2008**)

[154] Naumov, A.V., Kuznetsov, O.A., Harutyunyan, A.R., Green, A.A., Hersam, M.C., Resasco, D.E., Nikolaev, P.N. and Weisman, R.B. Quantifying the semiconducting fraction in single-walled carbon nanotube samples through comparative atomic force and photoluminescence microscopies. *Nano Letters*, 9 (9), 3203–3208 (**2009**)

[155] Nicolosi, V., Vrbanic, D., Mrzel, A., McCauley, J., O'Flaherty, S., McGuinness, C., Compagnini, G., Mihailovic, D., Blau, W.J. and Coleman, J.N. Solubility of $Mo_6S_{4.5}I_{4.5}$ nanowires in common solvents: A sedimentation study. *The Journal of Physical Chemistry B*, 109 (15), 7124–7133 (**2005**)

[156] Nikolaev, P., Bronikowski, M.J., Bradley, R.K., Rohmund, F., Colbert, D.T., Smith, K.A. and Smalley, R.E. Gas-phase catalytic growth of single-walled carbon nanotubes from carbon monoxide. *Chemical Physics Letters*, 313 (1-2), 91–97 (**1999**)

[157] Nish, A., Hwang, J.Y., Doig, J. and Nicholas, R.J. Highly selective dispersion of single-walled carbon nanotubes using aromatic polymers. *Nature Nanotechnology*, 2 (10), 640–646 (**2007**)

[158] O'Connell, M.J., Boul, P., Ericson, L.M., Huffman, C., Wang, Y., Haroz, E., Kuper, C., Tour, J., Ausman, K.D. and Smalley, R.E. Reversible water-solubilization of single-walled carbon nanotubes by polymer wrapping. *Chemical Physics Letters*, 342 (3-4), 265–271 (**2001**)

[159] O'Connell, M., Bachilo, S., Huffman, C., Moore, V., Strano, M., Haroz, E., Rialon, K., Boul, P., Noon, W., Kittrell, C., Ma, J., Hauge, R., Weisman, R. and Smalley, R. Band gap fluorescence from individual single-walled carbon nanotubes. *Science*, 297 (5581), 593–596 (**2002**)

[160] Ohmori, S., Saito, T., Tange, M., Shukla, B., Okazaki, T., Yumura, M. and Iijima, S. Fundamental importance of background analysis in precise characterization of single-walled carbon nanotubes by optical absorption spectroscopy. *The Journal of Physical Chemistry C*, 114 (22), 10077–10081 (**2010**)

[161] Ohno, Y., Iwasaki, S., Murakami, Y., Kishimoto, S., Maruyama, S. and Mizutani, T. Excitonic transition energies in single-walled carbon nanotubes: Dependence on environmental dielectric constant. *Physica Status Solidi (b)*, 244 (11), 4002–4005 (**2007**)

[162] Ohno, Y., Iwasaki, S., Murakami, Y., Kishimoto, S., Maruyama, S. and Mizutani, T. Chirality-dependent environmental effects in photoluminescence of single-walled carbon nanotubes. *Physical Review B*, 73 (23) (**2006**)

[163] Okazaki, T., Saito, T., Matsuura, K., Ohshima, S., Yumura, M., Oyama, Y., Saito, R. and Iijima, S. Photoluminescence and population analysis of single-walled carbon nanotubes produced by cvd and pulsed-laser vaporization methods. *Chemical Physics Letters*, 420 (4-6), 286–290 (**2006**)

[164] Ostojic, G.N., Zaric, S. and Kono, J. Interband recombination dynamics in resonantly excited single-walled carbon nanotubes. *Physical Review Letters*, 92 (11) (**2004**)

[165] Oyama, Y., Saito, R., Sato, K., Jiang, J., Samsonidze, G.G., Grüneis, A., Miyauchi, Y., Maruyama, S., Jorio, A., Dresselhaus, G. and Dresselhaus, M.S. Photoluminescence intensity of single-wall carbon nanotubes. *Carbon*, 44 (5), 873–879 (**2006**)

[166] Parker, C.A. and Rees, W.T. Fluorescence spectrometry. a review. *The Analyst*, 87 (1031), 83–111 (**1962**)

[167] Perebeinos, V., Tersoff, J. and Avouris, P. Effect of exciton-phonon coupling in the calculated optical absorption of carbon nanotubes. *Physical Review Letters*, 94 (2), 027402–027402 (**2005**)

[168] Poncharal, P., Berger, C., Yi, Y., Wang, Z.L. and de Heer, W.A. Room temperature ballistic conduction in carbon nanotubes. *The Journal of Physical Chemistry B*, 106 (47), 12104–12118 (**2002**)

[169] Qian, H., Georgi, C., Anderson, N., Green, A.A., Hersam, M.C., Novotny, L. and Hartschuh, A. Exciton energy transfer in pairs of single-walled carbon nanotubes. *Nano Letters*, 8 (5), 1363–1367 (**2008**)

[170] Rajan, A., Strano, M.S., Heller, D.A., Hertel, T. and Schulten, K. Length-dependent optical effects in single walled carbon nanotubes. *The Journal of Physical Chemistry B*, 112 (19), 6211–6213 (**2008**)

[171] Rance, G.A., Marsh, D.H., Nicholas, R.J. and Khlobystov, A.N. Uv-Vis absorption spectroscopy of carbon nanotubes: Relationship between the π-electron plasmon and nanotube diameter. *Chemical Physics Letters*, 493 (1-3), 19–23 (**2010**)

[172] Reich, S. and Strano, M.S. Excited-state carrier lifetime in single-walled carbon nanotubes. *Physical Review B*, 71 (3) (**2005**)

[173] Reich, S., Thomsen, C. and Robertson, J. Exciton resonances quench the photoluminescence of zigzag carbon nanotubes. *Physical Review Letters*, 95 (7), 077402/1–4 (**2005**)

[174] Rickard, D., Giordani, S., Blau, W.J. and Coleman, J.N. Quantifying the contributions of inner-filter, re-absorption and aggregation effects in the photoluminescence of high-concentration conjugated polymer solutions. *Journal of Luminescence*, 128 (1), 31–40 (**2008**)

[175] Riesz, J., Gilmore, J. and Meredith, P. Quantitative photoluminescence of broad band absorbing melanins: a procedure to correct for inner filter and re-absorption effects. *Spectrochimica Acta Part A: Molecular and Biomolecular Spectroscopy*, 61 (9), 2153–2160 (**2005**)

[176] Rubinstein, M. and Colby, R.H. *Polymer Physics*. Oxford University Press, USA (**2003**). ISBN 019852059X

[177] Ryabenko, A.G., Dorofeeva, T.V. and Zvereva, G.I. UV-Vis-NIR spectroscopy study of sensitivity of single-wall carbon nanotubes to chemical processing and van der Waals SWNT/SWNT interaction. verification of the SWNT content measurements by absorption spectroscopy. *Carbon*, 42 (8-9), 1523–1535 (**2004**)

[178] Saito, R., Dresselhaus, G. and Dresselhaus, M.S. *Physical Properties of Carbon Nanotubes*. World Scientific Publishing Company (**1998**). ISBN 1860942237

[179] Saito, R., Dresselhaus, G. and Dresselhaus, M.S. Trigonal warping effect of carbon nanotubes. *Physical Review B*, 61 (4), 2981–2990 (**2000**)

[180] Saito, R. and Fujita, M. Electronic structure of chiral graphene tubules. *Applied Physics Letters*, 60 (18), 2204–2206 (**1992**)

[181] Saito, T., Ohmori, S., Shukla, B., Yumura, M. and Iijima, S. A novel method for characterizing the diameter of single-wall carbon nanotubes by optical absorption spectra. *Applied Physics Express*, 2, 095006/1–3 (**2009**)

[182] Samsonidze, G.G., Saito, R., Jorio, A., Pimenta, M.A., Souza Filho, A.G., Grüneis, A., Dresselhaus, G. and Dresselhausa, M.S. The concept of cutting lines in carbon nanotube science. *Journal of Nanoscience and Nanotechnology*, 3, 431–458 (**2003**)

[183] Schmidt, R., Seikel, K. and Brauer, H.D. Determination of the phosphorescence quantum yield of singlet molecular-oxygen ($^1\Delta_g$) in 5 different solvents. *Journal of Physical Chemistry*, 93 (11), 4507–4511 (**1989**)

[184] Semonin, O.E., Johnson, J.C., Luther, J.M., Midgett, A.G., Nozik, A.J. and Beard, M.C. Absolute photoluminescence quantum yields of IR-26 dye, PbS, and PbSe quantum dots. *The Journal of Physical Chemistry Letters*, 1 (16), 2445–2450 (**2010**)

[185] Shaffer, M.S.P., Fan, X. and Windle, A.H. Dispersion and packing of carbon nanotubes. *Carbon*, 36 (11), 1603–1612 (**1998**)

[186] Shimizu, O., Watanabe, J., Imakubo, K. and Naito, S. Absolute quantum yields and lifetimes of photosensitized phosphorescence of singlet oxygen O_2 ($^1\Delta_g$) in air-saturated aqueous and organic solutions of phenalenone. *Chemistry Letters*, (1), 67–68 (**1999**)

[187] Siitonen, A.J., Tsyboulski, D.A., Bachilo, S.M. and Weisman, R.B. Dependence of exciton mobility on structure in single-walled carbon nanotubes. *The Journal of Physical Chemistry Letters*, 1 (14), 2189–2192 (**2010**)

[188] Silvera-Batista, C.A., Weinberg, P., Butler, J.E. and Ziegler, K.J. Long-term improvements to photoluminescence and dispersion stability by flowing SDS-SWNT suspensions through microfluidic channels. *Journal of the American Chemical Society*, 131 (35), 12721–12728 (**2009**)

[189] Spataru, C.D., Ismail-Beigi, S., Capaz, R.B. and Louie, S.G. Quasiparticle and excitonic effects in the optical response of nanotubes and nanoribbons. *Topics in Applied Physics*, 111, 195–227 (**2008**)

[190] Star, A., Lu, Y., Bradley, K. and Grüner, G. Nanotube optoelectronic memory devices. *Nano Letters*, 4 (9), 1587–1591 (**2004**)

[191] Strano, M.S., Huffman, C.B., Moore, V.C., O'Connell, M.J., Haroz, E.H., Hubbard, J., Miller, M., Rialon, K., Kittrell, C., Ramesh, S., Hauge, R.H. and Smalley, R.E. Reversible, band-gap-selective protonation of single-walled carbon nanotubes in solution. *Journal of Physical Chemistry B*, 107 (29), 6979–6985 (**2003**)

[192] Strano, M., Moore, V., Miller, M., Allen, M., Haroz, E., Kittrell, C., Hauge, R. and Smalley, R. The role of surfactant adsorption during ultrasonication in the dispersion of single-walled carbon nanotubes. *Journal of Nanoscience and Nanotechnology*, 3 (1-2), 81–86 (**2003**)

[193] Stürzl, N., Hennrich, F., Lebedkin, S. and Kappes, M.M. Near monochiral single-walled carbon nanotube dispersions in organic solvents. *The Journal of Physical Chemistry C*, 113 (33), 14628–14632 (**2009**)

[194] Stürzl, N., Lebedkin, S. and Kappes, M.M. Revisiting the laser dye Styryl-13 as a reference near-infrared fluorophore: Implications for the photoluminescence quantum yields of semiconducting single-walled carbon nanotubes. *The Journal of Physical Chemistry A*, 113 (38), 10238–10240 (**2009**)

[195] Subbarao, N.K. and MacDonald, R.C. Experimental method to correct fluorescence intensities for the inner filter effect. *The Analyst*, 118 (7), 913–916 (**1993**)

[196] Sun, S.F. *Physical chemistry of macromolecules: basic principles and issues*. Wiley-IEEE (**2004**). ISBN 9780471281382

[197] Sun, X., Zaric, S., Daranciang, D., Welsher, K., Lu, Y., Li, X. and Dai, H. Optical properties of ultrashort semiconducting single-walled carbon nanotube capsules down to sub-10 nm. *Journal of the American Chemical Society*, 130 (20), 6551–6555 (**2008**)

[198] Sun, Z., Nicolosi, V., Rickard, D., Bergin, S.D., Aherne, D. and Coleman, J.N. Quantitative evaluation of surfactant-stabilized single-walled carbon nanotubes: Dispersion quality and its correlation with zeta potential. *Journal of Physical Chemistry C*, 112 (29), 10692–10699 (**2008**)

[199] Tan, P.H., Hasan, T., Bonaccorso, F., Scardaci, V., Rozhin, A.G., Milne, W.I. and Ferrari, A.C. Optical properties of nanotube bundles by photoluminescence excitation and absorption spectroscopy. *Physica E: Low-dimensional Systems and Nanostructures* 2352–2359 (**2007**)

[200] Tan, P.H., Rozhin, A.G., Hasan, T., Hu, P., Scardaci, V., Milne, W.I. and Ferrari, A.C. Photoluminescence spectroscopy of carbon nanotube bundles: Evidence for exciton energy transfer. *Physical Review Letters*, 99 (13), 137402/1–4 (**2007**)

[201] Tans, S.J., Verschueren, A.R.M. and Dekker, C. Room-temperature transistor based on a single carbon nanotube. *Nature*, 393 (6680), 49–52 (**1998**)

[202] Thess, A., Lee, R., Nikolaev, P., Dai, H., Petit, P., Robert, J., Xu, C., Lee, Y.H., Kim, S.G., Rinzler, A.G., Colbert, D.T., Scuseria, G.E., Tomanek, D., Fischer, J.E. and Smalley, R.E. Crystalline ropes of metallic carbon nanotubes. *Science*, 273 (5274), 483–487 (**1996**)

[203] Treacy, M.M.J., Ebbesen, T.W. and Gibson, J.M. Exceptionally high Young's modulus observed for individual carbon nanotubes. *Nature*, 381 (6584), 678–680 (**1996**)

[204] Tsyboulski, D.A., Rocha, J.D.R., Bachilo, S.M., Cognet, L. and Weisman, R.B. Structure-dependent fluorescence efficiencies of individual single-walled carbon nanotubes. *Nano Letters*, 7 (10), 3080–3085 (**2007**)

[205] Wallace, P.R. The band theory of graphite. *Physical Review*, 71 (9), 622–634 (**1947**)

[206] Wang, F., Dukovic, G., Brus, L.E. and Heinz, T.F. The optical resonances in carbon nanotubes arise from excitons. *Science*, 308 (5723), 838–841 (**2005**)

[207] Wang, F., Dukovic, G., Brus, L.E. and Heinz, T.F. Time-resolved fluorescence of carbon nanotubes and its implication for radiative lifetimes. *Physical Review Letters*, 92 (17), 177401/1–4 (**2004**)

[208] Wang, J. Carbon-nanotube based electrochemical biosensors: A review. *Electroanalysis*, 17 (1), 7–14 (**2005**)

[209] Wang, J. and Musameh, M. Carbon nanotube/teflon composite electrochemical sensors and biosensors. *Analytical Chemistry*, 75 (9), 2075–2079 (**2003**)

[210] Wang, J., Musameh, M. and Lin, Y. Solubilization of carbon nanotubes by nafion toward the preparation of amperometric biosensors. *Journal of the American Chemical Society*, 125 (9), 2408–2409 (**2003**)

[211] Wang, S.C., Yang, H., Banerjee, S., Herman, I.P. and Akins, D.L. AOT dispersed single-walled carbon nanotubes for transistor device application. *Materials Letters*, 62 (6-7), 843–845 (**2008**)

[212] Weisman, R.B. and Bachilo, S.M. Dependence of optical transition energies on structure for single-walled carbon nanotubes in aqueous suspension: an empirical Kataura plot. *Nano Letters*, 3 (9), 1235–1238 (**2003**)

[213] Weisman, R.B., Bachilo, S.M. and Tsyboulski, D. Fluorescence spectroscopy of single-walled carbon nanotubes in aqueous suspension. *Applied Physics A: Materials Science & Processing*, 78 (8), 1111–1116 (**2004**)

[214] Wenseleers, W., Vlasov, I.I., Goovaerts, E., Obraztsova, E.D., Lobach, A.S. and Bouwen, A. Efficient isolation and solubilization of pristine single-walled nanotubes in bile salt micelles. *Advanced Functional Materials*, 14 (11), 1105–1112 (**2004**)

[215] White, C.T. and Todorov, T.N. Carbon nanotubes as long ballistic conductors. *Nature*, 393, 240–242 (**1998**)

[216] Whitehead, K.S., Grell, M., Bradley, D.D.C., Jandke, M. and Strohriegl, P. Highly polarized blue electroluminescence from homogeneously aligned films of poly(9,9-dioctylfluorene). *Applied Physics Letters*, 76 (20), 2946–2948 (**2000**)

[217] Wildöer, J.W.G., Venema, L.C., Rinzler, A.G., Smalley, R.E. and Dekker, C. Electronic structure of atomically resolved carbon nanotubes. *Nature*, 391 (6662), 59–62 (**1998**)

[218] Yao, Z., Kane, C.L. and Dekker, C. High-field electrical transport in single-wall carbon nanotubes. *Physical Review Letters*, 84 (13), 2941–2944 (**2000**)

[219] Yappert, M.C.. and Ingle, J.D.. Correction of polychromatic luminescence signals for inner-filter effects. *Applied Spectroscopy*, 43, 759–767 (**1989**)

[220] Yoshikawa, K., Matsuda, K. and Kanemitsu, Y. Exciton transport in suspended single carbon nanotubes studied by photoluminescence imaging spectroscopy. *The Journal of Physical Chemistry C*, 114 (10), 4353–4356 (**2010**)

[221] Yu, M.F., Files, B.S., Arepalli, S. and Ruoff, R.S. Tensile loading of ropes of single wall carbon nanotubes and their mechanical properties. *Physical Review Letters*, 84 (24), 5552–5555 (**2000**)

[222] Yu, M.F., Lourie, O., Dyer, M.J., Moloni, K., Kelly, T.F. and Ruoff, R.S. Strength and breaking mechanism of multiwalled carbon nanotubes under tensile load. *Science*, 287 (5453), 637–640 (**2000**)

[223] Zhang, C., Liu, M.S., Han, B. and Xing, X.H. Correcting for the inner filter effect in measurements of fluorescent proteins in high-cell-density cultures. *Analytical Biochemistry*, 390 (2), 197–202 (**2009**)

[224] Zhang, X.F., Zhang, X.B., Van Tendeloo, G., Amelinckx, S., Op de Beeck, M. and Van Landuyt, J. Carbon nano-tubes; their formation process and observation by electron microscopy. *Journal of Crystal Growth*, 130 (3-4), 368–382 (**1993**)

[225] Zhao, B., Itkis, M.E., Niyogi, S., Hu, H., Zhang, J. and Haddon, R.C. Study of the extinction coefficients of single-walled carbon nanotubes and related carbon materials. *The Journal of Physical Chemistry B*, 108 (24), 8136–8141 (**2004**)

[226] Zhao, H., Mazumdar, S., Sheng, C.X., Tong, M. and Vardeny, Z.V. Photophysics of excitons in quasi-one-dimensional organic semiconductors: Single-walled carbon nanotubes and π-conjugated polymers. *Physical Review B (Condensed Matter and Materials Physics)*, 73 (7), 075403/1–11 (**2006**)

[227] Zheng, M., Jagota, A., Semke, E.D., Diner, B.A., Mclean, R.S., Lustig, S.R., Richardson, R.E. and Tassi, N.G. DNA-assisted dispersion and separation of carbon nanotubes. *Nature Materials*, 2 (5), 338–342 (**2003**)